

by

Jenny Jiahui Wu

B.Sc., University of Toronto, 2017

A thesis submitted to the
Faculty of the Graduate School of the
University of Colorado in partial fulfillment
of the requirements for the degree of
Doctor of Philosophy
Department of Physics
2024

Committee Members:
Dietrich Leibfried, Chair
Scott Glancy
Adam Kaufman
James Thompson
Greg Rieker

Wu, Jenny Jiahui (Ph.D., Physics)

Quantum Control of Motional States in Mixed-Species Trapped-Ion Crystals

Thesis directed by NIST Fellow Dietrich Leibfried

Trapped ions are a powerful and flexible platform used for scientific applications ranging from studies of fundamental physics and precision spectroscopy to quantum simulation and quantum information processing. These applications are enabled by the excellent control that can be exerted over the long-lived atomic states of trapped ions using electromagnetic fields. In crystals containing multiple ions, the shared motion is used as a mediator to couple the atomic states of distant ions.

This thesis focuses on improving the control over ion motion, and in particular for crystals that contain multiple ion species. The first set of experiments discussed in this thesis is the application of a ground-state cooling method known as electromagnetically-induced-transparency (EIT) cooling to $^{25}\text{Mg}^+$. This ion has a complex hyperfine structure which enables the implementation of a long-lived qubit. By demonstrating EIT cooling on $^{25}\text{Mg}^+$, it is shown that such qubit ions are also compatible with this resource-efficient sub-Doppler cooling method.

The normal modes of trapped-ion motion are well-described by quantum harmonic oscillators, and the second set of experiments described in this thesis covers the direct, rapid, and parametric coupling between two harmonic oscillators in the motion modes of multi-ion crystals. This coupling can be used to indirectly cool ion modes that are otherwise difficult or inefficient to cool. It can also be used to perform mid-circuit non-destructive readout of trapped-ion motion, which is useful for the study of states encoded in the ion motion, such as those used for bosonic error correction.

Dedication

To those who inspire me, and to those who believe in me.

Acknowledgements

There are too many people that deserve credit for what I have been able to achieve during the past seven years. I would like to extend thanks to all my family, friends, and mentors; it would be impossible to mention everyone here.

First I would like to acknowledge my parents, who encouraged me to pursue my interests in physics from a young age, and my sister Nancy, who has been a constant source of support and inspiration throughout. My deepest appreciation is of my partner Chris, who has kept me grounded and nourished throughout the last seven years; the hardships of AMO experimental labwork were much easier to endure when I had a delicious meal and a fellow physicist who understood my woes to come home to. Thanks also to Chris's family who have welcomed me as one of their own, and who have made Colorado feel like my new home; and to Braxton, for the levity (and chaos) he has introduced to my life.

I would next like to acknowledge the teachers, scientists, and professors who have set me down this path and mentored me as I matured as a researcher: Henri van Bemmel, Bonny Biswas, Lothar Lilge, Carl Fisher, Don Lem, Piotr Roztocki, Catherine Sulem, Emanuel Istrate, Daniel F. V. James, and Amar Vutha. Also, my friends from both the TOPS program in high school and the University of Toronto, for always lifting me up and encouraging me to do more.

Last but not least, my sincerest thanks to the Ion Storage Group for taking in a student who barely knew how to align a laser, and transforming me into who I am today. To my mentors: Didi Leibfried who has taught me an immense amount about ion trapping and was always ready to lend a hand when problems emerged; Andrew Wilson who shared his wisdom and mindset on how to approach and communicate with others kindly; and Daniel Slichter who somehow always had the right advice, whether it be about physics or life. To Stephen Erickson, Yong Wan, and Daniel Kienzler who welcomed me to Quantum II. To Pan-Yu Hou, whose work ethic, kindness, and level-headedness is unmatched. To Giorgio Zarantonello for his unwavering support and sarcastic sense of humour. To Adam Brandt for recognizing when I needed a push in the right direction (and maybe his wit). To Ingrid Zimmerman and AJ Rasmusson who are inheriting the apparatus in Quantum II. And to the wider Ion Storage Group: the staff, postdocs, and fellow graduate students have all taught me, supported me, and made these years amazing and unforgettable.

Finally, thank you, the reader, for taking the time to read this work.

Contents

Chapter

1	Intro	oduction	n	1
2	The	heoretical Background		
	2.1	The T	heory of Trapped-Ion Motion	5
		2.1.1	The Trapped-Ion Harmonic Confinement Potential	5
		2.1.2	Trapped-Ion Equilibrium Positions	14
		2.1.3	Trapped-Ion (Axial) Normal Modes	15
	2.2	Manip	ulating Ion States Using Laser Fields	19
		2.2.1	The Laser Coupling Hamiltonian	20
		2.2.2	Motion Sidebands with the Laser Hamiltonian	23
		2.2.3	Fluorescence Detection	30
3	Exp	eriment	al Apparatus	33
	3.1	$^9\mathrm{Be}^+$	and $^{25}\mathrm{Mg^+}$	33
	3.2	Beaml	ines and Lasers	37
		3.2.1	⁹ Be ⁺ Photoionization	45
		3.2.2	${}^{9}\mathrm{Be^{+}} {}^{2}\mathrm{S}_{1/2} {\leftrightarrow} {}^{2}\mathrm{P}_{1/2} \text{ (a. k. a. } {}^{9}\mathrm{Be^{+}} \text{ RD)} \dots \dots$	47
		3.2.3	${}^{9}\mathrm{Be^{+}} {}^{2}\mathrm{S}_{1/2} \!\!\leftrightarrow^{2}\!\! \mathrm{P}_{3/2}$ (a. k. a. ${}^{9}\mathrm{Be^{+}}$ BD)	48
		3.2.4	⁹ Be ⁺ Raman	48
		3.2.5	²⁵ Mg ⁺ Photoionization	49

		3.2.6	$^{25}\text{Mg}^+$ $^2\text{S}_{1/2} \leftrightarrow ^2\text{P}_{1/2}$ (a. k. a. $^{25}\text{Mg}^+$ $^2\text{P}_{1/2}$) and $^2\text{S}_{1/2} \leftrightarrow ^2\text{P}_{3/2}$ (a. k. a.	
			$^{25}{ m Mg}^{+}$ $^{2}{ m P}_{3/2})$	50
		3.2.7	²⁵ Mg ⁺ Raman	50
		3.2.8	Sideband Cooling	52
		3.2.9	UV Fiber	55
		3.2.10	Laser Power Control and Pulseshaping	56
		3.2.11	Axial Micromotion Compensation with Electro-Optic Modulators	59
	3.3	The X	-trap	60
		3.3.1	Ion Loading	60
		3.3.2	Trapping Wells	62
		3.3.3	Radial Micromotion Minimization	63
	3.4	Contro	ol System	64
	3.5	Magne	tic Field Stabilization	66
	3.6	Ion Cr	ystals, Modes, and Ion Participations	68
	3.7	Trappi	ng RF Control	71
4	Elec	tromag	netically-Induced-Transparency Cooling of $^{25}\mathrm{Mg^+}$	7 5
	4.1	EIT C	ooling Theory: The Dressed-State Picture	78
		4.1.1	Dressed-State Basis Derivation	80
		4.1.2	Photon Emission/Collapse Operators in the Dressed-State Basis	85
		4.1.3	Using Rate Equations to Calculate Minimum Steady-State Occupation	88
		4.1.4	Calculating Cooling Rate and EIT Cooling Bandwidth	91
		4.1.5	Summary of Dressed-State Derivations	93
	4.2	EIT C	ooling Simulations	95
		4.2.1	Description of EIT Cooling Simulation	95
		4.2.2	Verification of Dressed-State Picture Decay Operator	98
		4.2.3	Fano-like EIT Cooling Lineshape with Motion	100

	4.3	EIT C	Cooling Experiment	100
		4.3.1	Physical Apparatus Changes	100
		4.3.2	Calibrating EIT Laser Beam Parameters	105
		4.3.3	Cooling Single ²⁵ Mg ⁺	108
		4.3.4	Probing the Bandwidth of EIT Cooling	109
		4.3.5	Cooling Mixed-Species Ion Chains with $^{25}{\rm Mg}^+$	112
		4.3.6	Double(-Dark) EIT Cooling	116
		4.3.7	Characterizing EIT Laser Beam Properties	119
	4.4	Summ	nary	121
5	Mod	le-Mode	e Coupling	123
	5.1	Theor	y	125
		5.1.1	Mode Coupling Potential and Hamiltonian	125
		5.1.2	Time Evolution of Coupled Motional States	128
	5.2	Wavef	orms	130
	5.3	Exper	imental Considerations for Performing Mode Coupling with the X-Trap	132
	5.4	Calibr	rations	134
		5.4.1	Lineshape of Mode Coupling Frequency Data	137
		5.4.2	Decoupling ²⁵ Mg ⁺ from the OOPH Mode in ⁹ Be ⁺ - ²⁵ Mg ⁺ - ⁹ Be ⁺	143
	5.5	Chara	cterization	144
		5.5.1	Characterizing Phase Coherence	144
		5.5.2	Mode Coupling with Varying Input States	146
		5.5.3	Error Due to Repeated Swaps	150
	5.6	Coolin	ng Using Mode-Coupling	152
		5.6.1	Cooling WCMs in a Same-Species Crystal	153
		5.6.2	Cooling Ion Crystals with Different Charge-to-Mass Ratios	157
		5.6.3	Modes with No Participation of the Coolant Ion	161

	5.7	Repea	ted Non-Destructive (Projective) Readout of Ion Motion
		5.7.1	Experimental Sequence
		5.7.2	Results
		5.7.3	Characterization of Heating from Measurement Sequence
		5.7.4	Effects of Recoil Heating
	5.8	Extens	sions
	5.9	Summ	ary
Re	efere	nces	179
A	ppei	ndix	
\mathbf{A}	Hard	dware a	nd Lab Tricks
	A.1	VECS	ELs
		A.1.1	1120 nm VECSELs
		A.1.2	VECSEL Lasing and Alignment Procedure
		A.1.3	Plumbing
	A.2	Acoust	to-Optic Modulators
		A.2.1	AOM Double-Pass Methods
		A.2.2	Injecting Beams through an AOM
	A.3	Digita	l Servos
	A.4	UV B	BO Doublers
		A.4.1	Ospelkaus-style UV Doubler Variations and Versions
		A.4.2	313 nm Doublers
		A.4.3	280nm Raman Doubler
		A.4.4	Oxygen Flow
		A.4.5	Hansch-Couillaud and Pound-Drever-Hall Locking
	A.5	Iodine	Locks

	A.6 Graphical Beam Overlay of Lab	. 203
В	Mode Coupling Extended Data	235
	B.1 Mode Coupling Joint Population Measurements	. 235
	B.2 Cooling Using Mode Coupling Two-Ion Fit Data	. 239
	B.3 Mode Coupling Repeated Measurement Results	. 240

Tables

Table

3.1	Field sensitivities of ${}^2S_{1/2}$ states of ${}^9Be^+$
3.2	Field sensitivities of selected ${}^2S_{1/2}$ states of ${}^{25}Mg^+$
3.3	Frequencies and field sensitivities of ${}^9\mathrm{Be^+}$ ${}^2\mathrm{S}_{1/2}$ microwave transitions 39
3.4	Frequencies and field sensitivities of ${}^{25}{\rm Mg}^{+}$ ${}^{2}{\rm S}_{1/2}$ microwave transitions 39
3.5	Summary of beamlines
3.6	Electrode voltages for the "S", "S_loadwell", and "HF_S" well 63
3.7	Characteristics of the relevant normal modes of the ion crystals used in this thesis. For
	the work discussed in Ch. 5, the ${}^9\mathrm{Be}^+$ - ${}^9\mathrm{Be}^+$ ion RF confinement voltage is changed
	during the sequence to bring the x -OOPH and z -OOPH frequencies closer together 70
3.8	Approximate heating rates of modes in ${}^{9}\text{Be}^{+}$ - ${}^{25}\text{Mg}^{+}$ - ${}^{9}\text{Be}^{+}$
4.1	Beam parameters for interleaved cooling of the ${}^{9}\mathrm{Be^{+}}^{-25}\mathrm{Mg^{+}}$ ion crystal 115
4.2	Beam parameters for interleaved cooling of the ${}^{9}\mathrm{Be}^{+}$ - ${}^{25}\mathrm{Mg}^{+}$ - ${}^{9}\mathrm{Be}^{+}$ ion crystal 115
5.1	Experiments to characterize heating associated with certain parts of the motional
	state measurement
A.1	Locations corresponding to beamline photos
B.1	Fit parameters from frequency-scan data for coupling operations used for indirect
	cooling of ${}^9\mathrm{Be}^+$ - ${}^9\mathrm{Be}^+$ and ${}^9\mathrm{Be}^+$ - ${}^{25}\mathrm{Mg}^+$

B.2	Fit parameters from time-scan data for coupling operations used for indirect cooling	
	of ${}^9\mathrm{Be}^+$ - ${}^9\mathrm{Be}^+$ and ${}^9\mathrm{Be}^+$ - ${}^{25}\mathrm{Mg}^+$	239
В.3	Sideband transition probabilities conditioned on different motional state measurement	
	outcomes for $N=1$	240
B.4	Sideband transition probabilities conditioned on different motional state measurement	
	outcomes for $N=2$	241
B.5	Sideband transition probabilities conditioned on different motional state measurement	
	outcomes for $N=3$	242

Figures

Figure

2.1	Diagram of hyperbolic four-electrode trap from Ref. [52]	7
2.2	Stability diagram for Mathieu equations relating to the radial motion of the ions	
	described by Eq. 2.6	8
2.3	Stability diagram for Mathieu equations for ions of two different masses	9
2.4	Simple diagrams of a linear 3D Paul trap with segmented DC electrodes	12
2.5	Cycling transitions in ${}^{9}\mathrm{Be^{+}}_{-}{}^{25}\mathrm{Mg^{+}}$	32
3.1	Energy level splittings of the ${}^2S_{1/2}$ manifold of ${}^9Be^+$	35
3.2	Energy level splittings of the ${}^2\mathrm{P}_{1/2}$ manifold of ${}^9\mathrm{Be}^+$	35
3.3	Energy level splittings of the ${}^2P_{3/2}$ manifold of ${}^9Be^+$	36
3.4	Energy level splittings of the $^2\mathrm{S}_{1/2}$ manifold of $^{25}\mathrm{Mg}^+$	36
3.5	Energy level splittings of the $^2\mathrm{P}_{1/2}$ manifold of $^{25}\mathrm{Mg}^+$	37
3.6	Energy level splittings of the $^2\mathrm{P}_{3/2}$ manifold of $^{25}\mathrm{Mg}^+$	37
3.7	Resonant and Raman lasers for ${}^{9}\mathrm{Be}^{+}$	41
3.8	Resonant and Raman lasers for $^{25}{\rm Mg}^+$	42
3.9	Beam entry directions for lasers relative to quantization axis	43
3.10	Frequency changing elements for ${}^9{\rm Be^+}$ ${}^2{\rm S}_{1/2} \leftrightarrow {}^2{\rm P}_{1/2}$	47
3.11	Frequency changing elements for ${}^9{\rm Be^+}$ ${}^2{\rm S}_{1/2} \leftrightarrow {}^2{\rm P}_{1/2}$	48
3.12	Frequency changing elements for ⁹ Be ⁺ Raman	49

4.16	Sample Ramsey experiment to determine EIT cooling beam powers	
4.17	Sample depumping experiment to determine EIT cooling beam powers	
5.1	Mode Coupling Principle Diagram, Trap Sketch, and Waveform	
5.2	Calibrating and the mode-coupling operation	
5.3	Characterizing phase coherence of mode coupling	
5.4	Characterizing mode coupling of various input states	
5.5	Diagrams for joint population determination using RAP pulses	
5.6	Joint-motional population dynamics during repeated swap operations	
5.7	Axial to radial mode coupling characterization of in a ${}^{9}\mathrm{Be^{+}}$ - ${}^{9}\mathrm{Be^{+}}$ ion crystal 154	
5.8	$^9\mathrm{Be}^+$ - $^9\mathrm{Be}^+$ cooling results using mode coupling	
5.9	Mode coupling characterization in a ${}^{9}\mathrm{Be}^{+}$ - ${}^{25}\mathrm{Mg}^{+}$ ion crystal	
5.10	$^9\mathrm{Be}^+$ - $^{25}\mathrm{Mg}^+$ indirect cooling results using mode coupling	
5.11	$^9\mathrm{Be}^+$ - $^2\mathrm{Mg}^+$ - $^9\mathrm{Be}^+$ indirect cooling results using mode coupling	
5.12	Repeated measurement sequence for distinguishing the 0 and 1 Fock states 165	
5.13	Cirac-Zoller phase calibration	
5.14	Repetitive readout results distinguishing $ 0\rangle$ and $ 1\rangle$ Fock states	
5.15	Sideband excitation data sorted by repeated readout result	
5.16	Average occupation after post-selecting on 0 Fock state mid-circuit results 172	
5.17	Effects of recoil heating on the protected mode	
A.1	Schematic for AOM double-pass based on polarization	
A.2	Schematic for AOM double-pass based on vertical beam angle	
A.3	Schematic for injecting a second beam through a switch AOM	
A.4	Beamline photo locations in lab	
A.5	Beamline photo overlay ${}^9\mathrm{Be^+}$ Raman SFG	
A.6	Beamline photo overlay ${}^9\mathrm{Be^+}$ Raman UV Doubler	
A.7	Beamline photo overlay ${}^9\mathrm{Be^+}$ Raman 2 AOMs	

A.8 Beamline photo overlay ${}^9\mathrm{Be^+}$ Raman 1 and 3 AOMs
A.9 Beamline photo overlay near Raman 1 input port
A.10 Beamline photo overlay near Raman 2 input port
A.11 Beamline photo overlay near Raman 3 input port
A.12 Beamline photo overlay near Mg Raman fiber inputs
A.13 Beamline photo overlay near ²⁵ Mg ⁺ Raman AOMs
A.14 Beamline photo overlay near Mg Raman UV doubler
A.15 Beamline photo overlay near Mg Raman 3 AOMs
A.16 Beamline photo overlay near Mg Raman 3 AOMs used in EIT cooling configuration . 214
A.17 Beamline photo overlay near ²⁵ Mg ⁺ resonant and PI fiber outputs
A.18 Beamline photo overlay near ${}^9\mathrm{Be^+}$ resonant fiber output and resonant beam port 210
A.19 Beamline photo overlay near ${}^{9}\mathrm{Be^{+}}$ resonant UV doublers
A.20 Beamline photo overlay near ${}^{9}\text{Be}^{+}$ resonant AOMs
A.21 Beamline photo overlay near ⁹ Be ⁺ resonant AOMs part 2
A.22 Beamline photo overlay near $^{25}{\rm Mg^+}$ $^2{\rm S}_{1/2}\leftrightarrow^2{\rm P}_{3/2}$ UV doubler
A.23 Beamline photo overlay near ${}^{25}{\rm Mg}^+$ ${}^2{\rm S}_{1/2} \leftrightarrow {}^2{\rm P}_{1/2}$ iodine lock
A.24 Beamline photo overlay near $^{25}{\rm Mg}^+$ $^2{\rm S}_{1/2}\leftrightarrow^2{\rm P}_{1/2}$ UV doubler
A.25 Beamline photo overlay near ²⁵ Mg ⁺ resonant AOMs
A.26 Beamline photo overlay near ²⁵ Mg ⁺ PI iodine lock
A.27 Beamline photo overlay near ²⁵ Mg ⁺ PI UV doubler
A.28 Beamline photo overlay near ${}^{9}\mathrm{Be^{+}}$ PI UV doubler
A.29 Beamline photo overlay near $^{25}{\rm Mg}^+$ $^2{\rm S}_{1/2}\leftrightarrow^2{\rm P}_{3/2}$ VECSEL
A.30 Beamline photo overlay near ²⁵ Mg ⁺ PI light distribution optics
A.31 Beamline photo overlay near ⁹ Be ⁺ PI VECSEL
A.32 Beamline photo overlay near $^{25}{\rm Mg}^+$ $^2{\rm S}_{1/2}\leftrightarrow^2{\rm P}_{3/2}$ iodine lock
A.33 Beamline photo overlay near $^{25}\text{Mg}^+$ $^2\text{S}_{1/2}\leftrightarrow^2\text{P}_{1/2}$ VECSEL
A.34 Beamline photo overlay near ${}^9{\rm Be^+}$ ${}^2{\rm S}_{1/2}\leftrightarrow {}^2{\rm P}_{3/2}$ ("BD") iodine lock

	xvii
A.35 Beamline photo overlay ${}^{9}\mathrm{Be^{+}}$ Resonant SFG	232
A.36 Beamline photo overlay near ${}^9{\rm Be^+}$ ${}^2{\rm S}_{1/2} \leftrightarrow {}^2{\rm P}_{1/2}$ ("RD") iodine lock	233
A.37 Beamline photo overlay near ${}^9\mathrm{Be}^+$ PI LBO doubler and light distribution system	234
	226
B.1 Joint-motional population dynamics: coupling time scans 1	230
B.2 Joint-motional population dynamics: coupling time scans 2	237
B.3 Joint-motional population dynamics: coupling phase	238

Chapter 1

Introduction

Trapped ions remain one of the most widely used platforms for atomic physics experiments ranging from demonstrations of quantum information processing [1–22] and quantum control [23–35] to studies of fundamental physics and precision measurements [36–46]. By carefully isolating the ions from their environment, many perturbations are reduced, controlled, or removed entirely, allowing for precise control and examination of quantum states of single or multiple atoms. Results within the past decade include clocks based on trapped ions with uncertainty below 10⁻¹⁸ [42], with increasing transportability [39], including ion clocks deployed in space [44]; sensing of displacements below the quantum limit with a few [34] to hundreds of ions [26, 35]; high-fidelity operations with trapped ions [9, 12, 19, 47]; and architectural and algorithmic advances in quantum information processing and quantum simulation [13, 20, 21, 48, 49].

The majority of applications (excepting the quantum sensing experiments listed above) have focused on the use of the atomic states of individual ions as the main quantum states of interest. This is for good reason, as these atomic states can be made very coherent and long lived [50, 51] and can be controlled with very high fidelity [9, 12, 19, 47]. However, there are other quantum degrees of freedom accessible with trapped ions in the ion motion, which can be described by quantum harmonic oscillators [1, 52, 53]. Each of these modes is an approximately infinite ladder of states¹

¹In principle, if the ion motional excitation is high enough that its energy is approximately equal to the depth of the trapping potential, the ion will escape the confinement, and when approaching this limit anhamonicities will alter the spacing of energy levels. This constitutes the upper limit of the harmonic oscillator ladder. In practice, the trapping potential is almost perfectly harmonic for at least the lowest few hundred energy levels, depending on trap electrode geometries. A higher motional excitation will result in a larger quantum wavepacket which "samples" a larger part of the potential landscape, making these anharmonicities "visible" to the ion.

that both offer rich potential for demonstrations of quantum control, sensing, and computing; and can present additional challenges for the use of trapped ions as a quantum system.

Each motion state involves the participation of some or all of the ions in a given crystal, and thus offers the all-to-all connectivity that is often touted as a benefit to using trapped ions as a quantum computing [4, 5, 14] and simulation [7, 8, 29, 54] platform. The theory describing these ion motion modes and how they interact with laser fields is discussed in Ch. 2. A shared motion mode can be used to couple the internal atomic states of spatially distant ions. However, if these motion modes are not carefully controlled or characterized, they may lead to sources of error [36, 50].

Two experimental investigations in the control of trapped-ion motion are detailed in this thesis, and the apparatus on which these experiments are performed is described in Ch. 3. A particular feature of this apparatus is that two different species of ions can trapped using it: ⁹Be⁺ and ²⁵Mg⁺. Co-trapping two different ion species enables global laser beams to individually address each species. This allows for the preservation of the internal atomic state of one ion when the other ion is illuminated (although the state of the unaddressed species can be altered by state projection if the internal states of the two species were previously entangled). Under these circumstances, each ion can be assigned to play a particular role, such as that of the entanglement distribution resource [13], the readout ion [25, 33, 38, 47] or a coolant ion [25, 38, 55, 56]. In other cases, it simplifies experiments greatly to co-trap an ion that is well controlled with another that is more difficult to control, such as an atomic ion together with a molecular ion [33, 38] or highly-charged ion [43, 46]; this can also be done to probe atomic ions that do not have easily accessible optical transitions [42].

In order to suppress imperfections, all relevant modes of a trapped-ion crystal, whether mixed-species or single-species, should be cooled as close to the ground state as possible; this will increase the fidelity even for operations that are first-order insensitive to motion such as the entangling operations first proposed by Mølmer and Sørensen [2]. An experiment on the rapid, resource-efficient cooling of both a single trapped ²⁵Mg⁺ ion and trapped-ion crystals sympathetically cooled using ²⁵Mg⁺ is detailed in Ch. 4. Electromagnetically-induced-transparency (EIT) cooling is demonstrated

despite particular difficulty in applying this technique to ²⁵Mg⁺ due to its nuclear spin of 5/2, which gives rise to a complex hyperfine structure. Compared to ²⁴Mg⁺, which was used to demonstrate sympathetic cooling using EIT in earlier experiments [56], ²⁵Mg⁺ has many more leakage states. ²⁵Mg⁺ is used instead of ²⁴Mg⁺ in this apparatus because the same complex hyperfine structure that complicates EIT cooling enables ²⁵Mg⁺ to have long-lived qubit states [51] not available in ²⁴Mg⁺. With a small modification of an additional repump beam, the technique was demonstrated to work reasonably well, despite the presence of micromotion that is especially strong in our apparatus. Micromotion was found to severely compromise the efficiency of the EIT cooling process, as confirmed by both experimental data and simulations.

A second experiment that focuses on the control of motion states by direct mode to mode coupling is discussed in Ch. 5. This type of coupling is useful because the ability to control each motion mode with a particular ion varies depending on the ion crystal structure as well as experimental factors such as laser beam projection along certain axes. Ions of different charge-to-mass ratio in the same ion crystal have less balanced participations in motion modes compared to ions in a single-species ion crystal [57]. In addition, there exist modes with odd symmetry in which the center ion does not participate at all in both mixed- and single-species ion crystals. This imbalance in ion participations can, for example, reduce the efficiency or make it impossible for coolant ions to sympathetically cool certain modes. By applying a spatially-varying potential at the difference frequency of two modes with appropriate curvatures at each ion position, a parametric coupling can occur where the quantum states of the two modes are mixed and can be exchanged over time. This was demonstrated in our apparatus to improve ion cooling efficiency by coupling weakly cooled modes to strongly cooled modes in a variety of ion crystals.

The mode-coupling operation was also used to demonstrate repeated mid-circuit fluorescence detection of trapped ions while protecting the motion state of interest from photon recoil. Past experiments requiring the detection of trapped-ion internal states correlated to a motion state have either relied on destructive readout [16, 23, 24, 58] which prevents mid-circuit detections, or post-selection based on detection results that indicate a lack of fluorescence to avoid recoil [32].

Mode coupling enables the use of a protected mode, in which the fluorescing ion does not participate, and therefore does not suffer recoil during detection. After motion state information is coupled to the atomic state of the readout ion using a secondary mode in which this ion does participate, the motion state of interest is swapped (using the mode-coupling operation) to the protected mode for fluorescence detection. Experiments utilizing this process are described in detail in Ch. 5.

The ability to (projectively) read out ion motion states without corrupting them is a crucial advance towards the use and control of the quantum harmonic oscillator degrees of freedom in trapped ions. Each normal mode of trapped-ion motion can be used as a bosonic quantum state, opening the door to many new areas of study. In particular, one application that has received increased attention in the last few years is that of bosonic or continuous-variable error correction, in which bosonic code states [59, 60] are implemented on trapped-ion modes [16, 61, 62]. There have also recently been several impressive demonstrations of control in bosonic systems within the superconducting-qubit/cavity-QED community [63–66]. The use of protected modes to encode and non-destructively read out trapped ion motion will likely aid and expand such endeavors in the trapped ion field and beyond.

Chapter 2

Theoretical Background

This chapter covers some theoretical background that is used throughout the rest of this thesis.

2.1 The Theory of Trapped-Ion Motion

This thesis relies heavily upon the use of trapped-ion motion. In this section, I review some of the theory of trapped-ion motion and how it is controlled in practice, as well as some background on the methods of quantum control and quantum operations used in this thesis.

2.1.1 The Trapped-Ion Harmonic Confinement Potential

Ions are typically trapped using a combination of static and radiofrequency (RF) electric fields (Paul traps [52, 67, 68]), or static electric and magnetic fields (Penning traps [69, 70]). The experimental apparatus used during my graduate studies is of the former category, and this section will deal with the description of the confining potential created by such an ion trap.

According to Earnshaw's theorem [71], in a region with no charge there cannot be a stable minimum of the electric potential, meaning that it is physically impossible to confine an ion (classically at rest) using a static 3D potential. However, it is possible to use a potential that is changing in time (i.e. an RF potential) to do so. This is the principle behind the Paul trap [52, 67, 68]. This section provides a brief description, following Ghosh [52].

A quadrupolar electric potential in 3D space can be written

$$\phi = \frac{\phi_0}{2r_0^2} \left(\lambda x^2 + \sigma y^2 + \gamma z^2 \right), \tag{2.1}$$

where ϕ is the potential at a point in 3D space described by coordinates x, y, and z (for example, the ion position); ϕ_0 describes the magnitude of the applied potential; r_0 is a geometric scaling factor with units of length; and λ , σ , and γ are dimensionless factors describing the magnitude and sign of the field in each direction. The Laplace condition, when applied to the potential above, reveals that $\lambda + \sigma + \gamma = 0$. If these parameters are static in time, one of them would be required to be negative and the potential would be non-confining, hence the need for RF fields (time-varying factors).

For RF confinement in two dimensions, the potential can be set as

$$\phi = \frac{1}{2r_0^2} (U - V \cos(\omega_{RF} t)) (x^2 - y^2), \qquad (2.2)$$

where U is a static potential, V is the magnitude of an oscillating potential with oscillation frequency $\omega_{\rm RF}$, and t denotes time. One way of physically implementing this is by applying half the potential $\pm (U - V \cos(\omega_{\rm RF} t))$ above to diagonally opposite pairs of a set of four long electrodes parallel to the \mathbf{z} axis that surround the area for which the potential is calculated (i.e. the area in which the ion is to be trapped) as shown in Fig. 2.1.³⁴

¹Similar to what is seen in Sec. 2.1.3, a more complex potential that is confining can be approximated as a quadrupolar field near the confinement minimum.

 $^{^2}$ For simplicity, I ignore the motion/confinement along ${f z}$ for now and set the potential along that direction to be zero.

³Often, instead of applying RF potentials to all four electrodes, only two opposite electrodes have an oscillating RF potential and the other pair are either grounded or held at a DC voltage, yielding effectively equivalent dynamics to that described here with slightly lower experimental complexity.

⁴In this scenario, if all four electrodes are regularly placed, identically shaped, and hyperbolic in shape with the curved sides facing inwards towards the origin (where x = 0 and y = 0, or as shown in Fig. 2.1), $2r_0$ is the distance between opposite pairs of electrodes. In reality, hyperbolic electrodes are more difficult to make than some other geometries (e. g. rods or blades) and result in unnecessary obstruction for optical access. Thus, r_0 is usually just taken to be a geometric scaling factor with units of length and Eq. 2.1 as an approximation that holds near the center of the region.

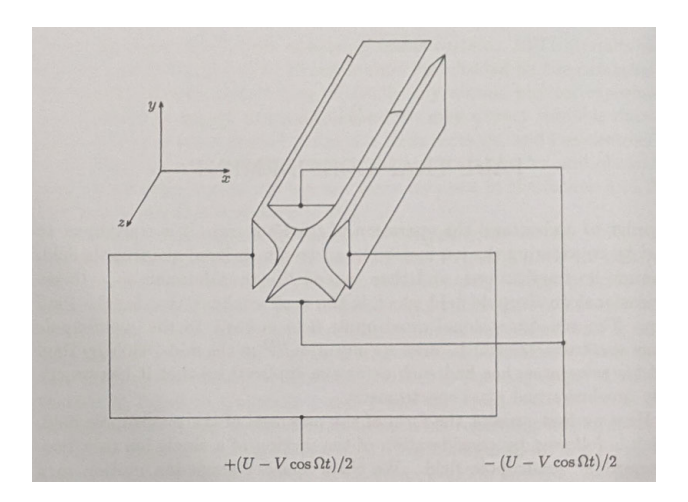


Figure 2.1: A set of four electrodes that have a hyperbolic inner shape can confine an ion in the x and y directions with oscillating voltages applied, as shown in this diagram from Ref. [52].

Under this potential, the equations describing the classical motion of the ion are

$$\ddot{x} + \frac{e}{mr_0^2} \left(U - V \cos \left(\omega_{\text{RF}} t \right) \right) x = 0, \tag{2.3}$$

$$\ddot{y} - \frac{e}{mr_0^2} \left(U - V \cos \left(\omega_{RF} t \right) \right) y = 0, \tag{2.4}$$

where e and m are the charge and the mass of the ion, respectively, and the dot denotes a derivative with respect to the time t.

After making the substitutions

$$\frac{4eU}{mr_0^2\omega_{\rm RF}^2} = a, \ \frac{2eV}{mr_0^2\omega_{\rm RF}^2} = q, \ \omega_{\rm RF}t = 2\xi, \tag{2.5}$$

the above can be rewritten

$$\frac{d^2x}{d\xi^2} + (a - 2q\cos(2\xi)) x = 0,
\frac{d^2y}{d\xi^2} - (a - 2q\cos(2\xi)) y = 0,$$
(2.6)

which both have the form of a Mathieu equation [72] with different signs on the a and q coefficients.⁵

⁵In principle the a and q parameters along the two directions can be different in magnitude but in order to satisfy

The Mathieu equations feature in mathematical problems involving periodic motion, such as that described here. The solution is unbounded for certain values of a and q and bounded for others; physically, the latter case means that the ion motion is contained within a defined region and periodic, while if the solution to the Mathieu equation is unbounded, the ion is able to escape the confinement of the ion trap in the \mathbf{x} and \mathbf{y} directions.

As shown in Fig. 2.2(a), there are wing-like regions for which the Mathieu equation solutions remain bounded; outside these regions the solutions are not bounded. When both the \mathbf{x} and \mathbf{y} directions are considered (i. e. with the inverted signs of a and q for \mathbf{y}) the ion motion should be stable in both dimensions simultaneously, which reduces the range of parameters that can be used as shown in Fig. 2.2(b). Assuming that the ion mass m and charge e are fixed, the DC voltage U, RF voltage amplitude V, and trapping frequency ω_{RF} can be chosen according to Eq. 2.5 to ensure that a and q fall within the desired region. Usually, the parameters used for this type of potential confinement fall within the small diamond-shaped overlap of orange and blue shaded regions in Fig. 2.2(b) near the origin.

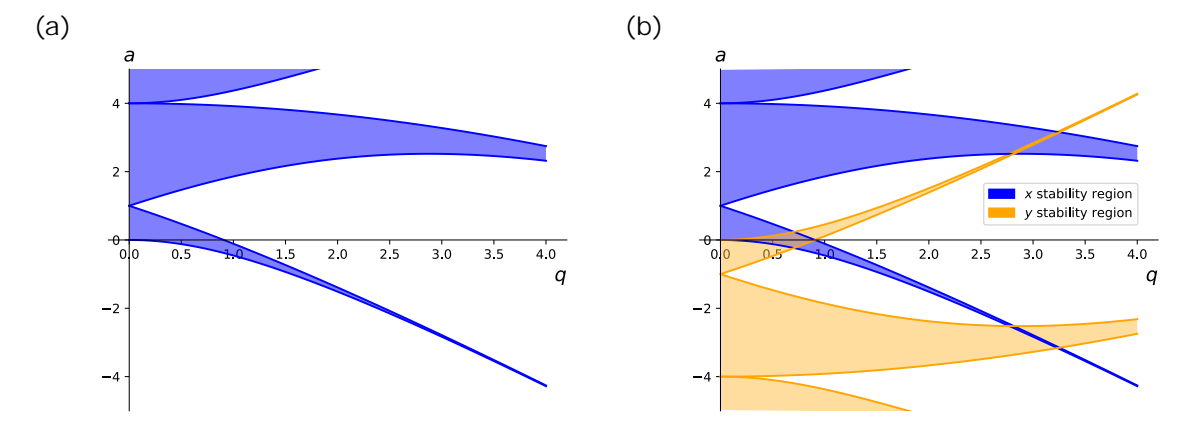


Figure 2.2: (a) shows the stability diagram for the Mathieu equation describing the x position of the ion in Eq. 2.6. The shaded blue regions indicate combinations of a and q parameters for which the equation describes bounded motion. (b) shows the stability diagram for both \mathbf{x} (blue) and \mathbf{y} (orange) motion overlapped; the stability regions are symmetric in q but not in a, so the stability region for the y is inverted along the vertical axis. Typically, the parameters are chosen so that they fall within the small diamond-shaped overlapped region near the origin.

For ions of different charge-to-mass ratios, the a and q values will be different, so the confinement potential parameters need to be considered for all ions of interest. An example is shown in Fig. 2.3, where the stability regions for confinement along one axis (i.e. for a shared set of electric potentials along that direction) for two ions of different masses m_1 and m_2 are shown. The example shown uses $m_2/m_1 = 25/9$, corresponding roughly to the two ions of interest in this thesis, ${}^9\mathrm{Be^+}$ and ${}^{25}\mathrm{Mg^+}$. The potential values are scaled so that the axes correspond to the a and q for " ${}^9\mathrm{Be^+}$ ". It can be seen that for these voltages,the confinement regions corresponding to " ${}^{25}\mathrm{Mg^+}$ " are smaller due to its higher mass; the trapping potentials used should then be restricted to the overlapping stability regions for both ions, and similar considerations should be made for all directions of confinement. For simplicity, for the rest of this section, the motion properties are derived for a single mass m. As

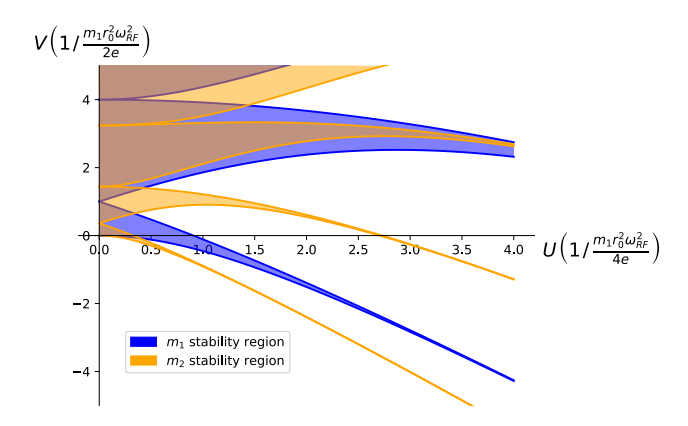


Figure 2.3: The stability diagram for the confinement of two ions of different masses in the same physical direction is shown. The vertical and horizontal axes are the RF and static confining voltages, respectively, scaled to the parameters of the first ion (with mass m_1) so that the axes are effectively the a and q parameters for this ion. The same voltage for the second ion (with mass m_2) is shown to correspond effectively to scaled a and q parameters.

shown above, however, the a and q parameters are different for ions of different masses, and so certain values, such as the frequency corresponding to the confinement and micromotion modulation index, both derived below, will be different for ions of different mass (or charge-to-mass ratio) confined using the same applied voltages.

As shown in Refs. [52, 68], the Mathieu equation can be analytically solved (assuming that we

restrict ourselves to stable solutions) using a solution of the form

$$u(\xi) = \alpha \sum_{n=-\infty}^{n=\infty} C_{2n} e^{(2n\pm\beta)i\xi} + \tilde{\alpha} \sum_{n=-\infty}^{n=\infty} C_{2n} e^{-(2n\pm\beta)i\xi}$$

$$(2.7)$$

where u is the relevant parameter of the ion position (either x or y); α and $\tilde{\alpha}$ are constants of integration that depend on initial conditions; and C_{2n} and β depend on a and q. It can be seen that this describes periodic motion that scales with the trapping potential frequency (recall $\omega_{RF}t = 2\xi$ from Eq. 2.5). The lowest frequency motion (corresponding to n = 0) from this solution is periodic with $\beta \xi/t = \beta \omega_{RF}/2$. When the approximation is taken that the system moves at this frequency only,⁶ the motion is completely harmonic, and thus the confinement potential Eq. 2.2 is reduced to an effective harmonic confinement.

Typically, only this lowest-frequency motion and the next-lowest frequency term (which is assumed to be small in amplitude, corresponding to n=1) is considered. This latter term adds an additional modulation of frequency ω_{RF} (a total oscillation with frequency $\beta\omega_{RF}/2 + \omega_{RF}$), and is called *micromotion*. Usually, for traps that have geometric symmetry it is possible to find a point in the $\mathbf{x} - \mathbf{y}$ plane where the RF electric field vanishes and the ion experiences minimal micromotion⁷; this is known as the *micromotion null*.

In Ref. [68], it can be seen that C_{2n} and β can be expressed in terms of recursion relations, and making the assumption $C_{\pm 4} \approx 0^8$ yields (for each of the x and y directions, and for each mass if ions of different mass are considered)

$$\beta = \sqrt{a + q^2/2},\tag{2.8}$$

when a solution assuming only secular motion and (small-amplitude) micromotion is substituted back into the Mathieu equation.

⁶For example, if the higher-frequency motion is taken as a time average.

⁷For example, in a trap with four hyperbolic electrodes and the potentials applied as in Fig. 2.1, this is along the **z** axis, at x = 0, y = 0. If two of the electrodes are grounded instead, this will ideally be along the line where the distance to both remaining RF electrodes is equal (x = y).

⁸Another method of arriving at this result is shown in Ref. [52].

The above discussion actually describes what is known as a quadrupole mass spectrometer; by tuning the DC and RF voltages, the charge-to-mass ratio of an unknown charged particle can be found by determining whether or not it remains in the channel defined by the four electrodes. It can be seen that unless the velocity in the \mathbf{z} direction is zero, the particle will end up passing through the electrodes even if it is stably confined in the \mathbf{x} and \mathbf{y} directions.

In order to modify this into an ion trap, a static confinement potential can be applied in the **z** direction.¹⁰ This can be done by situating electrodes on either end (along the **z** direction) of the trapping region with positive electric potentials. These electrodes do not have to be centered on the **z**-axis or perfectly opposing each other; they simply have to exert an approximately linear restoring force near the region where ions are to be trapped. The geometry that is used for the experimental apparatus in this thesis is shown in Fig. 2.4. Two (diagonally-opposite, blue) long electrodes carry an oscillating potential, and the other two sets of diagonally opposing electrodes (yellow) carry static (DC) potentials and are segmented into many smaller electrodes, so that the relative potential on a subset of electrodes may be chosen to create DC confinement centered at a z-position of choice. Ions may be transported along the **z** direction by raising and lowering the potential on these DC electrodes in a precisely coordinated way. For a configuration like this, DC electrodes that are diagonally opposite each other usually have similar, if not equal, voltages.

When static confinement in the z direction is added (here, for simplicity, the z-confinement is chosen to be centered at zero), the potential is given by

$$\phi = \frac{1}{2} \left[\left(\frac{U_x}{r_x^2} x^2 + \frac{U_y}{r_y^2} y^2 + \frac{U_z}{r_z^2} z^2 \right) - \cos\left(\omega_{RF} t\right) \left(\frac{V_x}{r_x^2} x^2 + \frac{V_y}{r_y^2} y^2 \right) \right]. \tag{2.9}$$

In order to satisfy the Laplace condition,

$$\frac{U_x}{r_x^2} + \frac{U_y}{r_y^2} + \frac{U_z}{r_z^2} = 0, \qquad \frac{V_x}{r_x^2} + \frac{V_y}{r_y^2} = 0.$$
 (2.10)

⁹This can be used in conjunction with a true ion trap to filter for certain ion species or isotopes.

¹⁰Another way to do this is to use a trap with cylindrical symmetry where a hyperbolic electrode surrounds the z-axis in a ring to provide the radial confinement, and two electrodes above and below this ring provide the z-confinement such that the equipotential surfaces are described by $(x^2 + y^2) - 2z^2$. This situation is described in Refs. [52, 73].

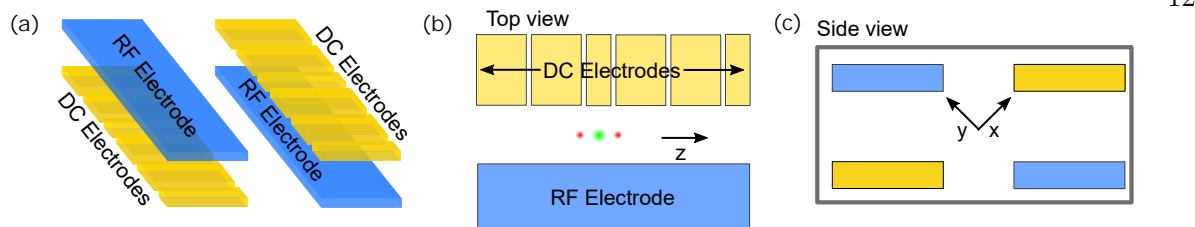


Figure 2.4: Simple diagrams of a linear 3D Paul trap with segmented DC electrodes. (a) shows a perspective diagram of the trap with the RF (blue) and DC (yellow) electrode positions relative to each other. (b) shows a top view of the ion trap, labeling the \mathbf{z} axial direction as the direction perpendicular to the segmentation of the DC electrodes. In our apparatus, this direction has the weakest confinement and therefore the ions (red and green discs) align along this direction. The origin is taken as the position of the middle (green) ion. (c) shows a side view of the trap with the radial \mathbf{x} and \mathbf{y} directions labeled.

Making the definitions

$$\frac{4eU_i}{mr_i^2\omega_{RF}^2} = a_i, \ \frac{2eV_i}{mr_i^2\omega_{RF}^2} = q_i, \ \omega_{RF}t = 2\xi,$$
 (2.11)

for $i = \{x, y, z\}$ (where $V_z = 0$), I obtain

$$\frac{d^2x}{d\xi^2} + (a_x - 2q_x \cos(2\xi)) x = 0,$$

$$\frac{d^2y}{d\xi^2} + (a_y - 2q_y \cos(2\xi)) y = 0,$$

$$\frac{d^2z}{d\xi^2} + a_z z = 0.$$
(2.12)

It should be noted that a_z (and therefore U_z , for a positively charged ion) should be positive for confinement of the ion. The last line in Eq. 2.12 can be written as

$$\frac{d^2z}{d\xi^2} + \omega_z^2 z = 0; \quad \omega_z = \sqrt{a_z}, \tag{2.13}$$

where it can be seen that the axial (**z**) confinement in this case is defined by the static potential only and the frequency corresponding to the confinement is given as ω_z above.

The dynamics of the radial (\mathbf{x} and \mathbf{y}) directions are similar to the case of the quadrupole mass spectrometer; because the a and q values are typically different in the two directions, ¹¹ an overlap in

¹¹If they are the same, the two axes will be degenerate, leading to difficulties cooling all modes since the cooling

their common stability regions should be found (similar to Fig. 2.2(b)).

The secular frequency corresponding to the confinement in each radial direction is given by

$$\omega_i = \frac{\beta \omega_{\rm RF}}{2} = \sqrt{\frac{eU_i}{mr_i^2} + \frac{e^2 V_i^2}{2m^2 r_i^4 \omega_{\rm RF}^2}}.$$
 (2.14)

As noted above, U_z should be positive, therefore at least one of U_x or U_y should be negative 12 to satisfy the conditions in Eq. 2.10.

The treatment of the problem up until here has been completely classical. The Hamiltonian corresponding to the potential described by Eq. 2.1 or 2.9 may be considered in a quantum treatment. In Ref. [74] (also shown in Ref. [68]), Glauber performs a derivation showing that in the Heisenberg picture of the motion Hamiltonian, the quantum operators of position (relative to the equilibrium position of each ion) and momentum are given by

$$\hat{x}(t) = \sqrt{\frac{\hbar}{2m\omega_{\text{mot}}}} \left(\hat{a}u^*(t) + \hat{a}^{\dagger}u(t) \right)$$

$$\hat{p}(t) = \sqrt{\frac{\hbar m}{2\omega_{\text{mot}}}} \left(\hat{a}\dot{u}^*(t) + \hat{a}^{\dagger}\dot{u}(t) \right)$$
(2.15)

where \hat{x} and \hat{p} are the time-dependent Heisenberg picture operators of position and momentum along a given direction, h is Planck's constant, m is the mass of the ion, \hat{a} is the annihilation operator corresponding to a mode of motion along this direction with (angular) secular motion frequency ω_{mot} , and u(t) is a time-dependent complex-valued function describing (normalized) time-dependent motion relating to the solution of the Mathieu equation (Eq. 2.7).

If the lowest-order approximation assuming only secular motion and micromotion is applied as above, then [68]:

$$u(t) = e^{i\omega_{\text{mot}}t} \frac{1 + (q_i/2)\cos(\omega_{\text{RF}}t)}{1 + q_i/2},$$
(2.16)

where q_i is the q parameter along the direction i. If the phase of the RF drive is considered, this

beam will "define" one axes, leaving the other with no cooling beam projection.

¹²The sign also places a restriction on the relative magnitudes of the trapping potential voltages and the RF frequency; if this frequency is imaginary then the ion motion becomes unbounded.

expression becomes more complex; this case is discussed in Ref. [75].

2.1.2 Trapped-Ion Equilibrium Positions

When multiple ions are confined in 3D space by a single harmonic potential generated by the electrodes of the ion trap, they experience mutual Coulomb repulsion. The harmonic confinement and Coulomb repulsion between ions determine the equilibrium positions of ions¹³ in a crystal once they undergo laser cooling. Often, ions are trapped in a harmonic potential that has weaker confinement along one axis compared to all others so that the ions align along that axis. In our apparatus, this is usually perpendicular to the direction of segmentation of our electrodes (see Fig. 2.4(b)); we refer to this as the z or axial direction, and the other two (radial) directions are referred to as the x- and y- directions (Fig. 2.4(c)). The rest of this thesis will focus on linear ion crystals under this type of confinement.

Under these conditions, the radial positions x, y of all ions can be assumed to be zero (i.e. they are all aligned along the \mathbf{z} axis), and it is assumed that the directions of motion are, to first order, decoupled from each other. With this, the equilibrium positions of the ions may be found by considering the \mathbf{z} dimension only. Following [53] and [68], the (classical) energy of N ions confined in a harmonic potential is:

$$V = \sum_{i=1}^{N} \frac{1}{2} k z_i^2 + \sum_{\substack{i,j=1\\i\neq j}}^{N} \frac{e^2}{8\pi\epsilon_0} \frac{1}{|z_i - z_j|},$$
(2.17)

where k is the effective confinement in the axial direction provided by the static electric potentials applied to the segmented electrodes, z_i is the position of the i^{th} ion along the axial direction, e is the fundamental charge, and ϵ_0 is the permittivity of free space.¹⁴ The first term is the external confining potential, while the second term describes the Coulomb repulsion between ions. In the second term, there is a factor of 8 rather than 4 in the denominator to account for the double sum, since for each combination $i, j \in 0, N, i \neq j$ appears twice in the summation. The ion positions are

¹³As shown in Ref. [76], for some confinement parameters there exist multiple configurations that represent local minima in energy and therefore somewhat stable.

¹⁴More generally, there is a coefficient of e^2 that is the product of the charges of ions i and j, but singly positively charged atoms are discussed in this thesis, so this coefficient is 1.

numbered so that $z_i < z_j$ for i < j.

The equilibrium position of each ion $z_{i,0}$ can be found by taking the derivative of Eq. 2.17 with respect to the position of each ion z_i , which will be proportional to the total force on ion i, and setting this to zero. This gives a system of equations with N constraints and N unknowns, which is solvable using numerical methods. In Ref. [53] this is cleverly done by rewriting Eq. 2.17 as follows:

$$\frac{2V}{l^2k} = \sum_{i=1}^{N} u_i^2 + \sum_{\substack{i,j=1\\i\neq j}}^{N} \frac{1}{|u_i - u_j|},$$
(2.18)

where the length scale l is defined as $e^2/4\pi\epsilon_0 k$, and coordinates are scaled by the dimensionless equilibrium position $u_i = z_{i,0}/l$.

The equilibrium values of the u_i 's can be found by taking the partial derivative of V with respect to u_i and setting this to zero, giving (for the derivative with respect to a particular ion a's dimensionless position u_a)

$$\left. \frac{\partial}{\partial u_i} \frac{2V}{l^2 k} \right|_{i=a} = 2u_a - 2\sum_{j=1}^{a-1} \frac{1}{(u_a - u_j)^2} + 2\sum_{j=a+1}^{N} \frac{1}{(u_a - u_j)^2}$$
 (2.19)

$$0 = u_a - \sum_{j=1}^{a-1} \frac{1}{(u_a - u_j)^2} + \sum_{j=a+1}^{N} \frac{1}{(u_a - u_j)^2}$$
 (2.20)

where the factors of 2 multiplying the sums in Eq. 2.19 are due to the double sum in the potential term in Eq. 2.17. This also gives a system of equations with N constraints and N unknowns. This is solveable analytically for N = 2, 3 [53] but higher numbers of ions require numerical solvers.

2.1.3 Trapped-Ion (Axial) Normal Modes

The ion motion can be rewritten in terms of normal modes, much like the modes of an array of masses connected by springs. Here, the motion of the ions along the dimension that they align is derived (the \mathbf{z} axis) because these are the primary modes that are used in this experimental

apparatus.¹⁵ Following Ref. [53], the Lagrangian of the ion motion can be written:

$$L = \frac{1}{2} \sum_{i=1}^{N} m_i (\dot{q}_i)^2 - \frac{1}{2} \sum_{i,j=1}^{N} q_i q_j \left. \frac{\partial^2 V}{\partial z_i \partial z_j} \right|_{q_i, q_j = 0}.$$
 (2.21)

Here, q_i is defined as the position of ion i relative to its equilibrium position ($q_i := z_i - z_{i,0}$ where $z_i = z_{i,0}$ denotes ion i at its equilibrium position) and m_i is the mass of ion i. The "potential" portion of the Lagrangian here (second term on the right hand side) is the first non-zero term in the Taylor expansion of the potential described by Eq. 2.17 about the ion equilibrium positions.¹⁶

By defining $\mu_i = \sqrt{m_i}q_i$, the Lagrangian may be expressed in the mass-weighted coordinate system:

$$2L = \sum_{i=1}^{N} (\dot{\mu}_i)^2 - \sum_{i,j=1}^{N} \frac{\mu_i \mu_j}{\sqrt{m_i m_j}} \left. \frac{\partial^2 V}{\partial z_i \partial z_j} \right|_{q_i, q_j = 0}.$$
 (2.22)

To calculate the latter term, Eq. 2.18 can be used:

$$\frac{\partial^2 V}{\partial z_i \partial z_j} \bigg|_{q_i, q_i = 0} = l^2 \frac{\partial^2 V}{\partial u_i \partial u_j} \tag{2.23}$$

$$= \frac{l^4k}{2} \frac{\partial^2}{\partial u_i \partial u_j} \left[\sum_{a=1}^N u_a^2 + \sum_{\substack{a,b=1\\a \neq b}}^N \frac{1}{|u_a - u_b|} \right]$$
(2.24)

$$= \frac{l^4k}{2} \frac{\partial}{\partial u_i} \left| 2u_j - 2\sum_{b=1}^{j-1} \frac{1}{(u_j - u_b)^2} + 2\sum_{b=j+1}^{N} \frac{1}{(u_j - u_b)^2} \right|$$
(2.25)

$$= \begin{cases} l^4 k \left(1 + \sum_{\substack{b=1 \ b \neq i}}^{N} \frac{2}{|u_i - u_b|^3} \right) & \text{if } i = j \\ -l^4 k \frac{2}{|u_i - u_j|^3} & \text{if } i \neq j \end{cases}$$
 (2.26)

This can be combined with Eq. 2.22 to yield

$$2L = \sum_{i=1}^{N} (\dot{\mu}_i)^2 - \sum_{i,j=1}^{N} A_{ij} \mu_i \mu_j$$
 (2.27)

 $^{^{15}}$ Expressions for radial modes can be derived in an analogous manner.

¹⁶The constant term in the Taylor series can be canceled by the non-uniqueness transformation of the Lagrangian (it can be changed by a constant value without changing the dynamics), and the first-order Taylor term is 0 because the ions being at their equilibrium positions sets $\partial V/\partial z_i|_{q_i=0}$ to zero.

where
$$A_{ij} = \begin{cases} \frac{l^4k}{\sqrt{m_i m_j}} \left(1 + \sum_{\substack{b=1\\b \neq i}}^{N} \frac{2}{|u_i - u_b|^3} \right) & \text{if } i = j, \\ -\frac{l^4k}{\sqrt{m_i m_j}} \frac{2}{|u_i - u_j|^3} & \text{if } i \neq j. \end{cases}$$
 (2.28)

The matrix $\mathbf{A} = A_{ij}$ can then be diagonalized to find eigenvalues c_p and orthonormal eigenvectors $\boldsymbol{\chi}_p = (\chi_{1,p},...\chi_{N,p})$ of the collective ion motion, such that

$$\sum_{j=1}^{N} A_{ij} \chi_{j,p} = c_p \chi_{i,p}, \tag{2.29}$$

where $p \in \{1, ..., N\}$ indexes the modes. $\chi_{i,p}$ is the (normalized, mass-weighted) participation vector of ion i in mode p, that is, it represents the motion of ion i in mode p as a fraction of unity. The normal modes Y_i of the collective motion in mass-weighted coordinates are given by

$$Y_p = \sum_{j=1}^{N} \chi_{j,p} \mu_j. \tag{2.30}$$

Using the orthonomality of χ_p ($\sum_{p=1}^N \chi_{i,p} \chi_{j,p} = \delta_{ij}$ and $\sum_{i=1}^N \chi_{i,p} \chi_{i,s} = \delta_{ps}$ where δ_{ij} is the Kronecker delta), and Eq. 2.30, the following expressions can be derived:

$$\mu_i = \sum_{p=1}^{N} \chi_{i,p} Y_p \tag{2.31}$$

$$\dot{\mu}_i = \sum_{p=1}^{N} \chi_{i,p} \dot{Y}_p. \tag{2.32}$$

These can then be used to rewrite Eq. 2.27 to obtain:

$$2L = \sum_{i=1}^{N} (\dot{\mu}_i)^2 - \sum_{i,j=1}^{N} A_{ij} \mu_i \mu_j$$
 (2.33)

$$= \sum_{p=1}^{N} \left(\dot{Y}_{p}\right)^{2} - \sum_{p=1}^{N} c_{p} Y_{p}^{2}$$
(2.34)

$$= \sum_{p=1}^{N} \left(\dot{Y}_p \right)^2 - \sum_{p=1}^{N} \omega_p^2 Y_p^2. \tag{2.35}$$

where $\omega_p := \sqrt{c_p}^{17}$ is the frequency of the corresponding normal mode Y_p .

From Eq. 2.30, the motion in physical coordinates of each ion in a mode Y_p , can be expressed as (recall $q_i = z_i - z_{i,0} = \mu_i / \sqrt{m_i}$):

$$Y_p = \sum_{i=1}^{N} \chi_{i,p} \mu_i = \sum_{i=1}^{N} \chi_{i,p} \sqrt{m_i} q_i.$$
 (2.36)

In order to account for ions of different mass (this derivation can also be modified straightforwardly for ions of different charge-to-mass ratios), Y_p does not have units of m, but rather $\sqrt{\text{kg}}$ m, as implied by Eq. 2.36. Finally, q_i can also be written in terms of Y_p :

$$q_i = \frac{1}{\sqrt{m_i}} \sum_{p=1}^{N} \chi_{i,p} Y_p.$$
 (2.37)

Eq. 2.35 describes exactly a particle in a harmonic potential, although it is in reality a collective mode of motion. Therefore, for each mode, position and momentum operators of the form Eq. 2.15 can be written using a quantum mechanical treatment of a system with harmonic confinement.

From Eq. 2.35 the Hamiltonian can be written in normal mode coordinates:

$$\hat{H} = \sum_{p=1}^{N} \left[\frac{1}{2} \left(\hat{\zeta}_p \right)^2 + \frac{1}{2} \omega_p^2 \hat{Y}_p^2 \right], \tag{2.38}$$

where $\hat{\zeta}_p = -i\hbar \hat{\partial}_{Y_p}$ is the mass-weighted momentum operator corresponding to the position operator of normal mode p, \hat{Y}_p . By defining ladder operators \hat{a}_p , \hat{a}_p^{\dagger} for each mode p and defining:

$$\hat{Y}_p = \sqrt{\frac{\hbar}{2\omega_p}} \left(\hat{a}_p^{\dagger} + \hat{a}_p \right), \tag{2.39}$$

$$\hat{\zeta}_p = i\sqrt{\frac{\hbar\omega_p}{2}} \left(\hat{a}_p^{\dagger} - \hat{a}_p \right), \tag{2.40}$$

¹⁷Since A_{ij} is non-negative definite, c_p is necessarily positive, meaning that ω_p is real.

the Hamiltonian can be rewritten

$$\hat{H} = \hbar \sum_{p=1}^{N} \omega_p \left(\hat{a}_p^{\dagger} \hat{a}_p + \frac{1}{2} \right). \tag{2.41}$$

The above equations are shown in the Schrödinger picture; they may be transformed into the interaction frame of the motion with time-dependent terms, obtaining forms similar to that seen in Eq. 2.15.

2.2 Manipulating Ion States Using Laser Fields

Because trapped ions are usually confined using electromagnetic fields in a vacuum apparatus, they are fairly well decoupled from the environment, enabling them to act as a good quantum resource. Primarily, ions are manipulated using electromagnetic fields such as lasers or microwaves, and the response or readout is observed as photons emitted during fluorescence. The photons of the electromagnetic field change the ion's internal atomic state (i.e. the hybridized angular momentum of the ion's nuclear and electronic spins), and depending on the photon wavelength, different transitions may be made, and the momentum of both absorbed and emitted photons can change the ion motion states.

The properties of transitions that are driven during experiments vary. For fluorescence detection, a short-lived state with a dipole-allowed transition (for example a P state that quickly decays to the S manifold) is desired. Long-lived states with dipole-forbidden transitions (for example the D states of certain ions like 40 Ca⁺ or hyperfine states within the 2 S_{1/2} manifold of 9 Be⁺ or 25 Mg⁺) play an important role in the storage of quantum states, and mutually coherent long-lived states are suitable for implementing coherent quantum dynamics [51].

This section will begin with a description of the laser-ion interaction, then describe how this enables spin-motion coupling, and show how various parameters, such as Lamb-Dicke parameter and micromotion modulation index, play a role in the coupling. Finally, fluorescence detection using cycling transitions in our apparatus will be discussed.

2.2.1 The Laser Coupling Hamiltonian

The motion states of trapped ions are the quantum harmonic oscillator normal modes derived in Sec. 2.1.3. An N-ion crystal has 3N normal modes (N modes along each of the trapping potential principal axes). For the majority of this thesis, only the axial (\mathbf{z}) direction of motion is used, therefore the discussion here is restricted to modes along \mathbf{z} . However, the radial (\mathbf{x} and \mathbf{y}) modes can be treated similarly and this discussion can be applied as well with minimal differences.

The main method of extracting information from a trapped ion is by fluorescence detection, as described in Sec. 2.2.3, and therefore information about any trapped-ion motion state of interest must first be transferred onto an ion atomic state. This is often done with lasers (but can also be done with microwaves [6, 11, 30]) and therefore the laser coupling Hamiltonian is reviewed here, following the treatment in Refs. [50, 68].

Consider the interaction between a laser and a single ion at position \mathbf{r} . In this section, the interaction frame of the ion motion is used, so that the position and momentum operators of the ion are defined by Eq. 2.15. The Hamiltonian of a laser interacting with the dipole moment of a single atom at position \mathbf{r} and time t is given by:

$$H_{\text{laser}} = -\boldsymbol{\mu}_{\text{dipole}} \cdot \mathbf{E} \left(\mathbf{r}, t \right),$$
 (2.42)

where μ_{dipole} is the dipole moment vector of the transition and

$$\mathbf{E}(\mathbf{r}, t) = \epsilon \left\{ \exp \left[i \left(\mathbf{k} \cdot \mathbf{r} - \omega_{\text{laser}} t + \phi \right) \right] + \exp \left[-i \left(\mathbf{k} \cdot \mathbf{r} - \omega_{\text{laser}} t + \phi \right) \right] \right\}$$
(2.43)

is the laser expressed as a plane wave electric field polarized along ϵ propagating along the vector \mathbf{k} . ω_{laser} denotes the laser's angular frequency and ϕ is the laser phase at the origin and t=0. If it is assumed that $\boldsymbol{\mu}_{\text{dipole}} \cdot \boldsymbol{\epsilon}$ is nonzero (i.e. the laser has at least some component of the polarization required to drive the transition represented by $\boldsymbol{\mu}_{\text{dipole}}$), the magnitudes of both can be absorbed into

the Rabi frequency Ω_0 and Eq. 2.42 can be rewritten as follows:

$$H_{\text{laser}} = \hbar \frac{\Omega_0}{2} \left(|\uparrow\rangle \left\langle \downarrow| + |\downarrow\rangle \left\langle \uparrow| \right) \left\{ \exp\left[i \left(\mathbf{k} \cdot \mathbf{r} - \omega_{\text{laser}} t + \phi\right)\right] + \exp\left[-i \left(\mathbf{k} \cdot \mathbf{r} - \omega_{\text{laser}} t + \phi\right)\right] \right\}, \quad (2.44)$$

where \hbar is the reduced Planck's constant and $|\uparrow\rangle$ and $|\downarrow\rangle$ represent the two internal states of the trapped ion that are coupled by μ_{dipole} . When defined in this manner, the ion internal states become a pseudo-spin- $\frac{1}{2}$ system.¹⁸

Because only the \mathbf{z} motion of the ion is considered, the dot product $\mathbf{k} \cdot \mathbf{r}$ is reduced to that particular component (for all three directions to be considered, the dot product may simply be expanded fully instead of isolating just one component as is done here):

$$(\mathbf{k} \cdot \delta \mathbf{r})_{z} = k_z(z_0 + \hat{z}) \tag{2.45}$$

$$= \phi_z + \eta \left(\hat{a}u^*(t) + \hat{a}^{\dagger}u(t) \right), \qquad \eta = k_z \sqrt{\frac{\hbar}{2m\omega_{\text{mot}}}}$$
 (2.46)

where k_z is the component of the laser wavevector along the \mathbf{z} axis, \hat{z} is the position operator of an ion along this axis relative to its equilibrium position z_0 , m is the mass of the ion, ω_{mot} is the angular frequency of the motion mode of the ion, $\hat{a}/\hat{a}^{\dagger}$ are the annihilation/creation operators corresponding to the motion mode, u(t) is a function describing the time-dependent motion of the ion (see Eq. 2.15 and Ref. [68, 74]¹⁹), ϕ_z is an effective phase equal to $k_z z_0$, and η is the Lamb-Dicke parameter of the interaction. Here, only one ion and one mode of interest is assumed, but this expression can be modified by (assuming that the index of the ion of interest is i and its equilibrium position is $z_{i,0}$)

 $^{^{18}}$ In practice, these two states are defined by convenience and experimental requirement, for example depending on which states have an easily addressable laser transition and/or long coherence times. These may or may not be the minimally fluorescing (|Dark \rangle) or maximally fluorescing (|Bright \rangle) states (fluorescence detection is discussed in Sec. 2.2.3); in the latter case the pseudo-spin states are each transferred to |Dark \rangle or |Bright \rangle before readout is performed.

¹⁹At this point, the simplification $u(t) = e^{i\omega_{\text{mot}}t}$ can be made because the axial confinement is purely static, but I will leave this more general form for now.

substituting the following in Eq. 2.45:

$$z_{i,0} + \hat{z}_i = z_{i,0} + \sum_{p=1}^{N} \chi_{i,p} \hat{z}_p = \sqrt{\frac{\hbar}{2m}} \sum_{p=1}^{N} \frac{\chi_{i,p}}{\sqrt{\omega_p}} \left(\hat{a}_p u_p^*(t) + \hat{a}_p^{\dagger} u_p(t) \right)$$
(2.47)

where the sum runs over all motion modes in the \mathbf{z} direction, N is the number of modes in this direction (equal to the number of ions in the crystal), $\chi_{i,p}$ is the participation vector component of ion i in mode p as defined in Eq. 2.29, \hat{z}_p , ω_p , and $\hat{a}_p/\hat{a}_p^{\dagger}$ are the motion operator, angular frequency, and annihilation/creation operators corresponding to mode p, and $u_p(t)$ express the time-dependence of the operators \hat{a}_p .

Returning to the case of a single ion and single mode (and for simplicity setting the ion equilibrium position to the origin $z_0 = 0$), obtain the total Hamiltonian, Eq. 2.46 is substituted into Eq. 2.44 and this is added to the Hamiltonian describing the spin state energies:

$$H_0 = H_{\text{atom}} + H_{\text{laser}} \tag{2.48}$$

$$= \hbar \frac{\omega_{\text{atom}}}{2} |\uparrow\rangle \langle\uparrow| - \hbar \frac{\omega_{\text{atom}}}{2} |\downarrow\rangle \langle\downarrow| + \hbar \frac{\Omega_0}{2} (|\uparrow\rangle \langle\downarrow| + |\downarrow\rangle \langle\uparrow|) \left\{ \exp \left[i\eta \left(\hat{a}u^*(t) + \hat{a}^{\dagger}u(t) \right) \right] e^{-i(\omega_{\text{laser}}t - \phi)} + h.c. \right\},$$
(2.49)

where ω_{atom} is the angular frequency corresponding to the atomic transition.

In general, any unitary transformation \hat{U} can be used to transform the system into a different basis; if $|\Psi(t)\rangle \to \hat{U} |\Psi(t)\rangle := |\tilde{\Psi}(t)\rangle$, the Hamiltonian transforms as

$$\hat{\hat{H}} = \hat{U}\hat{H}\hat{U}^{\dagger} - i\hbar\hat{U}\left(\frac{d}{dt}\hat{U}^{\dagger}\right). \tag{2.50}$$

Using the unitary

$$\hat{U} = |\uparrow\rangle \langle\uparrow| e^{i\omega_{\text{atom}}t/2} + |\downarrow\rangle \langle\downarrow| e^{-i\omega_{\text{atom}}t/2}, \qquad (2.51)$$

the system can transformed into the basis of the atomic transition $|\uparrow\rangle \leftrightarrow |\downarrow\rangle$, leaving

$$H = \hbar \frac{\Omega_0}{2} \left(|\uparrow\rangle \langle\downarrow| \exp\left[i\eta \left(\hat{a}u^*(t) + \hat{a}^{\dagger}u(t)\right)\right] e^{-i(\delta t - \phi)} + h.c. \right), \tag{2.52}$$

where $\delta = \omega_{\text{laser}} - \omega_{\text{atom}}$ is the detuning of the laser frequency from atomic resonance.

2.2.2 Motion Sidebands with the Laser Hamiltonian

From Eq. 2.52, it can be shown that the motion (both secular and micromotion) can be changed while driving a (pseudo-)spin flip $|\uparrow\rangle \leftrightarrow |\downarrow\rangle$; this is often described as "driving sidebands". The transitions described by the following Hamiltonians can be driven if the linewidth Γ of the transition between the pseudo-spins is narrow compared to the motion frequency ω_{mot} . This is called the *strong-binding regime*. If the linewidth is too broad, many transitions will be driven off-resonantly and the sidebands will not be resolved.²⁰

2.2.2.1 Secular Motion Sidebands

First, secular motion will be discussed. If the confinement is assumed to be purely harmonic as a result of static confinement, Eq. 2.52 can be written:

$$H = \hbar \frac{\Omega_0}{2} \left(|\uparrow\rangle \langle\downarrow| \exp\left[i\eta \left(\hat{a}e^{-i\omega_{\rm mot}t} + \hat{a}^{\dagger}e^{i\omega_{\rm mot}t}\right)\right] e^{-i(\delta t - \phi)} + h.c.\right). \tag{2.53}$$

If the exponential containing the ladder operators were to be expanded as a series, it is possible to see that certain terms would be slow-rotating if the laser detuning were to be set to a multiple of the secular frequency $\delta = s\omega_{\text{mot}}$, where s is an integer. This would then change the motion by s. Here, following Ref. [77], the effective Rabi frequency of such a transition will be calculated.

Suppose, an ion is in the state $|\uparrow, n\rangle$, where the \uparrow indicates the atomic pseudo-spin- $\frac{1}{2}$ state and n indicates the motional Fock population. Next, the motion is changed to the Fock state n+s

²⁰Another way to see this is that if $\Gamma \gg \omega_{\rm mot}$, the photon will be emitted much more quickly than one oscillation period occurs, and there is no coherence between the photons absorbed or emitted across oscillation periods [77]. This latter case is also known as the *weak-binding regime*.

while flipping the spin, to obtain $|\downarrow, n+s\rangle$ ($s \le n$, s may be positive or negative). The Hamiltonian can first be expanded using the Baker-Campbell-Hausdorff formula:

$$\langle \uparrow, n+s | H | \downarrow, n \rangle = \langle n+s | \hbar \frac{\Omega_0}{2} \left(\exp \left(i \eta \hat{a}^{\dagger} e^{i \omega_{\text{mot}} t} \right) \exp \left(i \eta \hat{a} e^{-i \omega_{\text{mot}} t} \right) e^{-\eta^2/2} e^{-i (s \omega_{\text{mot}} t - \phi)} \right) | n \rangle , \tag{2.54}$$

and then the exponential of each ladder operator is expanded as a series:

$$\langle \uparrow, n+s | H | \downarrow, n \rangle$$

$$= \hbar \frac{\Omega_0}{2} e^{-\eta^2/2} e^{-i(s\omega_{\text{mot}}t-\phi)} \langle n+s | \left(\sum_{u=0}^{\infty} \frac{1}{u!} (i\eta)^u \left(\hat{a}^{\dagger} \right)^u e^{iu\omega_{\text{mot}}t} \right) \left(\sum_{p=0}^{\infty} \frac{1}{p!} (i\eta)^p \hat{a}^p e^{-ip\omega_{\text{mot}}t} \right) |n\rangle ,$$

$$= \hbar \frac{\Omega_0}{2} e^{-\eta^2/2} e^{-i(s\omega_{\text{mot}}t-\phi)}$$

$$\times \left(\sum_{u=0}^{n+s} \frac{1}{u!} (i\eta)^u \langle n+s-u | \frac{\sqrt{(n+s)!}}{\sqrt{(n+s-u)!}} e^{iu\omega_{\text{mot}}t} \right) \left(\sum_{p=0}^{n} \frac{1}{p!} (i\eta)^p \frac{\sqrt{n!}}{\sqrt{(n-p)!}} |n-p\rangle e^{-ip\omega_{\text{mot}}t} \right) ,$$

$$= \hbar \frac{\Omega_0}{2} e^{-\eta^2/2} e^{-i(s\omega_{\text{mot}}t-\phi)} \left(\sum_{u=0}^{n+s} \sum_{p=0}^{n} \frac{1}{u!p!} (i\eta)^{(u+p)} e^{i(u-p)\omega_{\text{mot}}t} \frac{\sqrt{(n+s)!}}{\sqrt{(n+s-u)!}} \frac{\sqrt{n!}}{\sqrt{(n-p)!}} \delta_{(u-s,p)} \right) ,$$

$$= \hbar \frac{\Omega_0}{2} e^{-\eta^2/2} e^{i\phi} \sqrt{n!(n+s)!} \left(\sum_{u=max(s,0)}^{n+s} \frac{1}{u!(u-s)!(n-(u-s))!} (i\eta)^{2u-s} \right) .$$

$$(2.58)$$

If s is positive, the above can be expressed as

$$\langle \uparrow, n+s | H | \downarrow, n \rangle = \hbar \frac{\Omega_0}{2} e^{-\eta^2/2} e^{i\phi} \sqrt{n!(n+s)!} \left(\sum_{u=0}^n \frac{1}{(u+s)! u!(n-u)!} (i\eta)^{2u} (i\eta)^s \right). \tag{2.59}$$

On the other hand, if s is negative,

$$\langle \uparrow, n+s | H | \downarrow, n \rangle = \hbar \frac{\Omega_0}{2} e^{-\eta^2/2} e^{i\phi} \sqrt{n!(n+s)!} \left(\sum_{u=0}^{n+s} \frac{1}{u!(u-s)!(n-(u-s))!} (i\eta)^{2u} (i\eta)^{-s} \right). \tag{2.60}$$

Together they can be expressed as

$$\langle \uparrow, n+s | H | \downarrow, n \rangle = \hbar \frac{\Omega_0}{2} e^{-\eta^2/2} e^{i\phi} \sqrt{n_{<}!(n_{<} + |s|)!} \left(\sum_{u=0}^{n_{<}} \frac{(-1)^u (\eta)^{2u} (i\eta)^{|s|}}{u!(u+|s|)!(n_{<} - u)!} \right), \tag{2.61}$$

where $n_{\leq} = \min(n, n + s)$. It can be shown using the closed form of the Laguerre polynomial

$$L_n^{\alpha}(X) = \sum_{i=0}^n (-1)^i \binom{n+\alpha}{n-i} \frac{X^i}{i!} = \sum_{i=0}^n (-1)^i \frac{(n+\alpha)!}{(n-i)!(\alpha+i)!} \frac{X^i}{i!}$$
(2.62)

that the Eq. 2.61 can be rewritten

$$\langle \uparrow, n + s | H | \downarrow, n \rangle = \frac{\hbar}{2} \left[\Omega_0 e^{-\eta^2/2} e^{i\phi} \frac{\sqrt{n_{<}!}}{\sqrt{(n_{<} + |s|)!}} (i\eta)^{|s|} L_{n<}^{|s|} (\eta^2) \right]. \tag{2.63}$$

The part in the square brackets above may be taken as the Fock-state dependent Rabi frequency for a sideband of order s:

$$\Omega_{n,n+s} = \Omega_0 e^{-\eta^2/2} e^{i\phi} \frac{\sqrt{n_{<}!}}{\sqrt{(n_{<} + |s|)!}} (i\eta)^{|s|} L_{n<}^{|s|} (\eta^2).$$
(2.64)

For a fixed sideband order |s|, Eq. 2.64 shows that different Fock states have different effective Rabi frequencies. Therefore, if a sideband of order s is driven (by detuning the laser with $\delta = s\omega_{\text{mot}}$) for a period of time t, the population in $|\downarrow\rangle$ can be seen (using fluorescence detection, discussed in Sec. 2.2.3) to change according to [23, 68]:

$$P_{\uparrow} = \frac{1}{2} \left[1 + \sum_{n=0}^{\infty} P_n \cos(\Omega_{n,n+s} t) \exp(-\gamma_n t) \right], \qquad (2.65)$$

where γ_n is a phenomenological damping constant, which is taken to be $\gamma_n \approx \gamma_0 (n+1)^{0.7}$ [23] in this thesis. Usually $\gamma_n \ll \Omega_{n,n+s}$, so sometimes the exponential decay term is dropped entirely. By fitting such population oscillations, the probability of each Fock state being present P_n can be extracted, provided the values of $\Omega_{n,n+s}$ are distinct enough for different n.

The first and zeroth order sidebands ($s = \pm 1, 0$) are the most commonly used, and η is usually

a small value; if $\eta \ll 1$ the system is said to be in the *Lamb-Dicke regime*, and a Taylor expansion of Eq. 2.53 can be performed:

$$H = \hbar \frac{\Omega_0}{2} \left(|\uparrow\rangle \langle\downarrow| \left[\mathbb{1} + i\eta \left(\hat{a}e^{-i\omega_{\text{mot}}t} + \hat{a}^{\dagger}e^{i\omega_{\text{mot}}t} \right) + \mathcal{O}\left(\eta^2\right) \right] e^{-i(\delta t - \phi)} + h.c. \right). \tag{2.66}$$

When $\delta = 0$ (i.e. the laser is on resonance with the atomic transition), the most likely transition to occur is represented by the slowly rotating term corresponding to 1 in Eq. 2.66 which does not change motion; this is known as the *carrier transition*.

By setting $s = \pm 1$, the first-order motion changing sidebands are obtained:

$$H_{\rm rsb} = \hbar \frac{\Omega_0}{2} \left(i\eta |\uparrow\rangle \langle\downarrow| \hat{a}e^{i\phi} + h.c. \right), \tag{2.67}$$

$$H_{\rm bsb} = \hbar \frac{\Omega_0}{2} \left(i\eta |\uparrow\rangle \langle\downarrow| \hat{a}^{\dagger} e^{i\phi} + h.c. \right), \tag{2.68}$$

for $\delta = \omega_{\rm mot}$ and $\delta = -\omega_{\rm mot}$ respectively. Eq. 2.67 describes a Jaynes-Cummings type interaction while Eq. 2.68 describes an anti-Jaynes-Cummings interaction. These are the main way²¹ to transfer motion information onto the internal state which is then determined by fluorescence detection (discussed in Sec. 2.2.3). These operations can also be used to entangle spin and motion.

It should also be noted that if multiple motion modes are present in the apparatus, for example along different axes, or along the same axes due to more than one ion trapped in the potential as discussed in Sec. 2.1.3, this calculation may be repeated for each mode, taking into account the different projection of $\mathbf{k} \cdot \mathbf{r}$ for different directions and scaling of the Rabi frequency Ω_0 by the participation of the relevant ion according to Eq. 2.36. The same value of detuning δ then applies to all modes simultaneously, when a sideband transition is attempted.

If the multiple modes have very similar frequencies, then the driving of one mode can also cause unintentional driving of other modes; this issue is known as "mode crowding", which is a significant barrier to trapping large numbers of ions in the same potential well. Even if the mode

²¹In principle higher-order sidebands can be used, but for small η and low sideband orders |s|, the efficiency of these sidebands decrease proportionally to $\eta^{|s|}$, so the first-order sideband is the most frequently used in experiment.

frequencies are well separated, if the laser driving sideband transitions has projection along multiple modes,²² the Rabi frequency is affected by *Debye-Waller factors*, which is a modification of the effective Rabi frequency due to spectator modes [50].

2.2.2.2 Sideband Thermometry

When the motion of an ion is assumed to be thermal,²³ a clever trick may be implemented to find the average occupation number of the ion motion. This is known as *sideband thermometry*. A thermal state has distribution given by [68, 78]:

$$P_n = \frac{\bar{n}^n}{(\bar{n}+1)^{n+1}},\tag{2.69}$$

where P_n is the probability of observing population in Fock state n, and the bar denotes the average population. From Eq. 2.65, the probability of driving a sideband with s = -1 for this type of distribution is:

$$P_{\uparrow,RSB} = \frac{1}{2} \sum_{n=1}^{\infty} \frac{\bar{n}^n}{(\bar{n}+1)^{n+1}} \left[1 + \cos(\Omega_{n,n-1}t) \right],$$

$$= \frac{1}{2} \frac{\bar{n}}{\bar{n}+1} \sum_{n=0}^{\infty} \frac{\bar{n}^n}{(\bar{n}+1)^{n+1}} \left[1 + \cos(\Omega_{n+1,n}t) \right] = \frac{\bar{n}}{\bar{n}+1} P_{\uparrow,BSB},$$
(2.70)

where the index for the first sum starts at 1 instead of 0 because $|0\rangle$ is the lowest Fock state so a RSB cannot be driven, and $P_{\uparrow,BSB}$ is the probability of driving a sideband with s=+1. Therefore, for thermal states,²⁴ the average Fock state occupation \bar{n} can be calculated by comparing the two first-order motion sideband spin-flip probabilities.

²²Which can be all along the same axis!

²³This is, for example, true after Doppler cooling, but not necessarily true after sideband cooling because of the dependence of Rabi frequency on Fock number as shown in Eq. 2.64.

²⁴In this thesis, sideband-cooled states with low enough average occupation are treated as close enough to thermal states that this analysis can be applied.

It can be shown that if a system is described by the rate equation

$$\frac{d}{dt}P_n = A_-\left[(n+1)P_{n+1} - nP_n\right] + A_+\left[nP_{n-1} - (n+1)P_n\right],\tag{2.71}$$

where P_n is the probability of finding the state in Fock state n, and A_- and A_+ are n-independent motion-subtracting and motion-adding transition rates, then a thermal state that is input into the system will evolve into a thermal state as well. This equation describes both Doppler and EIT cooling (the later of which is discussed in Ch. 4).

2.2.2.3 Micromotion Sidebands

Due to the asymmetric geometry of the ion trap (see Fig. 3.18), the ion experiences micromotion that cannot be compensated by moving to a micromotion null point. Although the trap is mainly linear, there are parts that break the symmetry along the **z** axis, for example the bend ("goose-neck") on the left side of the ion trap wafer as well as the crossing of the RF electrode over the junction. This inadvertently results in the presence of an oscillating potential at the ion.

In this case, the motion can be treated as if it is being driven by an oscillating RF field, and the time-dependent functions u(t) modifying the motion operators in the Hamiltonian Eq. 2.52 should be defined by Eq. 2.16, yielding^{25,26}:

$$H = \hbar \frac{\Omega_0}{2} \left(|\uparrow\rangle \langle\downarrow| \exp\left[i\eta \left(\hat{a}e^{-i\omega_{\rm mot}t} + \hat{a}^{\dagger}e^{i\omega_{\rm mot}t}\right) \frac{1 + (q_z/2)\cos\left(\omega_{\rm RF}t\right)}{1 + q_z/2}\right] e^{-i(\delta t - \phi)} + h.c.\right). \quad (2.72)$$

Following Ref. [75], the term containing the cosine can be expanded using Bessel functions

$$\exp\left[i\eta \frac{(q_z/2)\cos(\omega_{\rm RF}t)}{1+q_z/2}\right] = \sum_{n=-\infty}^{\infty} iJ_n(\beta)e^{in\omega_{\rm RF}t},\tag{2.73}$$

²⁵By using Eq. 2.16, the problem is simplified to one dimension, and the phase of the RF potential is not considered. All three dimensions as well as the RF potential phase are considered in Ref. [75].

 $^{^{26}}$ If there is some effective RF potential present at the ion, the q parameter is nonzero, therefore even if micromotion itself is not considered, the Lamb-Dicke parameter in Eq. 2.53 and the equations that follow should be modified by a factor of 1/(1+q/2) as suggested by Eq. 2.16.

where β , known as the micromotion modulation index, is given as

$$\beta = \frac{\eta q_z}{2(1 + q_z/2)}. (2.74)$$

Combining again with Eq. 2.72:

$$H = \hbar \frac{\Omega_0}{2} \left(|\uparrow\rangle \langle\downarrow| \exp\left[\frac{i\eta}{1 + q_z/2} \left(\hat{a}e^{-i\omega_{\text{mot}}t} + \hat{a}^{\dagger}e^{i\omega_{\text{mot}}t}\right)\right] \left[\sum_{n=-\infty}^{\infty} iJ_n(\beta)e^{in\omega_{\text{RF}}t}\right] e^{-i(\delta t - \phi)} + h.c.\right). \tag{2.75}$$

Eq. 2.75 shows that the $l^{\rm th}$ micromotion sideband can be driven by tuning $\delta = l\omega_{\rm RF}$; the term containing $J_l(\beta)$ will be slowly rotating while all others will be rotating at integer multiples of $\omega_{\rm RF}$. Therefore, for this slow-rotating term, the Rabi frequency Ω_0 is modified by $J_l(\beta)$. A micromotion sideband and secular sideband can be driven simultaneously if desired by setting $\delta = l\omega_{\rm RF} + s\omega_{\rm mot}$; then the sideband will be modified both by $J_l(\beta)$ and the factor multiplying Ω_0 in Eq. 2.64.

In principle, it is possible to calculate the micromotion modulation index β using Eq. 2.74. However, the parameters used (such as q and η) are affected by experimental imperfections such as misalignment of the trap electrodes, tilting of the trapping axes, and non-ideal ion position. Therefore, in this apparatus β is determined empirically (as mentioned in Sec. 4.3.7) by comparing the observed Rabi frequency for various micromotion sidebands and the same secular sideband to extract $J_n(\beta)$ for different n.

2.2.2.4 Raman Transitions in ${}^{9}\mathrm{Be^{+}}$ and ${}^{25}\mathrm{Mg^{+}}$

In $^9\mathrm{Be^+}$ and $^{25}\mathrm{Mg^+}$ secular motion transitions between $^2\mathrm{S}_{1/2}$ and any of the P manifolds fall into the weak-binding regime. Therefore, resolved-sideband transitions are instead driven between two states both in the $^2\mathrm{S}_{1/2}$ manifold using stimulated Raman transitions. Because (for all experimental intents and purposes) a quantum cannot spontaneously transit between two states in the $^2\mathrm{S}_{1/2}$ manifold, this allows the effective modification of the decay rate $\Gamma \to 0$.

For a stimulated Raman transition, the theoretical description is much the same as that for a

single laser, with effective changes to Eq. 2.44 being

$$\frac{\Omega_0}{2} \to \frac{\Omega_{0,1}\Omega_{0,2}}{4\Delta}$$

$$\mathbf{k} \to \mathbf{k_1} - \mathbf{k_2}$$

$$\omega_{\text{laser}} \to \omega_{\text{laser}1} - \omega_{\text{laser}2}$$

$$\phi \to \phi_1 - \phi_2$$
(2.76)

where the 1 and 2 index the two Raman beams, and Δ is a large frequency detuning of both beams from a common excited state (in our apparatus this is ≈ 200 -300 GHz from the nearest state). These substitutions are valid assuming that the Raman transition may only be driven by a single combination of the polarizations of each beam (i.e. there is only one "path" between the effective $|\uparrow\rangle$ and $|\downarrow\rangle$); the detuning is large Δ compared to the nearest state; and there is only one common excited state (or a group of states that are very close together compared to Δ) for the two Raman beams with the given polarizations. This is the case in our experimental apparatus, as shown by Figs. 3.7 and 3.8. In general, it is possible that the Raman beams' common detuning can fall between two groups of states such that both contribute Stark shifts in opposite directions, or the polarization of the two beams are such that the transition may be driven with multiple combinations of polarizations; a more complex expression accounting for these is described in Ref. [3].

2.2.3 Fluorescence Detection

Ions are typically probed through fluorescence detection [50, 68, 79–83], where a certain transition is excited by light of the correct wavelength, and the resulting emitted photons are collected. This wavelength is often particular to a certain transition (or multiple transitions; if the excited state manifold has a short lifetime, this will give a broad bandwidth), so if the ion atomic state is not in the ground state of the given transition(s), there will be no fluorescence and no photons observed.²⁷ This yields a binary result as the main method of quantum measurement for

²⁷Up to experimental imperfections, such as dark counts and photon scatter off of the apparatus.

trapped ions, corresponding to whether or not the ion was in the given subset of states that the laser is capable of exciting. In our apparatus, only $\sim 1\%$ of photons scattered from the ions are collected by the imaging objective and detected by a photo-multiplier tube. To make it feasible to determine the state of the ion, a cycling transition is used, where the decay from the excited state is restricted by selection rules to return to the same initial state so it can be excited repeatedly and continuously scatter photons in the presence of resonant detection light.

More concretely, for our apparatus, in ${}^9\mathrm{Be}^+$ this cycling transition is chosen between the $|F=2,m_F=2\rangle^{28}$ state in ${}^2\mathrm{S}_{1/2}$ and the state with $|m_F=3\rangle$ in ${}^2\mathrm{P}_{3/2}$ 29 as shown in Fig. 2.5 and is driven by a σ_+ -polarized laser beam. Because selection rules dictate that m_F can only change by ± 1 or 0, the excited state can only decay back to ${}^2\mathrm{S}_{1/2}|2,2\rangle$. This state in the ${}^2\mathrm{S}_{1/2}$ manifold is labeled the $|\mathrm{Bright}\rangle$ state and any population in this state is trapped in a cycle between $|\mathrm{Bright}\rangle$ and $|m_F=3\rangle$ during fluorescence detection, up to the polarization purity of the detection light. If the beam has other polarization components, the population can be excited to a state with different m_F which would enable decay to states other than $|\mathrm{Bright}\rangle$ in the ${}^2\mathrm{S}_{1/2}$ manifold, resulting in depumping. In ${}^{25}\mathrm{Mg}^+$ the cycling transition occurs between the $|3,3\rangle$ state in ${}^2\mathrm{S}_{1/2}$ and the state with $|m_F=4\rangle$ in ${}^2\mathrm{P}_{3/2}$. Another option for cycling transitions in ${}^9\mathrm{Be}^+$ and ${}^{25}\mathrm{Mg}^+$ (used in other experiments in the Ion Storage Group) is found at the other side of the manifold, where a σ^- -polarized laser beam can be used and the cycling transition is controlled to be, for example for ${}^9\mathrm{Be}^+$, between the $|2,-2\rangle$ in ${}^2\mathrm{S}_{1/2}$ and the state with $|m_F=-3\rangle$ in ${}^2\mathrm{P}_{3/2}$.

For experiments, two hyperfine states of ${}^2S_{1/2}$ in either species are often chosen to implement a pseudo-spin- $\frac{1}{2}$ qubit state. During detection, one of the two "spin" states is transferred to the |Bright⟩ state and the other state is transferred to the |Dark⟩ state (shown for each species in Fig. 2.5) using microwaves in a process called *shelving*. The |Dark⟩ state is chosen to be the furthest away from

²⁸From this point onwards, unless otherwise specified, kets containing two numbers are assumed to denote $|F, m_F\rangle$. Also, if the manifold is not explicitly stated, a ket of this form can be assumed to refer to the atomic state in the $^2S_{1/2}$ manifold, as these are the most long-lived and can therefore be manipulated during experiments.

²⁹At a magnetic field of 11.945 mT, the ${}^{2}P_{3/2}$ states do not have well-defined F manifolds (i.e. F is no longer a good quantum number), as evidenced by the grouping of the states in Fig. 2.5. However, a state with $m_F = 3$ and 4 for ${}^{9}\text{Be}^{+}$ and ${}^{25}\text{Mg}^{+}$ respectively can be fairly straightforwardly defined.

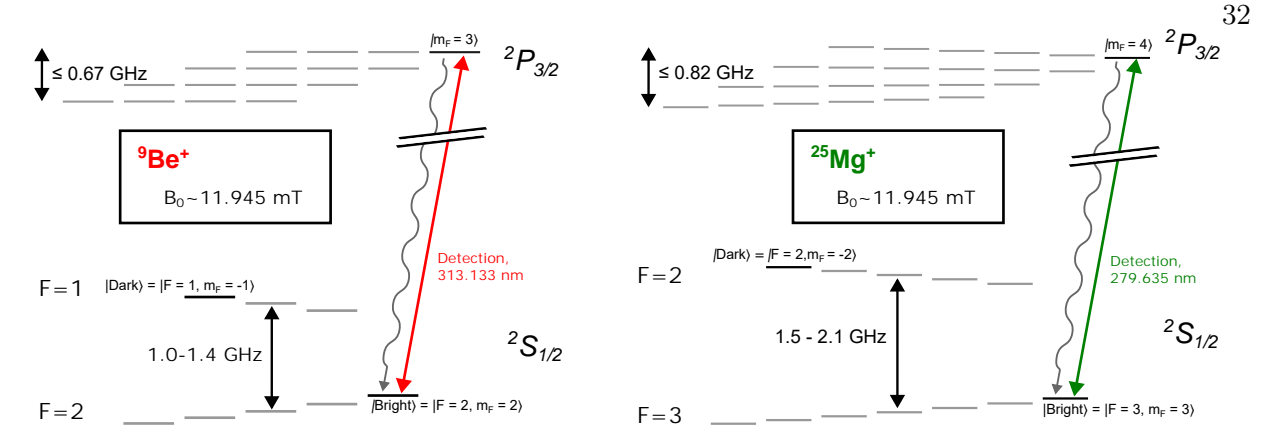


Figure 2.5: The states in ${}^9\mathrm{Be}^+$ (left) and ${}^{25}\mathrm{Mg}^+$ (right) used for the cycling transitions during detection in our apparatus. The ${}^2\mathrm{S}_{1/2}$ and ${}^2\mathrm{P}_{3/2}$ states are shown at a field of 11.945 mT. By using σ^+ -polarized light, the |Bright \rangle states, $|F=2,m_F=2\rangle$ ($|F=3,m_F=3\rangle$) in the ${}^2\mathrm{S}_{1/2}$ manifold of ${}^9\mathrm{Be}^+$ (${}^{25}\mathrm{Mg}^+$) are excited to states with $|m_F=3\rangle$ ($|m_F=4\rangle$) in the ${}^2\mathrm{P}_{3/2}$ state by lasers (illustrated by red (green) arrows) of wavelengths 313 (280) nm. Because m_F can only change by ± 1 or 0 for a photon decay, this excited state can only decay to the original |Bright \rangle state, which enables it to be excited again, completing the cycling transition. In order to perform maximal state discrimination in an experiment where the ion state is expected to be in one of two states in the ${}^2\mathrm{S}_{1/2}$ manifold, one state is transferred to the |Bright \rangle state and the other state is transferred to the |Dark \rangle state, which is chosen to be the furthest away in in m_F and a different F state from the |Bright \rangle state. More detailed level structures of ${}^9\mathrm{Be}^+$ and ${}^{25}\mathrm{Mg}^+$ at this field are given in Sec. 3.1.

 $|\text{Bright}\rangle$; of a different F state in order to make the detection beam photons more off-resonant, and the furthest away m_F state to ensure that as many as possible scattering events are required for a state beginning in $|\text{Dark}\rangle$ to transition to $|\text{Bright}\rangle$. More details can be found in Sec. 3.1.

Chapter 3

Experimental Apparatus

The experimental apparatus used for the work in this thesis is fairly mature and has gone through a series of upgrades during my graduate studies. Here, I aim to provide an overview of various parts of the apparatus that I am familiar with, as well as an updated record of the current state and components used. I also describe some techniques used, especially regarding our lasers—while they may be also described elsewhere, here I will describe how these are implemented specifically in this lab for future users of the experimental apparatus. There is also additional information in Appendix A.

$^9\mathrm{Be^+}$ and $^{25}\mathrm{Mg^+}$

Two ion species, ${}^{9}\mathrm{Be^{+}}$ and ${}^{25}\mathrm{Mg^{+}}$, are used in this lab to harness the benefits of "individual addressing", where certain ions can be addressed by laser or microwave fields without unintentionally affecting the states of others. Our laser beams are not very tightly focused, so using ions that respond to very different wavelengths enables each ion species to be manipulated individually. Compared to using tightly focused beams, this method avoids crosstalk of lasers between species and spontaneously emitted photons from one ion cannot damage the state of ions of a different species. Unfortunately, with this method if multiple ions of the same species are trapped in the same

¹This refers to direct absorption or significant shifts. While it has been suspected in the past that some extreme cases of crosstalk have occurred (for example where the Raman lasers of one species may be intense enough to affect the other via a Stark shift), every measurement made to investigate whether or not this is the case in this apparatus has found laser crosstalk between the ion species to have a negligible effect on the experiment. This may not be true in all cases.

harmonic confinement potential, they cannot be individually addressed.

Co-trapping ²⁵Mg⁺ with ⁹Be⁺ is a good choice because within the alkaline earth metals group,² they have the closest mass match.³ A similar charge-to-mass ratio is beneficial because the discrepancy in participations of each ion species (Secs. 2.1 and 3.6) in each mode will increase as the ratio increases. This difference in mode participations is especially disadvantageous when one ion species is assigned a particular role, such as cooling, which will become very inefficient due to the low participation of the coolant ion in some modes. Even though ²⁵Mg⁺ is one of the best choices to co-trap with ⁹Be⁺ the mass difference is already large enough to cause significant differences in participation; this is explored in Sec. 5.6.

 $^9\mathrm{Be^+}$ has nuclear spin I=3/2 and $^{25}\mathrm{Mg^+}$ has nuclear spin I=5/2; both have hyperfine structure with qualitatively similar $^2\mathrm{S}_{1/2}$, $^2\mathrm{P}_{1/2}$, and $^2\mathrm{P}_{3/2}$ manifolds which are assigned similar roles in our apparatus (i.e. fluorescence cycling transition state, cooling states). The ions are immersed in a magnetic field of 11.945 mT, where $^9\mathrm{Be^+}$ has a first-order field-insensitive transition between $^2\mathrm{S}_{1/2}$ $|F=2,m_F=0\rangle$ and $^2\mathrm{S}_{1/2}$ $|1,1\rangle$ (Tab. 3.3), and $^{25}\mathrm{Mg^+}$ has a minimally field-sensitive transition between $^2\mathrm{S}_{1/2}$ $|3,1\rangle$ and $^2\mathrm{S}_{1/2}$ $|2,0\rangle$ (Tab. 3.4). Level structure diagrams for both species from Breit-Rabi calculations at this quantization field are shown in Figs. 3.1, 3.2, 3.3, 3.4, 3.5, 3.6; within each diagram the energy level spacings are labeled and illustrated roughly to scale.

Other than the field sensitivity at 11.945 mT, the main differences between the two species are the resonant wavelengths, which are around 313 nm for ${}^9\mathrm{Be}^+$, and 280 nm for ${}^{25}\mathrm{Mg}^+$; and their excited (P) state decay rates, which are 19.4 MHz and 41.3 MHz for ${}^9\mathrm{Be}^+$ and ${}^{25}\mathrm{Mg}^+$ respectively. For reference, the field sensitivities of all states in the ${}^2\mathrm{S}_{1/2}$ manifolds of ${}^9\mathrm{Be}^+$ and ${}^{25}\mathrm{Mg}^+$ are listed in Tabs. 3.1, 3.2.

As the lightest two elements in the alkaline earth metals group, ${}^9\mathrm{Be^+}$ and ${}^{25}\mathrm{Mg^+}$ have the

²Elements in this group make a good choice for ion-trapping because when singly-ionized, they appear hydrogen-like, which simplifies calculations. It also simplifies the experiments greatly, for example it allows for nearly perfectly closed transitions and reduces the required number of repump lasers.

³Ions of *extremely* different charge-to-mass ratios have very different a and q parameters and thus cannot both be made to fit in the same stability region as will be illustrated in Sec. 2.1.1, and therefore are difficult to straightforwardly co-trap. Clever ways have been implemented to overcome this in some cases (for example, Ref. [84]).

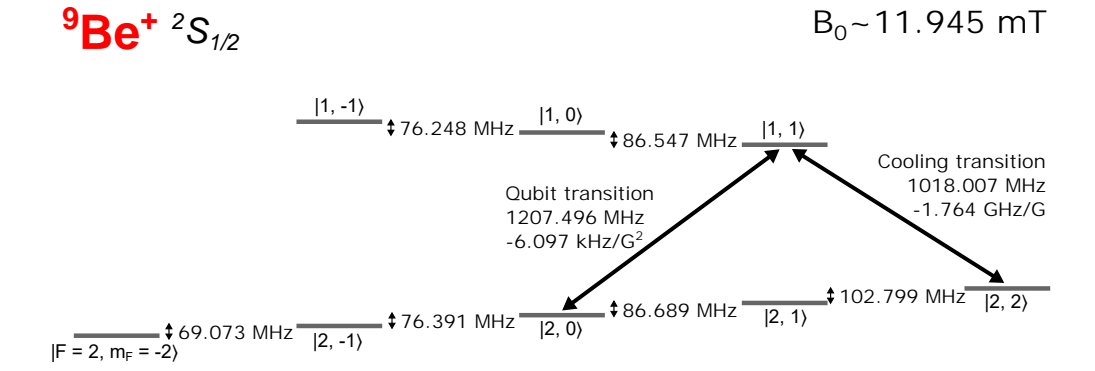


Figure 3.1: Calculated energy level splittings of the ${}^2S_{1/2}$ manifold of ${}^9Be^+$ near 11.945 mT, with the qubit transition (the least field sensitive transition) and the cooling transition (the extremal transition on which Raman sideband cooling is performed) labeled (black arrows). The magnetic field sensitivity of the two transitions are shown per gauss squared or per gauss, as appropriate.

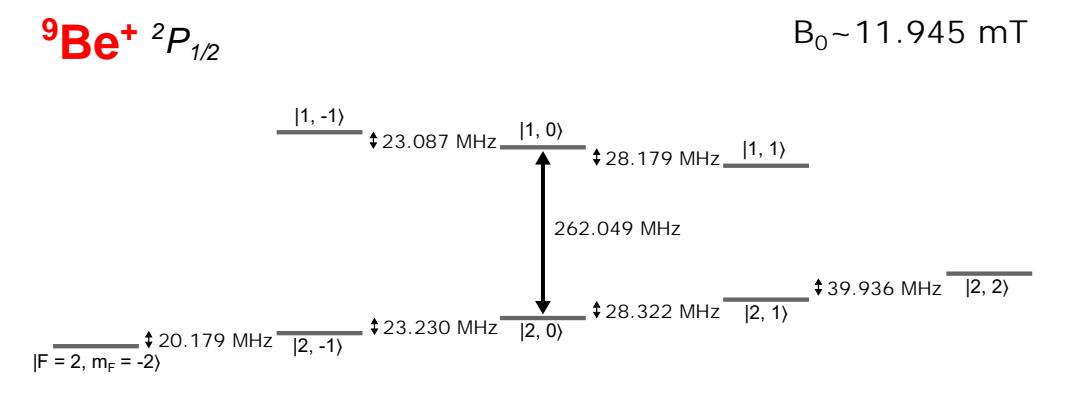


Figure 3.2: Calculated energy level splittings of the ${}^2\mathrm{P}_{1/2}$ manifold of ${}^9\mathrm{Be}^+$ near 11.945 mT. The hyperfine splitting between the two F manifolds is approximately 200-300 MHz, and the frequency splitting between states in the same hyperfine manifold is comparable to the decay rate of the ${}^9\mathrm{Be}^+$ 2P states.

strongest couplings to their motion. This manifests in their large Lamb-Dicke values (Eq. 2.46) and also enable them to be more rapidly transported with the same magnitude of electric field compared to ions of heavier mass. This comes at the practical cost of their less favorable laser frequencies.⁶ They also lack a low-lying D manifold, making a repump beam from such a manifold unnecessary, but this prevents them from being used for metastable qubits, as well as other tricks that can be implemented when such a manifold is available.

⁶The Ion Storage group has ample experience generating and using UV wavelengths. However, this also presents a practical barrier to many new optical technologies that can currently only be used with longer wavelengths, such as integrated photonics.

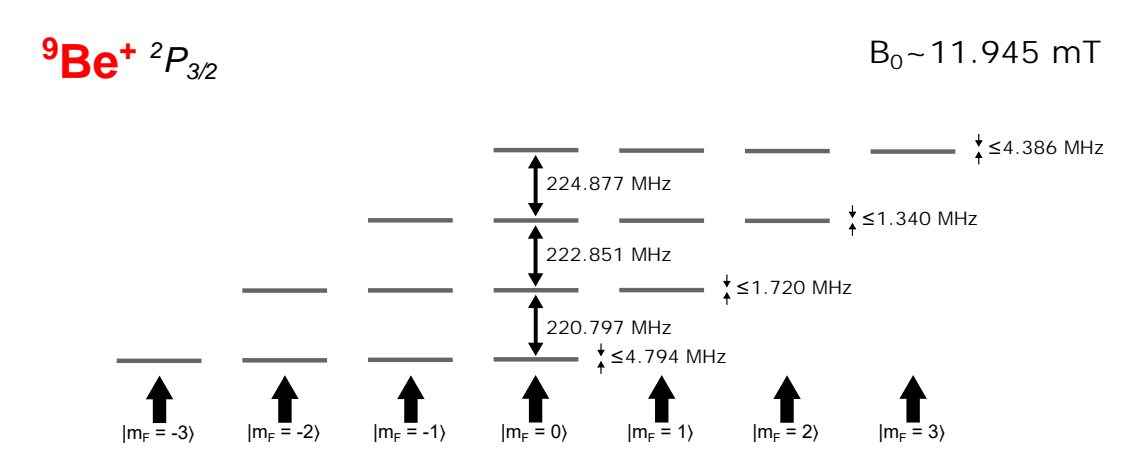


Figure 3.3: Calculated energy level splittings of the ${}^2\mathrm{P}_{3/2}$ manifold of ${}^9\mathrm{Be}^+$ near 11.945 mT. From the energy grouping of the manifolds, it is evident that F is no longer a good quantum number, but the m_F of the states can be labeled as indicated by the values of m_F underneath each column of states. Each group of four states is very narrowly separated but the whole ${}^2\mathrm{P}_{3/2}$ manifold spans 600 MHz.

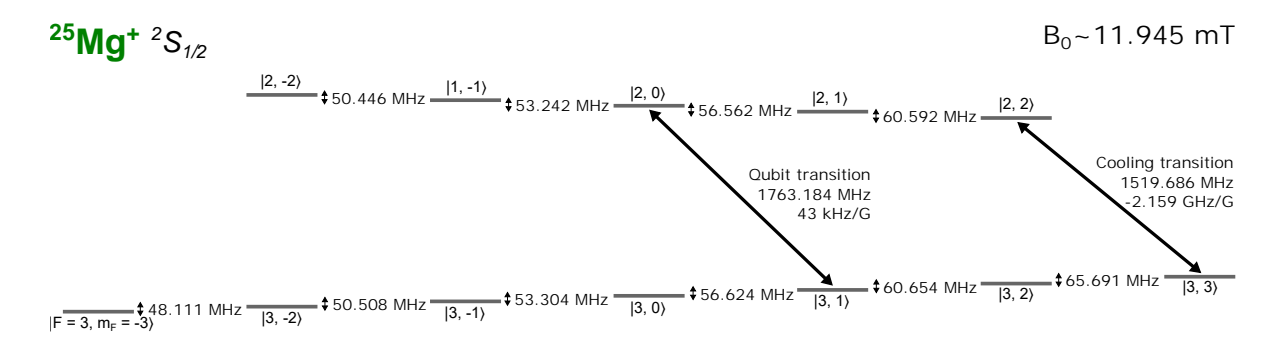


Figure 3.4: Calculated energy level splittings of the $^2\mathrm{S}_{1/2}$ manifold of $^{25}\mathrm{Mg}^+$ near 11.945 mT, with the qubit transition (the least field sensitive transition) and the cooling transition (the extremal transition on which Raman sideband cooling is performed) labeled (black arrows). The magnetic field sensitivity of the two transitions are shown.

While the $^{24}\text{Mg}^+$ isotope is also a potential choice instead of $^{25}\text{Mg}^+$ for the reasons above, $^{24}\text{Mg}^+$ has nuclear spin I=0, which means it does not have a magnetic-field-insensitive (or minimally sensitive) transition (Tab. 3.4). Field insensitivity enables the transition to have much longer coherence times in the presence of magnetic field noise, which makes it suitable for implementation of a qubit. For this reason, $^{25}\text{Mg}^+$ is chosen to complement $^9\text{Be}^+$ for the experiments performed in this apparatus. Rather than the four $^2\text{S}_{1/2}$ -manifold states of $^{24}\text{Mg}^+$, $^{25}\text{Mg}^+$ has 12 states in the $^2\text{S}_{1/2}$ manifold, making population leakage more difficult to deal with. This issue is explored further

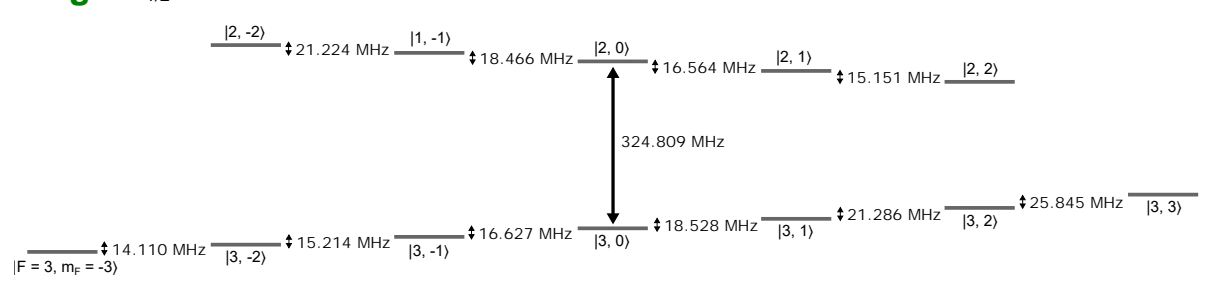


Figure 3.5: Calculated energy level splittings of the $^2P_{1/2}$ manifold of $^{25}Mg^+$ near 11.945 mT. Similar to the $^2S_{1/2}$ manifolds between the two species, the $^{25}Mg^+$ $^2P_{1/2}$ manifold has a larger hyperfine splitting than $^9Be^+$, but the states within each hyperfine manifold are not as separated from each other.

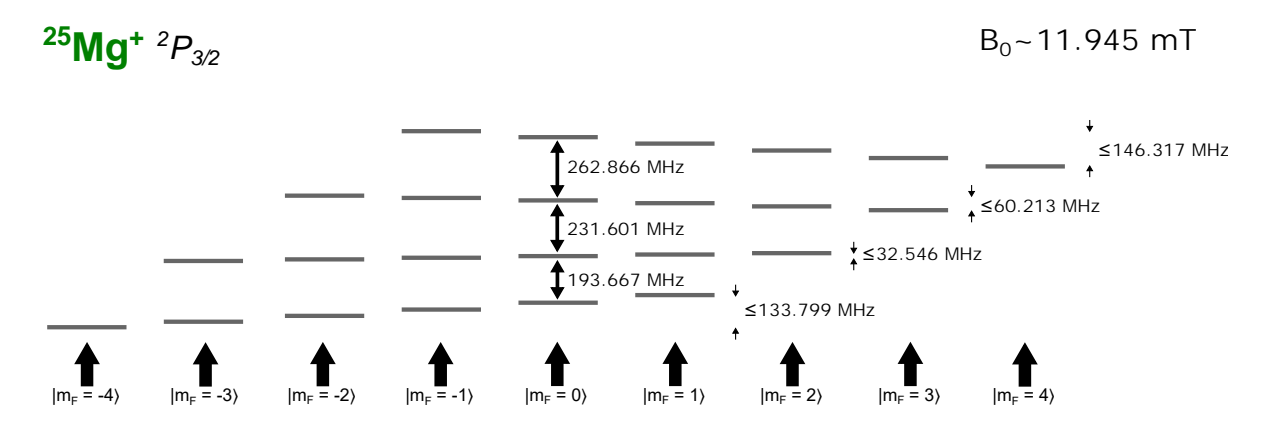


Figure 3.6: Calculated energy level splittings of the $^2\mathrm{P}_{3/2}$ manifold of $^{25}\mathrm{Mg}^+$ near 11.945 mT. From the energy grouping of the manifolds, it is evident that F is no longer a good quantum number, but the m_F of the states can be labeled as indicated by the values of m_F underneath each column of states. As can be seen above, frequency spacing of each "row" of states is much larger than that of $^9\mathrm{Be}^+$ therefore extra caution must be taken in cases where coupling to multiple states between the $^2\mathrm{S}_{1/2}$ and $^2\mathrm{P}_{3/2}$ manifolds is allowed.

in Ch. 4.

3.2 Beamlines and Lasers

A large portion of my time as a PhD student was devoted to the upgrading and maintenance of the laser systems. The laser beams are used to ionize, cool, prepare the atomic state of, and manipulate the motion of the trapped ions. In order to trap and have the same amount of control over both ion species used in this apparatus, about twice the amount of laser equipment is needed

State $(F, m_F\rangle)$	Field Sensitivity (MHz/ $2\pi/G$)
$ 2,-2\rangle$	-1.402
$ 2,-1\rangle$	-0.930
$ 2, 0\rangle$	-0.362
$ 2, 1\rangle$	0.363
$ 2, 2\rangle$	1.402
$ 1,-1\rangle$	0.929
$ 1, 0\rangle$	0.362
$ 1, 1\rangle$	-0.362

Table 3.1: Calculated field sensitivities of ${}^2S_{1/2}$ states of ${}^9Be^+$ near 11.945 mT. Because $|2,0\rangle$ and $|1,1\rangle$ have the same sensitivity at this field, this transition is suitable for implementing a field-insensitive "clock" qubit. Another potential choice is $|2,1\rangle\leftrightarrow|1,0\rangle$ which can be made field-insensitive with a slight increase in the magnetic field to 11.964 mT. It should be noted that the cooling and qubit transitions are the same polarization in this latter configuration, which may be advantageous for power distribution between the polarization of the microwaves (via positioning of the microwave antenna) and Raman beams (waveplate rotation).

Field Sensitivity (MHz/ $2\pi/G$)			
-1.402			
-1.056			
-0.677			
-0.258			
0.215			
0.759			
1.402			
1.055			
0.677			
0.258			
-0.214			
-0.758			

Table 3.2: Calculated field sensitivities of ${}^2S_{1/2}$ states of ${}^{25}Mg^+$ near 11.945 mT.

Transition $(F, m_F\rangle \leftrightarrow F, m_F\rangle)$	Frequency (MHz)	Field Sensitivity (MHz/ 2π /G)
$ 2,\ 0\rangle \leftrightarrow 1,-1\rangle$	1370.029	1.291
$ 2, 0\rangle \leftrightarrow 1, 0\rangle$	1294.042	0.725
$ 2, 0\rangle \leftrightarrow 1, 1\rangle$	1207.496	0
$\boxed{ 2, 2\rangle \leftrightarrow 1, 1\rangle}$	1018.007	-1.764

Table 3.3: Calculated frequencies and field sensitivities of selected (commonly used in our apparatus) microwave transitions ${}^2S_{1/2}$ states of ${}^9Be^+$ near 11.945 mT. The transition $|2,0\rangle \leftrightarrow |1,1\rangle$ is first-order field insensitive at this field and has a second-order field sensitivity of -6.097 kHz/ G^2 .

Transition $(F, m_F\rangle \leftrightarrow F, m_F\rangle)$	Frequency (MHz)	Field Sensitivity (MHz/ 2π /G)	
$ 3,-1\rangle \leftrightarrow 2,-2\rangle$	1976.801	1.732	
$ 3,-1\rangle \leftrightarrow 2,-1\rangle$	1926.355	1.354	
$ 3,-1\rangle \leftrightarrow 2,\ 0\rangle$	1873.113	0.935	
$ 3, 1\rangle \leftrightarrow 2, 0\rangle$	1763.184	0.043	
$ 3, 1\rangle \leftrightarrow 2, 2\rangle$	1646.031	-0.973	
$ 3, 3\rangle \leftrightarrow 2, 2\rangle$	1519.686	-2.159	

Table 3.4: Calculated frequencies and field sensitivities of selected (commonly used in our apparatus) microwave transitions $^2S_{1/2}$ states of $^{25}Mg^+$ near 11.945 mT. While there are no fully field-insensitive transitions for $^{25}Mg^+$ at this field, it an be seen that $|3,1\rangle \leftrightarrow |2,0\rangle$ is relatively field-insensitive; therefore it is used in experiments when long coherence times are beneficial.⁵

compared to a single-species trapped-ion apparatus. Much of the discussion in this section will apply to the laser beams for each ion species independently (for example "resonant beams" can be taken to mean "resonant beams for ${}^{9}\text{Be}^{+}$ and ${}^{25}\text{Mg}^{+}$, respectively"). Because much of the system was built before lasers at the desired wavelengths were commercially available, many modules used were built in the lab or elsewhere at NIST. Both ${}^{9}\text{Be}^{+}$ and ${}^{25}\text{Mg}^{+}$ have ultraviolet (UV) resonant wavelengths, adding extra difficulty both in sourcing the optics 7 and the number of frequency conversion stages used. All laser sources used for ${}^{9}\text{Be}^{+}$ and ${}^{25}\text{Mg}^{+}$ are emitted by sources in the infrared (IR), are converted into the visible, and then are converted to the UV, with the exception of the commercial

⁷Optical coatings, even if they are made for UV wavelengths, are more easily damaged at lower powers compared to visible optics.

Toptica system used for the ²⁵Mg⁺ Raman beamline which outputs visible light directly.⁸

In general, for each species there are four different laser frequencies that are far enough separated that different barium borate (BBO) UV frequency doublers (described in Sec. A.4) are used. The frequencies of each beam at the ion are derived from one of these UV doubler outputs and frequency-shifted via acousto-optic-modulator (AOM)⁹ as appropriate. There is one UV source for the photoionization (PI) of each species; one UV source for transitions between $^2S_{1/2}$ and $^2P_{1/2}$; one UV source for transitions between $^2S_{1/2}$ and $^2P_{3/2}$; and one UV beam that is split up to generate all the laser beams used for Raman transitions. This section will review how each UV doubler output frequency is generated and how these are then converted into the frequencies used at the ions using AOMs. Overlays of each beamline on photos of the optics tables in 1G121 can be found in Sec. A.6. At the end of this section will be discussion of some general aspects of our laser and optical systems.

The overall frequencies of the lasers for each species, as referenced to the atomic levels of ${}^{9}\mathrm{Be^{+}}$ and ${}^{25}\mathrm{Mg^{+}}$, are shown in Figs. 3.7 and 3.8 respectively. Not shown are the 235 nm and 285 nm beams, respectively, for PI of the two species.

In this apparatus, there is a subset of beams known as the resonant laser beams for both species; this includes the Doppler cooling (final Doppler cooling "BD" and higher-power detuned Doppler cooling "BDD") frequencies, the repumping frequencies, and the detection frequency the resonant beams do not include the Raman and PI laser beams. The purpose of the resonant beams (other than the detection beam) is in general to prepare the $|Bright\rangle$ state of both ion species $({}^2S_{1/2}|2,2\rangle$ for ${}^9Be^+$ and ${}^2S_{1/2}|3,3\rangle$ for ${}^{25}Mg^+$) and to perform Doppler cooling. For better state preparation, the two pairs of resonant repumpers are used to clear population out of the two states

⁸Technically, the source for this laser beam is also in the infrared but for the purposes here, this is considered part of the commercial Toptica system.

 $^{^9}$ Some of the devices used are actually acousto-optic deflectors, but they are both used in the same way in this lab. 10 This nomenclature is very confusing; it comes from the 9 Be $^+$ configuration as shown in Fig. 3.7. BD stands for "Blue Doppler" which refers to beams driving transitions between 2 S_{1/2}↔²P_{3/2}. This beam is "blue" compared to the RD beam, which stands for "Red Doppler", driving transitions between 2 S_{1/2}↔²P_{1/2}. In this apparatus, the RD beams are resonant repumpers, which is the name I use in this thesis. BDD stands for "Blue Doppler (red) Detuned", which also drives 2 S_{1/2}↔²P_{3/2} but with a ≈400 MHz to ≈600 MHz (for 9 Be $^+$ and 25 Mg $^+$ respectively) red detuning and high power in order to cool high-velocity ions.

¹¹As will be shown in the sections below, for both ion species the BD and detection beams are derived from the exact same beamline but shifted in frequency by $\Gamma/2$ using an AOM, where Γ is the linewidth of the respective species. The BDD beam follows a separate beamline for both species before being combined with the other resonant beams.

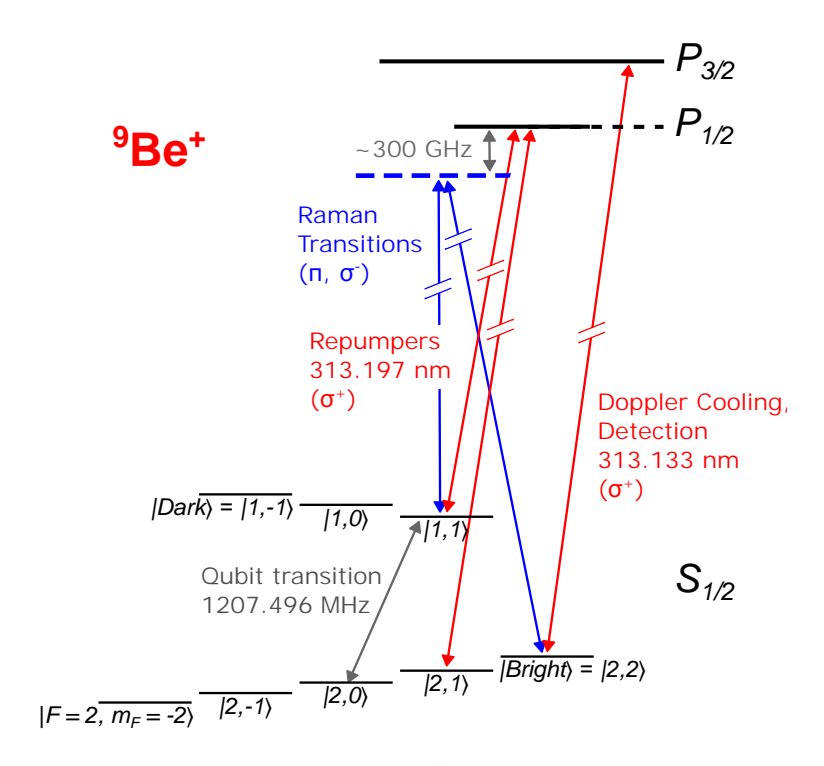


Figure 3.7: The resonant and Raman lasers for ${}^{9}\text{Be}^{+}$ are shown. The Doppler cooling ("BD"), higher-power detuned Doppler-cooling ("BDD"), and detection beams are all derived from a single UV doubler source ${}^{2}\text{S}_{1/2} \leftrightarrow {}^{2}\text{P}_{3/2}$. The repumpers ("RD"s) for the two states in the ${}^{2}\text{S}_{1/2}$ manifold nearest to $|\text{Bright}\rangle$ ($|2,1\rangle$ and $|1,1\rangle$) are both generated from the UV source driving ${}^{2}\text{S}_{1/2} \leftrightarrow {}^{2}\text{P}_{1/2}$. In order to avoid accidental coherent population trapping, these beams are detuned from each other by ≈ 10 MHz. While illustrated as driving transitions between ${}^{2}\text{S}_{1/2}|2,2\rangle \leftrightarrow |1,1\rangle$, the Raman beams are capable of driving most transitions between the hyperfine manifolds on the right hand side with $m_F \geq 0$. The Raman beams in this current configuration are not ideal for driving the qubit transition as they do not have the correct frequency/polarization combination. This thesis does not cover such experiments, but when this transition is important, a waveplate can be adjusted to modify the σ^- beam to have both σ^+ and σ^- polarizations, which would enable driving of the qubit transition using the Raman beams at the cost of decreased Rabi frequency on the Raman cooling transition.

closest to the $|\text{Bright}\rangle$ state in case a small amount of polarization impurity leaves any population in these states. These repumpers do not affect population already in $|\text{Bright}\rangle$ since there are no states in the ${}^2P_{1/2}$ manifold to drive to (and the ${}^2S_{1/2} \leftrightarrow {}^2P_{3/2}$ repumper for the $|2,2\rangle$ state for ${}^{25}\text{Mg}^+$ is too far off resonance).

For all experiments, the same Doppler-cooling and optical pumping procedure is used to prepare the |Bright\rangle states of both species. First, the BDD beams are turned on simultaneously

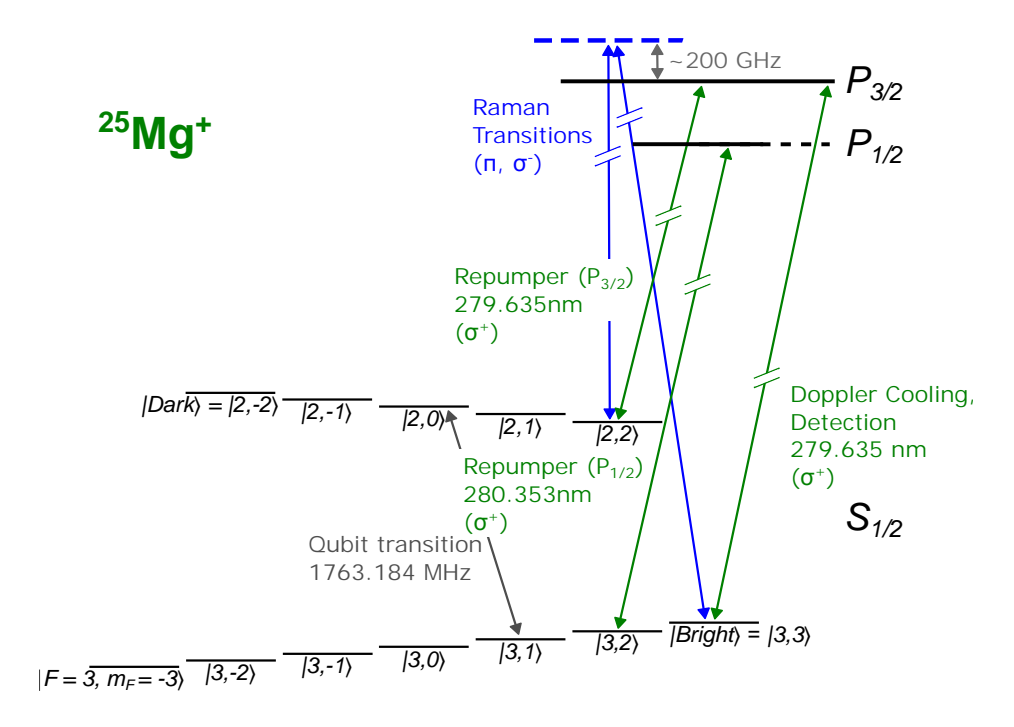


Figure 3.8: The resonant and Raman lasers for $^{25}\text{Mg}^+$ are shown. The Doppler cooling, higher-power detuned Doppler-cooling, detection, and one of the repumper beams are all derived from a single UV doubler source $^2\text{S}_{1/2}\leftrightarrow^2\text{P}_{3/2}$. The other repumper is generated by a separate UV doubler source $^2\text{S}_{1/2}\leftrightarrow^2\text{P}_{1/2}$. While illustrated as driving transitions between $^2\text{S}_{1/2}|3,3\rangle\leftrightarrow|2,2\rangle$, the Raman beams are capable of driving most transitions between the hyperfine manifolds on the right hand side with $m_F \geq 0$, including the qubit transition.

with both repumpers, 12 then the BD beam with both repumpers, then the BD beam without the repumpers, 13 and then a short repump pulse. This prepares both ion species with less than 2% error. 14

After passing through a fiber, the resonant beams are split using a polarization element so that part of the beam goes to the loading zone \mathcal{L} and the rest goes to the experimental zone \mathcal{S} (these

 $^{^{12}}$ Although the repumpers are likely not strictly necessary to use simultaneously with the BD and BDD for initial Doppler cooling and transferring the population to increasing m_F values, it was found empirically that in most cases, having the repumpers on made the state preparation more successful.

¹³This also serves the purpose of allowing the pulseshaping servo (Sec. 3.2.10) for the resonant beams to servo using this BD pulse, which is roughly the same power as the detection beam for both species. It was found that when the pulseshaping servo was not prepared in this manner, the servo changed the pulse height of the detection beam throughout the detection period, and the duty cycle/noise on the detectors would have a direct effect on the counts recorded for a standard detection pulse, especially for ²⁵Mg⁺.

 $^{^{149}\}mathrm{Be^+}$ is better prepared than $^{25}\mathrm{Mg^+}$ because the frequency difference between the $^{25}\mathrm{Mg^+}$ lasers driving transitions between $^2\mathrm{S}_{1/2}\leftrightarrow^2\mathrm{P}_{1/2}$ and $^2\mathrm{S}_{1/2}\leftrightarrow^2\mathrm{P}_{3/2}$ is much larger, so waveplates cannot make both frequencies as pure in polarization compared to those for $^9\mathrm{Be^+}$. Also, $^{25}\mathrm{Mg^+}$ has a larger $^2\mathrm{S}_{1/2}$ manifold so there are more states to depump to

zones are illustrated and described in Sec. 3.3). The light going to the loading zone is overlapped with the PI beam for both species. Both the resonant beams aimed at the loading zone and the PI beam are shuttered when not loading to prevent light from scattering off of trap features and being collected by the photomultiplier tube (PMT). All resonant beams aimed at the experiment zone are monitored using NIST-designed logarithmic photodetectors. The logarithmic photodetectors are necessary because the resonant beam powers vary from tens of nW (repumpers) to hundreds of μ W (BDD). These are the only logarithmic photodetectors used; all other photodetectors are linear.

Fig. 3.9 shows the beam entry directions, relative to the quantization axis, of all lasers. Most beams pass through a fiber for mode cleaning and power stabilization of certain pulses before reaching the trap. All resonant beams for each species are combined into the same fiber; the PI beam for $^{25}\text{Mg}^+$ passes through a separate fiber while the $^{9}\text{Be}^+$ PI beam is the only beam that does not pass through a fiber before reaching the trap. The Raman beams going into each of the three beam ports pass through distinct fibers. The beams for the two species are combined using a dichroic mirror near each entry port to the ion trap.

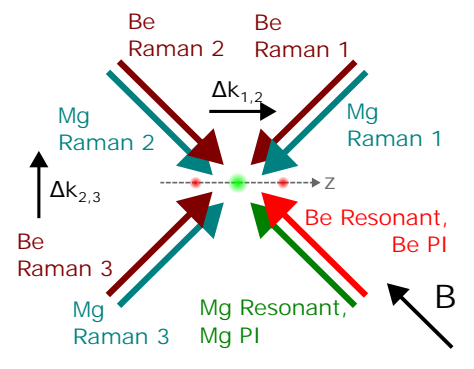


Figure 3.9: The laser beam entry directions relative to the axial direction of the pseudopotential confinement (labeled z above) and the magnetic field labeled B. The beams colinear or antilinear with the magnetic field can be made to have a superposition of σ^+ and σ^- polarizations; the beams perpendicular to the magnetic field can have a superposition of π and $\sigma = \frac{1}{\sqrt{2}} (\sigma^+ + \sigma^-)$ polarizations. The beamline labeled Mg Raman 3 was also used as the port for the $(\pi$ -polarized) probe beam for the electromagnetically-induced-transparency experiment (Ch. 4).

The Raman beams are generated from a single source (per ion species) for good coherence between the beams when driving Raman transitions. As a result, many AOMs are used in the Raman beamlines to bridge the hyperfine splitting of each ion, and the light output by the Raman UV doublers is quite intense (≈ 700 mW of 313 nm light for $^9\mathrm{Be^+}$ and ≈ 220 mW of 280 nm light for $^{25}\mathrm{Mg^+}$). For each ion species there are three Raman beams generated through a series of AOMs. Raman 15 and Raman 2 (as labeled in Fig. 3.9) are used to drive motion-sensitive transitions in the axial direction. Raman 3 is a beam that contains two tones, capable of driving the qubit transitions for each species using a motion-insensitive Raman transition. The configuration used for the experiments described in this thesis has all resonant laser beams (including all Doppler cooling, repumping, detection, and also photoionization beams) as σ^+ -polarized. The Raman 1 beams for both ion species are made to have pure π polarization, while Raman 2 is made to be pure. When used to drive the qubit transitions, Raman 3 should be made to have a mix of both π and $\sigma = \frac{1}{\sqrt{2}} (\sigma^+ + \sigma^-)$ polarizations.

For the experiment described in Ch. 5, Be Raman 3 was converted to a single-tone beam to be used with Be Raman 2 to perform radial motion-sensitive transitions; in this configuration the ideal polarization to use is pure π . Mg Raman 3 was used for a similar purpose for a period of time in order to explore the effects of radial mode cooling. The Mg Raman 3 port was also used for the π -polarized EIT cooling probe beam, which utilized some of the AOMs that were used for the Mg Raman 3 qubit-driving configuration above (experiment described in Ch. 4, beamline shown in Fig. A.16) meaning the two could not be used simultaneously.

In the following subsections, the equipment used to generate the light used for the experiments is detailed; each subsection is organized by UV doubler and contains a diagram of how the light output of the UV doubler is shifted by AOMs to meet the required frequencies to bridge the ${}^2S_{1/2}$

¹⁵The nomenclature used in the lab is usually "Co" and "90" but they are reversed per species and the ⁹Be⁺ Raman 1 and Raman 2 fiber outputs are sometimes exchanged in order to drive certain Raman transitions more efficiently. To avoid confusion, in this thesis I will refer to them by 1, 2, and 3. Unfortunately, some of the AOMs still retain these names.

¹⁶The wavevector difference is nearly zero for these beams because the two Raman beams propagate colinearly towards the ion. Because they travel very similar beam paths, this two-tone beam (which is often called the "CoCarrier" in this apparatus) has very little noise resulting from beam path differences.

 $^{^{17}}$ As mentioned previously, because many slightly different wavelengths are present in each resonant beams, not all beams can be perfectly polarized at once. The polarization purity for the detection/final Doppler cooling beams is prioritized.

hyperfine splitting of each species. The three beams at 626 nm that pump the ${}^9\mathrm{Be^+}$ ${}^2\mathrm{S}_{1/2} \leftrightarrow {}^2\mathrm{P}_{1/2}$, ${}^2\mathrm{S}_{1/2} \leftrightarrow {}^2\mathrm{P}_{3/2}$, and Raman UV doublers are generated using sum-frequency-generation (SFG) between four fiber-seed-laser-and-amplifier units, two outputting 1050 nm light and two outputting 1550 nm light [85]. For the purpose of differentiating these physical units, I will call them "1050 nm A" (NP Photonics The Rock seed laser, NKT Photonics Koheras Boostik HPA amplifier), "1550 nm A" (NKT Photonics Koheras Adjustik seed laser, NKT Photonics Koheras Boostik HPA amplifier), "1050 nm B" (NKT Photonics Koheras Adjustik seed laser, IPG Photonics YAR-10-1050-LP-SF amplifier), and "1550 nm B" (NKT Photonics Koheras Adjustik seed laser, IPG Photonics EAR-10-C-LP-SF amplifier). Both the "A" units are located near the SFG setup for the ${}^2\mathrm{S}_{1/2} \leftrightarrow {}^2\mathrm{P}_{1/2}$ and ${}^2\mathrm{S}_{1/2} \leftrightarrow {}^2\mathrm{P}_{3/2}$ units while the "B" units are located near the SFG setup for the Raman beams.

A summary of the purpose of each of the eight beamlines discussed is given in Tab. 3.5.

3.2.1 ⁹Be⁺ Photoionization

At the beginning of my graduate studies, the visible frequency (470 nm) for the ⁹Be⁺ PI beam was generated using an M Squared system. This consisted of multiple modules, including an oscillator, telescope, and lithium triborate (LBO) crystal doubler to reach the visible wavelength. The whole system was pumped by a Verdi titanium-sapphire laser at 10 W CW. Unfortunately, the power output of the oscillator unit dropped over time and it was finally replaced by a VECSEL (Sec. A.1) that output 940 nm directly around October 2021. This was used to pump the LBO crystal doubler module with a new telescope setup and while slightly less efficient than the original M Squared system, appears to operate stably.

The light for ${}^9\mathrm{Be^+}$ PI is shared between three experiments in three different labs; one other experiment, the "Triangle trap" in 1G125 uses the same PI frequency as needed for this apparatus. However, the Penning trap experiment in 1H128 requires a light frequency that differs by $\approx 16~\mathrm{GHz}$ in the IR. This can be accommodated by changing the VECSEL etalon temperature by $\approx 4^\circ\mathrm{C}$. The power is typically only enough for one experiment to use at a time, and is distributed between experiments using a series of polarizing beamsplitters and waveplates.

Beamline	UV Wave- length	IR Source	Conversion to Visible	UV Doubler Lock	Purpose
⁹ Be ⁺ PI	235 nm	VECSEL	M Squared LBO Doubler	Hänsch- Couillaud	Photoionization of ${}^{9}\mathrm{Be}^{+}$
$\begin{array}{c} & \\ & ^{9}\mathrm{Be^{+}} \\ & ^{2}\mathrm{S}_{1/2} \leftrightarrow ^{2}\mathrm{P}_{1/2} \end{array}$	313 nm	1050 nm B 1550 nm A	Covesion PPLN SFG	Hänsch- Couillaud	Repump $^2\mathrm{S}_{1/2}$ $ 2,1\rangle$ and $ 1,1\rangle$
$^{9}\mathrm{Be^{+}}$ $^{2}\mathrm{S}_{1/2} \leftrightarrow ^{2}\mathrm{P}_{3/2}$	313 nm	1050 nm A 1550 nm A	Covesion PPLN SFG	Hänsch- Couillaud	Detection and Doppler cooling
⁹ Be ⁺ Raman	313 nm	1050 nm B 1550 nm B	Covesion PPLN SFG	PDH	Raman transitions
$^{25}{ m Mg}^+{ m PI}$	285 nm	VECSEL	NTT PPLN Doubler	Hänsch- Couillaud	Photoionization of $^{25}{ m Mg}^+$
$\begin{array}{c} \hline \\ ^{25}\mathrm{Mg^{+}} \\ ^{2}\mathrm{S}_{1/2} \leftrightarrow ^{2}\mathrm{P}_{1/2} \end{array}$	280 nm	VECSEL	NTT PPLN Doubler	PDH	Repump $^2S_{1/2}$ $ 3,2\rangle$ and EIT cooling
$^{25}\mathrm{Mg^{+}}$ $^{2}\mathrm{S}_{1/2} \leftrightarrow ^{2}\mathrm{P}_{3/2}$	280 nm	VECSEL	NTT PPLN Doubler	Hänsch- Couillaud	Repump ${}^2S_{1/2} \mid 2, 2 \rangle$ Detection and Doppler cooling
$^{25}{ m Mg}^+$ Raman	280 nm	,	ptica -SHG-Pro	PDH	Raman transitions

Table 3.5: Table summarizing each beamline, organized by UV doubler. The infrared (IR) source is either a fiber seed laser/amplifier combination (outputting 1050 nm or 1550 nm, two of each are labeled with "A" or "B") or a VECSEL which is detailed in Sec. A.1. Multiple nonlinear elements are used for doubling, including lithium triborate (LBO) and periodically-poled lithium niobate (PPLN) for IR-to-visible light conversion. This visible light is then converted to UV using beta barium borate (BBO). The method used to lock the frequency of the UV doubler is either Hänsch-Couillaud or Pound-Drever-Hall (PDH). The only commercial systems used are the IR fiber lasers for ⁹Be⁺ and the Toptica DL-TA-SHG-Pro, which doubles IR light internally and outputs light at 560 nm.

The 470 nm light output by the LBO doubler is used to pump a resonant bow-tie cavity containing a beta barium borate (BBO) crystal to generate 235 nm light, which is delivered to the trap in free space. This is the only wavelength of light that is not routed through a UV fiber

(Sec. 3.2.9) to the trap, as it is found to have low fiber coupling efficiency, and this wavelength causes more rapid fiber degradation than the other wavelengths used in this apparatus. The 235 nm ⁹Be⁺ PI light is physically overlapped with all other beams aimed at the loading zone right before the final lens to the trap using a dichroic mirror.

$$3.2.2$$
 ${}^{9}\mathrm{Be^{+}}$ ${}^{2}\mathrm{S}_{1/2} \leftrightarrow {}^{2}\mathrm{P}_{1/2}$ (a. k. a. ${}^{9}\mathrm{Be^{+}}$ RD)

The light for the ${}^9\mathrm{Be^{+}}\ {}^2\mathrm{S}_{1/2} \leftrightarrow {}^2\mathrm{P}_{1/2}$ UV doubler is generated via SFG using a Covesion PPLN crystal (used in single-pass) from the fiber laser light of "1050 nm B" (which is transferred from the other side of the lab using a fiber) and light from "1550 nm A". Around 10 mW of the generated light at 626 nm is used for an iodine lock for feedback to the seed laser of "1550 nm A", while "1050 nm B" is allowed to drift freely.

The output light of the UV doubler is used to repump both ${}^2S_{1/2}|2,1\rangle$ and $|1,1\rangle$ (both with powers of ≈ 150 nW measured right before the trap, aimed at the experiment zone). The AOMs used to control these beams and the relative frequencies of each beam at each stage are schematically illustrated in Fig. 3.10. The beams repumping ${}^9Be^+$ ${}^2S_{1/2}|2,1\rangle$ and $|1,1\rangle$ are physically overlapped

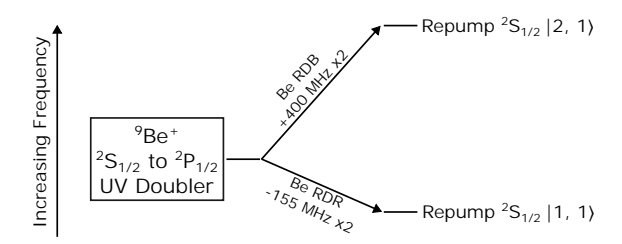


Figure 3.10: Frequency diagram for two repump beams (for ${}^2S_{1/2}|2,1\rangle$ and $|1,1\rangle$) generated from ${}^9Be^+\ {}^2S_{1/2}\leftrightarrow {}^2P_{1/2}$ UV doubler. The vertical direction indicates the frequency of the beams; both AOMs, named "Be RDB" and "Be RDR", are used in double-pass configuration (indicated by the "x2" in the diagram); the labeled frequencies are the RF drive frequencies of each AOM and each beam is shifted by twice that amount. "Be Dop Sw -" (not shown) must also be on for the two repump beams to pass into the ${}^9Be^+$ resonant beam fiber and reach the ion.

with each other using a 50/50 dielectric beam splitter and then combined with the ${}^{9}\text{Be}^{+}$ ${}^{2}\text{S}_{1/2} \leftrightarrow {}^{2}\text{P}_{3/2}$ light using the AOM beam injection trick described in Sec. A.2.2 with AOM "Be Dop Sw +".

3.2.3
$${}^{9}\text{Be}^{+} {}^{2}\text{S}_{1/2} \leftrightarrow {}^{2}\text{P}_{3/2}$$
 (a. k. a. ${}^{9}\text{Be}^{+}$ BD)

The light for the ${}^9\mathrm{Be^{+}}\ {}^2\mathrm{S}_{1/2} \leftrightarrow {}^2\mathrm{P}_{3/2}$ UV doubler is generated via SFG using a Covesion PPLN crystal with the fiber laser light from "1050 nm A" and "1550 nm A". Around 10 mW of the generated light at 626 nm is used for an iodine lock for feedback to the seed laser of "1050 nm A". Because the light used to generate this frequency relies on "1550 nm A" which is locked using the ${}^9\mathrm{Be^{+}}$ ${}^2\mathrm{S}_{1/2} \leftrightarrow {}^2\mathrm{P}_{1/2}$ light, the frequency of the latter beamline should be locked before locking the ${}^9\mathrm{Be^{+}}$ ${}^2\mathrm{S}_{1/2} \leftrightarrow {}^2\mathrm{P}_{3/2}$ frequency.

The output light of the UV doubler is used for the Doppler cooling beam (BD, ≈ 330 nW at the trap), the high-intensity detuned Doppler cooling beam (BDD $\approx 30~\mu$ W at the trap), and the detection light (similar power to the BD). The AOMs used to control these beams and the relative frequencies of each beam at each stage are schematically illustrated in Fig. 3.11.

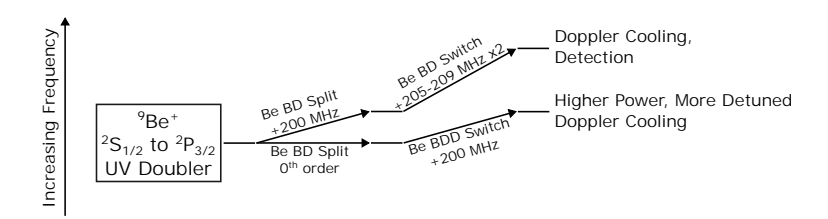


Figure 3.11: Frequency diagram for Doppler-cooling and detection beams generated from ${}^9\mathrm{Be}^+$ ${}^2\mathrm{S}_{1/2} \leftrightarrow {}^2\mathrm{P}_{3/2}$ UV doubler. The "Be BD Switch" AOM is used to change the beam frequency to perform Doppler cooling (205 MHz) or detection (209 MHz). All RF drive frequencies of each AOM are labeled; only the "Be BD Switch" AOM is used in double-pass configuration. "Be Dop Sw +" and "Be Dop Sw -" (not shown) must also be on for these beams to pass into the ${}^9\mathrm{Be}^+$ resonant beam fiber and reach the ion.

The detection/BD beam is overlapped with the BDD beam using the AOM trick described in Sec. A.2.2 with the "BDD Switch" AOM. The detection/BD beam and BDD beams are not typically used at the same time.

3.2.4 ⁹Be⁺ Raman

The light for the ${}^{9}\text{Be}^{+}$ Raman UV doubler is generated via SFG using a Covesion PPLN crystal with the fiber laser light from "1050 nm B" and "1550 nm B". The frequency of the ${}^{9}\text{Be}^{+}$

Raman beam is allowed to drift freely because any changes in the frequency of the UV doubler output will be common to all Raman beams and small compared to the ≈ 300 GHz detuning from the nearest states as shown in Fig. 3.7. The output is split into many different beams and sent to the trap from various directions with various polarizations, as shown in Fig. 3.9. The AOMs used to control these beams and the relative frequencies of each beam at each stage are schematically illustrated in Fig. 3.12.

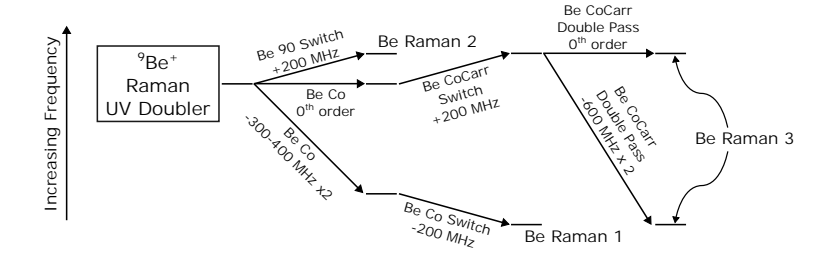


Figure 3.12: Frequency diagram for Raman beams generated from ${}^9\mathrm{Be}^+$ Raman UV doubler. Three beams are generated through a series of AOMs that are sent in through the three optical ports indicated in Fig. 3.9. While the beam going to Be Raman 2 has a fixed frequency, the frequency of Be Raman 1 can be varied to drive different Raman transitions within the ${}^9\mathrm{Be}^+$ ${}^2\mathrm{S}_{1/2}$ manifold, for example the cooling or qubit transition, by changing the frequency of the RF drive for the "Be Co" AOM. Be Raman 3 consists of two overlapped tones from the 0^{th} order and double-pass of the "Be CoCarr Double Pass" AOM. This part of the beamline is extremely difficult to align but has very little beam path difference between the two tones in Be Raman 3.

The Be Raman 1 and 2 beams can be used together to drive interactions involving the ion axial modes. To perform Raman laser interactions with the radial modes, the 0th order of the "Be CoCarr Double Pass" can be blocked, so that the lower-frequency tone of Be Raman 3 can be used with Be Raman 2. The powers of Be Raman 1 and Be Raman 2 at the trap are approximately 1-3 mW.

3.2.5 ²⁵Mg⁺ Photoionization

The IR frequency (1140 nm) for the ²⁵Mg⁺ PI beam is generated using a VECSEL, which is then used to pump an NTT periodically-poled lithium niobate (PPLN) waveguide doubler that outputs 570 nm light (WS-0570-000-A-B-C). This light is sent to a BBO UV doubler which then outputs 285 nm light, which is routed through a UV fiber before being sent to the trap. This beam

is overlapped with the resonant $^{25}\text{Mg}^+$ loading beam using a 50/50 dielectric beamsplitter, and is measured to have a power of $\leq 200~\mu\text{W}$ as it enters the trap.

3.2.6
$$^{25}{
m Mg^+}$$
 $^2{
m S}_{1/2}\leftrightarrow^2{
m P}_{1/2}$ (a. k. a. $^{25}{
m Mg^+}$ $^2{
m P}_{1/2}$) and $^2{
m S}_{1/2}\leftrightarrow^2{
m P}_{3/2}$ (a. k. a. $^{25}{
m Mg^+}$ $^2{
m P}_{3/2}$)

Similar to the 25 Mg⁺ PI beamline, the 25 Mg⁺ 2 S_{1/2} \leftrightarrow 2 P_{1/2} and 2 S_{1/2} \leftrightarrow 2 P_{3/2} IR wavelengths are generated using VECSELs outputting 1121 nm and 1118 nm respectively. ¹⁸ These outputs are also converted to 560 nm using NTT PPLN waveguide doublers (WS-0561-000-A-B-C, WS-0559-000-A-B-C) and then to 280 nm with a BBO UV doubler. As noted in Sec. A.1.1, these particular VECSELs are extremely temperamental, possibly due to a combination of an unfavorable IR wavelength and not completely suitable optical frequency-selective elements.

The $^{25}{\rm Mg}^+$ $^2{\rm S}_{1/2} \leftrightarrow ^2{\rm P}_{1/2}$ UV doubler output is mainly used to generate light to repump the $^2{\rm S}_{1/2}|3,2\rangle$ state (measured to be $\approx 1-2~\mu{\rm W}$ at the trap), as shown in Fig. 3.13, but it is also used to generate light for the $^{25}{\rm Mg}^+$ EIT cooling experiment as described in Fig. 4.6.

The $^{25}\mathrm{Mg^{+}}$ $^{2}\mathrm{S}_{1/2} \leftrightarrow ^{2}\mathrm{P}_{3/2}$ UV doubler output is used to generate the rest of the resonant light beams for $^{25}\mathrm{Mg^{+}}$ (Doppler cooling, with power $\approx 300-500$ nW at the trap; high-intensity detuned Doppler cooling beam, with power $\approx 30-60~\mu\mathrm{W}$ at the trap, repumping $^{2}\mathrm{S}_{1/2}|2,2\rangle$, with power $\approx 150-300$ nW at the trap; and detection, which has similar power to the Doppler cooling beam), as shown in Fig. 3.14.

3.2.7 $^{25}\mathrm{Mg}^{+}$ Raman

The source for the ²⁵Mg⁺ Raman beams is the largest commercial module used in our apparatus, a Toptica DL-TA-SHG-Pro outputting 560 nm light directly. This light is sent into a UV doubler with a 20 mm long BBO crystal (all other UV doublers in the lab use 10 mm long BBO crystals).¹⁹ The output of the UV light is split up into many different beams as illustrated

 $^{^{18}} These$ are sometimes respectively referred to as the $^{25} Mg^{+}$ $^{2} P_{1/2}$ and $^{25} Mg^{+}$ $^{2} P_{3/2}$ beamlines/VECSELs.

¹⁹The increased length of the crystal is intended to allow for an increased beam size at the crystal input and output faces to reduce the intensity. The previous UV doubler with a 10 mm long crystal had frequent burns on the faces,

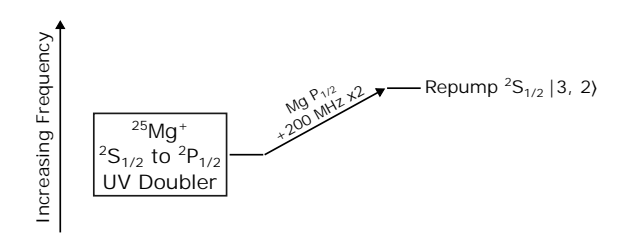


Figure 3.13: Frequency diagram for repump beam generated from $^{25}\mathrm{Mg}^+$ $^2\mathrm{S}_{1/2}\leftrightarrow^2\mathrm{P}_{1/2}$ UV doubler. In order for this beam to pass into the fiber for the $^{25}\mathrm{Mg}^+$ resonant beam and reach the ion, the "Mg Resonant Switch" AOM (not shown) must also be on. There is more than enough beam power generated by the UV doubler to drive the repump transition, so this AOM is usually driven much below saturation to avoid depumping due to slight polarization impurity of this beam at the ion. Only one beam repumping the state $^2\mathrm{S}_{1/2}|3,2\rangle$ is derived from this beamline, so in principle the AOM does not have to be used in double-pass configuration as shown. One possibility is that this light was also intended to replace the repump beam from the $^{25}\mathrm{Mg}^+$ $^2\mathrm{S}_{1/2}\leftrightarrow^2\mathrm{P}_{3/2}$ UV doubler for the $^2\mathrm{S}_{1/2}|2,2\rangle$ state, since that beam uses an AOM with 400 MHz center frequency (see Fig. 3.14), which combined with the "Mg $\mathrm{P}_{1/2}$ " AOM could span the necessary hyperfine splitting if both AOMs are used in double-pass configuration. However, implementing this is not recommended as it appears that it is difficult to obtain a purely polarized beam driving transitions $^2\mathrm{S}_{1/2}\leftrightarrow^2\mathrm{P}_{1/2}$ when prioritizing the polarization purity of $^2\mathrm{S}_{1/2}\leftrightarrow^2\mathrm{P}_{3/2}$ frequencies.

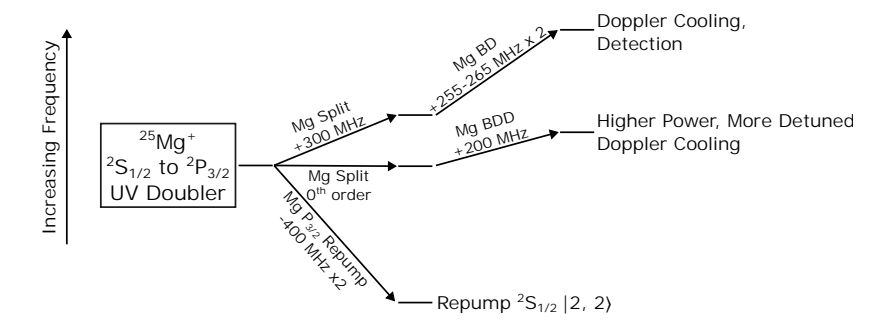


Figure 3.14: Frequency diagram for repump, Doppler-cooling, and detection beams generated from $^{25}\mathrm{Mg^{+}}$ $^{2}\mathrm{S}_{1/2} \leftrightarrow ^{2}\mathrm{P}_{3/2}$ UV doubler. Similar to $^{9}\mathrm{Be^{+}}$ the "Mg BD" AOM is used to change the beam frequency to perform Doppler cooling (255 MHz) or detection (265 MHz). The "Mg Split" and "Mg $\mathrm{P}_{3/2}$ " AOMs are driven below saturation since the diffracted beamlines do not require full power. In order for these beams to pass into the fiber for the $^{25}\mathrm{Mg^{+}}$ resonant beam and reach the ion, the "Mg Resonant Switch" AOM (not shown) must also be on.

in Fig. 3.15, and has been reconfigured for various purposes throughout my graduate studies (for example, as described in Sec. 4.3.1 and below).

Similar to what is done for ${}^{9}\text{Be}^{+}$, the Mg Raman 1 and 2 beams (with powers $\approx 1-5$ mW at the trap) can be used together to drive interactions involving the ion axial modes, and the Mg likely due to the high intensity of the beam in this particular cavity.

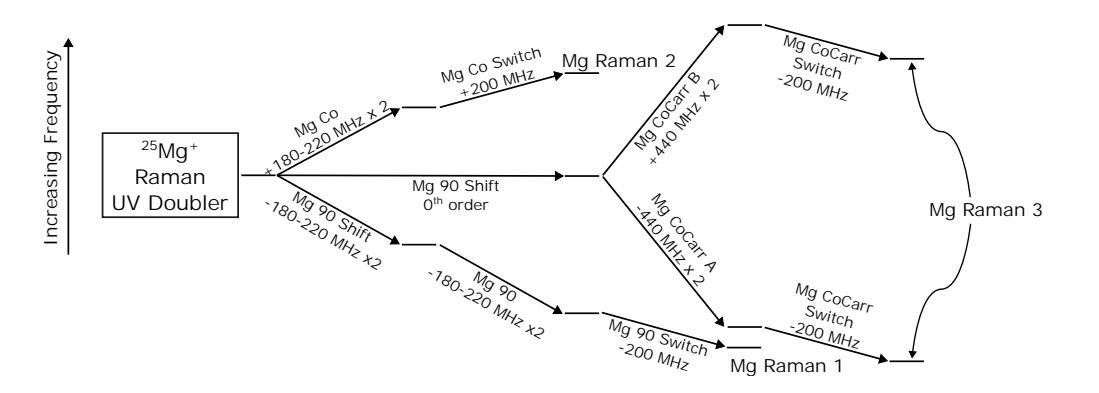


Figure 3.15: Frequency diagram for Raman beams generated from ²⁵Mg⁺ Raman UV doubler. Three beams are generated through a series of AOMs that are sent in through the three optical ports indicated in Fig. 3.9. The RF source driving the "Mg Co", "Mg 90 Shift", and "Mg 90" AOMs are the same and come from an ARTIQ DDS (and so can be changed in real time, for example for a frequency scan); all three are used in double-pass configuration. By doing this, both the cooling and qubit frequencies of ²⁵Mg⁺ can be driven without going outside the bandwidth of these AOMs, which all have 200 MHz center frequency and 40 MHz bandwidth. In order to use Mg Raman 3 at full power, the "Mg 90 Shift" AOM should be turned off when this beam is used. Similar to ⁹Be⁺ the lower-frequency tone of Mg Raman 3 can be used with Mg Raman 2 to perform radial-mode interactions.

Raman 3 (CoCarrier) beamline can be straightforwardly adapted to perform radial-mode Raman interactions by using the lower-frequency tone with Mg Raman 2. The configuration illustrated in Fig. 3.15 is for driving the qubit frequency using both tones, but the "Mg CoCarr A" and "Mg CoCarr B" are both AOMs with 400 MHz center frequency and 100 MHz bandwidth, so "Mg CoCarr A" can be driven at slightly lower frequencies to be used for radial modes.

3.2.8 Sideband Cooling

Sideband cooling (SBC) [86] is typically used for sub-Doppler cooling in this apparatus. Because a long-lived excited state is not found in the ${}^{2}P_{1/2}$ and ${}^{2}P_{3/2}$ manifolds of ${}^{9}\text{Be}^{+}$ nor ${}^{25}\text{Mg}^{+}$, Raman transitions are performed instead with the beams shown in Figs. 3.7 and 3.8, on the cooling transitions labeled in Figs. 3.1 and 3.4. There are two different methods of sideband cooling that can be implemented on this apparatus, pulsed sideband cooling and continuous sideband cooling. In the standard cooling sequences used, long periods of continuous sideband cooling are first applied (for hundreds of μ s to a few ms) and then about five additional pulsed sideband cooling pulses are

applied for each mode cooled at the end of the sequence.

For both methods of cooling, the second sideband (where s = 2 in Eq. 2.64) may be required if the Doppler-cooled thermal occupation is high. This often true for $^{25}\text{Mg}^+$. If the second sideband is not interleaved with cooling on the first sideband, there will be a bottleneck caused by the effective Rabi frequency of the transition being very small for certain Fock states due to the Laguerre polynomial in Eq. 2.64.

3.2.8.1 Pulsed Sideband Cooling

In pulsed sideband cooling, two steps are interleaved (for each species, per mode cooled) until the desired occupation is reached. The first is the Raman motion-subtracting sideband step, which is usually the driven on the transition ${}^2S_{1/2}|2,2\rangle|n\rangle \rightarrow {}^2S_{1/2}|1,1\rangle|n-1\rangle$ in ${}^9Be^+$ (and ${}^2S_{1/2}|3,3\rangle|n\rangle \rightarrow {}^2S_{1/2}|2,2\rangle|n-1\rangle$ in ${}^{25}Mg^+$), where the first ket denotes the atomic state and the second ket indicates the motion occupation. This transition is sometimes driven only partially (as discussed below) but ideally should be fully driven, and when fully driven constitutes a π -pulse in the atomic states.

The second step for ${}^9\mathrm{Be}^+$ is a repump pulse driving ${}^2\mathrm{S}_{1/2}|1,1\rangle\,|n\rangle\,\rightarrow{}^2\mathrm{P}_{1/2}|2,2\rangle\,|n\rangle^{20}$; the ${}^2\mathrm{P}_{1/2}|2,2\rangle$ state can decay to ${}^2\mathrm{S}_{1/2}|1,1\rangle,\,|2,1\rangle$, and $|2,2\rangle$, with the emission most likely not changing the motion. The goal is to transfer the population back to ${}^2\mathrm{S}_{1/2}|2,2\rangle$ so that the first step may be repeated again, so a repump from ${}^2\mathrm{S}_{1/2}|2,1\rangle\,\rightarrow{}^2\mathrm{P}_{1/2}|2,2\rangle$ is turned on simultaneously with the repump from ${}^2\mathrm{S}_{1/2}|1,1\rangle$. The intensities of the repumpers are calibrated so that within the pulse time of the second step (usually 20 μ s), the population is transferred back to ${}^2\mathrm{S}_{1/2}|2,2\rangle$ with $\geq 98\%$ probability. For ${}^{25}\mathrm{Mg}^+$ this step is similar, with the ${}^2\mathrm{S}_{1/2}|2,2\rangle\,\rightarrow{}^2\mathrm{P}_{3/2}|m_F=3\rangle$ and ${}^2\mathrm{S}_{1/2}|2,2\rangle\,\rightarrow{}^2\mathrm{P}_{1/2}|3,3\rangle$ repump beams pulsed for 20 μ s to prepare ${}^2\mathrm{S}_{1/2}|3,3\rangle$ again. It should be noted that the Raman transition driven in the first step is coherent, while this step is dissipative, which is necessary to extract energy from the system.

²⁰Here the most likely motion transition, the carrier, is given as an example; the repump and recoil have some probability of changing the motion state that scales relative to the Lamb-Dicke parameter which is not discussed here. A good discussion can be found in Ref. [68].

For this method of cooling, because the Rabi frequency of the transition varies as described by Eq. 2.64, Raman beam pulses of different durations are required throughout the cooling process, since different Fock states will be present. While the duration of a π -pulse for each Fock state present can be calculated using Eq. 2.64, they should ideally be calibrated using ions, which can be a long process. This can be avoided, as is done in this apparatus, by using continuous sideband cooling instead, discussed below.

3.2.8.2 Continuous Sideband Cooling

During my graduate studies, "continuous sideband cooling" (CSBC) was implemented in our apparatus. As opposed to pulsed sideband cooling, where a Raman motion-subtracting transition is alternated with a dissipative repump pulse, this method involves turning on the beams driving both processes at the same time. The repump beam(s) acts as an effective "decay path" out of the target state for the motion-subtracting sideband that is driven ($|1,1\rangle$ for ${}^9\text{Be}^+$ and $|2,2\rangle$ for ${}^{25}\text{Mg}^+$); this decay happens naturally in ions with transitions that support a one-photon resolved sideband transition, such as ${}^{40}\text{Ca}^+$.

When the rates of the repump and sideband cooling operations are well-matched, this method is most efficient. If the repump beam is too weak, the (coherent) sideband transition will begin to drive the transition ${}^2S_{1/2}|1,1\rangle |n-1\rangle \rightarrow {}^2S_{1/2}|2,2\rangle |n\rangle$ (for ${}^9Be^+$, and ${}^2S_{1/2}|2,2\rangle |n-1\rangle \rightarrow {}^2S_{1/2}|3,3\rangle |n\rangle$ for ${}^{25}Mg^+$) instead, leading to the addition of motional quanta. If the repump beam is too intense, the effective linewidth corresponding to the engineered decay will become too broad, increasing the cooling limit. In general, it is found that CSBC works well if the time required to transfer $\geq 98\%$ of the population from $|1,1\rangle$ back to $|2,2\rangle$ for ${}^9Be^+$ (and $|2,2\rangle$ back to $|3,3\rangle$ for ${}^{25}Mg^+$) to be approximately equal to that of the Raman sideband π time for the $|1\rangle \leftrightarrow |0\rangle$ Fock state transition.

Because this method is continuous, it does not require the calibration of the sideband pulse π -time for each Fock state as in pulsed sideband cooling. In this apparatus, pulsed sideband cooling is used after continuous sideband cooling in order to ensure that the motion is fully cooled; the π time for the $|1\rangle \leftrightarrow |0\rangle$ transition is used for the final pulsed sideband cooling pulses.

3.2.9 UV Fiber

When used at the required laser wavelengths for $^9\mathrm{Be^+}$ and $^{25}\mathrm{Mg^+}$, most optical fibers suffer from solarization, or damage due to UV light, which prevents the light from being efficiently transmitted. Certain fibers can be made robust to this process; the creation of such fibers is described elsewhere [87]. Nine UV fibers are used throughout the lab, and are used for mode cleaning, as well as power stabilization of the Raman beams, as described in Sec. 3.2.10. The majority of the fibers are fabricated using NKT LMA-10-UV, with the jacket, end-caps, and ferrules connectorized by ALPhANOV. The fiber is then hydrogen-loaded on-site at a NOAA facility, and then stored at \approx -80 °C until ready to cure. Fibers are cured in this laboratory at 100-120 mW of 313 nm input light for a minimum of 8 hours and they typically have 50-75% transmission efficiency, with most of the loss from input coupling of the beams. While it is expected that there should be loss as a function of fiber length, there is not a strong correlation found between transmission efficiency and fiber length for the fibers that are used in this apparatus, which are all between \approx 0.5 and 3 m long. It is likely that small differences in the fiber connectorization process affect the transmission much more strongly than losses from the length of the fiber for this range of lengths.

Fibers connectorized at ALPhANOV have not been observed to fail in this apparatus, although there have been reports from other experimental groups worldwide that these fail on the 5-year timescale (which is longer than/close to the length of time they have been used in this apparatus). In my experience, any loss in transmission is most often found to be caused by debris on the ends, likely from dust that is pulled onto the endcap by optical tweezing. If this debris cannot be removed using a fiber cleaner, it can usually be polished off using standard fiber polishing techniques; I typically polish with lapping film that has a 1 μ m particle size and then final polish (0.02 μ m particle size, 3M 863X) only to avoid taking off too much material. Some older fibers in the group are not connectorized by ALPhANOV and typically may not be polished, although I have been able to polish some of them.

 $^{^{21}\}mathrm{The}$ remainder are created with LMA-8-UV which just has a different core diameter.

²²It is recommended to cure them at a higher power than they will be used for.

3.2.10 Laser Power Control and Pulseshaping

Two methods of laser power stabilization are used throughout this apparatus: one for the detection light for each species to maintain a consistent number of counts per detection period, and another for the Raman beams to ensure a constant ac Stark shift so that the Raman Rabi frequencies and transition frequencies are reasonably stable.²³ Both make use of a NIST digital servo ([88], Sec. A.3) and feedback using photodetectors. By modulating the amplitude of the RF voltage going to an AOM²⁴ that diffracts a beam into the ion trap, the amount of light reaching the ion trap can be modulated as well, as long as the maximum available intensity of diffracted light is higher than the desired intensity. For this reason, this technique is sometimes called "noise-eating". This can correct for fluctuations in power and beam pointing from sources before the light is coupled into the UV fiber, since the feedback signal is taken at the output of the fiber and the AOM used to correct for power drifts is situated before the beam passes into the fiber. The voltage difference between the maximum intensity and the desired intensity determines the gain parameters that should be used for each digital servo. For this reason, pulses that are very different intensities from the same beamline (i.e. due to different frequencies within the AOM bandwidth or other factors) cannot all be stabilized to the same quality.²⁵

3.2.10.1 Pulseshaping for Resonant Detection Beams

The detection beam signal for each species is monitored using logarithmic photodetectors. The servo is implemented by changing the level of the RF driving voltage to the "Be BD Switch" AOM or the "Mg BD" AOM using a Minicircuits ZFM-3H-S mixer. The amplitude of the RF signal is adjusted before it passes through the RF amplifier that is connected to the AOM, as shown in Fig. 3.16. The NIST digital servo ([88], Sec. A.3) is used to servo the logarithmic photodetector

²³The Raman beams still require re-calibration of both the frequency and π -time daily due to small beam-pointing drifts that change the ac Stark shift.

²⁴For each beamline, there is at least one AOM that is used for that particular beam such that only the diffracted order is sent to the ion trap.

²⁵That is not to say that pulses of different intensity cannot be implemented from the same beamline. This will just result in pulses that are very poorly stabilized, with distortion of the pulse shape or some ringing, while others will be better shaped.

output voltage to a fixed value set using the digital servo GUI (SuperLaserLand); this corresponds to a specific intensity of the beam. The intensities of each detection beam are controlled to a level that yields ≈ 30 counts per ion for a detection period of 330 μ s for $^9\mathrm{Be^+}$ and 200 μ s for $^{25}\mathrm{Mg^+}$. The active state of the servo is controlled using an ARTIQ TTL that is sent to a digital input of the servo, so that the servo is only active when the beam is on.

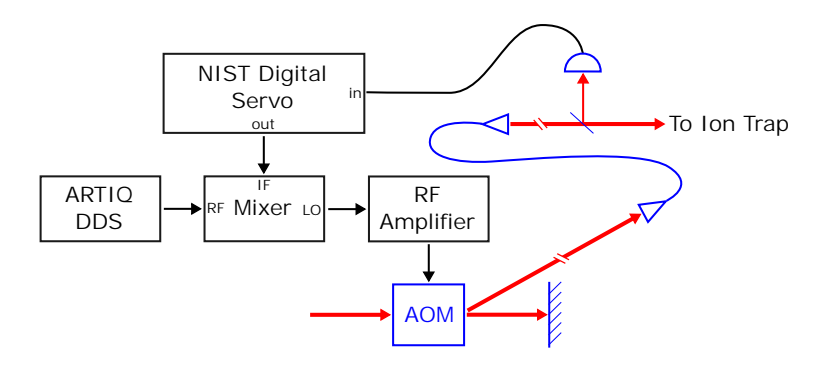


Figure 3.16: Schematic for beam power stabilization of the resonant beams. The electrical elements are illustrated in black, and optical elements are illustrated in blue. The laser beam is illustrated in red. The RF source for both species are individual ARTIQ DDSes, as the output must be changed between the detection and Doppler cooling frequencies. A Minicircuits mixer model ZFM-3H-S is used to modulate the amplitude of the signal sent to the RF amplifier (Minicircuits model ZHL-1-2W-S+ or ZHL-03-5WF+) and then to the appropriate AOM based on the voltage supplied by a NIST digital servo. The servo relies on a signal from a logarithmic photodetector (blue semicircle above) which monitors a small amount (typically on the order of 1% or less) laser light that is picked off from the main beam. There is an optical fiber (blue line with triangular terminations) in the laser beam path after the AOM and before the point where the laser light is monitored to clean the mode and reduce beam pointing fluctuations onto the ions.

3.2.10.2 Pulseshaping for Raman Beams

The light going into each Raman beam port (Fig. 3.9) for each species is monitored using a linear photodetector (six total). Much like the power servo method for the resonant beams, the RF power is modulated using the output of a NIST digital servo before being sent to the amplifier connected to each AOM, as appropriate. However, an Analog Devices ADL5390 multiplier is used instead of a mixer as it has faster response times, which is necessary because of the method used to pulse-shape the Raman beams.

The voltage signal from the linear photodetector is sent to one of the digital servo inputs. A

PDQ signal is sent to a different input of the digital servo, and the digital servo matches the voltage signal from the photodetector to that of the PDQ signal, as shown in Fig. 3.17. The amplitude of the voltage output by the PDQ is set in the ARTIQ dataset.

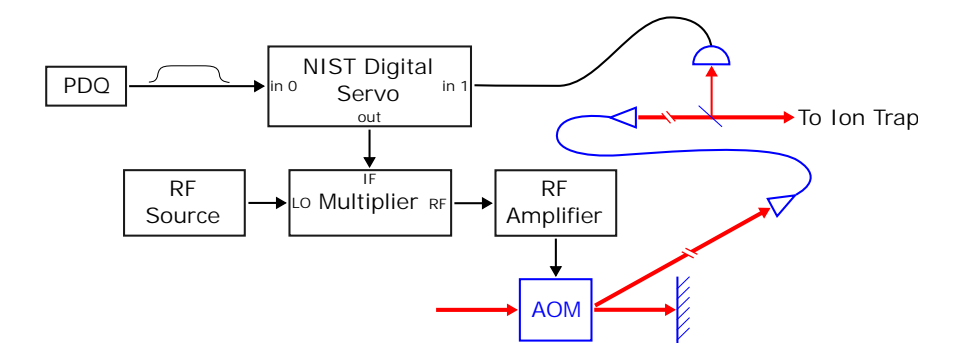


Figure 3.17: Schematic for beam power stabilization of the Raman beams. The electrical elements are illustrated in blue. The laser beam is illustrated in red. The RF source can be either an ARTIQ DDS or a fixed-frequency output DDS (usually this is a WindFreak SynthNV). An Analog Devices Multiplier ADL5390 is used to modulate the amplitude of the signal sent to the RF amplifier (Minicircuits model ZHL-03-5WF+ or ZHL-5W-1+) and then to the appropriate AOM based on the voltage supplied by a NIST digital servo. The servo relies on a signal from a linear photodetector (blue semicircle above) which monitors some laser light (typically on the order of 1% or less, but varies across beamlines) that is picked off from the main beam. There is an optical fiber (blue line with triangular terminations) in the laser beam path after the AOM and before the point where the laser light is monitored. The digital servo will servo the voltage corresponding to the monitored light (going into "in 1" in the diagram above) to match the voltage from the PDQ (going into "in 0").

As sketched in Fig. 3.17, the signal from the PDQ is a shaped voltage pulse; a cubic spline 26 is used to ramp from 0 V to the desired voltage corresponding to the stabilized intensity of the Raman beam in 2 μ s, and at the end of the pulse duration another 2 μ s pulse is applied to ramp back to 0V. These ramps are ideally imprinted onto the beam intensity as well by the servo. Our ARTIQ code currently implements the duration of each pulse as equal to the duration of the pulse top. However, the effective area of the pulse actually corresponds to the area of a pulse that is 2 μ s longer than the set duration, assuming the pulse is shaped ideally.²⁷

²⁶This is just the easiest to implement with the PDQ codes; the shape helps to reduce unintended couplings to other motion mode sidebands compared to square pulses.

²⁷Of course, the pulses are not shaped ideally and exhibit some asymmetry between the beginning and end of the pulse. This $\approx 2~\mu s$ offset has caused some difficulty when very short pulses are involved, or when the frequencies of the transitions have to be calibrated very accurately, since the ramped intensity will cause a varying Stark shift

3.2.11 Axial Micromotion Compensation with Electro-Optic Modulators

The geometry of the X-trap results in axial micromotion that cannot be compensated when the radial micromotion is compensated (Sec. 3.3.3, Refs. [89–91]). In the experiment zone of the ion trap, for ${}^{9}\text{Be}^{+}$ this micromotion modulation index is 2.67 for a beam with full projection along the axial direction [92], which means the majority of the power is not in the carrier frequency of the laser beam. This greatly decreases the efficiency of transitions and they are optimally driven on the second micromotion sideband, which was how ${}^{9}\text{Be}^{+}$ Raman transitions were performed in the past. In order to combat micromotion in situations where the micromotion cannot simply be nulled by moving the ion, techniques can be implemented such as the one used in this apparatus. 28

In this apparatus, electro-optic modulators (EOMs) are used to modulate laser beams so that the light appears as an unmodulated carrier in the ion frame; this requires careful control of the phase and power of the RF voltage used to drive each EOM. As shown in the lower part of Fig. 3.21, the RF signal comes directly from the same source that drives the RF voltage of the ion trap. The phase is coarsely controlled using delay lines that are simply lengths of SMA cable²⁹; the voltage is controlled using a variable attenuator (Kay Elemetrics 839). For the EOMs in the ⁹Be⁺ and ²⁵Mg⁺ resonant beamlines, the parameters can be tuned by maximizing the ion fluorescence for the appropriate species. The EOM for each resonant beam is situated slightly before the fiber that delivers the resonant light to the trap for each species. The parameters for the ⁹Be⁺ Raman micromotion modulation EOM³⁰ are tuned by attempting to drive Raman transitions on micromotion sidebands and slowing down the micromotion sidebands while verifying the carrier Rabi frequency is increasing.³¹ The ⁹Be⁺ Raman micromotion modulation EOM is situated after the

throughout that part of the pulse. For this reason, the intensity of the beams are set so that the majority of pulses have π -times no shorter than $\approx 10 \ \mu s$.

 $^{^{28}\}mathrm{This}$ technique originated from the ion trapping group at ETH Zurich.

²⁹Some of the lines have additional phase adjusters but they have a barely noticeable effect at 82.529 MHz and should be used for fine-tuning only, if desired.

 $^{^{30}}$ There is currently no micromotion compensation EOM for the 25 Mg $^+$ Raman beam as they are quite expensive and the optical coatings on the input/output windows are damaged by high power. Given the experience with other optical coatings used in the apparatus, the lower wavelength used 25 Mg $^+$ may likely exacerbate this problem. It may be implemented in the future if it is determined to be worthwhile.

³¹The decrease of the sideband Rabi frequencies is a significantly more sensitive signal than the increase of the carrier Rabi frequency if the beam is close to compensated. For this calibration, it suffices to ensure that the carrier

fiber going towards the trap (possibly to place it at a point in the beamline with the lowest possible power), and is in only one of the Raman beamlines (Be Raman 1 in Fig. 3.9).

3.3 The X-trap

The experiments described in this thesis were all performed in the "X-trap", a room-temperature 3D Paul trap shown schematically in Fig. 3.18. This trap has a unique geometry and was built originally to demonstrate junction transport and shuttling [17, 89–91], and was put under vacuum in \sim 2008. The trap features 44 individual electrodes, though some opposite pairs are shorted together where fine control is unnecessary (for example in the load zone near \mathcal{L}), and during the time period covered by this thesis, many of the electrodes and trapping regions (especially those near the right side of the diagram in Fig. 3.18) were not used; DC electrodes 27-44 were grounded and not connected to PDQs after the upgrade to ARTIQ, although there is hardware available to do so.

In addition to the electrodes shown in Fig. 3.18, there is a third electrode, the size and shape of all the electrodes combined (with no DC segmentation), that is situated underneath (offset in the \hat{y} direction in the main figure) the other two sets of RF/DC electrodes. This is called the "Bias" electrode. A DC voltage can be applied to this electrode to shift the ions, located anywhere in the ion trap, directly along the \hat{y} direction as labeled in Fig. 3.18.

3.3.1 Ion Loading

During the loading procedure, between 0.6 and 1.2 A of current is applied to the oven [89] heating solid samples of the desired species until neutral ${}^{9}\text{Be}^{+}$ or ${}^{25}\text{Mg}^{+}$ is emitted. The neutral atoms are photoionized by 235 nm or 285 nm light in a two-photon process for ${}^{9}\text{Be}^{+}$ or ${}^{25}\text{Mg}^{+}$ respectively,³⁴ and the ions are then trapped in the loading zone, labeled \mathcal{L} in Fig. 3.18. A separate set of resonant laser beams are aimed at \mathcal{L} for cooling, as well as the photoionization beams for both Rabi frequency does not appear to be significantly decreasing during the calibration, which could happen if the

photoionization light in the load zone) and increased the loading efficiency in ²⁵Mg⁺ by about a factor of two.

micromotion modulation index is very large. 34 Beginning around 2019, 313 nm light was used along with 285 nm light to load 25 Mg $^+$ since it is shown in Ref. [93] that ionizing with radiation near the continuum threshold is more efficient than ionizing with light of a shorter wavelength. This was tested in our experiment (simply turning on the 9 Be $^+$ BDD beams with the 25 Mg $^+$

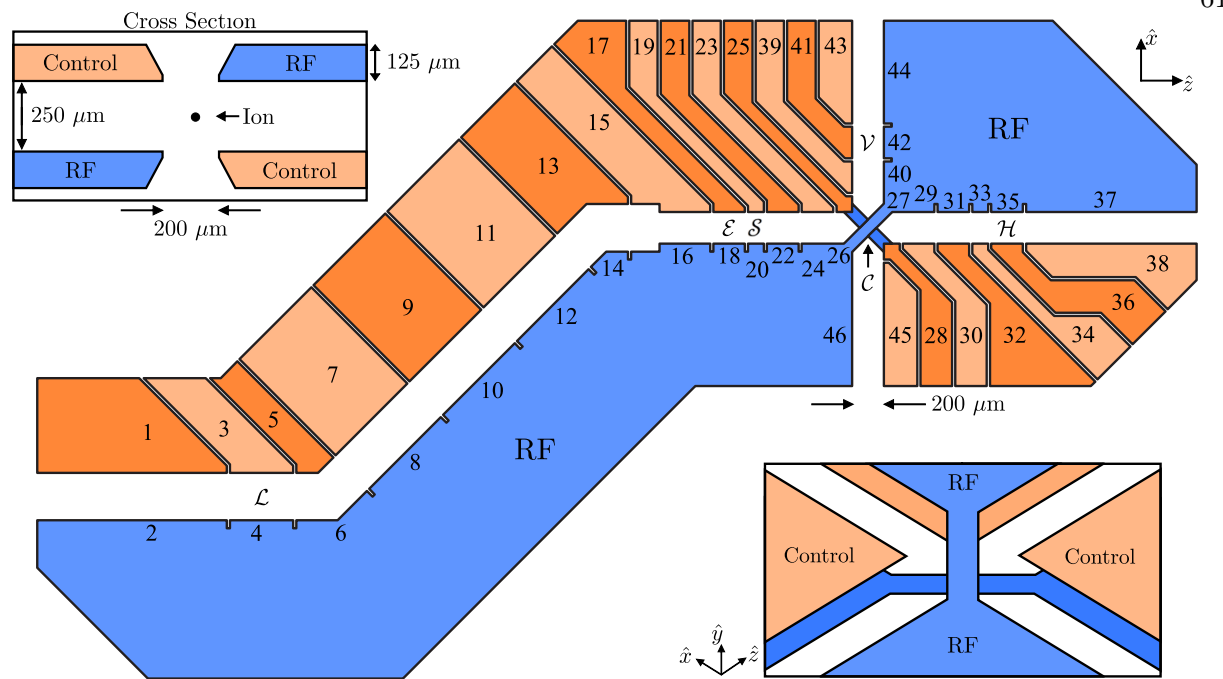


Figure 3.18: Schematics of the X-trap. This trap is fabricated using gold-plated alumina wafers, and consists of three layers [89]. Two layers implement the Paul trap itself, with the locations of the DC (Control) and RF electrodes on opposite sides in each layer (upper left inset). One layer is shown in the main image (with DC electrodes numbered 1, 3, 5 etc.). The numbers on the opposite RF electrode are the labels for the DC electrodes of the next trap wafer layer underneath. The last layer is a "Bias" board (not shown); a single electrode underneath the whole trap (with similar footprint) that controls the position of the ion perpendicular to the plane.³³ \mathcal{L} labels the load zone where ions are initially trapped before being shuttled to the experiment zone, labeled \mathcal{S} .

species; these beams are usually shuttered outside of loading attempts to prevent photon scatter off of the trap electrodes from reaching the PMT.

While attempting to capture ions at \mathcal{L} , high-intensity detuned light ("BDD" as described in Sec. 3.2) is turned on for long periods of time (approximately 1.5 seconds). Next, a sequence of voltages is applied to the electrodes between and around \mathcal{L} and \mathcal{S} in order to move ions from the former zone to the latter, which is the zone used for experiments.³⁵ Resonant detection light is pulsed on and if the desired amount of fluorescence from each ion species is detected (from a user-set threshold), the loading sequence is terminated: the oven current is turned off and the loading-zone

 $^{^{35}}$ In the experiments demonstrating ion transport and shuttling [13, 17], multi-ion crystals were moved to this zone (between electrodes 19 and 20 which are narrower than the nearby electrodes), before being split between two wells on either side of S. Therefore this is called the "separation" zone, although it is now used as the experimental region.

beams are shuttered.

3.3.2 Trapping Wells

There are several electrode voltage configurations used for trapping ions in the S region; the most frequently used is the "S" well. This is a well with relatively relaxed confinement, with mode frequencies given in Sec. 3.6 for various ion crystals, and a 30-minute average crystal lifetime for a linear string of ions ordered ${}^{9}\text{Be}^{+}_{-}{}^{25}\text{Mg}^{+}_{-}{}^{9}\text{Be}^{+}_{-}{}^{36}$ along the direction perpendicular to the segmentation of the electrodes (labeled \hat{z} in Fig. 3.18).³⁷ An alternate version of this well in zone S, "S_loadwell" (so named because it also contains DC voltages for an potential well at \mathcal{L} for the purposes of loading) can also be used; the mode frequencies in this well are nearly identical (within $\sim 1\%$) to those in "S". Another well that is used is "HF_S" which has tighter axial confinement, yielding higher axial frequencies. The voltages of all the DC electrodes near the trapping region are listed in Tab. 3.6; these are generated by a boundary-element-method simulation of the trap electrodes based on desired trapping potential parameters.

In the experiments detailed in Sec. 4.3.4 and Sec. 5.6.1, another confinement method is used in which the DC voltages of the "S" or "HF_S" well are all scaled by a fixed parameter. In an ion trap with ideal geometry, this would scale the harmonic confinement along **z**, scaling the axial mode frequencies according to Eq. 2.13 and Sec. 2.1.3; such mode frequency adjustments were required for those experiments. However, in this ion trap the "shim" voltages that are added to each DC electrode to compensate for the presence of the RF gradient caused by the unique shape of the X-trap (Fig. 3.18, compensation described in Sec. 3.3.3) and stray fields (for example, from patches of charge on dielectric parts of the trap from laser beams), have to be adjusted for each scaling factor.

It can be seen that the voltages for the "S" well are not straightforwardly confining/anticonfining

³⁶The lifetime is likely longer since experiments were being run that could perturb the ions, but on average this ion crystal will decrystallize (i.e. lose ions from this crystal or the whole crystal entirely) in 30 minutes with just the cooling light on (and saveion, described in Sec. 3.7 implemented).

³⁷From this point onwards, any ions notated with dashes in between denote ion crystals aligned along this same axis.

Electrode	S Well Voltage	S_loadwell Well	HF_S Well
	(Volts)	Voltage (Volts)	Voltage (Volts)
15	3.1690	0.1809	0.8145
16	2.7910	0.1711	0.7367
17	0.5449	0.4378	2.1993
18	-0.6012	0.3946	2.1760
19	-1.0126	-1.0592	-2.8574
20	0.1954	-1.0584	-2.8271
21	0.2520	0.2253	1.7024
22	-0.7969	0.2607	1.7026
23	2.7135	0.1902	0.8795
24	3.0768	0.1964	0.7580

Table 3.6: Electrode voltages for the 5 pairs of electrodes closest to the experiment zone for the "S", "S_loadwell", and "HF_S" wells. These were generated using a boundary-element-method simulation using models of the X-trap electrodes, and do not include shim voltages that are added on top of each DC voltage to shift the ion into the micromotion null point.

at the electrodes 19/20. The exact reason for this is not certain,³⁸ but it is possible that this potential is intended to tilt the radial modes in a controlled manner to be beneficial for cooling.

3.3.3 Radial Micromotion Minimization

The geometry of this trap results in ion micromotion that cannot be completely compensated [89–91]; usually the radial micromotion is compensated leaving only axial micromotion. There are two shim voltages (added to the default trapping voltages in Tab. 3.6) used to compensate the radial micromotion; one is applied to the bias board (Sec. 3.3) and one is split between the two opposite DC electrodes nearest to the ion (numbered 19 and 20) as a positive voltage on one and a negative voltage on the other, to push the ion along the direction transecting the two.³⁹

 $^{^{38}}$ The knowledge was lost as lab members left the group.

 $^{^{39}}$ This is done for simplicity; while the two voltages used here can move the ion in any direction along a plane perpendicular to the axial (**z**) direction, ideally the ion should be moved exactly along the two orthogonal radial directions during calibrations. To do this a combination of the voltages on the DC19/DC20 and Bias electrodes can be found that moves the ion in each desired direction.

In order to find the radial mode frequencies, a tickle frequency is applied to the RF electrodes of the trap (see Fig. 3.21 for tickle tone injection electronics). This frequency is scanned until a drop in ion fluorescence is observed, corresponding to the ion heating up from the parametric driving of a radial mode by the electric field. For a single ion, this reveals two motion frequencies that are simply referred to as the higher- and lower-frequency radial modes (see Sec. 3.6).

Micromotion compensation is done using a single ion of either species. In this apparatus, the best results are obtained when the bias voltage was used to compensate the ion position along the direction corresponding to the higher frequency axial mode, and the DC19/DC20 difference voltage was used for the lower frequency axial mode direction. A tickle of either the higher or lower radial mode frequency is applied while the corresponding shim voltage is scanned; the point yielding the least response from the ion (the least loss in fluorescence) is taken as the best shim voltage. Both shims should be iterated, and then the two radial mode frequencies must be determined again as this compensation method shifts these frequencies. It was also determined after the experiments discussed in Ch.s 4 and 5 that the method used to stabilize the RF drive amplitude interfered with micromotion compensation to some extent (see Sec. 3.7), yielding curves during the shim voltage scans that did not have a clear maximum; after rearranging the RF stabilization hardware as shown in Fig. 3.21, the data had much clearer results.

3.4 Control System

Around late 2018/early 2019, the HFGUI system in use for the experiments described in Refs. [13, 92, 94] and prior was retired and ARTIQ was installed. ARTIQ can be described briefly as a real-time input/output experimental control platform with a pseudo-python programming API geared towards atomic physics experiments. Further description of ARTIQ in our apparatus can be found in the thesis of Stephen Erickson [92]. The development of ARTIQ was initiated in collaboration with our group, and as a result of this, hardware that was designed and partially built in-house that precludes the commercially-developed Sinara hardware is used. This hardware is often referred to as the ARTIQ crate. In our particular ARTIQ hardware installation, a 2.7 GHz reference

 $\operatorname{clock}^{40}$ is used.

Throughout my time in the group, the ARTIQ crate was a source of some difficulty. Primarily, this was because the direct-digital synthesis (DDS) outputs (based on Analog Devices AD9914) for driving RF frequencies would spontaneously stop working or manifest noise. 41 After much debugging, this was determined not to be caused by the FPGA (AMD KC705), loose/damaged connectors, or incorrect clock reference signal amplitude. Often, it was found that this was not even caused by damage to the DDS card outputting the noise, although sometimes this was the case and the DDS chip was discovered to have signs of damage/discoloration. Our hardware supports up to 24 DDS cards on two backplanes of 12 each (each card was plugged into a set of pin headers), and towards the end of my graduate studies, it was found that in our ARTIQ crate, the position of the card on the backplane⁴² would determine whether a card would be likely to be noisy, or not work at all. If noisy, the noise is much smaller in amplitude than the signal, changes with the set frequency of the DDS, and sometimes could be fixed by a dac_cal sequence on the DDS chip. It was found that setting a higher frequency for the clock distribution signal to the DDS card (i.e. 3 GHz instead of 2.7 GHz) during the dac_cal sequence made it more likely for a larger subset of DDS cards to function after returning the clock signal to the operating frequency. In order to do this, two frequency sources were used, one for the DDS cards that was tuned, and another that was used for the KC705 in order to avoid clock errors from the FPGA. Both clock sources were referenced to a 10 MHz NIST maser signal. Such noise was not well characterized until after the experiments discussed in Chs. 4 and 5 and thus could be a source of error for experimental data in either of these projects.

Four PDQ [95] crates (upgraded from PDQ2 to PDQ3) were also installed as part of this upgrade, with 16-bit resolution running at 50 megasamples per second. Two of them are used to drive the DC electrodes of the ion trap; one is used for pulse-shaping of Raman beams; and one is not

⁴⁰This is stated to be outside the recommended operation frequency for the DDS clock but was likely not the cause of the DDS card issues described below, as other experiments experienced similar issues at different clock frequencies that were within the chip specifications.

⁴¹Posts on online forums indicate that this is a problem that is seen on this DDS chip in other hardware as well.

⁴²The position of "untrustworthy" DDSes was sometimes found to change with different clock reference signal amplitudes.

currently in use but can be used to control additional DC electrodes that are currently not connected. Each crate contains 15 PDQ outputs from 15 individual PDQ boards and is programmed via SPI communication with the ARTIQ crate but is triggered by a TTL to avoid latency.⁴³ One feature that is lacking in our current PDQ hardware is clock synchronization. For the mode-coupling experiments described in Ch. 5, the phase was reset on all the PDQ signals prior to each experimental shot and the drifts in phase between channels for the durations required for the experiments was found to be small enough to perform experiments reasonably. However, this still prevents the current hardware from being used to perform experiments where the microwaves/lasers and PDQ signals are required to have a controlled relative phase (for example experiments where motion states are created with a certain phase using the mode coupling operation which relies on the PDQs (Ch. 5) and analyzed using microwaves, or vice versa.)

3.5 Magnetic Field Stabilization

The magnetic field coil hardware used in this apparatus are described briefly in the theses of Ting-Rei Tan [96] and Stephen Erickson [92]. Therefore, this section will be dedicated to the methods of magnetic field stabilization used during the period of my graduate studies.

First, the magnetic field is coarsely stabilized. The current supplied to the main magnetic field coil (approximately 62.65 A at 4.7 V) (from an Agilent 6682 power supply) is monitored by a current sensor (DaniSense Flux Gate DS200IDSA) whose signal is converted to an error signal by a B-field servo board. This servo board takes the difference between the FluxGate's output and a pre-programmed value and amplifies this by a factor of 200 to increase the sensitivity of the servo. The error signal output of this servo board is sent to a NIST digital servo ([88], Sec. A.3), which then provides a voltage signal to the Agilent 6682 power supply that is used to modulate its output.

⁴³This latency does not arise inherently from the PDQ crates but rather from the use of an "SPI demultiplexer". This is a home designed piece of equipment capable of generating up to 8 SPI outputs using two SPI inputs. Because of the lack of spare TTL channels to convert into SPI signals in our ARTIQ crate, it was necessary to use this demultiplexer to control our 4 PDQ crates.

⁴⁴This board was designed or modeled after those designed in the Oxford ion trapping group.

⁴⁵This value has to be programmed into the board using a modified Cheetah cable after a power outage.

The servo is operated in a voltage-controlled manner and the Agilent 6682 power supply is operated in voltage-controlled mode.

While it is possible to use this magnetic field servo board in a feed-forward configuration, the experiments presented in this thesis operated by simply stabilizing the error signal voltage received by the digital servo to a fixed value. This fixed value can vary from day to day and is usually set so that the feedback signal output by the digital servo has the smallest amplitude, to allow for the largest amplitude of correction voltages. This stabilization value changed from day to day but most commonly was between -0.10 and -0.25 V. If the desired field cannot be reached using the secondary (shim) coil set in the next step, then the field generated by the main coil is too far from the desired value for the shim coil to compensate. In this case, the digital servo is unlocked, the supply current of the Agilent 6682 is adjusted, and the digital servo is locked using a different stabilization voltage value.

About once per year, this method of coarse field stabilization appeared to fail completely; the error signal received by the digital servo would be observably unstable even when the servo was locked, and this was coincident with poor coherence between the states. These symptoms could not be fixed by changing the digital servo unit or the digital servo's parameters; it was seen to be best corrected by exchanging the Agilent 6682⁴⁶ for a different one. Sometimes, up to three different power supplies were continuously exchanged until the noise no longer was present. It is possible that this instability is occurring due to aging of the capacitors in the device, or temperature changes, oxidation, or corrosion changing the overall impedance of the main magnetic field coil circuit to a specific, unfortunate value.

After the main coil current is set, the magnetic field is fine-tuned using the shim coil that is aligned to (i.e. it generates a magnetic field in the same direction as) the main coil using a calibration signal from the ion. The cooling transition frequencies⁴⁷ (as labeled in Figs. 3.1 and 3.4)

⁴⁶The Agilent should be modified from its stock configuration by removing the fan from the back of the unit to reduce noise. Christa Fluhmann's thesis [97] has a good guide for how to do this as the power supply will not operate without a fan connected by default. The fan can be powered from a separate source and a length of flexible ducting can be used to ensure air flow to the power supply.

⁴⁷These transitions are used because they are quite field-sensitive for both species, and include the (ideal) initial

are hard-coded into the code for this calibration. A current is passed through the shim coil and varied from 0 to 0.5 A while a microwave π -pulse is attempted on the cooling transition of the selected ion.⁴⁸ Since the π -pulse is attempted at a fixed frequency, it will only succeed when the magnetic field is at the value that tunes the transition frequency to the hard-coded value.

The magnetic field at the ion is then more precisely set by scanning the shim coil voltage about the previously-set value in a range of about ± 0.001 -0.003 mV and performing a microwave Ramsey experiment using the same transition as used in the previous step. This is usually repeated about every 10 minutes after initial calibrations to combat slow drifts of the magnetic field. The magnetic field is set at the beginning of each day that experiments are performed, and calibrations of microwave π -times follow.⁴⁹

There exist other magnetic field coils built around the X-trap: an anti-Helmholtz coil to tune the field gradient position, as well as coils that create fields along the two directions orthogonal to the main coil in order to align the magnetic field vector more precisely. These coils were not used for any experiments described in this thesis as the alignment of the magnetic field vector/magnetic field gradient did not appear to be an issue.

3.6 Ion Crystals, Modes, and Ion Participations

The ion crystals discussed in this thesis mainly are $^{25}\text{Mg}^+$, $^{9}\text{Be}^+$ - $^{25}\text{Mg}^+$, and $^{9}\text{Be}^+$ - $^{25}\text{Mg}^+$ - $^{9}\text{Be}^+$. The ion crystal $^{9}\text{Be}^+$ - $^{9}\text{Be}^+$ is also used in the experiment discussed in Sec. 5.6.1, and single $^{9}\text{Be}^+$ was used periodically for calibrations and testing. In illustrations, $^{9}\text{Be}^+$ will be represented by a red circle, while $^{25}\text{Mg}^+$ will be represented by a green circle. 50 In the most-commonly used trapping configuration, the "S" well, the motional mode frequencies for the axial and two radial modes are $2\pi \times \{1.18, 4.4, 4.6\}$ MHz, respectively, for a single $^{25}\text{Mg}^+$ ion (and $2\pi \times \{1.97, 12.9, 13.0\}$

atomic state for both species after Doppler cooling.

 $^{^{48}}$ Unless 25 Mg $^+$ is the only ion trapped, 9 Be $^+$ is usually used to set the field but either species can be used and it has been verified that they set the field to similar values based on the frequencies of the cooling and other transitions.

 $^{^{49}}$ Microwave frequencies are very stable and are rarely calibrated.

⁵⁰While previous members of the group have used different colors to represent these ions, I like this representation because each ion's color corresponds to the doubled (visible) resonant wavelength for that ion.

MHz for a single ${}^{9}\text{Be}^{+}$ ion). The mode frequencies, as well as the participations of each ion in each mode, for multi-ion crystals are shown in Figs. 3.19 and 3.20 and listed in Tab. 3.7.

The motion-sensitive Raman beams in the apparatus are nominally set up to address the axial modes of the ions, therefore most discussions will center around these and unless otherwise specified the radial modes are ignored (i.e. for the purposes of detection and cooling)⁵¹ — this is why Fig. 3.20 shows the axial modes only. For the mode-coupling experiment (Ch. 5), the out-of-phase (sometimes called "rocking") radial modes of ${}^{9}\text{Be}^{+}$ - ${}^{25}\text{Mg}^{+}$ and ${}^{9}\text{Be}^{+}$ - ${}^{9}\text{Be}^{+}$ are cooled as a proof-of-principle experiment. The axial and radial modes of ${}^{9}\text{Be}^{+}$ - ${}^{25}\text{Mg}^{+}$ are shown in Fig. 3.19; the ${}^{9}\text{Be}^{+}$ - ${}^{9}\text{Be}^{+}$ modes are similar but more symmetric, and a custom well was used for this latter crystal in the mode-coupling experiment.



Figure 3.19: The radial and axial modes of the ${}^9\mathrm{Be}^+$ - ${}^{25}\mathrm{Mg}^+$ ion crystal trapped in the "S" well are described above. ${}^9\mathrm{Be}^+$ is represented by the red circles, while ${}^{25}\mathrm{Mg}^+$ is represented by green circles. For each mode, the corresponding names, abbreviations, and frequencies of each mode are shown, as well as the participations of each ion in that mode (illustrated by the lengths of the arrows). The information corresponding to the radial modes are shown in purple, and the axial mode in blue. Due to the mass difference between the two ions, the mode participations are greatly asymmetric, especially in the radial modes (one arrow is used to illustrate both radial modes, as they have the same structure, just along different directions).

Because ${}^{9}\text{Be}^{+}$ - ${}^{25}\text{Mg}^{+}$ - ${}^{9}\text{Be}^{+}$ is a multi-ion crystal with an odd number of ions, it has a symmetric mode in which the middle ${}^{25}\text{Mg}^{+}$ ion does not participate: the out-of-phase (OOPH) mode as shown in Fig. 3.20. This means it is not possible to use ${}^{25}\text{Mg}^{+}$ to affect the OOPH mode

⁵¹During more recent experiments (after those discussed in Chs. 4 and 5), it was found that one of the alternating (ALT) lowest-frequency radial modes the ⁹Be⁺-²⁵Mg⁺-⁹Be⁺ ion crystal sometimes had extremely high motional occupation, on the order of hundreds or thousands of quanta. This "hot" radial mode caused a noticeable error when experiments were performed with our axial Raman beams and this error could be suppressed when cooling of the radial ALT modes was implemented. This did not appear to be an issue in prior experiments and could have manifested over time due to the aging of various components causing mode frequencies to drift in an unlucky manner relative to each-other (to cause unintentional coupling via sub/super-harmonics) or a new source of noise in the lab.

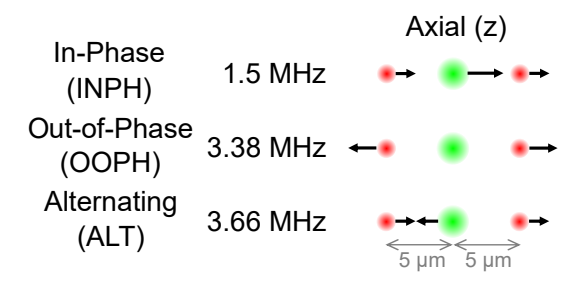


Figure 3.20: The axial modes of the ${}^9\mathrm{Be}^+-{}^{25}\mathrm{Mg}^+-{}^9\mathrm{Be}^+$ ion crystal trapped in the "S" well⁵³ of our ion trap, are described. ${}^9\mathrm{Be}^+$ is represented by the red circles, while ${}^{25}\mathrm{Mg}^+$ is represented by green circles. For each mode, the corresponding names, abbreviations, and frequencies of each mode are shown. The ion participation (the effective movement of each ion in that mode) for the ideal scenario where the ion is confined in a perfectly harmonic potential is illustrated with black arrows. Importantly, the middle frequency (OOPH) mode does not involve the ${}^{25}\mathrm{Mg}^+$ ion at all.

of ${}^{9}\mathrm{Be^{+}}$ - ${}^{25}\mathrm{Mg^{+}}$ - ${}^{9}\mathrm{Be^{+}}$ directly, which is an issue since it is designated as the cooling ion in our apparatus. Through the mode-coupling operation discussed in Ch. 5, this issue is overcome and instead turned into a powerful tool through which repeated measurements of motional modes is possible (Sec. 5.7).

Mode	Freq (MHz)	Participation
z-OOPH	6.304(1)	0.707, -0.707
x-OOPH	7.483(1)	0.707, -0.707
y-OOPH	6.437(1)	0.707, -0.707
z-OOPH	4.722(1)	0.930, -0.368
x-OOPH	4.04(3)	0.022, -0.999
y-OOPH	4.48(2)	0.022, -0.999
(z)-INPH	1.501(1)	0.396, 0.828, 0.396
(z)-OOPH	3.374(1)	-0.707, 0, 0.707
(z)-ALT	3.655(1)	0.586, -0.560, 0.586
	<i>z</i> -OOPH <i>x</i> -OOPH <i>y</i> -OOPH <i>z</i> -OOPH <i>y</i> -OOPH (<i>z</i>)-INPH (<i>z</i>)-OOPH	z-OOPH 6.304(1) x-OOPH 7.483(1) y-OOPH 6.437(1) z-OOPH 4.722(1) x-OOPH 4.04(3) y-OOPH 4.48(2) (z)-INPH 1.501(1) (z)-OOPH 3.374(1)

Table 3.7: Characteristics of the relevant normal modes of the ion crystals used in this thesis. For the work discussed in Ch. 5, the ${}^{9}\text{Be}^{+}$ - ${}^{9}\text{Be}^{+}$ ion RF confinement voltage is changed during the sequence to bring the x-OOPH and z-OOPH frequencies closer together.

The heating rate of the single ²⁵Mg⁺ ion in the "S" well is between 300-400 quanta/s; this

value was determined using sideband thermometry ([68], Sec. 2.2.2.2) and varied over time, most likely due to slow drifts in trapping parameters over time or changes in noise sources within the lab. These were not explored extensively. The heating rates of the axial modes of ${}^{9}\text{Be}^{+}$ - ${}^{25}\text{Mg}^{+}$ - ${}^{9}\text{Be}^{+}$ are shown in Tab. 3.8; this was a crystal that was used frequently in this apparatus. Other ion crystals were used less frequently and thus the heating rates were not monitored as closely; some heating rates may be found from Ref. [98] for the out-of-phase (OOPH) modes on ${}^{9}\text{Be}^{+}$ - ${}^{25}\text{Mg}^{+}$.

Mode	Frequency (MHz)	Heating Rate (quanta/s)
In-Phase (INPH)	1.50	700-1000
Out-of-Phase (OOPH)	3.38	0-2
Alternating (ALT)	3.66	70-90

Table 3.8: The range of heating rates for the three axial modes of ${}^{9}\text{Be}^{+}$ - ${}^{25}\text{Mg}^{+}$ - ${}^{9}\text{Be}^{+}$, determined using sideband ratios ([68], Sec. 2.2.2.2) over the last ≈ 5 years is given.

Another trapping well that was used sometimes for diagnostic purposes is "HF_S". The motional mode frequencies for the axial and two radial modes in this confinement potential are $2\pi \times \{2.13, 4.0, 4.6\}$ MHz, respectively, for a single 25 Mg⁺ ion and $2\pi \times \{3.4, 12.6, 13.2\}$ MHz for a single 9 Be⁺ ion.

3.7 Trapping RF Control

During my graduate study, the X-trap was operated with one standard RF voltage amplitude level that is used for the majority of the experimental cycle, and a lowered RF voltage amplitude that has two purposes described below; for both these applications, it was necessary to have at least these two different RF confinement voltage levels for the experiment that could be switched on and off in real time (i.e. within one experimental duty cycle).

(1) In order to have a deterministic order for the ${}^{9}\text{Be}^{+}_{}^{25}\text{Mg}^{+}_{}^{9}\text{Be}^{+}$ crystal (i.e. for the ${}^{25}\text{Mg}^{+}$ to be between the two ${}^{9}\text{Be}^{+}$), the ion crystal is reordered before each shot of an

experiment using ${}^{9}\text{Be}^{+}$ - ${}^{25}\text{Mg}^{+}$ - ${}^{9}\text{Be}^{+}$. The reordering sequence consists of an increase in axial confinement voltage coupled with a lowered RF voltage. ${}^{25}\text{Mg}^{+}$ is of higher mass, so it has weaker radial confinement (Eq. 2.14) and this will cause ${}^{25}\text{Mg}^{+}$ to move off-axis relative to the two ${}^{9}\text{Be}^{+}$. The most energetically favorable configuration of the three ions in this state has the ${}^{25}\text{Mg}^{+}$ between the two ${}^{9}\text{Be}^{+}$ ions, ideally forming an isosceles triangle with ${}^{25}\text{Mg}^{+}$ at the apex. The three ions are cooled towards this configuration by the high-power detuned cooling "BDD" light for both ion species (described in Sec. 3.2), which is on during the whole reorder sequence. The axial confinement is then relaxed as the RF voltage is increased to the regular operating value before proceeding with the rest of the experimental sequence.

(2) In order to maintain ion crystals in the trap for longer period of time, a pre_check can be implemented for each shot of the experiment, where a detection is performed to determine if the desired ion crystal remained trapped. To do this, a threshold of counts for each ion species is given to the pre_check function, and fluoresence counts for each of ⁹Be⁺ and ²⁵Mg⁺ are recorded using the standard detection durations of 330 μs and 200 μs respectively. If the fluorescence counts exceed the pre-set threshold, the experiment sequence proceeds as normal, but if the counts are too low, the ions are assumed to be decrystallized, and the saveion sequence will be implemented. In saveion, the "BDD" for both species is pulsed on for a period of time that increases with attempt number (the minimum of 2ⁿ ms and 1 s, where n is the recrystallization attempt number) up to a maximum number of recrystallization attempts. After this, one final recrystallization attempt will be made where the RF confinement is decreased while the BDD beams are left on. If this does not succeed, the saveion sequence terminates, and this will also terminate the experimental scan by default.⁵⁵

⁵⁴A reordering sequence is also performed when ${}^9\mathrm{Be}^{+}$ - ${}^{25}\mathrm{Mg}^{+}$ is used, but does not involve changing the RF voltage. ${}^{55}\mathrm{This}$ function significantly increases the chances of retaining a ${}^9\mathrm{Be}^{+}$ - ${}^{25}\mathrm{Mg}^{+}$ - ${}^9\mathrm{Be}^{+}$ crystal; otherwise this crystal is very difficult to take data with. Using this method reduces the number of crystal re-loading attempts required per day by about a factor of 10. Moreover, pre_check can be implemented during an experimental sequence and will not affect the data recording process if the ions are successfully recrystallized. However, it can also lead to ion loss when

The initial set up for electronics to switch between two RF levels in real time utilized a method very similar to that used for the Raman laser pulse-shaping (Fig. 3.17) in order to change the RF signal between a high and low level using shaped ramps.⁵⁶ While this worked for the majority of calibrations, initialization sequences, and experiments (for example the experiments performed in Chs. 4 and 5), it was found later to interfere with experimental signals that were used for micromotion minimization (Sec. 3.3.3). After some further suspicion that the digital servo used for pulse shaping could be introducing noise on the RF electrode and that the signal from the RF detector (Herotek DHM124AA) was not sensitive enough to reliably use as a servo signal, the components shown in Fig. 3.21 were installed.

The main difference between the new and old RF stabilization systems are the components in the "2-level RF Switching" dashed box as described in Fig. 3.21; the RF signal distribution to the micromotion compensation EOMs were also made more symmetric between ⁹Be⁺ and ²⁵Mg⁺. Instead of an active servo using the signal from the RF power detector (which is still monitored using an oscilloscope in the newer stabilization system), the re-arranged system relies on the inherent stability of the Rhode-Schwarz SMT 02 RF source, which was found to be extremely stable. The variation in the radial motion frequencies (which are more sensitive than axial motion frequencies to fluctuations in RF voltage) for a single ²⁵Mg⁺ ion over a week is less than a few tens of kHz.

Because the current system relies on passive stability of the RF source, there is a warm-up period after a power outage that affects the experimental data. Turning the RF source on after it is off for a long period of time will put the ion equilibrium position (for a single 25 Mg⁺, likely also for single 9 Be⁺ although the latter was not tested) in a location where the counts are 10-20% lower than expected for typical operating conditions. While this can be corrected by changing the pointing of the detection beams, this is not recommended, as the ion will return to the same position as before the power outage after a period of 3 days to 1 week, after which the detection beams will

used improperly, since without the presence of cooling light, the RF confinement relaxation will sometimes cause the loss of $^{25}\mathrm{Mg}^+$ ions due to their weaker radial confinement.

 $^{^{56}}$ Compared to Fig. 3.21 which shows the newer setup, the signal going to the oscilloscope was used as the servo input signal and the mixer/digital servo unit was installed in place of the components in the "2-level RF Switching" dashed box. The TTL signal from ARTIQ was used to trigger the PDQs to ramp up/down the PDQ output signal.

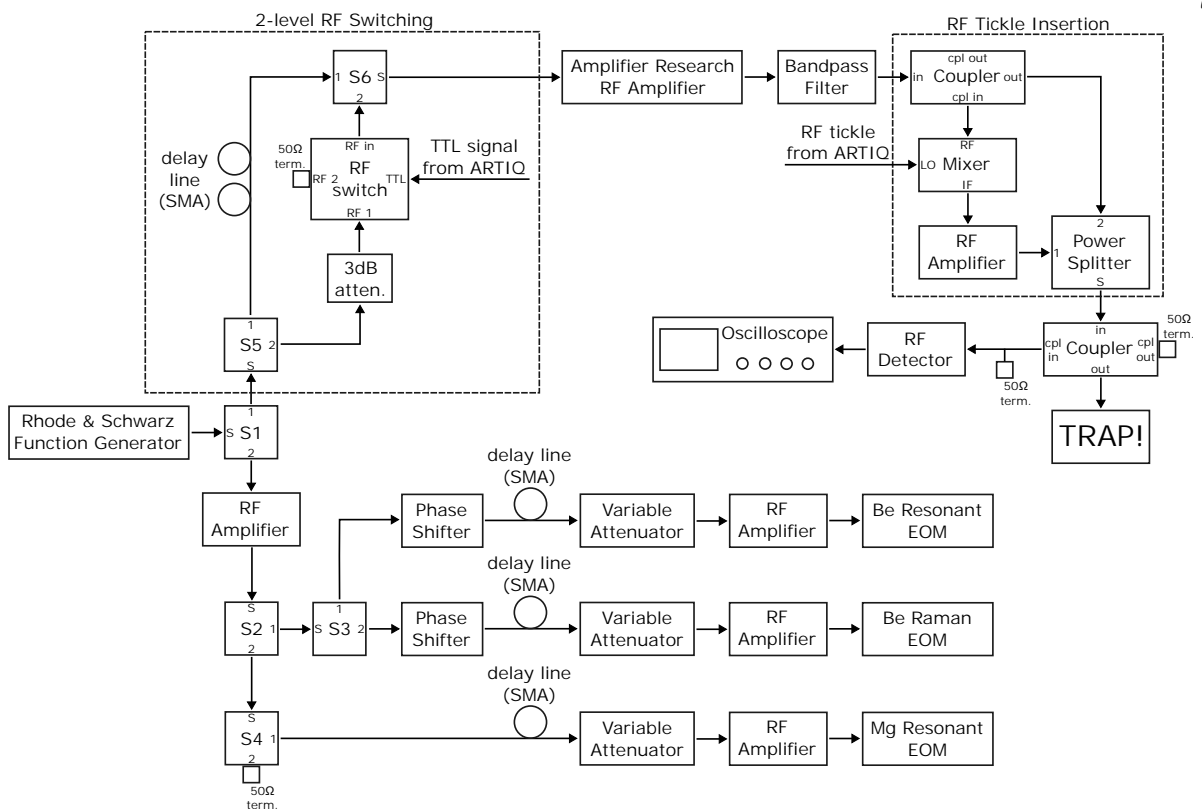


Figure 3.21: RF stabilization system for the X-trap as rewired late 2023. All RF splitters (Minicircuits ZFSC-2-1-S+) are labeled with "S" and a number. The upper part of the diagram shows how the RF signal is delivered to the trap. A series of components that is used to switch between two RF trapping levels using an ARTIQ TTL signal is contained in the dotted box on the upper left. The dotted box on the upper right shows how an additional RF signal is coupled to the RF electrodes for the purposes of probing the ion radial mode frequencies. The lower part of the diagram shows the signal being routed to micromotion stabilization EOMs for each beamline. There is currently no EOM for the 25 Mg⁺ Raman beamline.

have to be adjusted again.

Chapter 4

Electromagnetically-Induced-Transparency Cooling of ²⁵Mg⁺

Cooling the motional modes of a trapped-ion crystal beyond the Doppler limit to near the ground state is important for various applications including precision spectroscopy [36], quantum control and sensing [26], and quantum information processing [4, 5, 14]. If all relevant modes are not properly cooled or characterized, Debye-Waller factors [50] and other effects can lower the attainable fidelity of quantum operations and limit the precision of spectroscopic values measured [36]. Commonly used sub-Doppler cooling methods for trapped ions include resolved-sideband cooling [99–101], Sisyphus cooling [102–106], and electromagnetically-induced-transparency (EIT) cooling [56, 107–113].

Resolved-sideband cooling (which is used as the standard sub-Doppler cooling method in our apparatus, described in Sec. 3.2.8) is selective by mode frequency and can attain mode occupations close to zero ($\bar{n} \leq 0.1$), limited primarily by competition with the heating rates of each mode. The frequency selectivity of sideband cooling means that it can only be used to cool a single mode at a time, making it inefficient for large ion crystals that require cooling of many modes. In ions lacking single-photon transitions that are narrow enough for resolved-sideband cooling such as ${}^{9}\text{Be}^{+}$ and ${}^{25}\text{Mg}^{+}$, two-photon Raman transitions are used to create an effective narrow cooling transition between two long-lived states together with a repump field that couples to a quickly decaying level to repump the internal state.

On the other hand, Sisyphus cooling requires less laser power than Raman sideband cooling but requires the use of a laser beam with carefully-controlled rotating polarization, and can only attain average motional occupations on the order of unity.

EIT cooling is capable of reaching reasonably low motional occupations and does not require high laser power, and has been used widely on trapped ions since being demonstrated on ⁴⁰Ca⁺ in 2000 [109]. Moreover, it has a relatively broad cooling bandwidth (typically several MHz wide) and can often be used to cool multiple modes simultaneously, yielding a potential speed advantage over Raman sideband cooling in our system, especially for larger ion crystals.

For these reasons, after it was seen that approximately a third of the total duty cycle was used for sideband cooling in the gate teleportation experiment in this apparatus [13], it was decided that EIT cooling would be explored as an alternative cooling method. It is considered (to first order) sufficient to cool all axial motion modes, because the motion-sensitive Raman beams used for quantum gates have a nominally axial (z) projection and should not be very sensitive to high motional occupation of modes in other directions. ⁹Be⁺ has a field-insensitive hyperfine transition at the magnetic field used and is therefore used as the qubit that stores quantum information, so EIT cooling was to be performed on ²⁵Mg⁺, which plays the role of a helper ion. Prior to beginning this exploration, in trapped ions, EIT cooling had been demonstrated using ⁴⁰Ca⁺ [109, 110], ²⁴Mg⁺ [56], ¹ and ⁹Be⁺ in a Penning trap at a magnetic field of 4.46 T where the electron spin is effectively decoupled from the nuclear spin [111]. The ions in these three experiments have a common property that the relevant state manifolds are simple, where population loss to states that are not involved in the EIT cooling process is very unlikely.

Unfortunately, at this magnetic field, such a closed subset of states cannot be found in $^{25}\text{Mg}^+$ (nor in $^{9}\text{Be}^+$), even when using beams whose polarizations are well controlled. EIT cooling typically assumes two ground states and one excited state (a Λ structure, illustrated in Fig. 4.1(a)), and any excited state population in $^{25}\text{Mg}^+$ can decay to either one state (if the excited state is in $^{2}\text{P}_{3/2}$ and has $|m_F = \pm 4\rangle$) or three or more states, making it difficult to set up a Λ system. The approach that

 $^{^{1}}$ The EIT cooling experiments performed in this apparatus bear a particular similarity to this work, which uses 24 Mg $^{+}$ to sympathetically cool 9 Be $^{+}$. However, as discussed in the following paragraphs, the additional states in 25 Mg $^{+}$ compared to 24 Mg $^{+}$ adds complexity to the experiment and thus modification of the EIT cooling technique is required.

was implemented to circumvent this was to select a subset of states that include three ground states and one excited state, and to add an extra "repump" beam to remove population from the extra ground state, as shown in Fig. 4.1(b). This also allowed for the implementation of another method of EIT cooling known as "double-EIT" (Sec. 4.3.6) which is theoretically capable of reaching even lower final motional occupations than regular EIT cooling [114].

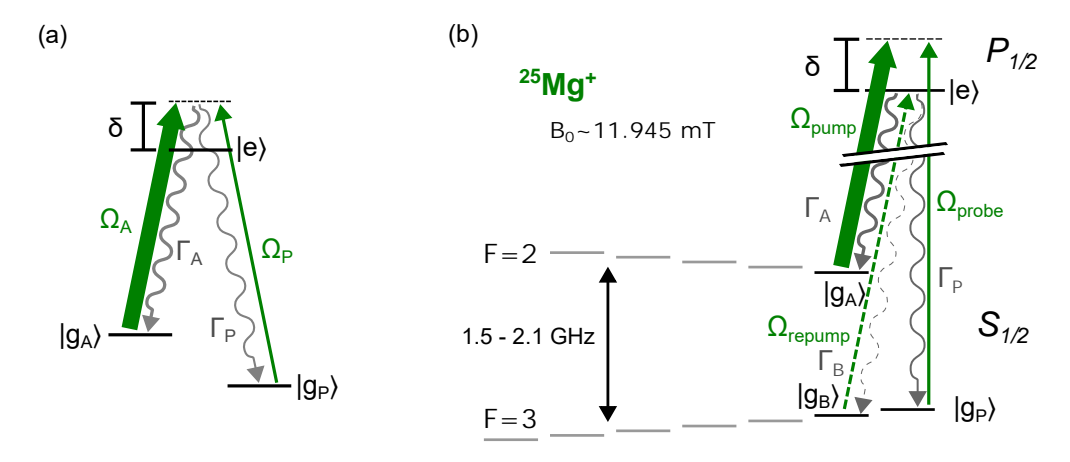


Figure 4.1: (a) shows the typical Λ -configuration for EIT cooling with two ground states, $|g_A\rangle$ and $|g_P\rangle$, and one excited state $|e\rangle$. The transitions $|g_A\rangle \leftrightarrow |e\rangle$ and $|g_P\rangle \leftrightarrow |e\rangle$ are driven with laser beams (green arrows) with on-resonance Rabi rates Ω_A and Ω_P respectively, detuned blue from resonance by δ . The decay rates from $|e\rangle \rightarrow |g_A\rangle$ and $|e\rangle \rightarrow |g_P\rangle$ are given by Γ_A and Γ_P respectively and illustrated by grey wavy arrows. (b) shows the implementation of the modified EIT cooling setup on $^{25}\text{Mg}^+$. For the discussion of the experimental implementation, the Rabi rates are denoted by Ω_{pump} and Ω_{probe} instead of Ω_A and Ω_P , which is used for the theoretical description. Because selection rules for $^{25}\text{Mg}^+$ necessitate the involvement of a third ground state, $|g_B\rangle$, a third (resonant) laser is added to repump this state to $|e\rangle$ with Rabi rate Ω_{repump} , illustrated with the dashed green arrow. The decay to this extra ground state has rate Γ_B and is illustrated by a dashed wavy arrow.

A similar method of EIT cooling with an additional beam of ¹⁷¹Yb⁺ ions has also been proposed [115] and (concurrently with these investigations) demonstrated [112, 113], and recently this modified EIT cooling was implemented on ¹³⁷Ba⁺ as well [116]. Importantly, the latter ion, as well as ⁹Be⁺ and ²⁵Mg⁺, all have complex hyperfine structure that enables the implementation of long-lived, magnetic-field-insensitive ground state qubits [51]. The success of this modified EIT-cooling method enables such ions to be used for both qubits and cooling.

This chapter will begin with Sec. 4.1 which focuses on the theoretical description of EIT cooling in a simple Λ system. Using the laser Hamiltonian Eq. 2.66 and a resulting dressed-state

basis, an alternative way of understanding the EIT cooling process is derived. Next, Sec. 4.2 reviews the master-equation simulations used to model our more complex system. These simulations reveal that one of the most significant barriers to EIT cooling in our system was the axial micromotion present in the apparatus; it was found that micromotion was the strongest contributor to the loss of cooling efficiency, rather than the presence of the third ground state. Finally, the experimental results are presented in Sec. 4.3, including explorations of EIT cooling dynamics with a single 25 Mg⁺ ion; using a single 25 Mg⁺ ion to probe the bandwidth of EIT cooling; cooling mixed-species multi-ion crystals with EIT; and efforts to perform double-EIT cooling in this apparatus.

4.1 EIT Cooling Theory: The Dressed-State Picture

Standard EIT cooling relies on the use of two laser beams, typically one strong "pump" beam and one weak "probe" beam, to dress a three-state system [107, 108]. These three states are usually assumed to be comprised of two ground states (which I will call $|g_A\rangle$ and $|g_P\rangle$) and one excited state $|e\rangle$, forming a Λ system, as shown in Fig. 4.1(a). The three states can also be arranged in a V system or a ladder of states. If the laser beam frequencies and intensities are chosen correctly, the dressed states formed by the system naturally scatter to states with lower energy.

Often, the theory of EIT cooling is derived using optical Bloch equations to arrive at a frequency-dependent scattering spectrum [68, 107]² in which the probe beam is assumed to be negligibly weak compared to the pump beam. By varying the probe beam frequency and calculating the theoretical absorption of this beam, a Fano-like lineshape can be derived in which the transparency feature appears at the frequency corresponding to carrier (motion-preserving) scatter, suppressing it; the absorption at the frequency corresponding to motion-subtracting scatter is enhanced; and motion-increasing scatter is minimally modified from that corresponding to the bare atomic resonances.³ This derivation is conceptually confusing because the calculation is performed by varying the probe beam

²A different derivation in which the Liouvillian is used is described in Ref. [108].

³It should be noted that the whole spectrum pictured in Fig. 4.2 exists centered at the common detuning of both EIT cooling laser beams relative to the original bare atomic absorption peak. Therefore, detuning both beams further will move the whole feature further from the center of the atomic resonance lineshape, suppressing motion-adding scatter. However, similar to resolved-sideband cooling, this comes at the cost of reduced cooling speed.

frequency, but it is held on resonance with the pump beam during the actual EIT cooling process. In reality, the motional sidebands of the ion probe the motion-adding and motion-subtracting sideband frequencies. The approach described in the rest of this section was motivated by this latter fact and relies heavily upon the laser Hamiltonian Eq. 2.66.

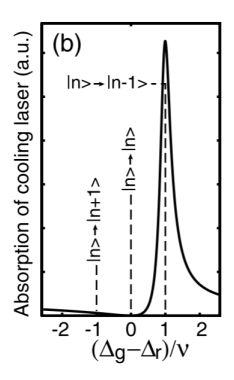


Figure 4.2: The absorption spectrum of EIT is revealed when the probe beam frequency is varied in this figure from Ref. [107]. The horizontal axis is labeled as the difference between the probe beam detuning (Δ_g) and the pump beam detuning (Δ_r) in units of the motion frequency ν . When the EIT cooling condition Eq. 4.10 is satisfied, the absorption peak corresponding to motion-subtracting scatter $(|n\rangle \rightarrow |n-1\rangle)$ is greatly enhanced. The "transparency" feature of EIT is seen in the suppression of the motion-preserving carrier scatter labeled at $|n\rangle \rightarrow |n\rangle$.

Before the rest of this section, a warning to the reader: It was my hope that this calculation would eventually lead to analytic expressions that would be able to inform experimental choices for EIT cooling (what transitions to use, laser beam powers, polarizations, and detunings, etc.), and while a few publications, for example Ref. [108] and the appendix in Ref. [112], appear to outline a similar approach, this exact derivation does not appear in the publications that I am aware of. Unfortunately, the calculations became non-trivial and thus remain incomplete, due to a lack of time during my PhD studies to continue pursuing this. However, in its current state the derivation reveals some interesting facts and provides an alternative way to view the EIT cooling process. In the limits assumed in Refs. [68, 107], some of the same expressions can be recovered, for example the condition for optimal EIT cooling and minimum theoretical achievable motional occupation. I cannot claim any of these interpretations are true with complete certainty but I find these derivations helpful in gaining insight about EIT, and some of them have been verified by simulation (Sec. 4.2.2).

4.1.1 Dressed-State Basis Derivation

All frequencies can be taken as angular frequencies in this derivation unless explicitly specified otherwise. Let the pump and probe laser beams (with Rabi frequencies Ω_A and Ω_P respectively and common detuning from atomic resonance δ) drive transitions between the excited state $|e\rangle$, and ground states $|g_A\rangle$ and $|g_P\rangle$ respectively. As usual with EIT cooling, it is assumed that $\delta \gg \{\Omega_A, \Omega_P, \Gamma\}$, where Γ is the total decay rate of the excited state, and the decay rates Γ_A and Γ_P from $|e\rangle$ to $|g_A\rangle$ and $|g_P\rangle$ respectively satisfy the relation $\Gamma = \Gamma_A + \Gamma_P$.

If only the atomic portion of the EIT Hamiltonian is considered (i.e. without considering motion) the rotating-wave approximation can be applied to write it in the laser frame,⁴ (setting $\hbar = 1$):

$$\hat{H}_{EIT,0} = \delta |g_A\rangle \langle g_A| + \delta |g_P\rangle \langle g_P| + \left(\frac{\Omega_A}{2} |g_A\rangle \langle e| + \frac{\Omega_P}{2} |g_P\rangle \langle e| + h.c.\right). \tag{4.1}$$

Here, a positive value for δ indicates that the laser driving transitions between $|e\rangle$ and the respective state is detuned blue of resonance with the $|g_A\rangle/|g_P\rangle\leftrightarrow|e\rangle$ transition. Because the same value δ appears before both $|g_A\rangle\langle g_A|$ and $|g_P\rangle\langle g_P|$, it is assumed that the two lasers are detuned by the same value, as is true in EIT cooling. Then, defining two generalized Rabi frequencies $\Omega^2 := \Omega_A^2 + \Omega_P^2$, $\tilde{\Omega}^2 := \Omega^2 + \delta^2$ (note that because $\delta \gg \{\Omega_A, \Omega_P\}$, $\tilde{\Omega} \approx \delta$), the eigenstates of Eq. 4.1 are found to be

$$|D\rangle = \frac{\Omega_P |g_A\rangle - \Omega_A |g_P\rangle}{\Omega},$$

$$|B_+\rangle = \frac{\Omega_A |g_A\rangle + \Omega_P |g_P\rangle + (\tilde{\Omega} - \delta) |e\rangle}{\sqrt{2\tilde{\Omega} (\tilde{\Omega} - \delta)}},$$

$$|B_-\rangle = \frac{\Omega_A |g_A\rangle + \Omega_P |g_P\rangle - (\tilde{\Omega} + \delta) |e\rangle}{\sqrt{2\tilde{\Omega} (\tilde{\Omega} + \delta)}}.$$

$$(4.2)$$

I will refer to this set of states as the "dressed-state basis". The state $|D\rangle$ is typically called the

⁴This is a transformation of the form Eq. 2.50; a detailed derivation of a similar Hamiltonian can be found in Ref. [117]. This form is sometimes called the *co-rotating* frame of the lasers because it rotates with both lasers simultaneously.

"dark state" as it only contains components of the two ground states. Both $|B_{+}\rangle$ and $|B_{-}\rangle$ contain components of $|e\rangle$ which implies that the two $|B\rangle$ states will eventually scatter to $|D\rangle$ and will emit photons in this process; these are sometimes referred to as "bright states". Discussion of this scatter or decay process is discussed in detail later in this section (Sec. 4.1.2).

In the dressed-state basis Eq. 4.2, the Hamiltonian 4.1 can be rewritten as

$$\hat{\tilde{H}}_{\text{EIT},0} = \delta |D\rangle \langle D| + \frac{\tilde{\Omega} + \delta}{2} |B_{+}\rangle \langle B_{+}| - \frac{\tilde{\Omega} - \delta}{2} |B_{-}\rangle \langle B_{-}|.$$
(4.3)

The total energy can then be shifted by δ (using $\hat{U} = \mathbb{1}e^{i\delta t}$ in Eq. 2.50, where $\mathbb{1}$ is the identity operator in the dressed-state basis) to clean up the equation:

$$\hat{\tilde{H}}_{EIT,0} = \frac{\tilde{\Omega} - \delta}{2} |B_{+}\rangle \langle B_{+}| - \frac{\tilde{\Omega} + \delta}{2} |B_{-}\rangle \langle B_{-}|.$$

$$(4.4)$$

It can be seen from the two Hamiltonians above that when motion is not considered, there is no transition between any of the states in this basis, since the Hamiltonian is diagonal, and $|D\rangle$ is a steady state solution. This is a mathematical description of the "transparency" feature, or carrier scatter suppression, that is characteristic of EIT cooling.

Now adding a motional degree of freedom (in the Lamb-Dicke regime), it can be seen that the initial Hamiltonian Eq. 4.1 is simply the carrier portion of Eq. 2.66 (with an implied motion identity operator).⁵ For simplicity, the rest of this derivation is performed with only one mode of motion with corresponding annihilation operator \hat{a} and motion frequency ν , which is assumed to satisfy $\nu \ll \delta$. The next (first-order term) in the Lamb-Dicke expansion can then be written (in the frame of the ion motion):

$$\hat{H}_{\text{EIT},1} = \left[i \eta_A \frac{\Omega_A}{2} \left| g_A \right\rangle \left\langle e \right| + i \eta_P \frac{\Omega_P}{2} \left| g_P \right\rangle \left\langle e \right| + h.c. \right] \times \left(\hat{a} e^{-i\nu t} + \hat{a}^{\dagger} e^{i\nu t} \right), \tag{4.5}$$

⁵To be totally precise, the Rabi frequency is slightly modified by the addition of the motion but after applying the Lamb-Dicke expansion, the 0th order term is equal to Eq. 4.1.

where η_A (η_P) is the Lamb-Dicke parameter associated with the projection of the lasers driving the transition $|g_A\rangle \leftrightarrow |e\rangle$ ($|g_P\rangle \leftrightarrow |e\rangle$) along the direction of the mode of motion under consideration. In this case, I define them to be proportional to $k_A \cdot \hat{z}$ ($k_P \cdot \hat{z}$) in such a way that if the two laser beams have projections in opposite directions along \hat{z} , the associated Lamb-Dicke parameters will have opposite sign. Considering this order of the expansion in Lamb-Dicke parameter alone is enough to reveal the main mechanisms of EIT cooling.⁶

In the new basis Eq. 4.2, Hamiltonian Eq. 4.5 is transformed into

$$\hat{H}_{\text{EIT},1} = \left[i \left(\frac{\eta_A - \eta_P}{2} \right) \frac{\sqrt{\tilde{\Omega} - \delta}}{\sqrt{2\tilde{\Omega}}} \frac{\Omega_A \Omega_P}{\Omega} |B_+\rangle \langle D| + i \left(\frac{\eta_A - \eta_P}{2} \right) \frac{\sqrt{\tilde{\Omega} + \delta}}{\sqrt{2\tilde{\Omega}}} \frac{\Omega_A \Omega_P}{\Omega} |B_-\rangle \langle D| + i \left(\frac{\eta_A \Omega_A^2 + \eta_P \Omega_P^2}{2\Omega} \right) |B_-\rangle \langle B_+| + h.c. \right] \times \left(\hat{a}e^{-i\nu t} + \hat{a}^{\dagger}e^{i\nu t} \right).$$
(4.6)

Now, to investigate the transition probabilities involving the addition and subtraction of motion associated with $|D\rangle \to |B_+\rangle$, the total Hamiltonian can be rotated with the unitaries

$$\hat{U}_{\pm} = |D\rangle\langle D| + e^{\pm i\nu t} |B_{+}\rangle\langle B_{+}| + |B_{-}\rangle\langle B_{-}|, \qquad (4.7)$$

where, depending on the sign chosen, either the motion-adding or motion-subtracting transitions will be slowly rotating, as discussed below.

Using the transformation of a Hamiltonian under a unitary (Eq. 2.50) to apply Eq. 4.7 to the sum of the carrier (Eq. 4.4) and first-order-in-Lamb-Dicke-parameter (Eq. 4.6) terms in the dressed-state basis $\hat{\tilde{H}}_{\text{EIT,tot}} = \hat{\tilde{H}}_{\text{EIT,0}} + \hat{\tilde{H}}_{\text{EIT,1}}$, I obtain, after simplification:

$$\hat{\hat{H}}_{\text{tot,r}} = \left[\hat{\hat{H}}_{\text{EIT,0}} - i\hat{U}_{\pm} \left(\partial_t \hat{U}_{\pm}^{\dagger}\right)\right] + \hat{U}_{\pm} \hat{\hat{H}}_{\text{EIT,1}} \hat{U}_{\pm}^{\dagger}. \tag{4.8}$$

The portion in the square brackets has only diagonal components in the dressed-state basis, while the rightmost term has off-diagonal components only. In other words, the term $i\hat{U}_{\pm}\left(\partial_{t}\hat{U}_{\pm}^{\dagger}\right)$ simply modifies the energy of the states as described in $\hat{H}_{\mathrm{EIT},0}$ (Eq. 4.4), while the last term $\hat{U}_{\pm}\hat{H}_{\mathrm{EIT},1}\hat{U}_{\pm}^{\dagger}$

⁶Indeed, standard EIT cooling is often quoted as being able to achieve motional occupations of order η .

describes transitions between the dressed states. That this latter term only appears after considering the motion (first-order Lamb-Dicke parameter expansion in Eq. 2.66) and all parts of that term are scaled by η_A or η_P , meaning that the cooling rate is scaled by the Lamb-Dicke parameters as expected.

Looking at the diagonal term in Eq. 4.8 first:

$$\hat{\tilde{H}}_{\text{EIT},0} - i\hat{U}_{\pm}(\partial_t \hat{U}_{\pm}^{\dagger}) = \left(\frac{\tilde{\Omega} - \delta}{2} \mp \nu\right) |B_{+}\rangle \langle B_{+}| - \frac{\tilde{\Omega} + \delta}{2} |B_{-}\rangle \langle B_{-}|. \tag{4.9}$$

Both terms in the coefficient of $|B_{+}\rangle\langle B_{+}|$ are fairly small values for standard EIT parameters (recall $\tilde{\Omega} \approx \delta$), while the coefficient of $|B_{-}\rangle\langle B_{-}|$ is much larger. A large coefficient can be interpreted physically as the transition is extremely off resonant or fast rotating (with respect to $|D\rangle$ which is stationary in this frame). Therefore, for the rest of this derivation terms containing $|B_{-}\rangle$ are dropped.

It can also be seen here that when

$$\frac{\tilde{\Omega} - \delta}{2} = \nu,\tag{4.10}$$

the coefficient of $|B_{+}\rangle\langle B_{+}|$ is equal to zero when \hat{U}_{+} is used — $|B_{+}\rangle$ rotates at the same rate as $|D\rangle$. Interestingly, Eq. 4.10 is exactly the EIT cooling condition: the relationship that should be satisfied for optimal cooling of a mode with frequency ν . As will be seen below, when Eq. 4.10 is satisfied, the rate of the motion-subtracting transition is also maximized.

Now, the term responsible for driving transitions between the dressed-basis states in Eq. 4.8 can be resolved (again dropping terms with $|B_{-}\rangle$):

$$\hat{U}_{\pm}\hat{\tilde{H}}_{\mathrm{EIT},1}\hat{U}_{\pm}^{\dagger} = i\left(\frac{\eta_{A} - \eta_{P}}{2}\right)\frac{\sqrt{\tilde{\Omega} - \delta}}{\sqrt{2\tilde{\Omega}}}\frac{\Omega_{A}\Omega_{P}}{\Omega}\left|B_{+}\right\rangle\left\langle D\right| \times \left(\hat{a}e^{i(\pm\nu - \nu)t} + \hat{a}^{\dagger}e^{i(\pm\nu + \nu)t}\right) + h.c. \quad . \tag{4.11}$$

Therefore, the simplified Hamiltonian probing the motion-adding and motion-subtracting

sidebands of the EIT Hamiltonian in the dressed-state basis is:

$$\hat{H}_{\text{tot,r}} = \left(\frac{\tilde{\Omega} - \delta}{2} \mp \nu\right) |B_{+}\rangle \langle B_{+}|
+ \left[i\left(\frac{\eta_{A} - \eta_{P}}{2}\right) \frac{\sqrt{\tilde{\Omega} - \delta}}{\sqrt{2\tilde{\Omega}}} \frac{\Omega_{A}\Omega_{P}}{\Omega} |B_{+}\rangle \langle D| \times \left(\hat{a}e^{i(\pm\nu - \nu)t} + \hat{a}^{\dagger}e^{i(\pm\nu + \nu)t}\right) + h.c.\right].$$
(4.12)

Because $|B_{+}\rangle$ contains components of $|e\rangle$, it can naturally decay to $|D\rangle$ which only contains groundstate components. For the purpose of interpretation, $|D\rangle$ is a ground state that can only be left via a motion altering transition, while $|B_{+}\rangle$ can only be reached by a motion altering transition but then can decay back to $|D\rangle$ without further changes of the motion.

Taking the upper sign (associated with rotation unitary \hat{U}_+), Eq. 4.12 reveals that when the EIT-cooling condition is satisfied, the transition is on resonance (since the diagonal $|B_+\rangle$ term reduces to zero)⁷ and the interaction term drives $|D\rangle \rightarrow |B_+\rangle$ at the loss of one motional quantum through \hat{a} .⁸ The cycle is completed when $|B_+\rangle$ decays to $|D\rangle$ through photon emission (discussed in the next section, Sec. 4.1.2). It can be seen that the absorption step is the main contributor to the EIT cooling mechanism in this analysis: the motion-subtracting absorption is resonant in this frame. On the other hand, taking the lower sign in Eq. 4.12 (associated with \hat{U}_-) reveals that the motion-adding interaction $|B_+\rangle \langle D| \hat{a}^{\dagger}$ is slightly off resonance (with associated energy 2ν on the term $|B_+\rangle \langle B_+|$ if the EIT cooling condition is satisfied).⁹ Both interaction terms have the same bare Rabi frequency.

Through this analysis I arrive at a similar conclusion to that obtained from the absorption spectrum picture — that motion-subtracting transitions are much more likely to be driven in the EIT cooling process, while motion-adding scatter is still possible but less likely. Moreover, as stated

⁷This Hamiltonian can be compared to that of a simple Rabi oscillation: when there are nonzero diagonal terms present, the Rabi drive frequency can be seen as off-resonant, and transitions will be driven less efficiently.

⁸While there is also an associated \hat{a}^{\dagger} term, it is rotating at $e^{2i\nu t}$ so it can be removed through an application of the rotating-wave approximation. This application of the rotating-wave approximation is somewhat weakly justified, since many energies are of the same scale as the rotation energies, but if terms are to be compared relative to each-other, it is undoubtedly true that \hat{a} dominates over $\hat{a}^{\dagger}e^{2i\nu t}$ in this case.

⁹This also straightforwardly reveals that if the sign of δ is the opposite (which would happen if the laser is reddetuned instead of blue-detuned), then the motion-adding interaction would be resonant while the motion-subtracting interaction would be less resonant, resulting in EIT heating! Of course, this is analogous to simply flipping the EIT cooling absorption spectrum.

earlier, rotating into the dressed-state picture naturally removes the possibility of motion-preserving absorption.¹⁰ If the EIT cooling condition is not fully satisfied (for example, when considering multiple modes along the same motional axis where the cooling is either optimized for only one mode or none of the modes in particular), the motion-subtracting sideband will be somewhat off-resonant, but still more resonant than the motion-adding sideband, according to the equations above. Concretely, the motion-subtracting sideband will be off resonance by $\left|\frac{\tilde{\Omega}-\delta}{2}-\nu\right|$ and the motion-adding sideband will be off resonance by $\left|\frac{\tilde{\Omega}-\delta}{2}+\nu\right|$; because $\frac{\tilde{\Omega}-\delta}{2}$ is positive, the latter will be greater than the former.

It can also be seen that, similar to Raman sideband cooling, a non-zero Δk (wavevector) projection is necessary for EIT cooling: the Lamb-Dicke parameters in this derivation were earlier defined to have a sign corresponding to the relative projection along the axis of the motional mode; the coefficient containing $(\eta_A - \eta_P)$ would be close to zero if the two laser fields were similar in frequency and copropagating, lessened if they had projection along the motion axis of the same sign, and is the greatest if the beams are counterpropagating along the motion axis of interest.

4.1.2 Photon Emission/Collapse Operators in the Dressed-State Basis

Atomic state decay or photon emission plays an important role in the process, enabling subsequent absorption events (favoring loss of motion) to take place. In the Lamb-Dicke regime, the decay process is most likely to leave the motion of the ion unchanged, while the next most likely process is proportional to the Lamb-Dicke parameter and can either increase or decrease the motion by one quantum. Scatter in the dressed-state basis can be treated as a two-step process of absorption and decay that returns $|D\rangle$ to $|D\rangle$. Since the absorption process is already revealed to be proportional to the Lamb-Dicke parameters η_A and η_P in the previous section, decay that further changes the motion of the ion will be of second order in the Lamb-Dicke parameter¹¹ in the

 $^{^{10}}$ Motion-preserving *scatter* is still possible via a motion-changing absorption and scatter that changes motion in the opposite direction, but this is suppressed compared to motion-changing absorption and carrier scatter by a factor proportional to η . Photon emission is further discussed in Sec. 4.1.2.

¹¹This is in contrast to the process for Doppler cooling, where carrier absorption is allowed, meaning there are two paths that are of first order in Lamb-Dicke parameter (carrier absorption and sideband decay; and sideband

Hamiltonian (and fourth order in probability or rate). Therefore, only carrier decay is considered in this section.

In the process described in the previous section, $|B_+\rangle$ was assumed to simply just decay to $|D\rangle$ due to its $|e\rangle$ component. While this is true overall, the role that decay plays in this process is complicated. Here, this subtlety is discussed, as well as some questions that arise from the form this operator takes. This begins with the introduction of collapse operators. These are non-unitary operators and result from the interaction of the quantum system under consideration with its environment, which is not a state that is "tracked" in the calculation. This can be used to represent effects such as anomalous heating or, as is done here, emission of a photon. In the latter case, the collapse operators can be derived by first considering both the ion and (emitted) photon as part of a whole system. From there, tracing the photon states out in order to consider the ion states only results in the appearance of the non-unitary collapse operator [118].

The master equation for multiple collapse operators can be written [118]:

$$\dot{\hat{\rho}} = -i\left[\hat{H}, \hat{\rho}\right] + \frac{1}{2} \sum_{i} \left[2\hat{C}_{i}\hat{\rho}\hat{C}_{i}^{\dagger} - \hat{\rho}\hat{C}_{i}^{\dagger}\hat{C}_{i} - \hat{\rho}\hat{C}_{i}\hat{C}_{i}^{\dagger}\right], \tag{4.13}$$

where $\hat{\rho}$ denotes the density operator of the system, the dot in $\dot{\hat{\rho}}$ denotes a time derivative, \hat{H} is the Hamiltonian of the system, and \hat{C}_i are the collapse operators.

For the Λ EIT cooling system under consideration, let Γ_A (Γ_P) denote the decay rate of the $|e\rangle \to |g_A\rangle$ ($|e\rangle \to |g_P\rangle$) transition in the standard (not dressed) basis. Then, the collapse operators are given by

$$\hat{C}_A = \sqrt{\Gamma_A} |g_A\rangle \langle e|, \qquad \hat{C}_P = \sqrt{\Gamma_P} |g_P\rangle \langle e|, \qquad (4.14)$$

so that in the standard atomic basis,

$$\dot{\hat{\rho}} = -i \left[\hat{H}_{\text{tot}}, \hat{\rho} \right] + \frac{\Gamma_A}{2} \left[2 \left| g_A \right\rangle \left\langle e \right| \hat{\rho} \left| e \right\rangle \left\langle g_A \right| - \hat{\rho} \left| e \right\rangle \left\langle e \right| - \hat{\rho} \left| g_A \right\rangle \left\langle g_A \right| \right],
+ \frac{\Gamma_P}{2} \left[2 \left| g_P \right\rangle \left\langle e \right| \hat{\rho} \left| e \right\rangle \left\langle g_P \right| - \hat{\rho} \left| e \right\rangle \left\langle e \right| - \hat{\rho} \left| g_P \right\rangle \left\langle g_P \right| \right]$$
(4.15)

where \hat{H}_{tot} is the EIT-cooling Hamiltonian to first order in the Lamb-Dicke parameter in the standard basis.

Let \hat{U}_b be the change-of-basis matrix from the standard basis to the dressed-state basis defined by Eq. 4.2. It can be shown that all operators in the master equation Eq. 4.13 transform straightforwardly under $\hat{\tilde{\rho}} = \hat{U}_b^{\dagger} \hat{\rho} \hat{U}_b$, $\hat{\tilde{C}}_i = \hat{U}_b^{\dagger} \hat{C}_i \hat{U}_b$, etc. Applying this transformation to the photon collapse operators Eq. 4.14:

$$\hat{C}_{A} = \sqrt{\Gamma_{A}} \left[-\frac{\sqrt{\tilde{\Omega} - \delta}}{\sqrt{2\tilde{\Omega}}} \frac{\Omega_{P}}{\Omega} |D\rangle \langle B_{+}| + \frac{\sqrt{\tilde{\Omega} + \delta}}{\sqrt{2\tilde{\Omega}}} \frac{\Omega_{P}}{\Omega} |D\rangle \langle B_{-}| + \frac{\Omega_{A}}{2\tilde{\Omega}} |B_{+}\rangle \langle B_{+}| - \frac{\tilde{\Omega} + \delta}{2\tilde{\Omega}} \frac{\Omega_{A}}{\Omega} |B_{+}\rangle \langle B_{-}| + \frac{\tilde{\Omega} - \delta}{2\tilde{\Omega}} \frac{\Omega_{A}}{\Omega} |B_{-}\rangle \langle B_{+}| - \frac{\Omega_{A}}{2\tilde{\Omega}} |B_{-}\rangle \langle B_{-}| \right],$$

$$\hat{C}_{P} = \sqrt{\Gamma_{P}} \left[-\frac{\sqrt{\tilde{\Omega} - \delta}}{\sqrt{2\tilde{\Omega}}} \frac{\Omega_{A}}{\Omega} |D\rangle \langle B_{+}| + \frac{\sqrt{\tilde{\Omega} + \delta}}{\sqrt{2\tilde{\Omega}}} \frac{\Omega_{A}}{\Omega} |D\rangle \langle B_{-}| + \frac{\Omega_{P}}{2\tilde{\Omega}} |B_{+}\rangle \langle B_{+}| - \frac{\tilde{\Omega} + \delta}{2\tilde{\Omega}} \frac{\Omega_{P}}{\Omega} |B_{+}\rangle \langle B_{-}| + \frac{\tilde{\Omega} - \delta}{2\tilde{\Omega}} \frac{\Omega_{P}}{\Omega} |B_{-}\rangle \langle B_{+}| - \frac{\Omega_{P}}{2\tilde{\Omega}} |B_{-}\rangle \langle B_{-}| \right].$$

$$(4.16)$$

Ideally, I would now proceed to find decay rates Γ_+ describing decay $|B_+\rangle \to |D\rangle$ and Γ_- describing decay $|B_-\rangle \to |D\rangle$. However, the expressions above have forms that are difficult to interpret¹² in the dressed-state basis: there are terms with coefficients of $|B_+\rangle \langle B_+|$ or $|B_-\rangle \langle B_-|$ and transitions between the $|B_+\rangle$ and $|B_-\rangle$ states, calling into question whether or not $|B_-\rangle$ can truly be simply neglected as done in the previous section.¹³ Unfortunately, many terms in Eq. 4.16 cannot be discarded without changing the dynamics, as seen in simulation (Sec. 4.2.2).

If all the terms except those containing $|D\rangle\langle B_+|$ were to be discarded, it can be shown that

¹²Beyond the fact that the decay operators between the standard basis states result in the possibility for a state to decay to itself, since some dressed-basis states contain both components of excited and ground states.

 $^{^{13}}$ One argument in favor of allowing the discarding of terms associated with $|B_{-}\rangle$ can be seen by examining the terms in Eq. 4.16 carefully. Because $\left(\tilde{\Omega}+\delta\right)$ is large and $\left(\tilde{\Omega}-\delta\right)$ is small, the terms sending $|B_{-}\rangle\rightarrow|B_{+}\rangle$ are relatively large while the inverse transition through this modified decay operator is much less likely. Moreover, the transition $|B_{-}\rangle\rightarrow|D\rangle$ is fairly rapid compared to $|B_{+}\rangle\rightarrow|D\rangle$; this appears to suggest that $|B_{-}\rangle$ has a tendency to decay into the main EIT-cooling manifold with relatively high likelihood and therefore can possibly be neglected in calculations.

the two operators Eq. 4.16 may be substituted for a single operator in Eq. 4.13,

$$\hat{C}_{\text{eff}} = \sqrt{\Gamma_{\text{eff}}} |D\rangle \langle B_{+}|, \qquad (4.17)$$

where

$$\Gamma_{\text{eff}} = \frac{\tilde{\Omega} - \delta}{2\tilde{\Omega}} \frac{\Gamma_P \Omega_A^2 + \Gamma_A \Omega_P^2}{\Omega^2}.$$
(4.18)

For the next section, I assume this approximation to be true (in order to make further calculations possible ¹⁴).

4.1.3 Using Rate Equations to Calculate Minimum Steady-State Occupation

In general, the steady-state occupation of a system that has Fock-state-number-dependent transition rates (rates resulting from dynamics containing \hat{a} and \hat{a}^{\dagger}) may be calculated as a competition between competing rates [68, 107, 108]:

$$\langle n_{ss} \rangle = \frac{A_+}{A_- - A_+},\tag{4.19}$$

where A_{+} is the rate of motion-adding scatter and A_{-} is the rate of motion-subtracting scatter. As mentioned in the previous section, the lowest-order-in-Lamb-Dicke-parameter scattering process in EIT cooling in the dressed-state basis is of first order in the Lamb-Dicke parameter (with rates that are second order in the Lamb-Dicke parameter), where absorption of a photon changes the motion and emission does not change the motion.

Assuming that $|B_{-}\rangle$ can be neglected due to its large detuning from the other states, the

¹⁴Unfortunately, if such an approximation is not made, the decay operator cannot be reduced in this manner, and some truly bizarre terms appear later in this derivation, even if terms related to $|B_-\rangle$ are discarded. For example, I end up with a term linear in Lamb-Dicke parameter in Eq. 4.27. This term, $(\eta_A - \eta_P)$, is highly problematic, since the sign of these Lamb-Dicke parameters is assumed to come from the projection along an arbitrary direction corresponding to the motion axis (as defined earlier). Flipping the direction of this motion axis by 180 degrees should not affect the dynamics, yet it would flip the sign of $(\eta_A - \eta_P)$, changing the estimate of steady-state motional occupation, which it physically should have no effect on.

above can be calculated by:

$$A_{+} \approx \Gamma_{+} (\rho_{B})_{\text{MA}}, \qquad A_{-} \approx \Gamma_{+} (\rho_{B})_{\text{MS}},$$

$$(4.20)$$

where $(\rho_B)_{\mathrm{MS}}$ and $(\rho_B)_{\mathrm{MA}}$ are the probabilities of the $|B_+\rangle$ state occurring due to being excited on the motion-subtracting and motion-adding sidebands respectively¹⁵ described by Eq. 4.12, and Γ_+ is the decay rate from $|B_+\rangle \to |D\rangle$ on the carrier transition. For the remainder of this calculation, I will use Γ_{eff} as defined in Eq. 4.18 as an approximation of Γ_+ .

In order to make the notation simpler, I define:

$$\epsilon := \frac{\tilde{\Omega} - \delta}{2\tilde{\Omega}},\tag{4.21}$$

$$\Omega_0 := \frac{\Omega_A \Omega_P}{\Omega},\tag{4.22}$$

$$\Gamma_0 := \left[\frac{\Omega_P^2}{\Omega^2} \Gamma_A + \frac{\Omega_A^2}{\Omega^2} \Gamma_P \right], \tag{4.23}$$

where if the EIT cooling condition is satisfied, then $\epsilon = \frac{\nu}{\tilde{\Omega}} \approx \frac{\nu}{\delta}$.

With the above definitions,

$$\Omega_{\text{eff}} = i(\eta_A - \eta_P)\sqrt{\epsilon}\Omega_0, \qquad \Gamma_{\text{eff}} = \epsilon\Gamma_0,$$
(4.24)

where Ω_{eff} is the coefficient of $|B_{+}\rangle\langle D|$ in Eq. 4.12, defined so that $\frac{\Omega_{\text{eff}}}{2}$ would appear as the coefficient in the equation.

Finally, it is assumed that the transition is not saturated, ¹⁶ and that the best EIT cooling results from the EIT cooling condition (Eq. 4.10) is satisfied, as this maximizes the motion-subtracting absorption rate. From this, the minimum steady-state average occupation can be calculated using

¹⁵In order to make this approximation, it is necessary to assume (in addition to neglecting state $|B_-\rangle$) that such a small amount of the population is in $|B_+\rangle$ at any given time that the motion-adding and motion-subtracting processes can be treated as unaffected by eachother. This may not be true, especially because the motion-subtracting absorption process is significantly enhanced during the EIT cooling process, potentially causing the probability represented by $(\rho_B)_{\rm MA}$ to be an overestimate. This may be true, however, if $\Omega_P \to 0$, which would slow down the process so that the population in $|B_+\rangle$ becomes infinitesimally small.

¹⁶Again, this is also assumed when writing the two excited state populations independently in Eq. 4.20.

an equation for steady-state excited population for $(\rho_B)_{\text{MA,MS}}$ [119]:

$$\langle n_{ss} \rangle_{\min} = \frac{A_{+}}{A_{-} - A_{+}}$$

$$= \frac{\Gamma_{\text{eff}} (\rho_{B})_{\text{MA}}}{\Gamma_{\text{eff}} (\rho_{B})_{\text{MS}} - \Gamma_{\text{eff}} (\rho_{B})_{\text{MA}}}$$

$$= \frac{\frac{s/2}{1+s+(2\delta_{\text{eff},\text{MA}}/\Gamma_{\text{eff}})^{2}}}{\frac{s/2}{1+s+(2\delta_{\text{eff},\text{MS}}/\Gamma_{\text{eff}})^{2}} - \frac{s/2}{1+s+(2\delta_{\text{eff},\text{MA}}/\Gamma_{\text{eff}})^{2}}}, \qquad (\delta_{\text{eff},\text{MS}} = 0)$$

$$= (1+s) \left(\frac{\Gamma_{\text{eff}}}{2\delta_{\text{eff},\text{MA}}}\right)^{2},$$

where $\delta_{\rm eff,MS}$ and $\delta_{\rm eff,MA}$ are the values associated with $|B_+\rangle\langle B_+|$ in Eq. 4.12 on the motionsubtracting and motion-adding (upper and lower signs, respectively) transitions, so that $\delta_{\rm eff,MS} = 0$ due to the EIT cooling condition being satisfied, and

$$s = \frac{2 |\Omega_{\text{eff}}|^2}{\Gamma_{\text{eff}}^2}$$

$$= 2 (\eta_A - \eta_P)^2 \frac{\tilde{\Omega}}{\nu} \left(\frac{\Omega_A \Omega_P \Omega}{\Omega_P^2 \Gamma_A + \Omega_A^2 \Gamma_P} \right)^2.$$
(4.26)

In some cases, s can be quite small, for example if $\Omega_P \ll \Omega_A$ (or vice versa).¹⁷ However, in most practical cases $s \gtrsim 1$.

Then, Eq. 4.25 can be rewritten:

$$\langle n_{ss}\rangle_{\min} = \left[1 + 2\left(\eta_A - \eta_P\right)^2 \frac{\tilde{\Omega}}{\nu} \left(\frac{\Omega_A \Omega_P \Omega}{\Omega_P^2 \Gamma_A + \Omega_A^2 \Gamma_P}\right)^2 \right] \frac{\Gamma^2}{(4\tilde{\Omega})^2} \left(\frac{\Omega_P^2 \Gamma_A + \Omega_A^2 \Gamma_P}{\Omega^2 \Gamma}\right)^2. \tag{4.27}$$

In the limit $\frac{\Omega_P}{\Omega_A} \to 0$ ($\Omega_A \gg \Omega_P$, as assumed in Refs. [68, 107]), the above can be reduced to the expression for minimum steady-state occupation from Refs. [68, 107]:

$$\langle n_{ss} \rangle_{\min} \ge \frac{\Gamma_P^2}{(4\tilde{\Omega})^2} \approx \frac{\Gamma_P^2}{(4\delta)^2}.$$
 (4.28)

¹⁷Practically, this is undesirable, because if Ω_P is excessively small, cooling will become very slow, and the heating rate (which is not considered here) will increase the final temperature. s also contains a factor of $(\eta_A - \eta_P)^2$, making it dependent on the ion species and wavelength used, in addition to the motion frequency.

As can be seen from the term that is added to 1 in the square brackets in Eq. 4.27, the next-order correction is likely one of second order in the Lamb-Dicke parameters.

4.1.4 Calculating Cooling Rate and EIT Cooling Bandwidth

By assuming that the EIT cooling condition is satisfied, the optimal theoretical steady-state cooling rate of a mode can be found by

$$-(A_{-} - A_{+}) = \Gamma_{\text{eff}} ((\rho_{B})_{\text{MA}} - (\rho_{B})_{\text{MS}})$$

$$= -\frac{8\nu^{2}s}{\Gamma_{\text{eff}}} \frac{1}{(1+s)\left(1+s + \left(\frac{4\nu}{\Gamma_{\text{eff}}}\right)^{2}\right)}.$$
(4.29)

Further simplification depends on the order of magnitude of s, therefore, I will leave the cooling rate in the form above.

In order to calculate the bandwidth of frequencies over which cooling will be effective, a bound can be set, for example, following Ref. [112], by finding the frequencies for which the average motional temperature $\langle n_{ss} \rangle$ can be cooled to ~ 1 . First, the frequency $\nu_0 \left(:= \frac{\tilde{\Omega} - \delta}{2} \right)$ is defined as the frequency for which EIT cooling is optimal. Next, the bandwidth is defined to be the range of frequencies over which EIT cooling can achieve $\langle n_{ss} \rangle \leq 1$ around the frequency ν_0 , so that cooling is effective for modes with frequencies between $(\nu_0 - \nu_-, \nu_0 + \nu_+)$.

After performing a calculation similar to that in Eq. 4.25 and simplifying, the following expression is obtained for the steady state average occupation for a mode of frequency $\nu_0 + \nu_\Delta$:

$$\langle n_{ss} \rangle (\nu_{\Delta}) = \left[1 + s + \left(\frac{2\nu_{\Delta}}{\Gamma_{\text{eff}}} \right)^2 \right] \frac{\Gamma_{\text{eff}}^2}{(4\nu_0 + 2\nu_{\Delta})^2 - (2\nu_{\Delta})^2}. \tag{4.30}$$

The main difference between this calculation and Eq. 4.25 is that the coefficients of $|B_+\rangle\langle B_+|$ (i.e. $\delta_{\rm eff,MS}$ and $\delta_{\rm eff,MA}$) depend on ν_Δ : for any given mode with frequency $\nu=\nu_0+\nu_\Delta$, $\delta_{\rm eff,MS}=\nu_0-\nu=\nu_\Delta$ and $\delta_{\rm eff,MS}=\nu_0+\nu=2\nu_0+\nu_\Delta$.

Setting the condition $\langle n_{ss} \rangle = 1$ in Eq. 4.30 to solve for ν_{\pm} yields a quadratic relation for ν_{Δ}

which can be solved to yield

$$\nu_{\Delta,bandwidth} = 2\nu_0 \pm \sqrt{8\nu_0^2 - \frac{1}{4}\Gamma_{eff}^2(1+s)}.$$
 (4.31)

Again taking the limit $\frac{\Omega_P}{\Omega_A} \to 0$ and adding $\Gamma_A \to 0$ (which is also assumed in Ref. [107]) causes $\Gamma_{eff} \to 0$, allowing to simplify:

$$\nu_{-} = 2(1 - \sqrt{2})\nu_{0}, \qquad \qquad \nu_{+} = 2(1 + \sqrt{2})\nu_{0}$$

$$(4.32)$$

which gives the range of frequencies that can be cooled to $\langle n_{ss} \rangle \leq 1$ as $\nu_0 + (-0.83, 4.83)\nu_0 = (0.17, 5.83)\nu_0$. The knowledge that this cooling bandwidth is extremely asymmetric may be useful, as it suggests that if multiple modes are to be cooled simultaneously, the frequency at which optimal cooling occurs should not be set at the middle of the desired range, but rather closer towards the lower part of the frequency range. Moreover, this bandwidth can be seen to scale directly with the frequency that is most optimally cooled (ν_0) ; if the modes to be cooled have a higher frequency overall, the range of frequencies around ν_0 that can be cooled is larger as well.¹⁹

Anomalous heating (diffusion due to electric field noise) can also be included by writing $A_- \to A_- + H_-$ and $A_+ \to A_+ + H_+$.²⁰ This gives the more complex expression

$$\langle n_{ss} \rangle = \left[1 + s + \left(\frac{2\nu_{\Delta}}{\Gamma_{eff}} \right)^{2} \right] \frac{A_{+} + \frac{H_{+}}{\Gamma_{eff}}}{A_{+} \frac{(4\nu + 2\nu_{\Delta})^{2} - (2\nu_{\Delta})^{2}}{\Gamma_{eff}^{2}} + \frac{H_{-} - H_{+}}{\Gamma_{eff}} \left(1 + s + (2\nu_{\Delta})^{2} \right)}, \tag{4.33}$$

which can be solved numerically.

¹⁸While this is perhaps unexpected, the asymmetry is evident if one examines the absorption spectrum; the Fano-like peak that represents motion-subtracting scatter has a fairly long tail.

¹⁹Note that according to the EIT condition Eq. 4.10, increasing ν_0 for a fixed detuning δ requires an increase in the overall laser power.

 $^{^{20}}$ By having both H_{-} and H_{+} I acknowledge that the electric field noise is a random displacement of the motion state and not necessarily only motion increasing.

4.1.5 Summary of Dressed-State Derivations

In this section, I have derived some relations based on the dressed-state basis, under many assumptions. While these assumptions hold very loosely or have questionable validity in certain applications, some intuition on the EIT cooling process and indeed some relations matching the current literature can be extracted. The main points that hold for me from this exploration are:

- (1) The "carrier" portion of the laser Hamiltonian (as viewed from Eq. 2.66) establishes the dressed-state basis, which naturally eliminates carrier transitions to first order in Lamb-Dicke parameter; suppression of carrier absorption is one of the hallmarks of EIT cooling. One of the dressed states (labeled $|B_{-}\rangle$ in this thesis) is very off-resonant from the other two dressed states and plays a minimal role in the cooling, as illustrated in Fig. 4.3.
- (2) The first-order Lamb-Dicke terms in the expansion of the laser Hamiltonian (Eq. 2.66) become coupling terms between the dressed-state basis states when transformed into the dressed-state basis. As terms that are of first order in the Lamb-Dicke parameter, they are necessarily motion-changing. While the motion-adding and motion-subtracting sidebands that drive transitions between the dark state and the (slowly rotating) bright state |D⟩ → |B₊⟩ have the same "Rabi frequency" coefficient (Eq. 4.12), the motion-subtracting sideband is on-resonance if the EIT cooling condition is satisfied,²¹ and the motion-adding sideband is off-resonant. This yields an asymmetry in the likelihood of either transition being driven, strongly favoring the motion-subtracting scatter, analogous to what is shown by the scattering spectrum (Fig. 4.2).
- (3) Photon emission $|B_{+}\rangle \rightarrow |D\rangle$ is necessary to complete the process after the excitation described in the previous point. However, the math concerning photon emission (Sec. 4.1.2) is difficult to interpret and has unusual forms in the dressed-state basis.

²¹If the EIT cooling condition is not satisfied, as long as the detuning δ from the excited state is blue of resonance with the excited state (as illustrated in Fig. 4.1(a)), the motion-subtracting sideband should be more resonant than the motion-adding one for a certain range of motion frequencies, leading to an overall cooling effect. This is what enables EIT cooling to have a large bandwidth.

(4) Some expressions, such as the EIT cooling condition and the cooling limit (under certain assumptions) can be matched with current literature.

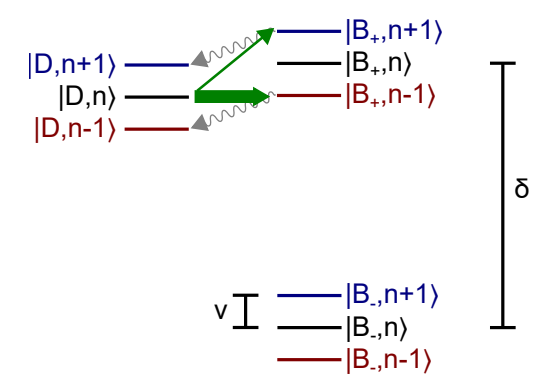


Figure 4.3: The main transitions responsible for EIT cooling as viewed in the dressed-state basis are shown above. The energy between Fock states is given by the motion frequency ν (when \hbar is set to 1) and the energy difference between $|B_{+}\rangle$ and $|B_{-}\rangle$ is δ , the EIT cooling detuning of the system. The illustrated situation shows the energies when the EIT cooling condition is satisfied; $|D, n\rangle$ is has the same energy as $|B_{+}, n-1\rangle$, where the left part of the ket denotes the dressed internal atomic state and the right part denotes the motion state, and n is the Fock number. Carrier transitions are not allowed, and motion-changing transitions starting from $|D, n\rangle$ are illustrated. Because of the higher likelihood due to the resonance in energy, the motion-subtracting transition $|D, n\rangle \rightarrow |B_{+}, n-1\rangle$ is illustrated with a thicker green arrow than the motion-subtracting transition $|D, n\rangle \rightarrow |B_{+}, n+1\rangle$. The following carrier decay is illustrated with grey wavy lines. No transitions to or from $|B_{-}\rangle$ states are shown because it is far off-resonant in energy.

Finally, it should be noted that all derivations in this section were performed considering only the effects that are of first-order in Lamb-Dicke parameter. Higher-order terms could further modify the dynamics; for example, a motion-adding absorption followed by motion-subtracting emission will be a second-order-in-Lamb-Dicke effect but will result in an overall motion-preserving scatter.

The theory presented in this section is incomplete and requires a lot more work to be presented outside an experimentalist's graduate thesis. As stated in the beginning of the section, it was my hope that this exploration would eventually lead to expressions that could inform good experimental choices, especially for situations outside the assumptions typically made during EIT cooling, such as in the regime where $\Omega_A \approx \Omega_P$, as in Ref. [111], and provide higher-order corrections (for example, those proportional to the Lamb-Dicke parameter) to theoretical expressions such as the cooling speed or the cooling limit. Extending it even further to a tripod-EIT situation as is applicable to the

experiments in this thesis is another goal that I had in mind when initially pursuing this derivation, but is now seen to be much beyond the scope of my graduate studies.

4.2 EIT Cooling Simulations

As presented in Sec. 4.1, the analytic expressions for EIT cooling are difficult to obtain beyond what has already been derived in publications. Moreover, in order to model our experimental system, further modifications to the Hamiltonian are required: the addition of a third state, and then the effect of micromotion. Therefore, I decided to use the Quantum Toolbox in Python (QuTiP [120]) to simulate EIT cooling in our system. Only one dimension and one mode was considered in this simulation, as it became apparent that the main benefit of the simulation would be to reconcile the effects of micromotion rather than simulate multiple modes, and therefore the code was developed primarily for the purpose of simulating a system with micromotion. The effects of polarization impurity were briefly considered in the beginning of the investigation, but this error source was later removed because the simulation became too complex and time-consuming; initial results indicated that it caused only a small effect compared to micromotion.

4.2.1 Description of EIT Cooling Simulation

Most simulations were completed with either the mesolve (master equation solver) or, more rarely, the steadystate (steady state solver) function in QuTiP [120]. The simulation begins with a Breit-Rabi calculation of the energy eigenstates and eigenvalues in 25 Mg⁺ at 11.945 mT²² in the absence of laser fields and selects a subset of these states to "keep" in the simulation; most often these are the $|2,2\rangle$, $|3,3\rangle$ and (when modeling EIT with three ground states) $|3,2\rangle$ in 2 S_{1/2} and $|3,3\rangle$ in 2 P_{1/2}. States in 2 P_{3/2} were considered to be too far away in frequency to be involved. These states were stored as custom c_state objects whose main purpose was to calculate proper branching ratios and store the detuning values of laser frequencies. Otherwise, they effectively function as

 $^{^{22}}$ A few initial simulations were also performed at low field (approximately 0.1 mT) and EIT cooling appeared to work for 25 Mg $^+$ at that field as well.

regular quantum states in QuTiP.

The branching ratios (as a fraction of unity) from $^2P_{1/2}|3,3\rangle$ to $^2S_{1/2}|3,3\rangle$, $|2,2\rangle$, and $|2,3\rangle$ at a field of 11.945 mT were calculated to be 0.333, 0.514, and 0.153 respectively (the total decay rate of the excited state is 41.3 MHz).

The lasers were coded as custom c_{laser} objects that mainly function to keep track of a matrix that indicates which c_{states} are coupled by each laser, an on-resonance Rabi frequency for the laser interaction, the detuning of the laser from resonance with the coupled states, and the Lamb-Dicke parameter of the laser (with sign to indicate the projection). When micromotion was considered, more c_{laser} objects would be added with different frequencies according to the order n of the micromotion and powers scaled relative to the initial laser which was treated as the carrier, according to the nth Bessel function of the micromotion modulation index (Eq. 2.75) [75].

The simulated Hamiltonians consist of three parts: a part that is diagonal in the atomic states representing off-resonant energies, a part that is diagonal in the motion representing the Fock states, and a part that represents the laser coupling (both carrier and motion-changing). The part that is diagonal in the motion is simple:

$$\hat{H}_{\text{mot}} = I_{\text{atomic}} \otimes \nu \hat{a}^{\dagger} \hat{a}, \tag{4.34}$$

where I_{atomic} is the identity operator in the atomic portion, ν is the motion frequency, and \hat{a} is the annihilation operator in the motion. Generally, simulations are performed in the co-rotating frame of the pump and probe beam lasers (described in detail in Ref. [117]). Therefore, the Hamiltonian describing the effect of the laser beams is given by (for each laser):

$$\hat{H}_{\text{laser}} = \frac{\Omega_{\text{laser}}}{2} \sigma_{\text{laser}}^{+} \otimes \exp\left(i\eta_{\text{laser}} \left(\hat{a} + \hat{a}^{\dagger}\right)\right) e^{-i\delta_{\text{laser}}t} + h.c. , \qquad (4.35)$$

where Ω_{laser} is the on-resonance Rabi frequency of the laser, σ_{laser}^+ is a Hamiltonian coupling the appropriate atomic states for the given laser (and not affecting the other atomic states), η_{laser} is the Lamb-Dicke parameter of the laser (including sign, so that the pump and probe lasers should have opposite signs of Lamb-Dicke parameter because they have opposite projections in our apparatus),

 δ_{laser} is the residual detuning of the laser after the co-rotating wave approximation is applied,²³ and t is time. The exponential operator was implemented using the expm function in QuTiP. The part that is diagonal in the atomic states is the effective detuning of each beam after a transformation of the form Eq. 2.51 is applied:

$$\hat{H}_{\text{atomic}} = \left(\delta_{\text{pump}} | 2, 2\right) \langle 2, 2| + \delta_{\text{probe}} | 3, 3 \rangle \langle 3, 3| + \delta_{\text{repump}} | 3, 2 \rangle \langle 3, 2| \right) \otimes I_{\text{motion}}, \tag{4.36}$$

where the $\delta_{\rm pump/probe/repump}$ are the residual detunings from resonance of each respective laser in the subscript; typically this is simply the EIT cooling detuning ($\approx 2\pi \times 180$ MHz) for the pump and probe beams, and 0 for the repump beam which is on resonance. The ket describes the atomic states as $|F, m_F\rangle$ of the $^2\mathrm{S}_{1/2}$ manifold, and I_{motion} is the identity operator in the motion. There are extra terms if off-resonant couplings are considered, which are effective Stark shifts of the pump and repump beams on the $|3,2\rangle$ and $|2,2\rangle$ states respectively, but these are very small and have negligible effect on the simulation outcome.²⁴

The collapse operators used for the master equation simulations include those representing photon decay²⁵ (scaled by $\Gamma_{^{25}\text{Mg}^+} = 2\pi \times 41.3$ MHz with appropriate Clebsch-Gordan coefficients) and anomalous heating, modeled as $\sqrt{\Gamma_{\text{heat}}} I_{\text{atomic}} \otimes (\hat{a} + \hat{a}^{\dagger})$, where Γ_{heat} was determined to be 320 quanta/s at the motion frequency used $(2\pi \times 1.18 \text{ MHz}).^{26}$

A supercomputer was not used for any of these simulations,²⁷ and some simulations required weeks to run, even on a very upgraded desktop computer, due to the large number of states used; when micromotion sidebands were considered, the time-dependent terms could not be neglected

²³For example, if only the pump and probe EIT cooling beams are considered, this term is zero, but it will be nonzero for micromotion sidebands and the repump beam, and the latter only if off-resonant couplings are considered, due to the repump beam having the same polarization as the pump beam.

²⁴An exception to this is micromotion sidebands of the pump beam, as mentioned in Sec. 4.3.2.

²⁵Photon recoil up to second order in the Lamb-Dicke parameter was considered; recoil causing transitions associated with σ^+ , σ^- , and π photons were distributed according to the ratio 1:1:2 (this was a guess based upon a complex radiation pattern, 1:1:1 was also used and no significant difference in cooling dynamics was observed).

²⁶I assume that the heating rate scales inversely with the square of motion frequency [121].

²⁷Unfortunately, I fell into the sunk-cost fallacy where I believed that I was close to finished with performing simulations and that it would require more time to set up the code to run on a supercomputer than just waiting for the code to run on my NIST desktop.

and this, combined with a state-space of 3 or 4 atomic states and 50 motion states, ²⁸ made most simulations very slow.

4.2.2 Verification of Dressed-State Picture Decay Operator

In order to verify the dressed-state picture discussed in Sec. 4.1, several simulations were performed. All simulations included anomalous heating and photon recoil up to first order in the Lamb-Dicke parameter, and are of EIT cooling in a simple Λ system. These are the only simulations performed in the dressed-state basis; all the other simulations discussed in this thesis for EIT cooling were performed in the standard basis. An extremely simplified code was used where states and lasers were not implemented using c_states and c_lasers but rather coded as matrix Q0bjs in QuTiP.

First, the system was simulated in the standard basis, and then in the transformed basis using the same parameters under three different levels of approximations: one after the system is just rotated into the dressed-state basis, one with the state $|B_-\rangle$ decoupled completely (including any transitions or decay processes) but including the term containing $|B_+\rangle \langle B_+|$ in Eq. 4.16, and finally one without $|B_-\rangle$ and including only the terms with $|B_+\rangle \langle D|$ in Eq. 4.16. These four simulations were each performed under three different parameter sets: one with typical parameters used where $\Omega_{\text{pump}} > \Omega_{\text{probe}}$, one where $\Omega_{\text{pump}} \approx \Omega_{\text{probe}}$, and one where $\Omega_{\text{pump}} > \Omega_{\text{probe}}$ as in the first set of conditions, but the Lamb-Dicke parameter was decreased by a factor of 10 (0.03 was used as opposed to 0.3 in the first two cases). Fig 4.4 reveals that for all three sets of parameters, the various simulations all yield somewhat similar results, with the notable exception of when the decay operator was simplified to have the terms proportional to $|B_+\rangle \langle D|$ only. This means that the term containing $|B_+\rangle \langle B_+|$ in Eq. 4.16 is important to the dynamics.

 $^{^{28}}$ Thermal states with average occupation ≈ 3 could be accurately modeled without too much population being cut off by the limited number of motion states used. Some simulations that started with higher average occupation had significant population in higher Fock states which would increase in Fock number and then build up at the upper bound of Fock states (N=49) during tripod-EIT simulations with micromotion considered. This is an unphysical effect that skewed the average motional occupation so the starting motion occupation was restricted to lower values after this was discovered.

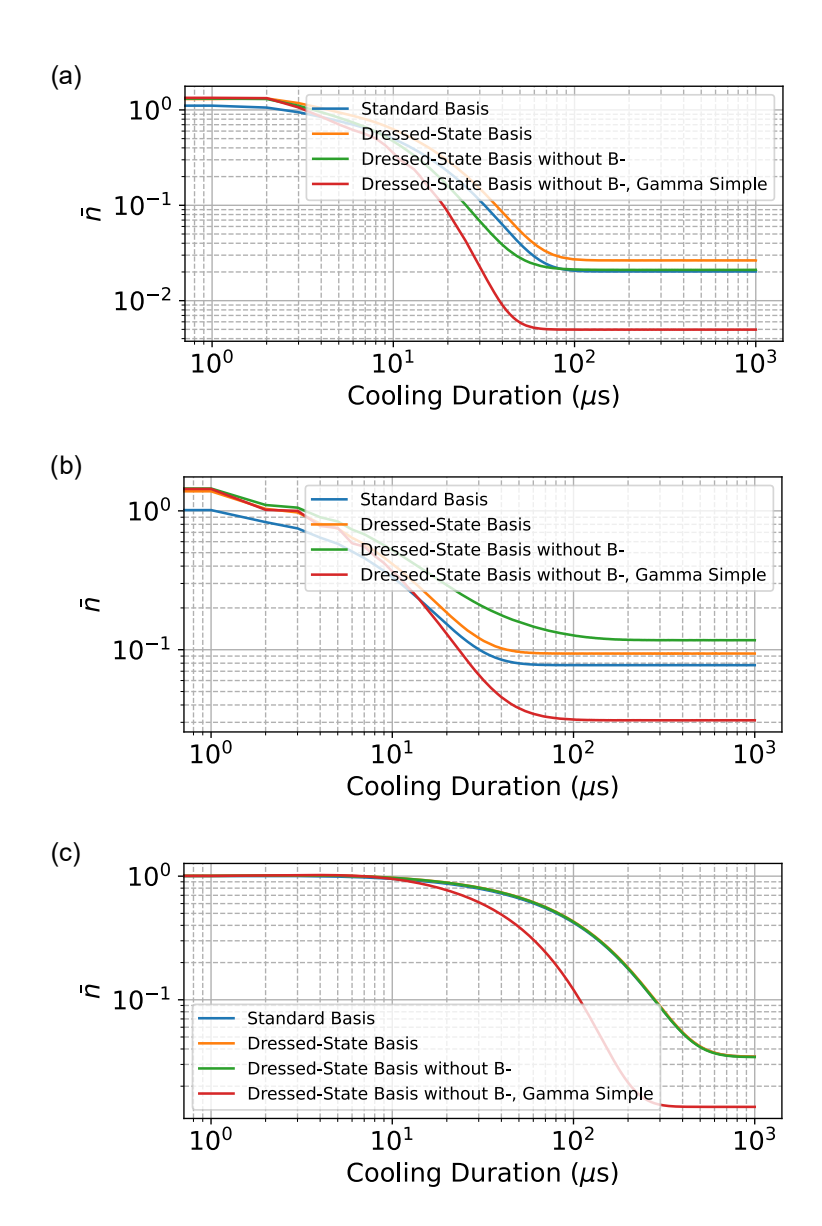


Figure 4.4: Simulations of average occupation number \bar{n} vs. cooling duration for various parameter sets, bases, and approximations. (a) uses $\Omega_{\text{pump}} = 2\pi \times 28.6 \text{ MHz}$, $\Omega_{\text{probe}} = 2\pi \times 5.87 \text{ MHz}$, and a Lamb-Dicke parameter of 0.3. (b) uses $\Omega_{\text{pump}} = \Omega_{\text{probe}} = 2\pi \times 20.7 \text{ MHz}$, and a Lamb-Dicke parameter of 0.3. (c) uses $\Omega_{\text{pump}} = 2\pi \times 28.6 \text{ MHz}$, $\Omega_{\text{probe}} = 2\pi \times 5.87 \text{ MHz}$, and a Lamb-Dicke parameter of 0.03. In (c), the blue, orange, and green lines are nearly overlapped. All simulations use $\delta = 2\pi \times 180 \text{ MHz}$ and decay parameters corresponding to the experiment with $^{25}\text{Mg}^+$ where $|g_A\rangle = ^2\text{S}_{1/2}|F = 2, m_F = 2\rangle$, $|g_P\rangle = ^2\text{S}_{1/2}|F = 3, m_F = 3\rangle$, and $|e\rangle = ^2\text{P}_{1/2}|F = 3, m_F = 3\rangle$. For all subfigures, the blue line corresponds to the simulation performed in the standard basis; the orange line corresponds to the simulation performed in the dressed-state basis with all the coupling and decay terms included; the green line corresponds to the simulation in the dressed-state basis with all couplings to $|B_-\rangle$ removed (including decay); and the red line corresponds to the dressed-state basis with all couplings to $|B_-\rangle$ removed and the decay operator further simplified to couplings with terms containing $|B_+\rangle\langle D|$ only.

4.2.3 Fano-like EIT Cooling Lineshape with Motion

It was also found using simulations that the EIT cooling absorption spectrum (shown in Fig. 4.2) had multiple peaks spaced according to the motion frequency in addition to the Fano-like peak responsible for cooling when higher-order Lamb-Dicke terms in the laser Hamiltonian were considered. In fact, as shown in Fig. 4.5, the single-peak absorption spectrum only appears when motion is not considered at all; as soon as motion is considered, multiple peaks spaced by the motion frequency appear.

4.3 EIT Cooling Experiment

In this section, the experimental results and procedures for EIT cooling of ²⁵Mg⁺ in our apparatus are described.

4.3.1 Physical Apparatus Changes

In order to implement EIT cooling in the existing apparatus while minimizing changes to other capabilities, the EIT-cooling beamline was built around existing optical components with some unused portions of the $^{25}\mathrm{Mg^+}$ motion-insensitive Raman beamline. Three additional laser beams (pump, probe, and repump, driving transitions from $^{25}\mathrm{Mg^+}$ $^2\mathrm{S}_{1/2}|2,2\rangle$, $|3,3\rangle$, and $|3,2\rangle$ respectively to $^2\mathrm{P}_{1/2}|3,3\rangle$) were set up for this experiment. These beams were required to be coherent with each other, so they were all be derived from the same source. Because the power needed for EIT cooling was not very high and the detuning from resonance should be fairly low (precluding the use of light from the Raman beamline), the $^0\mathrm{th}$ -order tone from the $^2\mathrm{S}\mathrm{Mg^+}$ $^2\mathrm{S}_{1/2}\leftrightarrow^2\mathrm{P}_{1/2}$ UV doubler was used. This also allowed for the use of the $^2\mathrm{S}_{1/2}|3,2\rangle$ repump frequency as a reference to the $^2\mathrm{S}\mathrm{Mg^+}$ atomic transitions.

In order to span the hyperfine splitting of the $^{25}\text{Mg}^+$ $^2\text{S}_{1/2}$ manifolds, the "Mg CoCarr A" and "Mg CoCarr B" AOMs were used. ²⁹ A third AOM of the same model (labeled "Mg EIT Probe"

²⁹This meant that while the EIT beamline was active, the Mg Raman 3 beam could not be used to drive motion-insensitive qubit transitions, and it could not be used to help drive radial Raman transitions either.

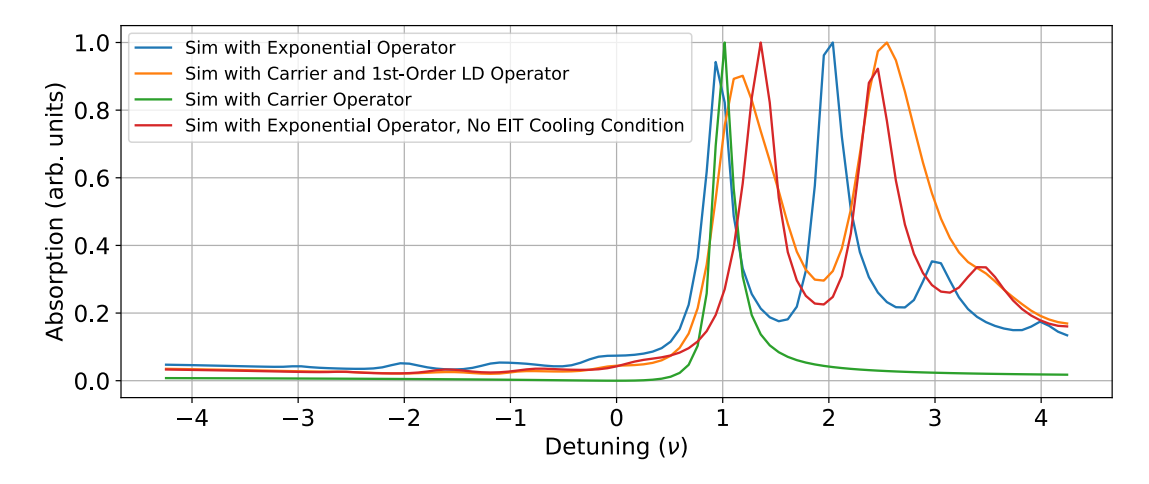


Figure 4.5: A simple Λ -EIT system was simulated, and the absorption of the probe beam (with Rabi frequency $2\pi \times 0.5$ MHz) of the system dressed by the pump beam (with Rabi frequency $2\pi \times 35.0$ MHz) is shown under various conditions as the probability of finding the system in the excited state. The motion frequency used is $2\pi \times 1.178$ MHz, the EIT cooling detuning is $2\pi \times 180$ MHz, and the Lamb-Dicke parameter is 0.3. The absorption is scaled to the maximum point of each respective curve for visibility, and the detuning of the probe beam is scaled in units of motion frequency and referenced to the pump beam detuning (ν is the detuning of the probe beam minus that of the pump beam). The blue curve shows the spectrum with the full laser Hamiltonian exponential in the motion Eq. 2.53 simulated, and can be seen to have peaks that are equally spaced at the motion frequency. The orange curve shows the spectrum when the laser Hamiltonian is approximated with only the carrier and first-order in Lamb-Dicke parameter term Eq. 2.66, and also has peaks, though the location of these peaks is no longer precisely at integer multiples of the motion frequency (this is possibly due to a change in the effective Rabi rate when the Lamb-Dicke parameter is very large). The green curve simulates the laser Hamiltonian with the motion carrier term in Eq. 2.66 only; in other words, it does not consider motion. This appears most like typically-shown EIT cooling absorption spectra. Finally, the red curve shows the same situation as the blue curve, with the full laser Hamiltonian motion exponential, but without the EIT condition satisfied (the pump beam Rabi frequency is scaled by a factor of 1.2). This shows that the spacing between the peaks observed do not depend on the location of the first peak relative to resonance with the pump beam, but rather the motion frequency.

in Fig. 4.6) was set up for the third (probe) beam. Most experiments consisted of a period of EIT cooling where the power of one laser beam, frequency of one laser beam, or the cooling duration was varied, so having three AOMs, one controlling each of the EIT cooling beams, was ideal. The directions of the EIT cooling beams at the ion is shown in Fig. 4.7.

As mentioned earlier in this thesis, the motion-sensitive Raman beams in our apparatus are

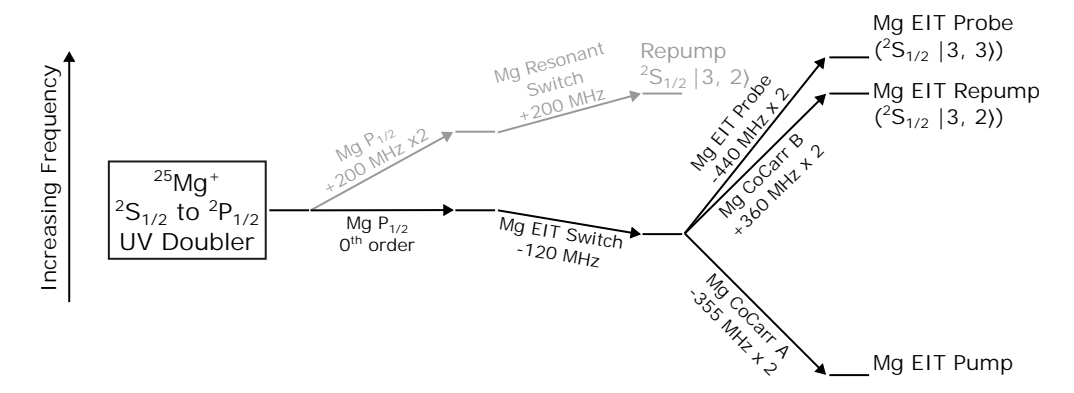


Figure 4.6: Frequency diagram for EIT cooling beams generated from $^{25}\mathrm{Mg^+}$ $^2\mathrm{S}_{1/2} \leftrightarrow ^2\mathrm{P}_{1/2}$ UV doubler. The $^2\mathrm{S}_{1/2}|3,2\rangle$ repump frequency is shown for reference; the "Mg Resonant Switch" AOM is also included to better show the relative frequencies of each beam. The Mg EIT cooling repump beam is able to attain the same frequency as the doppler-cooling repump beam, and the pump and probe beams are at the correct frequency to drive transitions from $^2\mathrm{S}_{1/2}|2,2\rangle$ and $^2\mathrm{S}_{1/2}|3,3\rangle$ with a +180 MHz detuning, as desired. It is also possible to drive the "Mg CoCarr B" AOM at a higher frequency such that the repump beam is also detuned close to +180 MHz (for double EIT cooling, Sec. 4.3.6), but this requires realignment of the AOM.

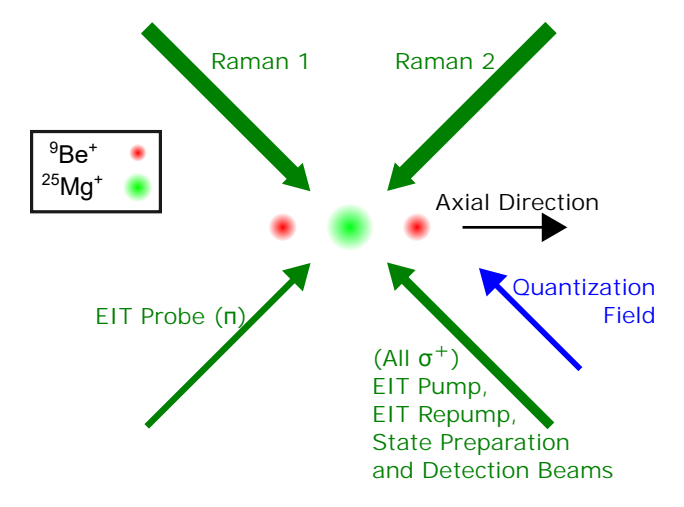


Figure 4.7: The laser beam geometry relevant to the EIT experiment at the ion are shown. All arrows have a 45° angle relative to the axial direction along which the ions line up, as illustrated by the three-ion crystal. The two Raman beams (Raman 1 and Raman 2) that are used for sideband thermometry have a wavevector difference that is nominally along the axial direction; most experiments are performed with the axial modes only. The EIT cooling beams (probe and pump) also have a wavevector difference along this direction. The EIT cooling pump and repump beams are injected into the same fiber as the $^{25}{\rm Mg}^+$ state preparation and detection beams using a method described in Sec. A.2.2 through the "Mg Resonant Switch" AOM and are therefore colinear with those beams (but not used simultaneously); these beams are all colinear with the quantization field and have a σ^+ polarization.

well-suited for performing operations involving the axial modes, as shown in Fig. 4.7. Therefore, the EIT cooling beams were set up to cool the axial modes only in all crystals discussed for this experiment, with the pump (and repump) beams having σ^+ polarization and the probe beam having π polarization. Laser beam powers at the ion trap were tens of μ W or less. After taking the frequency bandwidth of available AOMs into account, the EIT-cooling detuning was set to $\delta = 2\pi \times 180$ MHz; this was also set to avoid unintentionally driving any micromotion sidebands at frequency multiples of $\omega_{\rm RF} = 2\pi \times 82.529$ MHz. All other parameters were experimentally determined separately, as described in Sec. 4.3.7.

During the experiment, the uncompensated axial micromotion (with frequency 82.529 MHz) present at the experiment zone of the ion trap was found to be a significant contributor to non-idealities in the EIT cooling process.³⁰ The micromotion was determined to have a modulation index (Eq. 2.75, Ref. [75]) of $\beta = 0.823 \pm 0.028$ on the pump, probe, and repump beams, using the method described in Sec. 4.3.7. At this micromotion modulation index value, the micromotion sidebands were weaker than the carrier. However, for beams that are blue detuned from resonance such as the pump and probe beams, the micromotion sidebands at lower frequency than the carrier will be closer to resonance with the ion's optical transitions, making their effects non-negligible during EIT cooling, as illustrated in Fig. 4.8.

Recoil from photon scattering on these sidebands can cause heating or otherwise make cooling inefficient³¹ and slow down progress towards the system's steady state, while the Stark shifts they cause complicated optimization of EIT parameters (as described in Sec 4.3.2). The first and second red micromotion sidebands of both the pump and probe beams had detunings from resonance

 $^{^{30}}$ An attempt was made to mitigate this by buying a micromotion modulation compensation EOM to be placed in the 25 Mg⁺ resonant beamline (which would modulate the pump and repump beams as well) as is done for the 9 Be⁺ resonant and Raman beams (see Sec. 3.2.11). Unfortunately, the product received was defective and had 30% transmission through the two EOM windows at 280 nm, and thus could not be used. A second attempt was made to perform EIT cooling with the ion at a different point in space so that the micromotion vector was perpendicular to the pump EIT cooling beam. Because motion state readout operations and detection had to be performed at the typical micromotion values, the ion was shifted between the standard location and micromotion-vector-adjusted location over a period of 50 μ s. This sometimes caused ion loss and motional heating was also observed, so this was abandoned as well.

³¹These micromotion sidebands can also be thought of as making their own EIT cooling resonances, but these will enhance the motion-subtracting scatter at the wrong frequencies, making cooling less efficient than if they were not present.

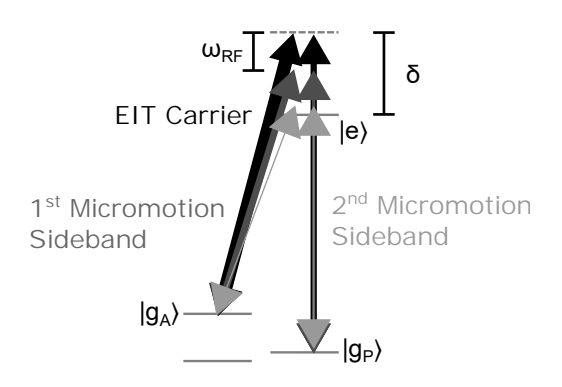


Figure 4.8: The frequency detunings relative to atomic resonance of the EIT cooling micromotion sidebands are sketched for the pump and probe beam. The carrier beams are illustrated in black, with a blue detuning δ from the excited state. It can be seen that while the micromotion sidebands (detuned from the carrier by ω_{RF}) are weaker in power (illustrated by the thicknesses of the beams as well as the faintness of the beams and text), they are closer to resonance with the atomic transitions.

of $2\pi \times 97.5$ MHz and $2\pi \times 14.9$ MHz, and powers relative to the carrier of $\approx 20\%$ and $\approx 1\%$, respectively.

During the period of time that this experiment and the mode-coupling experiment (Chp. 5) were performed, there were mysterious "instabilities" that were independently observed by all data-taking members in the lab. For example, it would appear that on some days it would be possible to reach a certain low motional occupation using sideband cooling, and on other days it would be impossible to do so, despite recalibrating many relevant parameters. This instability would come and go over days. A potential source of this instability was discovered years later coming from the Artiq DDSes. These DDSes drive many of the AOMs throughout the lab that require frequencies or amplitudes to be changed, including the $^{25}\text{Mg}^+$ Raman beams, EIT cooling beams, and some state preparation beams. They also provide the signal for the $^{25}\text{Mg}^+$ microwave drives. The DDSes would manifest noise on the hundreds-of-kHz to MHz range on the driving tones; this would likely prevent Raman transitions from being driven cleanly. After this source of error was found, similar problems with driving motion sidebands cleanly using Raman beams were fixed by performing the dac_cal sequence on the DDSes (described in Sec. 3.4). This instability could result in some discrepancies between datasets taken on different days and explain why some Ramsey experiments used for EIT cooling parameter calibration failed (described in Sec. 4.3.7), but unfortunately the source was not

found until much after the conclusion of the EIT experiment.

4.3.2 Calibrating EIT Laser Beam Parameters

As described in Sec. 4.3.1, each beam passed through an individual acousto-optic modulator (AOM) before being combined with other beams (if necessary) before reaching the ion. This enabled both the frequency and power of each beam to be varied independently. The laser light used originated from the Mg $^2P_{1/2}$ UV doubler, which also is used as the source for the (state preparation) repump beam from $^2S_{1/2}$ $|3,2\rangle$ to $^2P_{1/2}$ $|3,3\rangle$. This repump beam was known to be on resonance with the transition within a few MHz, therefore the EIT detuning δ could be straightforwardly referenced to the necessary states using calibrated microwave transitions, which were known within a few kHz. The only additional error would come from the frequency accuracy of the Artiq DDSes. These were all determined to be small compared to uncertainties on other variables relevant to EIT cooling, so the detuning in the experiment is quoted without uncertainty.

In order to change the power of a given EIT cooling laser beam, the RF power supplied to the AOM was varied using the amplitude of the driving signal from the appropriate Artiq DDS. However, feedback stabilization of beam powers as described in Sec. 3.2.10 was difficult to implement due to lack of space for a photodetector and lack of total power, so the powers of EIT cooling beams fluctuated during the experiment.³² The EIT cooling beam power at the ion could change due to many reasons: the output power of the UV source changing over time; beam pointing drifts at the input of a fiber in each beamline; and temperature-dependent diffraction efficiency changes in AOMs in the beamline due to duty cycle variations. To mitigate this last problem, the EIT cooling beams were turned on for the same total amount of time for every shot of the experiment, with an extra EIT cooling beam pulse after ion fluorescence was detected (i.e. after the effective conclusion of each shot) to make up any extra time required in addition to the experiment pulse. The various forms of power fluctuations were suspected to be the main sources of error for the experiment, as changes in

 $^{^{32}}$ These fluctuations were not measured rigorously but based on the required AOM drive amplitude changes could be estimated to be between 10-30% over hours.

the beam power would change the frequency at which optimal cooling occurred (breaking the EIT condition) and changing the cooling rate.

For calibrations, Doppler cooling is first performed on the ion(s), then EIT cooling for 5 ms, to ensure that a steady state was reached for the EIT cooling parameter set used. Finally, the motional occupation was determined using sideband thermometry ([68], Sec. 2.2.2.2), and for each power or frequency scan, the point yielding the lowest motional occupation was chosen to be the new value for that parameter. Several iterations of calibrations were performed (as described in the next paragraphs) until a stable value was reached for each parameter.

For a single $^{25}{\rm Mg}^+$ ion, calibrations progressed as follows. For the first iterations of any particular EIT cooling experiment, the Rabi frequency of the pump beam (calculated using methods described in Sec. 4.3.7) was first set to a value close to, but slightly less than, $\sqrt{4\delta\nu}$ (recall that the EIT condition is given by $\nu = (\Omega_{pump}^2 + \Omega_{probe}^2)/4\delta$), using the known EIT-cooling detuning of approximately $\delta = 2\pi \times 180$ MHz and axial motion frequency of either $\nu = 2\pi \times 1.18$ MHz (for the single- $^{25}{\rm Mg}^+$ cooling duration scans) or $\nu = 2\pi \times 1.5$ MHz (for EIT bandwidth experiments). This ensured that the majority of the dressing was done by this beam, and therefore it would be the main contributor to other errors as well. This was done for simplicity and to minimize depumping towards the negative spin side of the $^2{\rm S}_{1/2}$ manifold. The powers of the probe and repump beams were then set to low values, typically corresponding to Rabi frequencies of $2\pi \times 1-5$ MHz.

The pump and repump beam frequencies were set using the Mg $^2P_{1/2}$ repumper as a reference. In order to account for the Stark shift from the pump beam micromotion sidebands³³ on the common excited state $^2P_{1/2}|3,3\rangle$, the detuning of the probe beam was adjusted by a calculated value, typically $2\pi \times 0.3 - 0.8$ MHz.

To complete the initial calibration, each beam power was scanned and set to the optimal value, beginning with the pump beam (the cooling was found not to be sensitive to the probe or repump beam powers, as long as they were not too weak). Then, the probe beam detuning was scanned and

³³For EIT-cooling, the pump beam Stark shift should, of course, not be calibrated out, since it is part of the effect responsible for EIT cooling. However, these micromotion sidebands are not part of the process and therefore Stark shifts resulting from them should be accounted for.

set.³⁴ This process was iterated a few times until a steady state for the experimental parameters was reached. After the probe beam frequency is set in this manner, there was found to be an extra detuning (assumed to be compensating for micromotion sidebands of the pump beam) required for optimal cooling. For subsequent experiments with the same motion mode frequency, the optimal value of the probe beam frequency did not change noticeably when re-calibrated, and therefore the frequency was treated as a set parameter: typical daily calibrations for EIT cooling only consisted of scanning each beam power until a steady state was reached, beginning with the pump beam power.

For the multi-ion cooling scans, a similar procedure was performed, where each beam power was varied in turn. For EIT cooling of multi-ion crystals, two different methods, called the "interleaved cooling method" and "simultaneous cooling method" were used. The interleaved cooling method involved optimizing a separate parameter set for each mode cooled. The parameter set for a given mode was found by optimizing for the lowest temperature of that mode, while all other modes are cooled using sideband cooling to remove any extraneous effects on the data. For the simultaneous cooling method, the aim was to use a single EIT cooling parameter set to cool all modes simultaneously, so the calibration results were chosen to obtain (approximately) the lowest total temperature of all modes.

The order of the modes to be cooled in the interleaved multi-ion cooling scans were chosen so that the mode with the highest heating rate was cooled last, to minimize the amount of time that mode would experience anomalous heating after being cooled. The minimum duration required for each mode to reach its steady-state temperature was used, with the final pulse stopped before steady-state was reached to ensure the previously cooled modes did not heat up too much (see Figs. 4.11(b) and 4.12(b)). It was found that iterating through the modes multiple times did not further decrease the final temperature.

³⁴Initially, the calibration routine involved the probe beam frequency being scanned first, prior to scanning any beam powers. Doing this often caused a runaway effect where it appeared that the probe beam's frequency was compensating for an incorrect pump beam power. This would cause the probe beam frequency to be calibrated incorrectly, which then caused the pump beam's optimal power to appear different, resulting in difficulty reaching a stable EIT parameter set.

4.3.3 Cooling Single ²⁵Mg⁺

In order to set up the EIT cooling experiment and develop all the relevant calibration procedures on our apparatus, experiments were initially performed with a single $^{25}\text{Mg}^+$ ion in the S well, with axial frequency $2\pi \times 1.18$ MHz. It is seen from Fig. 4.9 that the axial mode of this ion was cooled below $\bar{n} \approx 1$ in a few hundred μ s, which is comparable with sideband cooling durations in our apparatus. Data were taken only when \bar{n} was close to one to avoid excessive uncertainty when estimating higher \bar{n} values using sideband thermometry ([68], Sec. 2.2.2.2). However, the minimum achievable steady-state motional occupation was much higher than expected according to Eq. 4.28. Even a simulated Λ -system with imperfections such as recoil and anomalous heating gave an EIT-cooled steady state occupation that is much lower (red solid line in Fig. 4.9) than experimental data. Adding effects such as the third ground state (making a "tripod" EIT cooling system giving the cooling limit illustrated by the purple dashed line), and most importantly the micromotion sidebands on the EIT-cooling beams ("tripod-with-micromotion", blue dash-dot line) resolved the majority of the discrepancy.

The laser beam intensities used for this experiment, expressed as equivalent resonant Rabi frequencies, are estimated (see Sec. 4.3.7 for details) to be $\Omega_{\text{pump}}/2\pi = 29.4 \pm 0.7 \text{ MHz}$, $\Omega_{\text{probe}}/2\pi = 5.61 \pm 0.17 \text{ MHz}$, and $\Omega_{\text{repump}}/2\pi = 0.87 \pm 0.07 \text{ MHz}$. Using these experimental parameters, the simulated steady-state axial mode \bar{n} for the Λ , tripod, and tripod-with-micromotion systems were found to be $\bar{n}_{\Lambda} = 0.028$, $\bar{n}_{\text{tripod}} = 0.055$, and $\bar{n}_{\text{MM}} = 0.216$ respectively. The small difference between the experimentally determined occupation of $\bar{n}_{exp} = 0.26 \pm 0.02$ and \bar{n}_{MM} is attributed to additional experimental imperfections, such as beam power fluctuations resulting from beam pointing drifts and AOM temperature instability, or noise on the RF signals that were used to drive relevant AOMs.

All simulations shown in Fig. 4.9 incorporate the same experimentally-determined motional heating rate of 320 quanta/s and the recoil from scattered photons as described in Sec. 4.2. The two models of tripod systems use the estimated Ω values, while the Λ -EIT model uses the experimentally

³⁵Comparing the EIT cooling limit to more recent data (Sept 2024) of sideband cooling on a ²⁵Mg⁺ ion trapped under similar conditions (which was able to attain $\bar{n} \approx 0.2 - 0.3$) reveals that both methods appear to cool equally well.

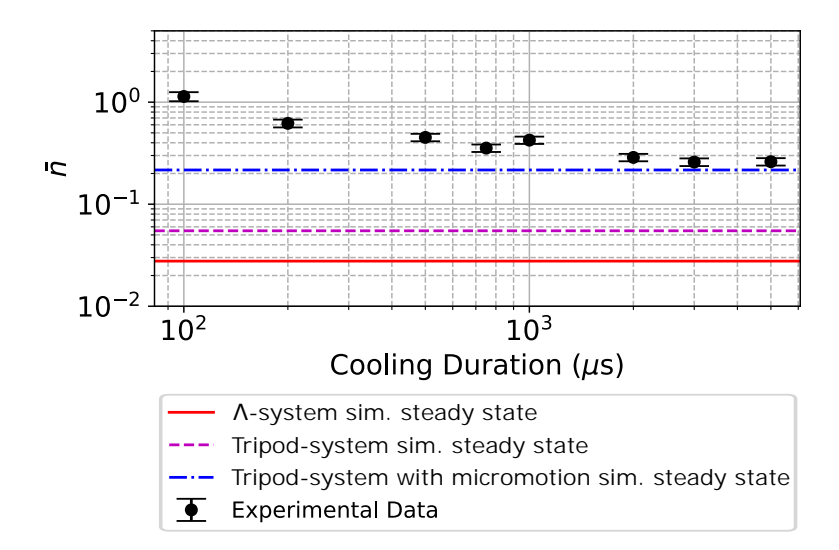


Figure 4.9: EIT cooling of a single $^{25}\text{Mg}^+$ ion. Data points (black) show sideband thermometry results, and were not taken at motional occupations far above unity to avoid excessive error when determining the average occupation. The steady-state values of three different cooling simulations are also shown. The red solid line corresponds to standard Λ -system EIT, while the dashed purple line shows the cooling limit for a system with three ground states and one excited state, and the blue dash-dot line shows the cooling limit for a system with micromotion sidebands considered in addition to three ground states.

determined Ω_{probe} and a calculated ideal Ω_{pump} assuming the EIT-cooling condition is satisfied. The model that includes micromotion also incorporates an extra detuning of the probe beam beyond $\delta = 2\pi \times 180 \text{ MHz}$ of $2\pi \times 0.75 \text{ MHz}$ to account for Stark shifts due to off-resonant micromotion sidebands.

4.3.4 Probing the Bandwidth of EIT Cooling

As mentioned previously, one powerful feature of EIT cooling is the large cooling bandwidth: as long as a given mode frequency is within a range of frequencies where the motion-subtracting scatter is more likely than motion adding scatter (as described in Sec. 4.1.4) and the difference wavevector of the EIT cooling pump and probe beams has a projection along the given mode, the mode is cooled simultaneously with any other modes satisfying these conditions. This feature makes EIT cooling suitable for large crystals. This is in contrast to sideband cooling, where each mode needs to be addressed individually, and therefore requires either multiple tones on the cooling beams

(thereby splitting the power of the beam and slowing down cooling) or multiple pulses iterating over each mode. This large bandwidth of EIT cooling has been featured in multiple investigations [56, 109–113]; in all of these publications, multiple modes of the same ion crystal were cooled. For the investigation in this experiment, a different approach is taken in which a fixed set of EIT-cooling parameters was used while the axial frequency of a single ²⁵Mg⁺ ion was varied by changing the voltages creating the confinement potential.

In retrospect, this method of probing the bandwidth of EIT cooling came with many drawbacks. The method that was used as a standard way to change the confinement of an ion in our apparatus was to scale all the DC trapping voltages by a common scaling factor. It was found that the axial frequency of a single ²⁵Mg⁺ ion trapped in a scaled S well could realistically be changed between $2\pi \times 0.655$ MHz and $2\pi \times 2.605$ MHz. At the lower end, the ion became difficult to cool beyond the Doppler limit and its fluorescence counts over the typical detection sequence (200 μ s) would drop by 10-20%. This was attributed to a higher heating rate at these lower frequencies and/or the center of the potential well shifting when the well was scaled; this latter effect could change the intensity of the detection beam on the ion as well as expose the ion to stronger micromotion, and both effects would result in reduced counts. The equilibrium position of the ion changing was also a concern as this would change the EIT beam intensities on the ion. The highest ²⁵Mg⁺ ion axial frequency was limited by the maximum voltage that could be supplied by the PDQs [95] to the trap electrodes $(\pm 10 \text{ V})$. Another complication with using this method to change the frequency was that the ion's radial micromotion would no longer be compensated for each scaling setting,³⁷ requiring a new set of shim voltages for each scaled well; this latter problem was solved using the preparation process described in the next paragraph.

Prior to the acquisition of main data, each scaled well was roughly characterized: the first and second motion-adding sidebands were driven on the ²⁵Mg⁺ cooling transition³⁸ in order to determine

³⁶Because of stray fields and a micromotion gradient, this did not necessarily result in a similar potential well with different frequency as intended.

³⁷It was also unknown whether our micromotion modulation index in the axial direction changed significantly due to these adjustments, but this was not explored at the time.

³⁸This was done on the red sideband, $|2,2\rangle|0\rangle \rightarrow |3,3\rangle|1\rangle/|3,3\rangle|2\rangle$ where the first ket is the state within the ${}^2S_{1/2}$

the motion frequency corresponding to the DC voltage scaling factor. Then, a tickle experiment was performed to determine the two radial-mode frequencies, and a standard radial micromotion minimization sequence (Sec. 3.3.3) was performed, with the resulting optimized electrode shims recorded.

Next, the EIT cooling parameters were optimized with the well set at the scaling factor giving a $2\pi \times 1.498$ MHz mode, yielding $\Omega_{\text{pump}}/2\pi = 27.2 \pm 0.7$ MHz, $\Omega_{\text{probe}}/2\pi = 4.62 \pm 0.13$ MHz, and $\Omega_{\text{repump}}/2\pi = 0.70 \pm 0.15$ MHz. Then the well was set using the scaling parameter yielding the lowest axial mode frequency; the electrode shims were set to the recorded values for that well to minimize radial micromotion; the Raman beam frequency and π time were calibrated based on the previously recorded values corresponding to that motion frequency in order to perform sideband thermometry; and EIT cooling was performed for up to 5 ms at the lowest-frequency well setting with data being acquired for various cooling durations. This process was repeated for each axial frequency probed: $2\pi \times (0.655, 0.810, 1.055, 1.340, 1.498, 1.903, 2.129, 2.332, 2.605)$ MHz. It took over five hours to acquire the complete dataset shown in Fig. 4.10; earlier data acquisition attempts for a single set of data took even longer. Because of this, it is likely that laser beam powers dropped overall throughout the day from their initial optimized settings, lowering the efficiency of EIT cooling.

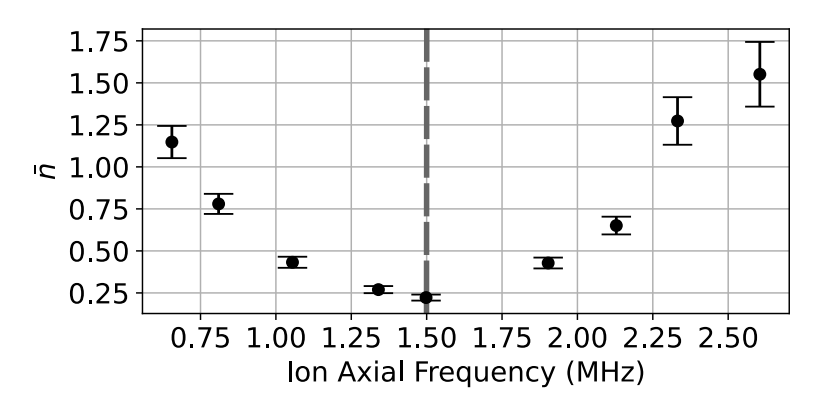


Figure 4.10: EIT cooling results, shown as motional occupation extracted using sideband thermometry, after 3 ms of cooling. Data are taken for a single $^{25}\mathrm{Mg}^+$ ion as the well confinement is changed, resulting in changing axial frequency. EIT cooling is optimized at the confinement corresponding to $2\pi \times 1.498$ MHz, illustrated by the vertical dashed line.

manifold and the second ket is the motion occupation in the single axial mode.

The mode frequency for which EIT cooling is optimized $(2\pi \times 1.5 \text{ MHz})$ was relatively low, therefore the bandwidth was not expected to be particularly large. Eq. 4.32 predicts that the frequency range between $2\pi \times 0.255$ MHz and $2\pi \times 8.745$ MHz should be cooled to $\bar{n} \leq 1$, with this range somewhat narrowed by the presence of heating, especially towards the lower frequencies. However, it is likely that micromotion and EIT cooling beam power drifts further narrowed the EIT cooling bandwidth, resulting in the data shown in Fig. 4.10. While the cooling data at each well confinement were taken for a total of 5 ms, the motional occupations determined using sideband thermometry reached a steady-state value by 3 ms, therefore the data taken at that cooling duration is shown.

4.3.5 Cooling Mixed-Species Ion Chains with $^{25}{ m Mg}^+$

One of the main motivations for this work was to cool mixed-species ion crystals using ²⁵Mg⁺. The two mixed-species ion crystals that were investigated for this part of the experiment were ${}^{9}\text{Be}^{+}$ - ${}^{25}\text{Mg}^{+}$ and ${}^{9}\text{Be}^{+}$ - ${}^{25}\text{Mg}^{+}$ - ${}^{9}\text{Be}^{+}$. The latter crystal poses a particular problem because the ${}^{25}\text{Mg}^{+}$ ion does not participate at all in the middle-frequency OOPH mode (Fig. 3.20 and 4.12(a)), and so the mode-coupling technique described in Ch. 5 is used in order to exchange that mode with the ALT mode where ${}^{25}\text{Mg}^{+}$ does participate. The sideband thermometry data of each mode is taken in an interleaved fashion (the sidebands of each mode are probed sequentially, iterating through each mode), and for the ${}^{9}\text{Be}^{+}$ - ${}^{25}\text{Mg}^{+}$ - ${}^{9}\text{Be}^{+}$ crystal, the information on the OOPH mode motion was always accessed through the ${}^{25}\text{Mg}^{+}$ using the ALT mode via a state swap. For both mixed-species crystals, all axial modes were cooled using EIT cooling for this part of the experiment (except during calibrations as described in Sec. 4.3.2).

Two different ways of applying EIT cooling were investigated — one where EIT-cooling parameters were optimized for each mode and pulsed in an interleaved fashion (which I will call "interleaved cooling", shown in Figs. 4.11(b) and 4.12(b)) and one where a single set of EIT-cooling parameters was optimized to cool all the axial modes of the crystal simultaneously (which I will call "simultaneous cooling", shown in Figs. 4.11(c) and 4.12(c)).

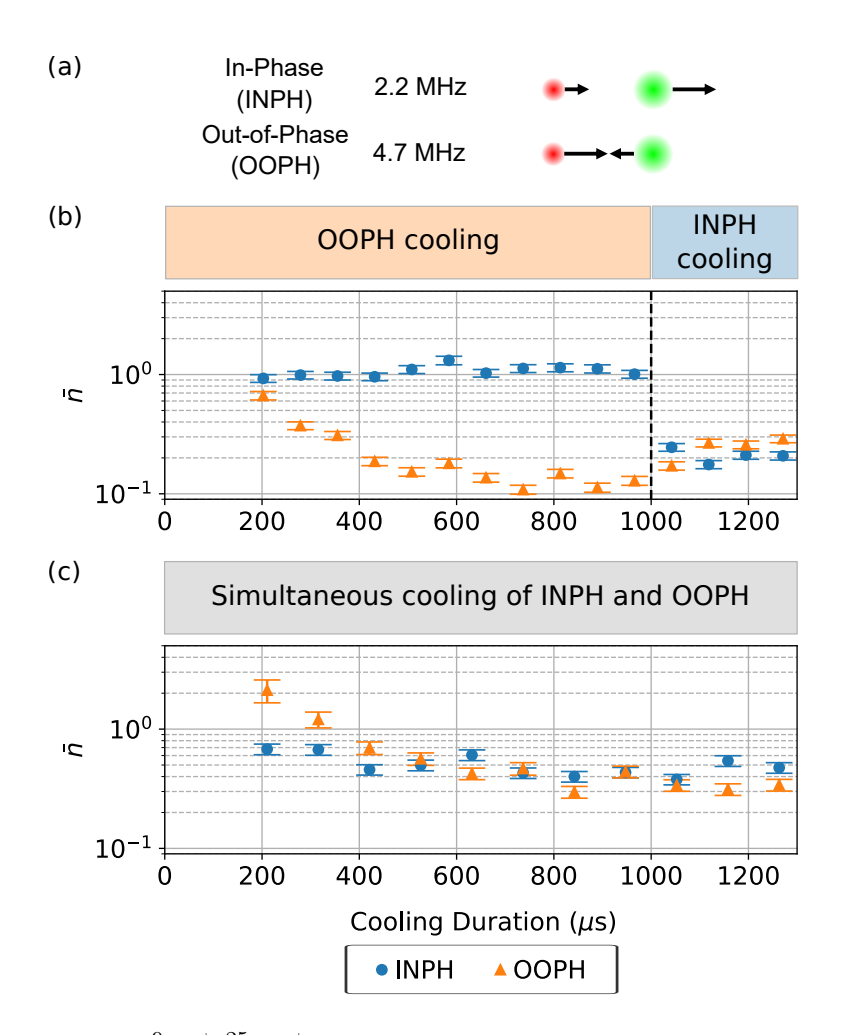


Figure 4.11: EIT cooling of ${}^9\mathrm{Be}^+$ - ${}^{25}\mathrm{Mg}^+$ ion crystal. (a) shows the frequencies of the cooled modes as well as the participation of each ion (${}^9\mathrm{Be}^+$ in red, ${}^{25}\mathrm{Mg}^+$ in green) in the respective mode as black arrows. (b) shows interleaved cooling, with 1000 $\mu\mathrm{s}$ of cooling optimized for the OOPH mode followed by 300 $\mu\mathrm{s}$ of cooling optimized for the INPH mode. (c) shows simultaneous cooling with a single EIT parameter set. Cooling sequences for (b) and (c) are described in colored blocks above each plot.

During interleaved cooling of ${}^{9}\text{Be}^{+}$ - ${}^{25}\text{Mg}^{+}$ - ${}^{9}\text{Be}^{+}$, in order to cool the OOPH mode, the OOPH and ALT modes were completely interchanged with a single swap operation after the ALT mode was sufficiently cooled, which was counted as part of the cooling sequence time, as shown in the pulse sequence illustrated above the plot in Fig. 4.12(b). For simultaneous cooling, the mode-coupling modulation signal was turned on at the same time as the EIT cooling beam, enabling the ALT mode to act as a cooled reservoir for the OOPH mode in a continuously-coupled manner.

Usually, for a reasonable EIT cooling parameter set, each mode has an equilibrium phonon

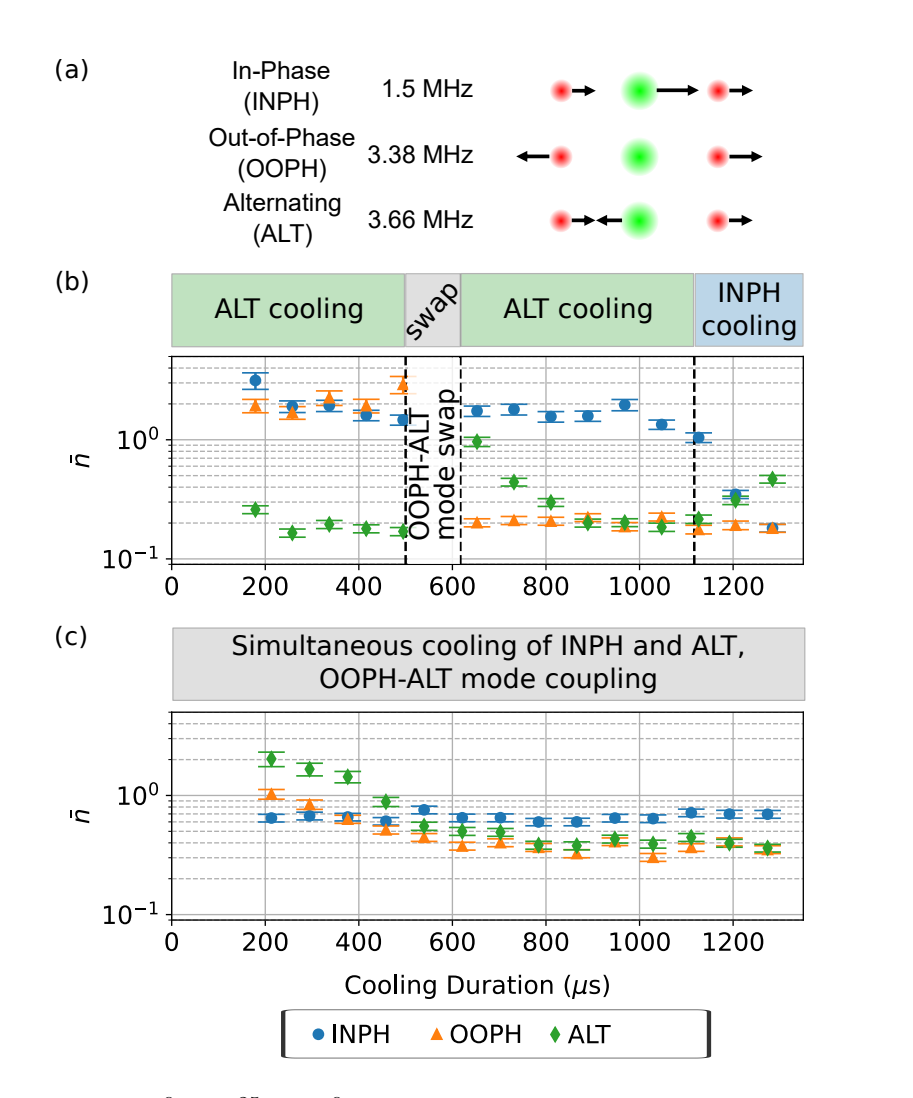


Figure 4.12: EIT cooling of ${}^9\mathrm{Be}^+$ - ${}^2\mathrm{SMg}^+$ - ${}^9\mathrm{Be}^+$ ion crystal. (a) shows the frequencies of the cooled modes as well as the participation of each ion (${}^9\mathrm{Be}^+$ in red, ${}^{25}\mathrm{Mg}^+$ in green) in the respective mode as black arrows. (b) shows interleaved cooling, with 500 $\mu\mathrm{s}$ of ALT-mode-optimized cooling, a coherent swap between the OOPH and ALT modes taking 117 $\mu\mathrm{s}$, 500 $\mu\mathrm{s}$ of ALT-mode-optimized cooling again, and finally 183 $\mu\mathrm{s}$ of INPH-mode-optimized cooling. (c) shows simultaneous cooling of all three axial modes. The coupling between the OOPH and ALT modes is turned on simultaneously with an EIT pulse that is optimized to cool all three modes. Cooling sequences for (b) and (c) are described in colored blocks above each plot.

occupation that is lower than the mode's Doppler-cooled occupation, even if the mode frequency does not satisfy the EIT cooling condition (Eq. 4.10). However, when the interleaved method is used, cooling a second mode b after the first mode a will cause mode a to heat up towards its equilibrium occupation given the second parameter set that is optimized for mode b, as seen in Figs. 4.11(b) and 4.12(b) at the end of the cooling sequence. Thus, the last EIT pulse is typically stopped before the

mode occupations reach equilibrium to achieve a lower final occupation for all modes.

As seen in Figs. 4.11 and 4.12, the simultaneous method cools all modes more quickly, but cannot achieve the same minimum occupation for each mode compared to the interleaved method, since the cooling is not optimized for any of the modes. For ${}^9\mathrm{Be}^{+}$ _25Mg $^+$, the interleaved method achieved $\bar{n}_{\mathrm{INPH}} = 0.21 \pm 0.02$ and $\bar{n}_{\mathrm{OOPH}} = 0.29 \pm 0.02$, while the simultaneous method achieved $\bar{n}_{\mathrm{INPH}} = 0.46 \pm 0.05$ and $\bar{n}_{\mathrm{OOPH}} = 0.39 \pm 0.04$, where the subscripts correspond to the mode whose occupation is being observed. For ${}^9\mathrm{Be}^{+}$ _25Mg $^+$ _9Be $^+$, the interleaved method achieved $\bar{n}_{\mathrm{INPH}} = 0.35 \pm 0.03$, $\bar{n}_{\mathrm{OOPH}} = 0.19 \pm 0.02$, and $\bar{n}_{\mathrm{ALT}} = 0.31 \pm 0.03$ (in this case taking the points closest to 1200 μ s as the "final" occupations), while the simultaneous method achieved $\bar{n}_{\mathrm{INPH}} = 0.70 \pm 0.05$, $\bar{n}_{\mathrm{OOPH}} = 0.35 \pm 0.03$, and $\bar{n}_{\mathrm{ALT}} = 0.36 \pm 0.03$.

For simultaneous cooling in the ${}^9\mathrm{Be}^{+}$ - ${}^{25}\mathrm{Mg}^{+}$ crystal, the beam parameters were $\Omega_{\mathrm{pump}}/2\pi = 29.3 \pm 0.8$ MHz, $\Omega_{\mathrm{probe}}/2\pi = 4.40 \pm 0.11$ MHz, and $\Omega_{\mathrm{repump}}/2\pi = 1.51 \pm 0.05$ MHz. The beam parameters used for interleaved cooling of ${}^9\mathrm{Be}^{+}$ - ${}^{25}\mathrm{Mg}^{+}$ are shown in Table 4.1.

Mode	$\Omega_{\mathrm{pump}}/2\pi \ (\mathrm{MHz})$	$\Omega_{\mathrm{probe}}/2\pi \ (\mathrm{MHz})$
INPH	31.8 ± 0.8	3.94 ± 0.11
ООРН	44.1 ± 1.1	4.48 ± 0.12

Table 4.1: The beam parameters for interleaved cooling of the $^9\mathrm{Be}^+$ - $^{25}\mathrm{Mg}^+$ ion crystal, with $\Omega_\mathrm{repump}/2\pi=1.47\pm0.05$ MHz for both cooling settings.

The beam parameters used for interleaved cooling of ${}^9\mathrm{Be}^+$ - ${}^{25}\mathrm{Mg}^+$ - ${}^9\mathrm{Be}^+$ are shown in Table 4.2. For simultaneous cooling in the ${}^9\mathrm{Be}^+$ - ${}^{25}\mathrm{Mg}^+$ - ${}^9\mathrm{Be}^+$ crystal, the beam parameters were $\Omega_{\mathrm{pump}}/2\pi = 40 \pm 5 \mathrm{\ MHz}$, $\Omega_{\mathrm{probe}}/2\pi = 4.81 \pm 0.14 \mathrm{\ MHz}$, and $\Omega_{\mathrm{repump}}/2\pi = 1.64 \pm 0.05 \mathrm{\ MHz}$.

Mode	$\Omega_{\mathrm{pump}}/2\pi \ (\mathrm{MHz})$	$\Omega_{ m probe}/2\pi~({ m MHz})$
INPH	32.2 ± 0.9	3.92 ± 0.11
ALT	50.2 ± 1.2	5.59 ± 0.15

Table 4.2: The beam parameters for interleaved cooling of the $^9\mathrm{Be}^+$ - $^2\mathrm{Mg}^+$ - $^9\mathrm{Be}^+$ ion crystal, with $\Omega_{\mathrm{repump}}/2\pi = 1.48 \pm 0.05$ MHz for both cooling settings.

4.3.6 Double(-Dark) EIT Cooling

Laser-cooled systems with complex state structure such as ²⁵Mg⁺ can also be used for extensions to EIT cooling, by making use of a "double EIT" [114] configuration, which should enable a lower final temperature for the mode of interest. This requires the addition of a third laser beam and third ground state; instead of being used as a repump as described up until this point, the third laser beam can be set at a similar detuning to the pump and probe laser in order to create an additional interference feature in the absorption spectrum, as shown in Fig. 4.13. Such interference features have been observed (but not used for cooling) in Ref. [122]. In contrast to the work shown in Ref. [123] where a second mode is cooled by a second bright resonance (which can be called "double-bright EIT cooling"),³⁹ the intention of this method is to use the third beam to better cool a single mode ("double-dark EIT cooling"). This clever use of the third EIT cooling beam was one of the motivations for investigating EIT cooling in this apparatus. For the purposes of differentiating the two methods, the EIT cooling (with repump) method discussed in previous sections will be referred to as "single-EIT cooling" in this section.

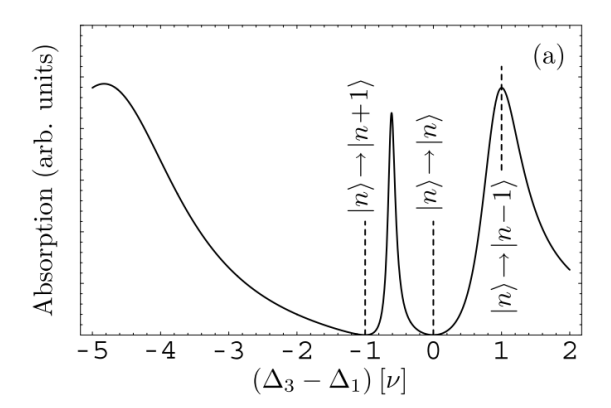


Figure 4.13: Double-EIT absorption spectrum from Ref. [114]. The first-order motion-adding scatter $|n\rangle \to |n+1\rangle$ is suppressed in addition to carrier $|n\rangle \to |n\rangle$ scatter, while motion-adding scatter is enhanced (labeled $|n\rangle \to |n-1\rangle$). The horizontal axis is the difference between the probe detuning Δ_3 and the pump detuning Δ_1 in units of the motion frequency ν .

³⁹It does not appear that it is possible to set up this kind of cooling using a tripod system; an "M" shaped system with three ground states and two excited states as in Ref. [123] is required.

In addition to the primary transparency feature that the Λ -EIT-cooling system creates, a second transparency feature can be created by blue-detuning this third beam to $\delta - \nu$, where δ is the detuning of the first two EIT-cooling beams and ν is the motional frequency, instead of using it on-resonance. This should create a second absorption minimum at the motion-adding scatter frequency as shown in Fig. 4.13, which may suppress the dominant motion-increasing effect during regular EIT cooling. This should reduce the expected final temperature to $\mathcal{O}(\eta^2)$, where η is the Lamb-Dicke parameter. Similar schemes for suppressing the motion-adding sideband are proposed in Refs. [124, 125].

The third beam is typically assumed to have similar power to the original pump beam. Therefore, in this section I will refer to the original pump beam as "pump A" and the repump beam as "pump B". For double-EIT cooling, the condition that must be satisfied is [114]

$$\nu = \frac{1}{4\delta} \left(\Omega_{\text{pumpA}}^2 + \Omega_{\text{probe}}^2 + \frac{\Omega_{\text{pumpB}}^2}{2} \right), \tag{4.37}$$

where Ω_{pumpA} and $\Omega_{\text{pumpB}}^{40}$ are the on-resonance Rabi frequencies of the pump A and pump B beams.

Double-EIT cooling was attempted in our experiment on a single 25 Mg⁺ ion crystal with axial frequency $\nu = 2\pi \times 1.18$ MHz using the configuration shown in Fig. 4.14. Unfortunately, the expected significant decrease in steady-state occupation compared to single-EIT [114] was not observed, as seen in Fig. 4.15. This is likely due to the uncompensatable axial micromotion in our apparatus; if it causes an effect as significant as that seen with single-EIT as shown in Fig. 4.9, any property of double-EIT cooling enabling a lower steady state occupation than single-EIT would be completely washed out by the effects of the micromotion sidebands.

For the double-EIT experiments, the probe and pump A beams were detuned to +180 MHz, while pump B was detuned to +178.82 MHz for optimal cooling of the axial mode at frequency 1.18 MHz. The steady-state motional occupation was not significantly affected when the pump B beam

 $^{^{40}}$ The Stark shift contribution of pump B is halved because only the shift on the common excited state matters for the EIT cooling condition.

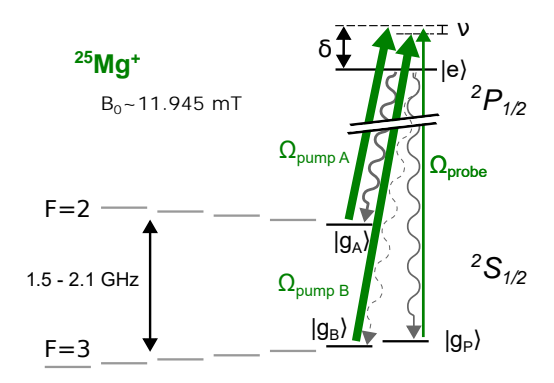


Figure 4.14: Diagram of double EIT cooling configuration for $^{25}{\rm Mg}^+$. Double EIT is performed by using two pump beams (labelled above as "pump A" and "pump B") with similar powers. One of the beams is detuned from resonance by $\delta - \nu$ (where ν is the frequency of the motional mode of interest) while the other two are detuned by δ .

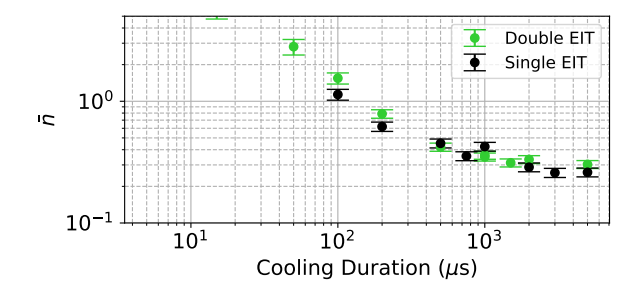


Figure 4.15: Average motional mode occupation after double-EIT cooling (green points) compared to single-EIT-with-repump cooling as described in Sec. 4.3.3.

frequency was changed by $\pm 2\pi \times 1$ MHz, so this frequency was treated as a set parameter, while all three beam powers and the frequency of the probe beam were scanned as described for other EIT cooling experiments in Sec. 4.3.2. It was also found during calibrations that a lower thermal occupation was reached when pump B was significantly weaker in intensity compared to pump A.⁴¹ The calibrated Rabi rates were $\Omega_{\text{pumpA}}/2\pi = 26.33 \pm 0.19$ MHz, $\Omega_{\text{pumpB}}/2\pi = 1.12 \pm 0.10$ MHz, and $\Omega_{\text{probe}}/2\pi = 4.11 \pm 0.32$ MHz, determined as described in Sec. 4.3.7.

The lower steady-state motional occupation expected from double-EIT cooling was not observed, therefore one may be skeptical of this demonstration since an off-resonant repump beam may work

⁴¹This is possibly because the Stark shifts from micromotion sidebands were only easy to account for when they are non-negligible for a single beam.

just as well as a resonant repumper. It could be asked whether I am simply doing the same experiment here as shown in Fig. 4.9! However, frequency scans of the pump B beam appear to indicate that double-EIT cooling was indeed being observed; if the frequency is lowered by $\approx 2\pi \times 2$ MHz, the experimentally determined steady-state motional occupation increased fairly significantly, indicating that there was a local maximum of EIT cooling efficiency for the parameters where it was expected that double-EIT would occur.

4.3.7 Characterizing EIT Laser Beam Properties

The frequencies of each EIT beam were directly referenced to a laser resonant with the $^2S_{1/2}|3,2\rangle \rightarrow ^2P_{1/2}|3,3\rangle$ transition, and thus did not have to be determined.

Radial micromotion was minimized by adjusting voltages on the dc trap electrodes, leaving predominantly axial micromotion (as described in Sec. 3.3.3). The axial micromotion modulation index was then determined by driving the carrier (n=0), first-order (n=1), and second-order (n=2) micromotion sidebands of a Raman transition between hyperfine states. The relative Rabi frequencies of these transitions were then compared⁴² to determine the micromotion modulation index $\beta = 1.164 \pm 0.040$ for the Raman beams. The Raman beams have a difference wavevector along the axial direction, while each of the EIT cooling beams have a wavevector at a 45° angle to the axial direction, therefore, the micromotion modulation index of the EIT cooling beams must be scaled by $1/\sqrt{2}$, giving $\beta = 0.823 \pm 0.028$.

The beam parameters Ω_{pump} , Ω_{probe} , and Ω_{repump} were determined by finding the ac Stark shifts on the ${}^2S_{1/2}|2,2\rangle$, $|3,2\rangle$, and $|3,3\rangle$ states using Ramsey interferometry. Depending on the EIT cooling beam that was characterized, the ion state was put in a superposition of two states in the ${}^2S_{1/2}$ manifold using microwave pulses and the beam was turned on for a certain period of time t_{Stark} before the superposition was reversed again with microwaves. The resulting state would change depending on the length of t_{Stark} with a sinusoidal relationship, as shown in Fig. 4.16.

⁴²Only the data from the carrier and first sideband were used to calculate the micromotion modulation index; the second-sideband Rabi frequency was used to differentiate between micromotion modulation indices that gave the same ratio of carrier-to-first-sideband Rabi frequencies.

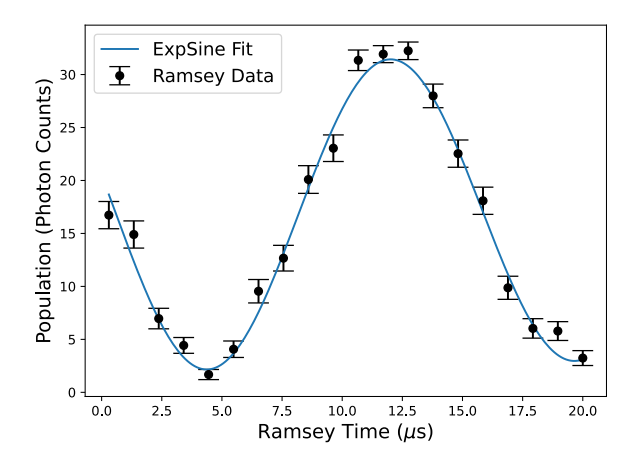


Figure 4.16: A sample Ramsey experiment using a superposition between the ${}^2S_{1/2}|3,2\rangle$ and ${}^2S_{1/2}|3,3\rangle$ states to determine the Pump beam Rabi frequency (black points). The oscillation time (fit shown in blue) was extracted from an exponential sinusoidal fit, and was attributed to a frequency shift of the ${}^2S_{1/2}|3,2\rangle$ state because of the polarization of the beam, which was then used to calculate the on-resonance Rabi frequency of the carrier beam assuming additional Stark shifts from micromotion sidebands, as detailed in text.

The frequency of this oscillation $\Delta f_{\rm Stark}$ is the (angular) frequency shift due to the EIT beam, which is then related to the extracted Ω value for the beam under investigation as

$$\Delta f_{\text{Stark}} = \sum_{j} \sum_{n=-5}^{5} \left(\frac{J_{|n|}(\beta)}{J_{0}(\beta)} \right)^{2} \frac{\Omega^{2}}{4\delta_{nj}},$$
 (4.38)

where $\beta=0.823\pm/0.028$ is the experimentally determined micromotion modulation index, n is the order of micromotion sideband (calculations assumed the total Stark shift was generated by each beam plus its micromotion sidebands up to $\pm 5^{\rm th}$ order; sidebands beyond this order should be negligible for $\beta=0.823\pm0.028$), j indexes all the allowed transitions between the pair of states whose transition shift is being determined and states in the $^2\mathrm{P}_{1/2}$ manifold, and δ_{nj} is the detuning of the nth micromotion sideband from the transition indexed by j. The factor of $J_0(\beta)$ normalizes the extracted Ω so that it is equivalent to an on-resonance Rabi frequency of the carrier only. This choice of definition means that one can directly compare Ω values across cases either with or without micromotion.

Stark shifts due to the ${}^{2}P_{3/2}$ manifold are not considered in this analysis as they are significantly

smaller than that due to states in the ${}^2P_{1/2}$ manifold. The pump beam intensity was determined from the frequency shift on the ${}^2S_{1/2}|3,2\rangle \leftrightarrow {}^2S_{1/2}|3,3\rangle$ transition, which only produces an ac Stark shift on ${}^2S_{1/2}|3,2\rangle$ because of the σ^+ beam polarization. Keeping population in ${}^2S_{1/2}|2,2\rangle$ during the Ramsey sequence when investigating the pump beam was avoided because population was lost from this state too quickly.

The probe beam intensity was determined from the shift on the ${}^2S_{1/2}|2,2\rangle \leftrightarrow {}^2S_{1/2}|3,3\rangle$ transition, which is primarily due to coupling of ${}^2S_{1/2}|3,3\rangle$ to ${}^2P_{1/2}|3,3\rangle$ but contains contributions from the coupling of ${}^2S_{1/2}|2,2\rangle$ to ${}^2P_{1/2}(|2,2\rangle$, $|3,2\rangle$). The hyperfine splitting of around $2\pi \times 1.6$ GHz in the ${}^2S_{1/2}$ manifold and $2\pi \times 250$ MHz in the ${}^2P_{1/2}$ manifold causes the Stark shifts from some of these transitions to have opposing signs. The +180 MHz detuning of the probe beam from resonance with the ${}^2S_{1/2}|3,3\rangle \leftrightarrow {}^2P_{1/2}|3,3\rangle$ transition, and its relatively low power, kept population loss during the Ramsey sequence manageable.

Similar to the pump beam, the repump beam intensity was determined from the frequency shift on the ${}^2S_{1/2} | 2, 2 \rangle \leftrightarrow {}^2S_{1/2} | 3, 3 \rangle$ transition, in which only the shift on the ${}^2S_{1/2} | 2, 2 \rangle$ state was considered. This beam was of low enough intensity that population loss was not a concern.

In some cases, the beam was either too intense or too weak to allow for Stark shift determination.⁴³ In these cases, a depumping experiment was performed. First, the $^{25}\text{Mg}^+$ state was prepared in the nominal ground state of the beam being investigated (for example, the $^2\text{S}_{1/2}|3,2\rangle$ state for the repump beam). Next, the beam was turned on, and the rate at which the population left the prepared state was observed. This was then compared to simulation to find the beam intensity within $\approx 10-20\%$ uncertainty, as shown in Fig. 4.17.

4.4 Summary

In summary, EIT cooling was successfully demonstrated on ²⁵Mg⁺, an ion that has good properties for implementing a field-insensitive qubit but has a complex state structure. ²⁵Mg⁺ was

⁴³It is also possible that there was noise on the Artiq DDS microwaves which prevented a clean Ramsey experiment from being performed.

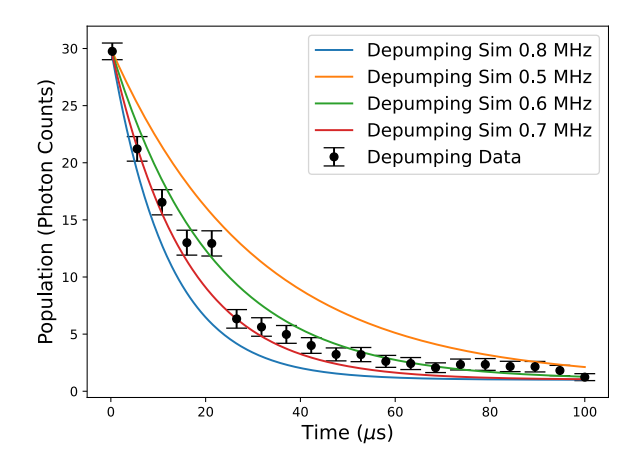


Figure 4.17: A sample depumping scan (black points) of the population found in the ${}^2S_{1/2}|3,2\rangle$ state. The ion was prepared in ${}^2S_{1/2}|3,2\rangle$ and only the pepump beam was turned on. Simulations with repump Rabi frequency $2\pi \times 0.5 - 0.8$ MHz including micromotion sidebands were performed and the curves (solid lines) were compared to the data. In this case, the Rabi frequency was quoted to be $2\pi \times (0.7 \pm 0.15)$ MHz based on the observed similarities between experiment and simulation.

cooled by itself, cooled using non-ideal parameters to demonstrate a broad EIT cooling bandwidth, and used to cool mixed-species ion crystals ${}^{9}\text{Be}^{+}-{}^{25}\text{Mg}^{+}$ and ${}^{9}\text{Be}^{+}-{}^{25}\text{Mg}^{+}-{}^{9}\text{Be}^{+}$. In simulations the axial micromotion present in our apparatus was found to strongly affect the cooling, suggesting that this method would be possibly more successful in ion traps without this experimental imperfection.

A theoretical examination of a simple Λ -structure EIT cooling system was also performed, with a focus on the role of the motion operators. This analysis led to some complex results which are difficult to interpret but appear to be consistent with current theory.

Chapter 5

Mode-Mode Coupling

In an ion trap, the ion internal (atomic) states are well controlled. Very stable, coherent, and long-lived qubits may be implemented using an appropriately-selected subset of these states [51]. In contrast, the quantum harmonic oscillator degree of freedom present in the trapped-ion motion is often relegated to the role of a mediator which enables the atomic states of distinct ions to couple to each other [2, 6, 11, 25, 28, 30, 94, 126]. Motional modes can be chosen so that some or all ions are coupled, so they also play a powerful role in quantum simulation [7, 8, 29, 54].

The control of ion motion is important: at a minimum, this can take the form of good ground-state cooling of all relevant modes, which is either beneficial or necessary for a wide range of experiments. Better motion control can also open up new avenues of exploration using trapped ion motion, including the implementation of bosonic states for quantum error correction [16, 61, 62]. In this chapter, the experimental demonstration of a powerful tool for the motional control of ions is described: the direct coupling of two ion motional modes using an oscillating electronic potential.¹

The idea of coupling two modes of ion motion together in order to exchange their states either partially or fully has been previously investigated using trapped ions [18, 70, 128–130]. An ion motion state can be moved from one mode to another using laser² fields [25, 28, 38, 42, 94, 126] through the ion internal states, by tuning the frequencies of ions trapped in two separate wells close to each other [128, 130], or by a modulation of the electric field that the ion is immersed in [70,

¹A related work using static potentials was inspired by this work [127].

²To my knowledge, demonstrations of motion state transfer between modes using microwave fields have not been made, but this should also be possible using techniques similar to those in Refs. [6, 11, 30].

129]. However, the former two techniques have relatively slow coupling rates (for example, in [18] a conditional beamsplitter operation is completed in 2.5 kHz). In this experiment, we extend the latter technique, parametric modulation of the electric field, to apply it in a more general way, demonstrating coupling rates that are useful (in the tens to hundreds of kHz range) compared to the motional coherence time of our trapped ions.

The "mode-mode coupling" project (henceforth referred to as "mode coupling" for brevity) was initially inspired by the paradigm in our experimental team of using ${}^{9}\text{Be}^{+}$ as the "qubit" ion and ${}^{25}\text{Mg}^{+}$ as the "helper" ion, for example in [13, 47], where ${}^{25}\text{Mg}^{+}$ would ideally perform any dissipative functions, including cooling. The glaring issue with this paradigm is that in the three-ion crystal 3 ${}^{9}\text{Be}^{+}$ - ${}^{25}\text{Mg}^{+}$ - ${}^{9}\text{Be}^{+}$, ${}^{25}\text{Mg}^{+}$ (ideally) does not participate in the middle-frequency axial mode 4 (out-of-phase or OOPH mode) at all (see Fig. 3.20), making direct cooling of this mode using ${}^{25}\text{Mg}^{+}$ impractical.

To counter this, the OOPH mode and alternating (ALT) modes of a ${}^{9}\text{Be}^{+}_{}^{25}\text{Mg}^{+}_{}^{9}\text{Be}^{+}$ ion crystal were coupled using a parametrically modulated voltage on the DC ion trap electrodes, and thus the "mode-coupling" operation was born.⁵ The idea was to use this modulation to exchange the motional state of the ALT mode that is straightforwardly cooled by the ${}^{25}\text{Mg}^{+}$ with the OOPH mode in order to enable cooling of this mode through ${}^{25}\text{Mg}^{+}$. After this was found to be successful, a few more immediate applications of the mode-coupling operation were explored, as will be discussed in Sec. 5.6 and 5.7. The results that are described in this chapter are contained primarily in the publications Refs. [98, 131].

In particular, the mode-coupling operation is useful in circumventing one of the barriers to exploring trapped-ion motion states: because fluorescence detection is usually used to read out trapped ions, data collection means exposing the fluorescing ions to photon recoil. Thus, even if the ion motion state is correctly represented by the result of the fluorescence detection (i.e. all

³This is the smallest possible type of ion crystal with one helper and two qubits (between which to do a two-qubit gate). Also around 2019-2020 it was found that it was very difficult to keep a four-ion crystal in our aging apparatus.

⁴While this is true of the radial modes too, here we focus on the axial modes as most of our operations are on this mode. Radial modes are discussed in Section 5.6.

⁵In our apparatus at least.

operations occur without errors), it is possible that the resulting recoil will corrupt the motion state, making repeated projections⁶ or mid-circuit readout (where the motion state needs to be manipulated further after readout) difficult.⁷

In order to prevent the motion state from being affected by photon recoil without using post-selection on dark detections, the "problem" that inspired the mode-coupling investigation, the inability of $^{25}\text{Mg}^+$ to directly affect the OOPH mode of $^{9}\text{Be}^{+}$ - $^{25}\text{Mg}^{+}$ - $^{9}\text{Be}^{+}$, is utilized for the implementation of a protected mode (also investigated concurrently by groups at the university of Oregon [132] and MIT Lincoln Labs). The OOPH mode is unaffected by photon recoil of $^{25}\text{Mg}^+$, and rapid swap operations enabled by the mode coupling operation enables the use of a second mode to access the motion state information through $^{25}\text{Mg}^+$, as described in Sec. 5.7.

In this chapter, $|\downarrow\rangle_{\rm M}$ can be taken as $^{25}{\rm Mg}^+$ $^2{\rm S}_{1/2}|3,3\rangle$ (which fluoresces), and $|\uparrow\rangle_{\rm M}$ as $^{25}{\rm Mg}^+$ $^2{\rm S}_{1/2}|2,2\rangle$ which is transferred to $^2{\rm S}_{1/2}|2,-2\rangle$ (which is minimally fluorescing) before detection, except when performing the Cirac-Zoller sequence shown described in Sec. 5.7.1.

5.1 Theory

In this section, the theoretical expressions describing the mode coupling potential as well as the time-evolution of the creation and annihilation operators of the two modes under the mode coupling potential are described.

5.1.1 Mode Coupling Potential and Hamiltonian

The calculations here rely heavily on the theoretical background shown in Sec. 2.1.3. While the derivations shown in that chapter rely on the assumption that the modes in the radial direction are completely decoupled from the axial modes and are not of interest, the radial modes will play a role in this chapter, so that assumption is dropped. Suppose that *on top of the confining potential*,

⁶I like to think of this in a similar manner to fluorescence detection, where multiple results increase the chances of a correct readout result.

⁷One way this has been circumvented in the past is by post-selecting results on "dark detections" [16, 18, 32]. Because photon recoil should ideally only occur if the ion fluoresces, the result corresponding to lack of fluorescence does not corrupt the motion. However, this means that any result corresponding to fluorescence must be discarded, greatly decreasing the efficiency of experimental data collection.

an oscillating electric potential to couple two modes with frequency ω_{a,i_a} and ω_{b,i_b} (where a,b index the mode, and $i_a, i_b \in \{x, y, z\}$ index the corresponding direction) is applied:

$$\Phi_{\text{mod}}(\mathbf{r}, t) = \Phi_{\text{m}}(\mathbf{r}) \cos(\omega_m t + \phi), \qquad (5.1)$$

where $\mathbf{r} = (r_x, r_y, r_z)$ is the position of the ion, t is time, $\Phi_{\rm m}(\mathbf{r})$ describes the spatial variation of the potential at position \mathbf{r} , ϕ is the phase of the coupling drive, and $\omega_m = \omega_{(b,i_b)} - \omega_{(a,i_a)}$ is the applied coupling drive frequency, which is set to be at the difference of the two mode frequencies.

The spatial variation term can be expanded about the equilibrium position $\mathbf{r}_{0,n}$ of ion n by

$$\Phi_{\mathbf{m}}(\mathbf{r}_{0,n} + \delta \mathbf{r}_{n}) \approx \Phi_{\mathbf{m}}(\mathbf{r}_{0,n}) + \sum_{i \in \{x,y,z\}} \left. \frac{\partial \Phi_{\mathbf{m}}}{\partial i} \right|_{\mathbf{r} = \mathbf{r}_{0,n}} \delta r_{n,i} + \frac{1}{2} \sum_{i,j \in \{x,y,z\}} \left. \frac{\partial^{2} \Phi_{\mathbf{m}}}{\partial i \partial j} \right|_{\mathbf{r} = \mathbf{r}_{0,n}} \delta r_{n,i} \delta r_{n,j}, \quad (5.2)$$

where $\delta \mathbf{r}_n = (\delta r_{n,x}, r_{n,y}, r_{n,z})$ is a small deviation of the position of ion n from its equilibrium position.

By combining Eq. 2.37 and Eq. 2.39, operating in the interaction frame of the ion motion, this movement from the ion equilibrium position may be expressed as:

$$\delta r_{n,i} = \hat{q}_{n,i} = \frac{1}{\sqrt{m_n}} \sum_{p=1}^{N} \chi_{n,(p,i)} \sqrt{\frac{\hbar}{2\omega_{(p,i)}}} \left(\hat{a}_{(p,i)}^{\dagger} e^{i\omega_{(p,i)}t} + \hat{a}_{(p,i)} e^{-i\omega_{(p,i)}t} \right), \tag{5.3}$$

where $i \in \{x, y, z\}$ indexes the direction of motion, N is the total number of ions or modes along a single direction, m_n is the mass of ion n, $\chi_{n,(p,i)}$ is the participation of ion n in mode p along direction i, and $\hat{a}_{(p,i)}$ and $\omega_{(p,i)}$ are the corresponding annihilation operator and frequency of motion.

Now, Eq. 5.3 can be substituted into Eq. 5.2 and the result can then be substituted into Eq. 5.1. Assuming all mode frequencies are fairly distinct, the rotating wave approximation can be applied to simplify the resulting equation. There will be terms rotating at sums and differences of motion frequencies (which are on the order of MHz) everywhere from Eq. 5.3, except for those that

⁸While this notation is a bit unwieldy, the double index (p, i) is done to index N modes in each of the three directions.

nearly cancel with the $\cos(\omega_m t + \phi)$ term in Eq. 5.1. The term required for this cancellation is the difference of two mode frequencies from the contributions of Eq. 5.3, which can only result from the last term in Eq. 5.2 which is a product of two $\delta r_{n,i}$ terms. In addition to the directions i and j, the modulation frequency $\omega_m = \omega_{b,i_b} - \omega_{a,i_a}$ also picks out the modes in the sum in Eq. 5.3 that are part of the slowly rotating terms to be the modes indexed by (a, i_a) and (b, i_b) .

With this simplification (where I use p = a, b to indicate a particular term from Eq. 5.3 inside the sum), the potential at ion n is given by

$$\hat{\Phi}_{\text{mod}}(\mathbf{r}_n, t) \approx \left[\frac{1}{2} \left. \frac{\partial^2 \Phi_{\text{m}}}{\partial i_a \partial i_b} \right|_{\mathbf{r} = \mathbf{r}_{0,n}} (\delta r_{i_a})_{p=a} (\delta r_{i_b})_{p=b} + \frac{1}{2} \left. \frac{\partial^2 \Phi_{\text{m}}}{\partial i_b \partial i_a} \right|_{\mathbf{r} = \mathbf{r}_{0,n}} (\delta r_{i_b})_{p=b} (\delta r_{i_a})_{p=a} \right]$$
(5.4)

$$= \left[\frac{\partial^2 \Phi_{\mathrm{m}}}{\partial i_a \partial i_b} \Big|_{\mathbf{r} = \mathbf{r}_{0,n}} \frac{\hbar}{2m_n} \frac{\chi_{n,(a,i_a)}}{\sqrt{\omega_{(a,i_a)}}} \left(\hat{a}^{\dagger}_{(a,i_a)} e^{i\omega_{(a,i_a)}t} + \hat{a}_{(a,i_a)} e^{-i\omega_{(a,i_a)}t} \right) \times \frac{\chi_{n,(b,i_b)}}{\sqrt{\omega_{(b,i_b)}}} \left(\hat{a}^{\dagger}_{(b,i_b)} e^{i\omega_{(b,i_b)}t} + \hat{a}_{(b,i_b)} e^{-i\omega_{(b,i_b)}t} \right) \cos(\omega_m t + \phi)$$

$$(5.5)$$

$$\approx \frac{\hbar}{4m_n} \left. \frac{\partial^2 \Phi_{\rm m}}{\partial i_a \partial i_b} \right|_{\mathbf{r} = \mathbf{r}_{0,n}} \frac{\chi_{n,(a,i_a)} \chi_{n,(b,i_b)}}{\sqrt{\omega_{(a,i_a)} \omega_{(b,i_b)}}} \left(\hat{a}^{\dagger}_{(a,i_a)} \hat{a}_{(b,i_b)} e^{i\phi} + \hat{a}_{(a,i_a)} \hat{a}^{\dagger}_{(b,i_b)} e^{-i\phi} \right), \tag{5.6}$$

where \mathbf{r}_n is the position of ion n, and I have used the equivalence of mixed partial derivatives as well as the fact that creation/annihilation operators of different modes commute in order to combine the two terms in Eq. 5.4 into one.

The Hamiltonian term from the modulation potential can be treated as a sum over the potential at the position of each ion times the charge q_n of that ion:

$$\hat{H}_{\text{mod}} = \sum_{n=1}^{N} q_n \hat{\Phi}_{\text{mod}}(\mathbf{r}_n, t). \tag{5.7}$$

Making the definitions

$$\alpha_{n,(a,b)} := \frac{\partial^2 \Phi_{\mathbf{m}}}{\partial i_a \partial i_b} \Big|_{\mathbf{r} = \mathbf{r}_{0,n}}, \qquad g_{n,(a,b)} := \frac{q_n \alpha_{n,(a,b)}}{4m_n} \frac{\chi_{n,(a,i_a)} \chi_{n,(b,i_b)}}{\sqrt{\omega_{(a,i_a)} \omega_{(b,i_b)}}}, \qquad g_{(a,b)} := \sum_{n=1}^N g_{n,(a,b)}, \quad (5.8)$$

where $\alpha_{n,(a,b)}$ is the element along directions (a,b) of the curvature matrix of the potential Φ_m at the position of ion n, and $g_{n,(a,b)}$ and $g_{(a,b)}$ are the coupling rates for each ion n and the total coupling rate of the operation respectively. Using these, the Hamiltonian can be written as

$$\hat{H}_{\text{mod}} = \hbar g_{(a,b)} \left(\hat{a}_{(a,i_a)}^{\dagger} \hat{a}_{(b,i_b)} e^{i\phi} + \hat{a}_{(a,i_a)} \hat{a}_{(b,i_b)}^{\dagger} e^{-i\phi} \right). \tag{5.9}$$

For ease of notation, for the rest of this chapter

$$g_{(a,b)} \to g, \qquad \hat{a}_{(a,i_a)} \to \hat{a}, \qquad \hat{a}_{(b,i_b)} \to \hat{b},$$
 (5.10)

so that

$$\hat{H}_{\text{mod}} = \hbar g \left(\hat{a}^{\dagger} \hat{b} e^{i\phi} + \hat{a} \hat{b}^{\dagger} e^{-i\phi} \right). \tag{5.11}$$

From this calculation, it can be seen that the coupling rate (which is also referred to as the coupling constant) g is a sum of coupling rates due to each ion g_n . Depending on the sign of α_n and $\chi_{n,(a,i_a)}\chi_{n,(b,i_b)}$, it is possible that the g_n 's will sum constructively or destructively. For efficient coupling, it is important for the curvature to match the product of the mode participations χ so that destructive interference between coupling terms g_n is minimized.

5.1.2 Time Evolution of Coupled Motional States

When two modes represented by ladder operators \hat{a} and \hat{b} are coupled by the Hamiltonian Eq. 5.11, their states of motion will become entangled and, after an exchange of population, disentangled, in a periodic fashion. The time-dependent states can be found by first performing a

basis transformation

$$\hat{c}_{+} = \frac{1}{\sqrt{2}} \left(\hat{a} + e^{i\phi} \hat{b} \right)$$

$$\hat{c}_{-} = \frac{1}{\sqrt{2}} \left(\hat{a} - e^{i\phi} \hat{b} \right), \qquad (5.12)$$

which diagonalizes the interaction Hamiltonian Eq. 5.11

$$\hbar g \left(\hat{a}^{\dagger} \hat{b} e^{i\phi} + \hat{a} \hat{b}^{\dagger} e^{-i\phi} \right) = \hbar g \left(\hat{c}_{+}^{\dagger} \hat{c}_{+} - \hat{c}_{-}^{\dagger} \hat{c}_{-} \right). \tag{5.13}$$

The right hand side represents two harmonic oscillators with energies separated by twice the interaction energy $\hbar g$. In the interaction frame of reference, these oscillators have simple equations of motion

$$\hat{c}_{\pm}^{\dagger}(t) = \hat{c}_{\pm}^{\dagger}(0) \exp(\pm igt). \tag{5.14}$$

Writing $\hat{a}^{\dagger}(0) = \hat{a}^{\dagger}$, $\hat{b}^{\dagger}(0) = \hat{b}^{\dagger}$ for brevity and inserting the time dependence into the equations for $\hat{a}(t)$ and $\hat{b}(t)$ yields

$$\hat{a}^{\dagger}(t) = \hat{a}^{\dagger}\cos(gt) + ie^{i\phi}\hat{b}^{\dagger}\sin(gt)$$

$$\hat{b}^{\dagger}(t) = \hat{b}^{\dagger}\cos(gt) + ie^{-i\phi}\hat{a}^{\dagger}\sin(gt).$$
(5.15)

Any state of the oscillators at time t can be written as a superposition of number states with complex amplitudes c_{mn} by acting with different combinations of creation operators on the vacuum state $|0\rangle_a |0\rangle_b$,

$$|\Psi_a(t)\rangle |\Phi_b(t)\rangle = \sum_{m,n=0}^{\infty} \frac{c_{mn}}{\sqrt{m!n!}} \left[\hat{a}^{\dagger}(t) \right]^m \left[\hat{b}^{\dagger}(t) \right]^n |0\rangle_a |0\rangle_b, \qquad (5.16)$$

such that the time dependence is fully captured in the creation operators. For general times t this implies a rather complicated entangled state of the modes, which becomes simpler for certain evolution times. For example by setting $\tau_{\rm BS}=\pi/(4g)$ and applying the trigonometric factors

 $\sin(g\tau_{\rm BS}) = \cos(g\tau_{\rm BS}) = 1/\sqrt{2}$, Eq.(5.11) turns into a beamsplitter relation [133] that can be used to demonstrate the Hong-Ou-Mandel effect, here for two modes at different frequencies.

Eq.(5.11) simplifies even more for $\tau_k = k\pi/(2g)$ with k a positive integer. For k odd this yields

$$\hat{a}^{\dagger}(\tau_k) = ie^{i(g\tau_k + \phi)}\hat{b}^{\dagger}$$

$$\hat{b}^{\dagger}(\tau_k) = ie^{i(g\tau_k - \phi)}\hat{a}^{\dagger}, \qquad (5.17)$$

which implies that $|\Psi_a(\tau_k)\rangle |\Phi_b(\tau_k)\rangle$ with k odd has the original states of modes a and b swapped and shifted by a phase $g\tau_k$ per phonon, plus or minus ϕ . This phase difference arises relative to that of the uncoupled evolution of the modes and can be thought of as a consequence of the coupling that modifies the energies of the eigenstates with the additional factors due to the phase ϕ of the applied drive. For k even

$$\hat{a}^{\dagger}(\tau_k) = e^{ig\tau_k}\hat{a}^{\dagger}$$

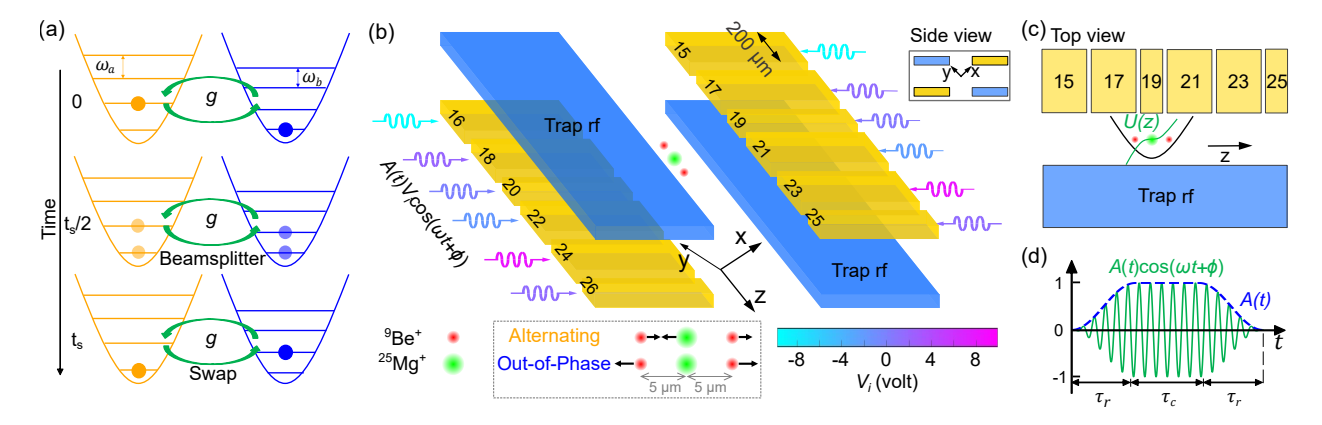
$$\hat{b}^{\dagger}(\tau_k) = e^{ig\tau_k}\hat{b}^{\dagger}, \qquad (5.18)$$

which signifies one or several complete back-and-forth exchanges and a phase shift due to the coupling energy. Up to this phase shift, the state $|\Psi_a(\tau_k)\rangle |\Phi_b(\tau_k)\rangle$ with k even is identical to the one at t=0 in the interaction frame of reference.

5.2 Waveforms

The mode-coupling waveforms are applied to the twelve DC electrodes nearest to the trapping region (numbered DCs 15-26, see Fig. 5.1(b)). The voltage amplitudes required on each electrode to generate the desired spatial variation at the ion(s) are calculated using a trap potential simulation based on the boundary element method [89]. The relative voltage amplitude for each electrode is indicated by the color of the wavy arrow to each electrode in Fig. 5.1(b). These fields were tailored to

couple the desired modes depending on the "optimal" theoretical potential according to Eqs. 5.8 and 5.11. For example, to couple the OOPH and ALT axial modes of ${}^{9}\text{Be}^{+}$ - ${}^{25}\text{Mg}^{+}$ - ${}^{9}\text{Be}^{+}$, the waveform was optimized for the largest cubic potential term in the axial direction (maximizing $\partial^{2}\Phi/\partial z^{2}$) while minimizing the linear term which will displace the ion (Fig. 5.1(c)). To couple axial and radial modes in ${}^{9}\text{Be}^{+}$ - ${}^{9}\text{Be}^{+}$ or ${}^{9}\text{Be}^{+}$ - ${}^{25}\text{Mg}^{+}$, a potential proportional to xz or yz was applied (where the radial mode along the \mathbf{x} or \mathbf{y} direction is coupled to the axial mode, respectively). Only modes with the same parity in both the axial and radial directions were coupled (OOPH modes in all dimensions only), so this curvature allowed the coupling constants g_n of the two ions to add constructively.



In order to reduce the impact of unintentional off-resonant driving of modes by the mode-

⁹While for three ions a good potential curvature can be found, it may be difficult to create the curvatures required for the highest possible g value (according to Eq. 5.8) for larger ion crystals where the mode participation products become more complicated, especially if the electrodes are large compared to the ion crystal extent. However, in these cases it is still possible to perform mode-coupling as long as g does not equal zero.

coupling operation or (sub)harmonics thereof, the oscillating voltage waveform applied to each electrode was shaped with an envelope with on and off ramps of 20 μ s duration that were approximately \sin^2 shaped and flat otherwise (see Fig. 5.1(d)). Because of this, the minimum pulse area is limited to that equivalent to a square pulse of 20 μ s duration,¹⁰ and the calibration procedure yields the duration of the flat part between the ramp up and ramp down sections. With this choice of ramp durations, swap durations near or below 20 μ s could not be used (resulting in the irregular spacing between the first and second points in some of the time scans). Square coupling pulses without shaping caused significant off-resonant heating of the in-phase (INPH) mode at 1.5 MHz when attempting to couple two modes with a 0.28 MHz frequency difference in the 9 Be⁺- 2 Mg⁺- 9 Be⁺ ion crystal.

5.3 Experimental Considerations for Performing Mode Coupling with the X-Trap

Before beginning this project, it was already possible to generate the desired curvatures to couple various modes of a few different ion crystals together given the existing DC electrode geometry of the X-trap [89, 90]. Moreover, these electrodes are driven by a set of arbitrary waveform generators (PDQs [95]) that are capable of generating many of the necessary frequencies and reasonable voltages (±10V max). For all mode-coupling potentials, an extra oscillating voltage was added on top of the usual trapping voltage that was sent to each electrode using these PDQs.

Unfortunately, two major barriers to rapid mode coupling exist in the current configuration. First, the output amplifiers of the PDQs have a 1 MHz bandwidth, and there are low-pass filters to each DC electrode¹¹ within the vacuum chamber on the ion trap wafer with a corner frequency of 810 KHz (in addition to external filters with an even lower cutoff frequency of about 50 kHz) to suppress noise at our motion frequencies [89], which are typically 1-2 MHz (Sec. 3.6). These

 $^{^{10}}$ The integrated area under the two cubic-spline envelope sections ideally gives the same area as a full-amplitude 20 μs long pulse.

¹¹It is possible to use the RF electrodes for coupling (although these also have bandpass filters for the RF drive frequency of 82.529 MHz), but curvatures other than that of the rf-quadrupole would not be possible to implement.

frequency filters are difficult to modify and strongly attenuate mode-coupling signals with frequencies above the filter cutoff frequencies. Therefore, the demonstrations of coupling realized in the X-trap are limited to modes with low frequency differences, with decreasing coupling rates achievable as the frequency increases due to the various forms of frequency-dependent attenuation present. This precludes, for example, coupling of the axial in-phase (INPH) and OOPH or ALT modes of the ${}^9\text{Be}^+$ - ${}^2\text{SMg}^+$ - ${}^9\text{Be}^+$ crystal, which have a frequency difference greater than 1.8 MHz. The maximum frequency difference between modes coupled in this apparatus is ≈ 0.7 MHz. By adjusting the well slightly to bring target coupled modes closer together (as is described in Sec. 5.6), this problem can be alleviated but such an adjustment reduces the experimental duty cycle. Moreover, care must be taken to ensure that the modes do not mix in an uncontrolled manner while this adjustment is performed.

The second experimental barrier is that the PDQs are not phase-synchronized to our ARTIQ crate (as discussed in Sec. 3.4), meaning that coherent operations involving both the mode-coupling operation and the lasers and/or microwaves could not be performed.¹² Therefore, operations were restricted to those where phases in all motion superpositions were controlled (such as in a Ramsey-style experiment) by either the lasers/microwaves or the mode-coupling operation. For example, in some experiments, the lasers and microwaves were used to establish a superposition of motional Fock states, then the mode-coupling operation was used to perform full swaps, before microwaves were again used at the end of the sequence. Because the mode-coupling operation in this case was only used to fully swap the motion states with each other, no issues arose from the lack of phase synchronization of the different pulses.

Finally, while the trap has good flexibility (outside of frequency restrictions from filters) in terms of coupling axial modes, the trap geometry would make it difficult to couple two (ideal) radial modes along the same axis if one has odd ion participation symmetry (about the middle ion) and the other is even, since the required cubic potential cannot be generated with the available DC electrodes.

¹²The phase between PDQ channels also tended to drift, but this was slow enough that re-setting the phases at the beginning of each experimental data collection sequence enabled the required operations to be completed before this error became a significant issue.

While some attempt may be made by involving the RF and bias electrodes, it would be difficult to properly null the linear term which could cause uncontrolled changes in the ion position. There is a trap in use at the University of Oregon that is a 3D four-rod-type Paul trap with an additional four rods outside the main trapping rods for shim adjustments [132]. A trap of this geometry is suitable for coupling two such radial modes, but it should be noted that this particular trap cannot perform the same coupling along the axial modes as demonstrated here because it lacks segmented DC electrodes in the axial direction. The desired coupling in these cases may also be achieved by coupling to a third mode that can be coupled to both modes of interest (for example, a coupling between two \mathbf{x} modes can be performed by coupling the first \mathbf{x} to a \mathbf{z} mode, then coupling that \mathbf{z} mode to the second \mathbf{x} mode). This extra step will add infidelity and extra time to the experiment.

5.4 Calibrations

In order to calibrate the mode-coupling operation, the sequence shown in Fig. 5.2(a) was performed. Here, the calibration procedure for the coupling of the OOPH and ALT axial modes in ${}^{9}\text{Be}^{+}$ - ${}^{25}\text{Mg}^{+}$ - ${}^{9}\text{Be}^{+}$ is described as an example, but the calibrations for coupling other pairs of modes in other crystals proceeded similarly; calibrations for other crystals cooled using mode-coupling is discussed in Sec. 5.6.

First, all relevant modes¹³ were cooled as close to the ground state as experimentally possible on our apparatus: $\bar{n} \approx 0.25$, 0.02, and 0.07 for the INPH, OOPH, and ALT modes respectively.¹⁴ Then, one phonon was added to the ALT mode using a motion-adding Raman sideband on ²⁵Mg⁺, preparing $|0\rangle_{\rm O}$ and $|1\rangle_{\rm A}$ on the OOPH and ALT modes respectively (where the first letter of each mode is used to indicate the motion state in that mode). Using mode frequencies determined with Raman sidebands to make an initial guess, the mode coupling operation was applied, and the frequency of the operation was scanned around the expected frequency difference of the two modes

¹³In this case, only the axial modes were cooled, but any modes found to negatively impact the fidelity of the motion data should be cooled as close to the ground state as possible.

 $^{^{14}}$ In the experiment described in Sec. 5.7 on repeated motion state detections, the ALT mode was cooled to $\bar{n} \approx 0.02$ at the beginning of each sequence using increased $^{25}\text{Mg}^+$ Raman beam power compared to other experiments in this chapter.

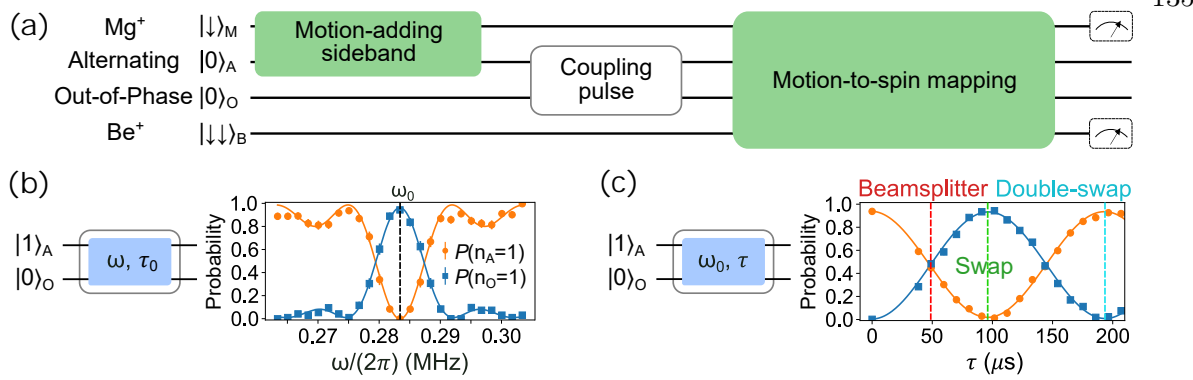


Figure 5.2: (a) shows the sequence for performing calibrations of the mode coupling operation between the ALT and OOPH mode. With all ion internal states initialized in $|\downarrow\rangle$ and the Fock states of both modes cooled close to the ground state, a phonon is added to the ALT mode using a motion-adding sideband pulse through $^{25}\mathrm{Mg}^+$. Then, the coupling pulse is applied with either the frequency (results shown in (b)) or time (results shown in (c)) scanned, while the other is fixed to the resonant frequency ω_0 or time for a full swap, as appropriate. Afterwards, a motion-subtracting sideband is used to check whether there is a phonon present in the ALT or OOPH mode using fluorescence detection on $^9\mathrm{Be}^+$. The data shown was observed after iterating both the frequency and time scan to find the correct ω_0 and swap time. When the calibration parameters are close to ideal, this step (the motion-subtracting sideband and fluorescence detection) may be done using $^{25}\mathrm{Mg}^+$ as well. The data shown in (b) and (c) have the ALT mode probed using $^{25}\mathrm{Mg}^+$ and the OOPH mode probed using $^9\mathrm{Be}^+$; the data in (b) is fit to a sinc² function while the data in (c) is fit to a sinusoidal function with an exponential decay envelope.

(Fig. 5.2(b)). In order to determine whether a phonon existed in a mode, a motion-subtracting sideband (MSS) of the form Eq. 2.67 was driven¹⁵ on ⁹Be⁺ (this was also be done on ²⁵Mg⁺ when appropriate¹⁶). If the phonon was present in the mode that is probed, the ion internal state changed; this was read out by fluorescence detection.

In order to determine whether the ${}^{9}\text{Be}^{+}$ ions were in the $|\text{Bright}\rangle$ state or not, the photon counts of a reference dataset were extracted using maximum likelihood estimation (MLE) to determine the Poissonian mean photon counts of N=0,1,2 ${}^{9}\text{Be}^{+}$ ions in the bright state. Then, the probability $P_{b}(N)$ of N ${}^{9}\text{Be}^{+}$ ions being present in the bright state was determined for the coupling calibration

 $^{^{15}}$ In order to make the operation ambiguous, I use the language "motion-adding" and "motion-subtracting" sideband; depending on which pseudo-spin- $\frac{1}{2}$ state is the initial state, the operation described by either Eq. 2.67 or Eq. 2.68 is used.

 $^{^{16}}$ The detection is initially performed using 9 Be $^{+}$ because both the OOPH and ALT modes can be probed using lasers on that ion species since it participates in both. However, the presence of a phonon on the ALT mode can be checked using 25 Mg $^{+}$, and if the mode-coupling operation is well-calibrated, it can be used to read out the state of OOPH using 25 Mg $^{+}$.

data shown in Fig. 5.2 using MLE with the fixed and pre-determined Poissonian means.

However, for the characterization experiments described in Sec. 5.5.2, correlations of the populations in different motional modes needed to be evaluated within a single experimental trial so MLE could not be used. For this, photon count thresholds were chosen such that the number of bright ions was distinguished with minimal error for both ion species in each trial and the probability of the joint state (for a certain number of ${}^{9}\text{Be}^{+}$ and ${}^{25}\text{Mg}^{+}$ ions to be bright at the same time) being occupied was obtained over many experiment repetitions. For two ${}^{9}\text{Be}^{+}$ ions, the ions were identified to be both in the bright state when the counts $c_{Be} > 46$; one bright ${}^{9}\text{Be}^{+}$ ion when $13 \le c_{Be} < 46$; and zero bright ions otherwise. A single ${}^{25}\text{Mg}^{+}$ ion was determined to be in the bright state when the photon count $c_{Mg} > 9$, and in the dark state otherwise. The histogram for one bright ion had an overlap of about 1.4% with that of two bright ions and has nearly zero overlap with that of zero bright ions assuming ideal Poisson distributions. In the repeated motional state measurements (Sec. 5.7), the single ${}^{25}\text{Mg}^{+}$ ion population was determined using the threshold method.

The results shown in Fig. 5.2(b),(c) were obtained by mapping the occupation of the OOPH mode onto the spins of the two ${}^9\mathrm{Be^+}$ ions using an MSS (mapping $|0\rangle_\mathrm{O} \to |\downarrow\downarrow\rangle_\mathrm{B}$ and $|1\rangle_\mathrm{O} \to |\uparrow\downarrow\rangle_\mathrm{B}$, where the two ${}^9\mathrm{Be^+}$ ions are not distinguished from each other), while the ALT mode was mapped onto ${}^{25}\mathrm{Mg^+}$ also using an MSS.

The data in Fig. 5.2(a) were both fit to a function of the form

$$P(\omega) = \frac{A\Omega_0^2 \sin^2\left(\frac{\Omega T}{2}\right)}{\Omega^2} + P_0, \tag{5.19}$$

where $\Omega = \sqrt{\Omega_0^2 + (\omega - \omega_0)^2}$ is a generalized frequency, ω is the scanned frequency, ω_0 is the center of the feature, Ω_0 corresponds to the width of the feature (which, according to the derivation performed in Sec. 5.4.1 should equal 2g where g is the coupling rate), A is an amplitude scaling factor (which is negative to fit the oscillation of one of the two modes being probed), T is the pulse time, and P_0 is an offset in the fit (i.e. for dark counts, imperfect state preparation resulting in ground-state population, or the base line of the inverted fit for the opposite mode). The form of this lineshape is

derived in Sec. 5.4.1. Also shown in that section is the fact that two ⁹Be⁺ ions participate when driving ⁹Be⁺ sidebands, which complicates the process somewhat, but the overall lineshape of the feature remains approximately the same.

The center of the transition feature (which may not correspond to a full exchange if the coupling time is not correctly chosen) ω_0 is taken as the correct mode-coupling frequency, which for the scan in Fig. 5.2(b) yields a resonant frequency $\omega_0 \approx 2\pi \times 0.283$ MHz. After the correct coupling frequency is identified, the time of the coupling operation may then be scanned to observe an oscillation of the phonon initially in the ALT mode transferring to the OOPH mode and back (Fig. 5.2(c)). The mode coupling frequency and time scans may be iterated several times to determine the optimal values for the coupling frequency ω_0 as well as the pulse times for beam-splitter, swap, and double-swap operations. The oscillations observed from both the OOPH and ALT modes were then fit to a function of the form

$$P(\tau) = A\sin(\Omega_c \tau + \phi_c)\exp(-\tau/\tau_c) + y_0 \tag{5.20}$$

where A is an amplitude scaling factor, Ω_c is the coupling exchange frequency, ϕ_c is the oscillation phase, and τ_c is the time constant describing the coherence loss, for example through population loss from the oscillation subspace, and y_0 is a vertical offset to the fit, usually close to half of A. The data sets in Fig. 5.2(c) for both modes yield the same exchange rate $\Omega_c/(2\pi) \approx 5.1$ kHz, $A \approx 0.46$ and $y_0 \approx 0.47$. The coherence time was $\tau_{c,E}=24(14)$ ms for $P(n_0=1)$ and $\tau_{c,S}=19(11)$ ms for $P(n_S=1)$, both of which are approximately 200 times longer than the duration of a swap. The results of these calibrations are extremely stable and hold over the course of several months.

5.4.1 Lineshape of Mode Coupling Frequency Data

Here, the frequency-dependent lineshape used for parameter fitting (Eq. 5.19) is derived from the mode coupling Hamiltonian for coupling frequencies slightly detuned from the motion frequency:

$$\hat{H}_{\text{mod}} = \hbar g \left(\hat{a}^{\dagger} \hat{b} e^{i\delta t} + \hat{a} \hat{b}^{\dagger} e^{-i\delta t} \right), \tag{5.21}$$

where δ is the frequency difference from the optimal cooling frequency $\omega - \omega_0$. For simplicity, compared to Eq. 5.11, the phase ϕ is set to 0 for this section.

In the calibration experiments, the coupling pulse duration τ is fixed to be approximately that of a single exchange $\frac{\pi}{2g}$ and the coupling frequency is scanned near the difference between the two modes to be coupled (labeled here with a and b, and $\omega_0 = \omega_b - \omega_a$). The motional information is then extracted through the internal state of either a single ion or two ions. These cases are discussed separately in the following sections.

5.4.1.1 Readout With a Single Ion

When reading out motional information using a single ion, the two motional modes are initially prepared in $|1\rangle_a |0\rangle_b$. Since the Hamiltonian (Eq. 5.21) conserves the total phonon number, this initial state can only ideally couple to $|0\rangle_a |1\rangle_b$. Following a coupling pulse, the motional state can be expressed as

$$|\psi\rangle = c_{10} |1\rangle_a |0\rangle_b + c_{01} |0\rangle_a |1\rangle_b.$$
 (5.22)

By solving the differential equations

$$i\dot{c}_{10} = ge^{i\delta t}c_{01},$$

 $i\dot{c}_{01} = ge^{-i\delta t}c_{10},$ (5.23)

with initial conditions $c_{10}(t=0)=1$ and $c_{01}(t=0)=0$, we obtain

$$c_{10} = \frac{1}{r} \left[\left(\frac{r - \delta}{2} \right) e^{\frac{i(r + \delta)t}{2}} + \left(\frac{r + \delta}{2} \right) e^{-\frac{i(r - \delta)t}{2}} \right] = e^{\frac{i\delta t}{2}} \left[\cos\left(\frac{rt}{2}\right) - \frac{\delta}{r} i \sin\left(\frac{rt}{2}\right) \right]$$

$$c_{01} = -\frac{g}{r} \left(e^{\frac{i(r - \delta)t}{2}} - e^{-\frac{i(r + \delta)t}{2}} \right) = -\frac{g}{r} e^{-\frac{i\delta t}{2}} 2i \sin\left(\frac{rt}{2}\right)$$

$$(5.24)$$

where $r = \sqrt{4g^2 + \delta^2}$. The state populations are

$$p_{10} = |c_{10}|^2 = 1 - \frac{4g^2}{r^2} \sin^2\left(\frac{rt}{2}\right),$$

$$p_{01} = |c_{01}|^2 = \frac{4g^2}{r^2} \sin^2\left(\frac{rt}{2}\right).$$
(5.25)

A BSB π pulse (Eq. 2.68) on mode a drives $|\uparrow\rangle (c_{10}|1\rangle_a|0\rangle_b + c_{01}|0\rangle_a|1\rangle_b$ to $c_{10}|\downarrow\rangle |0\rangle_a|0\rangle_b + c_{01}|\uparrow\rangle |0\rangle_a|1\rangle_b$, which results in the probability of finding the ion in $|\downarrow\rangle$: $p(|\downarrow\rangle) = p_{10}$. A BSB π pulse on mode b yields $p(|\downarrow\rangle) = p_{01}$ by similar logic. Both populations in Eq. (5.25) can be re-expressed in the form of Eq. 5.19 with suitable parameter substitutions.

5.4.1.2 Readout With Two Ions

In the experiments where motional information is read out through two globally addressed ions of the same species, the dynamics appear slightly different than that with one ion. This applies to the ${}^{9}\text{Be}^{+}$ - ${}^{25}\text{Mg}^{+}$ - ${}^{9}\text{Be}^{+}$ crystal and ${}^{9}\text{Be}^{+}$ -green crystal (which is only discussed in Sec. 5.6).

In the case of the ${}^{9}\text{Be}^{+}$ - ${}^{9}\text{Be}^{+}$ ion crystal, a single excitation cannot be prepared with global Raman beams addressing both ions, and this section primarily discusses such an example. The preparation is instead as follows. The crystal is initially prepared in $|\uparrow\uparrow\rangle|0\rangle_{a}|0\rangle_{b}$. A RSB pulse on mode a with a duration of $\pi/(\sqrt{6}\Omega_{0})$ is applied resulting in the state $\frac{2\sqrt{2}}{3}|\downarrow\downarrow\rangle|2\rangle_{a}|0\rangle_{b}-\frac{1}{3}|\uparrow\uparrow\rangle|0\rangle_{a}|0\rangle_{b}$, where Ω_{0} is the ground-state sideband Rabi rate for a single ion. A subsequent repump pulse resets the two ions to $|\downarrow\downarrow\rangle$ and also destroys the coherence of the two components, resulting in a mixture of two states

$$\rho = \frac{1}{9} |\psi\rangle\langle\psi| + \frac{8}{9} |\phi\rangle\langle\phi|, \tag{5.26}$$

where $|\psi\rangle = |\downarrow\downarrow\rangle |0\rangle_a |0\rangle_b$ and $|\phi\rangle = |\downarrow\downarrow\rangle |2\rangle_a |0\rangle_b$. The first component $|\psi\rangle\langle\psi|$ does not evolve into different motion states under the mode coupling operation nor does it change under the second RSB pulse which will be applied later for readout. The second component, $|\phi\rangle$ evolves into $|\phi_{ex}(t)\rangle = |\downarrow\downarrow\rangle (c_{20}|2\rangle_a |0\rangle_b + c_{11}|1\rangle_a |1\rangle_b + c_{02}|0\rangle_a |2\rangle_b)$ during mode coupling. The evolution of the

coefficients in $|\phi_{ex}(t)\rangle$ is governed by

$$i\dot{c}_{11} = \sqrt{2}g(e^{-i\delta t}c_{20} + e^{i\delta t}c_{02})$$

$$i\dot{c}_{20} = \sqrt{2}ge^{i\delta t}c_{11}$$

$$i\dot{c}_{02} = \sqrt{2}ge^{-i\delta t}c_{11}.$$
(5.27)

Solving these equations with the initial conditions $c_{02}(t=0) = 0$, $c_{11}(t=0) = 0$, $c_{20}(t=0) = 1$, the coefficients for $|\phi_{ex}(t)\rangle$ can be seen to be, at a given time t:

$$c_{02} = \frac{2e^{-i\delta t}g^{2}[-1 + \cos(rt)]}{r^{2}}$$

$$c_{11} = \frac{\sqrt{2}g[-\delta(1 - \cos(rt)) - ir\sin(rt)]}{r^{2}}$$

$$c_{20} = \frac{e^{i\delta t}[2g^{2} + (2g^{2} + \delta^{2})\cos(rt) + i\delta r\sin(rt)]}{r^{2}}.$$
(5.28)

After the motion exchange, the system further evolves under an RSB pulse on either mode a or b for analysis, governed by

$$i\dot{c}_{|\downarrow\downarrow\rangle|2\rangle} = \sqrt{2}\Omega_{0}(c_{|\downarrow\uparrow\rangle|1\rangle} + c_{|\uparrow\downarrow\rangle|1\rangle})$$

$$i\dot{c}_{|\downarrow\downarrow\rangle|1\rangle} = \Omega_{0}(c_{|\downarrow\uparrow\rangle|0\rangle} + c_{|\uparrow\downarrow\rangle|0\rangle})$$

$$i\dot{c}_{|\downarrow\uparrow\rangle|1\rangle} = \Omega_{0}(\sqrt{2}c_{|\downarrow\downarrow\rangle|2\rangle} + c_{|\uparrow\uparrow\rangle|0\rangle})$$

$$i\dot{c}_{|\uparrow\downarrow\rangle|1\rangle} = \Omega_{0}(\sqrt{2}c_{|\downarrow\downarrow\rangle|2\rangle} + c_{|\uparrow\uparrow\rangle|0\rangle})$$

$$i\dot{c}_{|\downarrow\uparrow\rangle|0\rangle} = \Omega_{0}c_{|\downarrow\downarrow\rangle|1\rangle}$$

$$i\dot{c}_{|\uparrow\uparrow\rangle|0\rangle} = \Omega_{0}c_{|\downarrow\downarrow\rangle|1\rangle}$$

$$i\dot{c}_{|\uparrow\uparrow\rangle|0\rangle} = \Omega_{0}c_{|\downarrow\downarrow\rangle|1\rangle}$$

$$i\dot{c}_{|\uparrow\uparrow\rangle|0\rangle} = \Omega_{0}(c_{|\downarrow\uparrow\rangle|1\rangle} + c_{|\uparrow\downarrow\rangle|1\rangle}).$$
(5.29)

In this notation, the spectator mode (b if the RSB pulse is on a or vice versa) is omitted as it has no impact on the final population of the internal state. The coefficient of the reduced state is denoted $|i,j\rangle |n\rangle$ where $i,j \in \{\uparrow,\downarrow\}$ and $n \in \{0,1,2\}$, as $c_{|i,j\rangle|n\rangle}$ (and this denotes the motion occupation of the mode involved in the RSB pulse).

In order to track the probability of observing fluorescence results from either $|\uparrow\rangle$ or $|\downarrow\rangle$ after applying an RSB analysis pulse with duration $\pi/(\sqrt{6}\Omega_0)$ on mode a, the coefficients $c_{|i,j\rangle}$ can be calculated using Eq. 5.28 and 5.29. The initial conditions can be set as $c_{|\downarrow\downarrow\rangle|2\rangle_a}(0) = c_{20}$, $c_{|\downarrow\downarrow\rangle|1\rangle_a}(0) = c_{11}$. The other state with significant population c_{02} , is not involved in the calculation as $|\downarrow\downarrow\rangle|0\rangle_a|2\rangle_b$ does not evolve under an RSB on mode a. All other coefficients may be set to zero.

Eqs. 5.29 are be solved to calculate the probabilities $p_{|i,j\rangle|n\rangle_w}(t) = |c_{|i,j\rangle|n\rangle_w}(t)|^2$ for the relevant states:

$$\begin{aligned} p_{|\downarrow\downarrow\rangle|2\rangle_{a}} &= \frac{1}{9r^{4}} \left[\delta^{2} + 2g^{2} \left(1 + \cos\left(rt\right) \right) \right]^{2} \\ p_{|\downarrow\downarrow\rangle|1\rangle_{a}} &= \frac{8g^{2}}{r^{4}} \cos^{2}\left(\frac{\pi}{\sqrt{3}}\right) \left[\delta^{2} + 2g^{2} \left(1 + \cos(rt) \right) \right] \sin^{2}\left(\frac{rt}{2}\right) \\ p_{|\downarrow\uparrow\rangle|1\rangle_{a}} &= 0 \\ p_{|\uparrow\downarrow\rangle|1\rangle_{a}} &= 0 \\ p_{|\downarrow\uparrow\rangle|0\rangle_{a}} &= \frac{4g^{2}}{r^{4}} \sin^{2}\left(\frac{\pi}{\sqrt{3}}\right) \left[\delta^{2} + 2g^{2} \left(1 + \cos(rt) \right) \right] \sin^{2}\left(\frac{rt}{2}\right) \\ p_{|\uparrow\downarrow\rangle|0\rangle_{a}} &= \frac{4g^{2}}{r^{4}} \sin^{2}\left(\frac{\pi}{\sqrt{3}}\right) \left[\delta^{2} + 2g^{2} \left(1 + \cos(rt) \right) \right] \sin^{2}\left(\frac{rt}{2}\right) \\ p_{|\uparrow\uparrow\rangle|0\rangle_{a}} &= \frac{8}{9r^{4}} \left[\delta^{2} + 2g^{2} \left(1 + \cos^{2}\left(\frac{rt}{2}\right) \right) \right]^{2}. \end{aligned}$$

The average number of dark ions ($|\uparrow\rangle$) based on this analysis pulse on mode a is given by

$$D_{a} = \frac{8}{9} (p_{|\downarrow\uparrow\rangle|1\rangle_{a}} + p_{|\uparrow\downarrow\rangle|1\rangle_{a}} + p_{|\downarrow\uparrow\rangle|0\rangle_{a}} + p_{|\uparrow\downarrow\rangle|0\rangle_{a}} + 2p_{|\uparrow\uparrow\rangle|0\rangle_{a}})$$

$$= 2 \left(\frac{8}{9}\right)^{2} \left(1 - \frac{4g^{2}}{r^{2}} \sin^{2}\left(\frac{rt}{2}\right)\right) (1 - d_{a}),$$

$$(5.31)$$

where

$$d_a = \frac{7 + 9\cos\left(\frac{2\pi}{\sqrt{3}}\right)}{16} \frac{4g^2}{r^2} \sin^2\left(\frac{rt}{2}\right). \tag{5.32}$$

Since $4g^2 \le r^2$, $d_a \le \frac{7+9\cos\left(\frac{2\pi}{\sqrt{3}}\right)}{16} \approx 0.06$. Therefore, d_a can be neglected, so that

$$D_a \approx 2\left(\frac{8}{9}\right)^2 \left(1 - \frac{4g^2}{r^2}\sin^2\left(\frac{rt}{2}\right)\right) \tag{5.33}$$

This expression has the same form as the fit function Eq. 5.19. Since d_a is symmetric around resonance ($\delta = 0$) the neglected term is not expected to change the value of the coupling frequency found by fitting to Eq. 5.19.

Similarly, when a RSB pulse on mode b is applied, Eqs. 5.29 can be solved with different initial conditions, $c_{|\downarrow\uparrow\rangle|1\rangle_b}(0) = c_{11}$, $c_{|\downarrow\downarrow\rangle|2\rangle_b}(0) = c_{02}$, and the rest are set to zero. (In this case, the state $|\downarrow\downarrow\rangle|2\rangle_w|0\rangle_b$ with initial coefficient c_{20} does not evolve under the RSB interaction on mode b.) The probabilities $p_{|i,j\rangle|n\rangle_b}(t)$ are

$$p_{|\downarrow\downarrow\rangle|2\rangle_b} = \frac{16g^4}{9r^4} \sin^4\left(\frac{rt}{2}\right)$$

$$p_{|\downarrow\downarrow\rangle|1\rangle_b} = \frac{8g^2}{r^4} \cos^2\left(\frac{\pi}{\sqrt{3}}\right) \left[\delta^2 + 2g^2\left(1 + \cos\left(rt\right)\right)\right] \sin^2\left(\frac{rt}{2}\right)$$

$$p_{|\downarrow\uparrow\rangle|1\rangle_b} = 0$$

$$p_{|\uparrow\downarrow\rangle|1\rangle_b} = 0$$

$$p_{|\downarrow\uparrow\rangle|0\rangle_b} = \frac{4g^2}{r^4} \sin^2\left(\frac{\pi}{\sqrt{3}}\right) \left[\delta^2 + 2g^2\left(1 + \cos\left(rt\right)\right)\right] \sin^2\left(\frac{rt}{2}\right)$$

$$p_{|\uparrow\downarrow\rangle|0\rangle_b} = \frac{4g^2}{r^4} \sin^2\left(\frac{\pi}{\sqrt{3}}\right) \left[\delta^2 + 2g^2\left(1 + \cos\left(rt\right)\right)\right] \sin^2\left(\frac{rt}{2}\right)$$

$$p_{|\uparrow\downarrow\rangle|0\rangle_b} = \frac{4g^2}{r^4} \sin^2\left(\frac{\pi}{\sqrt{3}}\right) \left[\delta^2 + 2g^2\left(1 + \cos\left(rt\right)\right)\right] \sin^2\left(\frac{rt}{2}\right)$$

$$p_{|\uparrow\uparrow\rangle|0\rangle_b} = \frac{128g^4}{9r^4} \sin^4\left(\frac{rt}{2}\right).$$

The average number of dark ions $(|\uparrow\rangle)$ based on this analysis pulse on mode b is given by

$$D_b = 2\left(\frac{8}{9}\right)^2 \frac{4g^2}{r^2} \sin^2\left(\frac{rt}{2}\right) [1 + d_b], \qquad (5.35)$$

where

$$d_b = \frac{9\sin^2\left(\frac{\pi}{\sqrt{3}}\right) - 8}{8} \left(1 - \frac{4g^2}{r^2}\sin^2\left(\frac{rt}{2}\right)\right). \tag{5.36}$$

Similar to the case with mode a, since $d_b < \frac{9\sin^2(\frac{\pi}{\sqrt{3}})-8}{8} \approx 0.06$, D_s can be approximated as

$$D_b \approx 2\left(\frac{8}{9}\right)^2 \frac{4g^2}{r^2} \sin^2\left(\frac{rt}{2}\right),\tag{5.37}$$

which is also of the form Eq. 5.19.

5.4.2 Decoupling ²⁵Mg⁺ from the OOPH Mode in ⁹Be⁺-²⁵Mg⁺-⁹Be⁺

When performing the non-destructive (projective) readout (Sec. 5.7) experiments with the ${}^{9}\text{Be}^{+}$ - ${}^{25}\text{Mg}^{+}$ - ${}^{9}\text{Be}^{+}$ crystal, it was found, unsurprisingly, that the well was not perfectly symmetric about the center of the ion crystal, and therefore the ${}^{25}\text{Mg}^{+}$ ion was not totally decoupled from the OOPH axial mode. During initial mode-coupling attempts in ${}^{9}\text{Be}^{+}$ - ${}^{25}\text{Mg}^{+}$ - ${}^{9}\text{Be}^{+}$, the OOPH mode experienced unexpected heating when detection was performed on ${}^{25}\text{Mg}^{+}$. It was suspected that likely there was some asymmetry in the well causing some amount of coupling of the ${}^{25}\text{Mg}^{+}$ to the OOPH mode.

Asymmetry in the external trap potential can impact mode participation of a multi-ion string [57, 134]. Three types of asymmetric terms are considered: the radial gradients $\partial U/\partial x$ and $\partial U/\partial y$, the twist curvature term $\partial^2 U/(\partial x \partial z)$, and the axial cubic term $\partial^3 U/\partial z^3$. Non-zero values for these terms lead to non-zero participation of the $^{25}\text{Mg}^+$ ion in the OOPH mode, which will then be coupled to recoil from $^{25}\text{Mg}^+$ scattering events. The presence of this recoil was used to calibrate scaling values for shim voltages that were calculated from trap simulations designed to minimize the relevant anharmonic terms. These calibrated values were then added to the trapping voltages.

Radial gradients were controlled by a differential voltage shim on the pair of control electrodes closest to the ions (DC19 and DC20) and an additional voltage shim applied to the bias electrode on a third-layer wafer outside the two main wafers ([89], Sec. 3.3). The twist term was controlled by the two pairs of electrodes next to the two electrodes closest to the ions (DC17, DC18, DC21, and DC22). By applying a differential voltage shim of V on the pair of electrodes on one side and -V on the other, the twist of the ion string in the $\mathbf{x} - \mathbf{z}$ plane relative to the trap axis was minimized. The cubic term z^3 was minimized using the same electrodes and calculated values used to create the ALT-OOPH mode coupling.

The optimal shim values were determined as follows. All three axial modes were sidebandcooled close to their ground states, then the voltage shims controlling one of the anharmonicity terms were set to a certain strength. ²⁵Mg⁺ resonant light was pulsed for 1 ms to cause scattering on ²⁵Mg⁺, then the applied anharmonicity shims were set to zero (to restore the initial conditions for detection) and the probability of a state change of ⁹Be⁺ when driving a MSS pulse on the OOPH mode was determined. The shim with minimal MSS spin-flip probability was retained as the optimal value and applied for subsequent experiments. Since the shims were not perfectly decoupled from each other, the minimization of all three anharmonic terms was iterated for several rounds to find the overall best shims. While this process significantly minimized the heating of the OOPH mode when ²⁵Mg⁺ is detected, there were still some residual effects, as characterized in Sec. 5.7.4.

5.5 Characterization

After calibrating frequencies and pulse times, the mode-coupling operation was characterized through a variety of pulse sequences and input states. For the rest of the chapter, unless explicitly addressed, the INPH mode in the ${}^{9}\text{Be}^{+}$ - ${}^{25}\text{Mg}^{+}$ - ${}^{9}\text{Be}^{+}$ ion crystal can be assumed to be cooled along with the other axial modes during initial state preparation and otherwise not involved.

5.5.1 Characterizing Phase Coherence

Fig. 5.3(a) shows the schematic for an experiment probing the motional coherence of a state that is transferred between modes using the mode-coupling operation, using a Ramsey-type experiment. First, to begin the Ramsey experiment an effective motion $\pi/2$ pulse was implemented with a microwave $\pi/2$ pulse with phase $\phi_1 = 0$ between $|\uparrow\rangle_M$ and $|\downarrow\rangle_M$ and then a motional red sideband, as shown in Fig. 5.3(b), upper schematic. With a microwave pulse of phase ϕ , this ideally created the state $\frac{1}{\sqrt{2}}|\downarrow\rangle_M$ ($|0\rangle_A + |1\rangle_A$) (when the Raman pulse phase is carefully tracked and set at 0). This superposition precessed at the motion frequency which was tracked.

Next, during the Ramsey precession time, either a swap between OOPH and ALT, a double-swap between the two modes, or a delay equivalent to a double-swap was performed. The resulting motion state in the ALT mode was then mapped back to the internal states using a second motion $\pi/2$ pulse with varying phase: to close the Ramsey sequence, the motion sideband was applied before

the microwave pulse for this second motion $\pi/2$ pulse, as shown in Fig. 5.3(b), lower panel. The resulting fluorescence data is shown in Fig. 5.3(c).

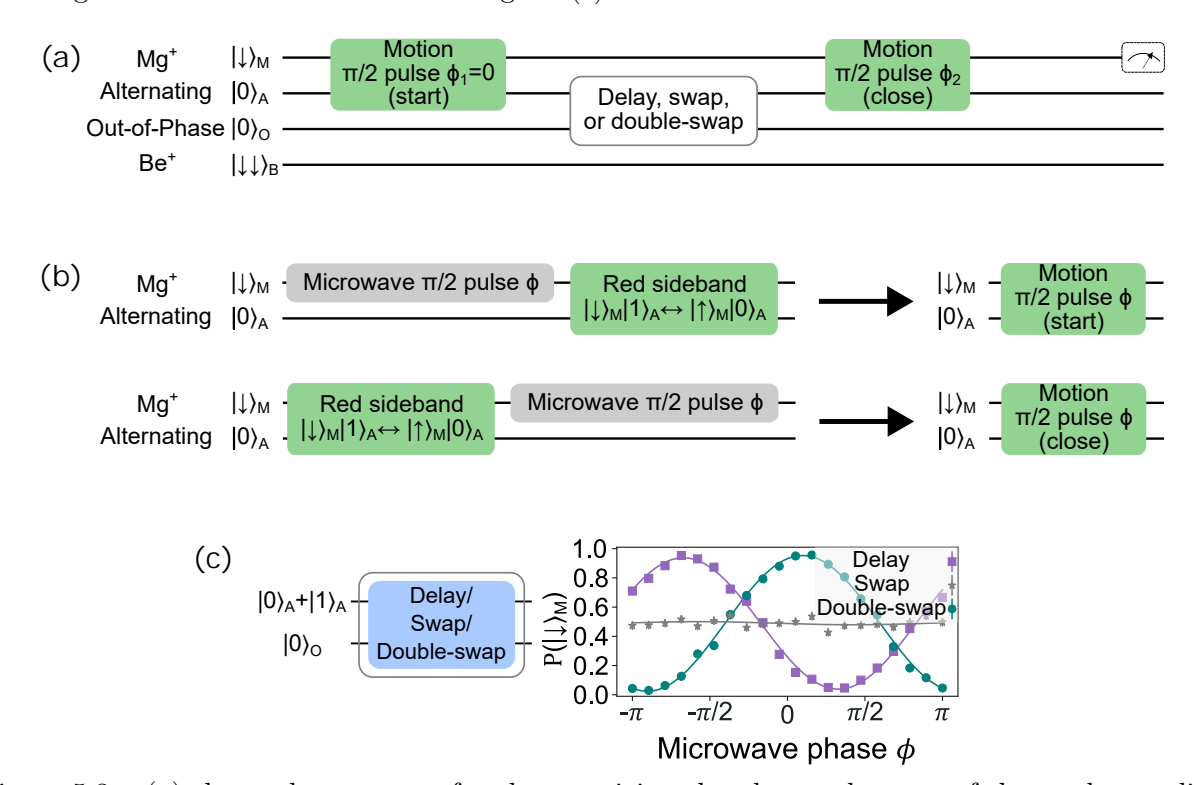


Figure 5.3: (a) shows the sequence for characterizing the phase coherence of the mode coupling operation between the ALT and OOPH mode. With all ion internal states initialized in $|\downarrow\rangle$ and the Fock states of both modes cooled close to the ground state, an effective motional $\pi/2$ pulse was implemented, which is a microwave $\pi/2$ pulse and a motional red sideband on $^{25}\mathrm{Mg}^+$, as shown in the upper schematic in (b). The microwave phase of this first $\pi/2$ pulse is denoted $\phi_1 = 0$. After, either a mode-coupling swap operation, double-swap operation, or a delay equivalent to the duration of the double-swap operation was applied. Then, a second motional $\pi/2$ pulse was implemented, completing a Ramsey-type experiment; the effective motional $\pi/2$ pulse to close the Ramsey sequence has the red sideband applied before the microwave pulse, as shown in the lower part of (b). The phase ϕ_2 of this second motion $\pi/2$ pulse was scanned, resulting in the data shown in (c) after fluorescence detection on $^{25}\mathrm{Mg}^+$.

When the motional superposition state was swapped to the OOPH mode with a single swap during the Ramsey precession time, the ALT mode ends up with the motion occupation of the sideband-cooled OOPH mode, meaning the second half of the Ramsey sequence simply caused the $^{25}\text{Mg}^+$ internal state to become an equal superposition of $|\uparrow\rangle_{\text{M}}$ and $|\downarrow\rangle_{\text{M}}$. The Ramsey sequence was completed (i.e. the motion superposition was closed by the second $\pi/2$ pulse) when the delay or, more importantly, the double-swap is applied instead, since these both resulted in a motional

superposition state in the ALT mode and a π phase shift due to the swap operation. The data corresponding to the double-swap in Fig. 5.3(c), teal dots, shows that the motional coherence was maintained during the mode-coupling operation, since the Ramsey oscillation contrast appears quite high, and similar to that of the delay (Fig. 5.3(c), purple squares).

5.5.2 Mode Coupling with Varying Input States

Fig. 5.4(a) shows the pulse sequence for characterizing the mode-coupling operation with varying input states, with increasing numbers of total phonons in the two modes from 0 to 2. The input states were prepared by motion-adding sideband pulses, with the $|1\rangle$ Fock state prepared using a sideband on $^{25}\text{Mg}^+$, and the $|2\rangle$ Fock state prepared by driving a $\pi/\sqrt{6}$ motion-adding sideband on the two $^9\text{Be}^+$ as described in Sec. 5.4.1.2. Then, either a mode-coupling pulse was applied with varying duration, or an effective Ramsey sequence consisting of two motional (50/50) beam-splitter operations¹⁷ was applied, with the second beam-splitter operation phase varied. Then, a sequence involving rapid adiabatic passage (RAP) pulses [135] (see Sec. 5.5.2.1) was used to transfer the motion information of the ALT and OOPH modes to the internal states of all three ions for fluorescence detection, which we call "joint population determination". The results for the time scans are shown in Fig. 5.4(b)-(e), while the results for the Ramsey sequence are shown in Fig. 5.4(f),(g).

In the time scans Fig. 5.4(b)-(e), it can be seen that the time required to couple the modes is not dependent on phonon number in either mode. The relative phase between two consecutive beamsplitter operations was scanned to obtain the data shown in Fig. 5.4(f),(g); these show that the operation is phase-coherent. Moreover, it can be seen that the total number of phonons in the system was conserved by the interaction, as expected; the remaining populations for the data shown in Fig. 5.4(b)-(g) can be found in Appendix B.1.

Of special note are the results shown in Fig. 5.2(g); at the beamsplitter time ($\approx 50 \ \mu s$), it can be observed that the original state of $|1\rangle_A |1\rangle_O$ transits to $|2\rangle_A |0\rangle_O$ and $|0\rangle_A |2\rangle_O$ with equal

 $^{^{17}}$ This is defined as a mode-coupling pulse with fixed duration corresponding to equal population in both modes, as shown in Fig. 5.2(c).

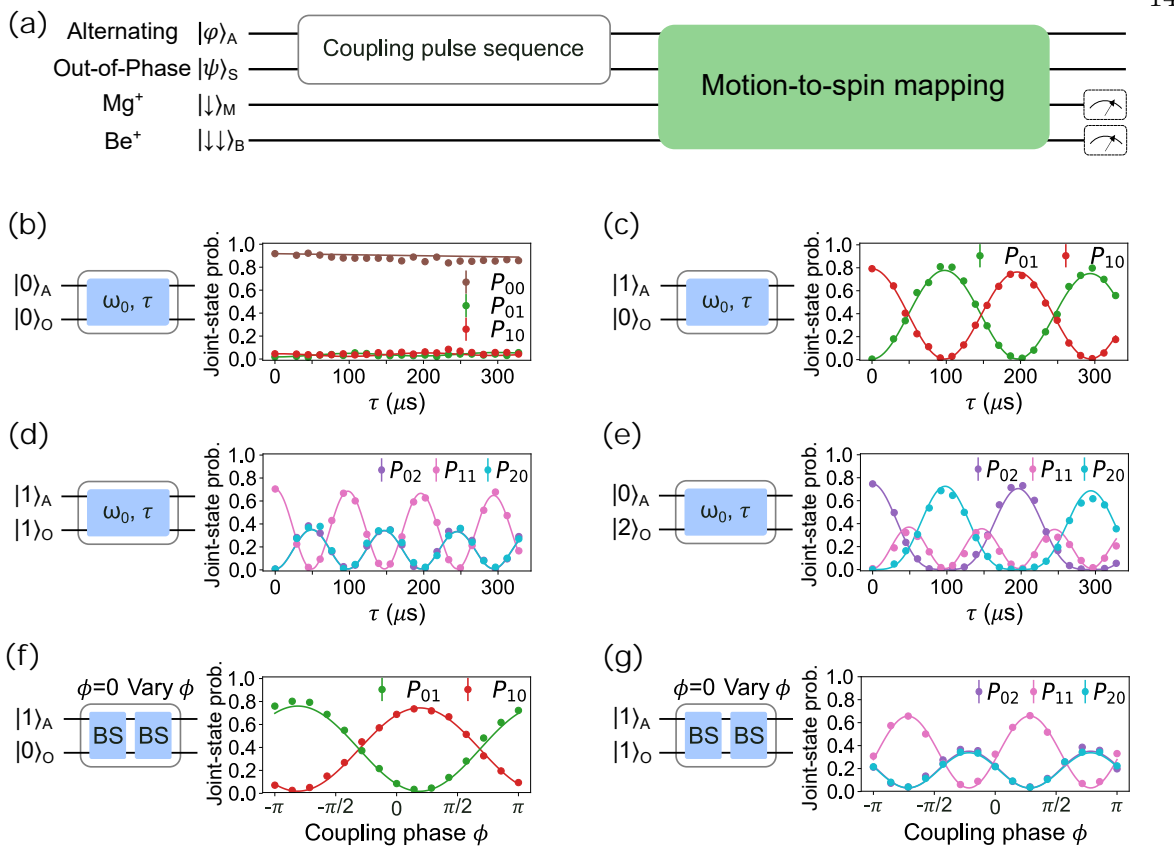


Figure 5.4: (a) shows the sequence for characterizing the mode coupling operation between the ALT and OOPH mode with various input states. The Fock states were prepared (nominally) as the states indicated to the left of each subfigure (b)-(g). With all ion internal states initialized in $|\downarrow\rangle$, a single coupling pulse was applied for a varying time (b)-(e). In (f) and (g), two beam-splitter operations, which are mode-coupling pulses with times calibrated as in Fig. 5.2(c), were applied with the second having varying phase. The resulting motion states on both the ALT and OOPH modes were read out by transferring the motion information onto the internal states of all three ions using RAP pulses (Sec. 5.5.2.1). The Fock state populations with significant occupations are shown, with $P_{a,b}$ indicating a phonons in the ALT mode and b phonons in the OOPH mode. The lines shown are simulations using the initial states of each time scan.

probability, in analogy to the Hong-Ou-Mandel effect [31, 136], except that the two modes involved in this case have different energies. The difference in energy between the two modes that have their motion states exchanged was made up by the driving potential. We estimate an 84% confidence lower bound of the average fidelity in the one-phonon subspace of the beamsplitter operation to be 97.9% (see Methods of Ref. [131]). The beamsplitter operation plays an important role in forming a universal gate set for continuous-variable quantum computing, since it allows for interaction between

5.5.2.1 Joint Population Determination Using Rapid Adiabatic Passage

The results shown in Fig. 5.4(b)-(g) were obtained by joint population determination using the six-state space defined by the fluorescence results $\{|\uparrow\rangle_{\rm M}\,,|\downarrow\rangle_{\rm M}\}\otimes\{|\uparrow\uparrow\rangle_{\rm B}\,,\frac{1}{\sqrt{2}}\,(|\uparrow\downarrow\rangle_{\rm B}+|\downarrow\uparrow\rangle_{\rm B})\,,|\downarrow\downarrow\rangle_{\rm B}\}$. By using fluorescence detection of all three ions in ${}^9{\rm Be}^+$ - ${}^2{}^5{\rm Mg}^+$ - ${}^9{\rm Be}^+$, the populations of six motion states could (in theory) be recorded at once. The OOPH Fock state populations were transferred to the ${}^9{\rm Be}^+$ internal ion states using RAP Raman pulses [135] to allow the mapping $|0\rangle_{\rm O} \to |\downarrow\downarrow\rangle_{\rm B}$, $|1\rangle_{\rm O} \to |\uparrow\downarrow\rangle_{\rm B}\,/\,|\downarrow\uparrow\rangle_{\rm B},\,|2\rangle_{\rm O} \to |\uparrow\uparrow\rangle_{\rm B}$ in the same operation as shown in Fig. 5.5(c).

Unfortunately, in the case of ${}^{25}{\rm Mg}^+,$ since three Fock states had to be read out using a binary result, two Fock states had to be assigned to the same fluorescence detection result. As shown in Fig. 5.5(a) and (b), one Fock state was assigned to the bright readout result (25Mg⁺ $^2\mathrm{S}_{1/2}|3,3\rangle_{\mathrm{M}}=|\uparrow\rangle_{\mathrm{M}}$) and the other two Fock states were assigned to a dark readout result. In the case shown in Fig. 5.5(a), $|\uparrow\rangle_{\rm M}|0\rangle_{\rm A}$ was assigned to the bright result (which is itself), and $|\uparrow\rangle_{\rm M}|1\rangle_{\rm A}$ and $|\uparrow\rangle_{\mathrm{M}}|2\rangle_{\mathrm{A}}$ were assigned to $|2,-2\rangle_{\mathrm{M}}|0\rangle_{\mathrm{A}}$ and $|2,-2\rangle_{\mathrm{M}}|1\rangle_{\mathrm{A}}$ (where $|2,-2\rangle_{\mathrm{M}}$ does not fluoresce). In the other two cases (shown in Fig. 5.5(b), where $|\uparrow\rangle_{\rm M}|1\rangle_{\rm A}$ or $|\uparrow\rangle_{\rm M}|2\rangle_{\rm A}$ was assigned to the bright result), the two other Fock states were assigned to $^{25}{\rm Mg^+}$ $^2{\rm S}_{1/2}$ $|2,-2\rangle_{\rm M}$ and $|2,-1\rangle_{\rm M}$ (since both are relatively dark during fluorescence detection). Because the dark ²⁵Mg⁺ detection result corresponded to two Fock states, such results were discarded, meaning only half of the six-state ion fluorescence result subspace could be used at a time. Therefore, in order to determine the populations in the total nine-state motion subspace, three iterations of the detection had to be performed with the three mapping sequences shown in Fig. 5.5(a), (b). As mentioned previously, the joint state was determined in each shot of the experiment by setting a count threshold for each species to determine whether the ion was in the dark or bright state, and in the case of two ⁹Be⁺ how many ions were in the bright state.

As can be seen by the number of pulses required in some cases, these RAP pulse sequences were quite slow, which allowed a significant amount of heating to occur; this is the main reason for

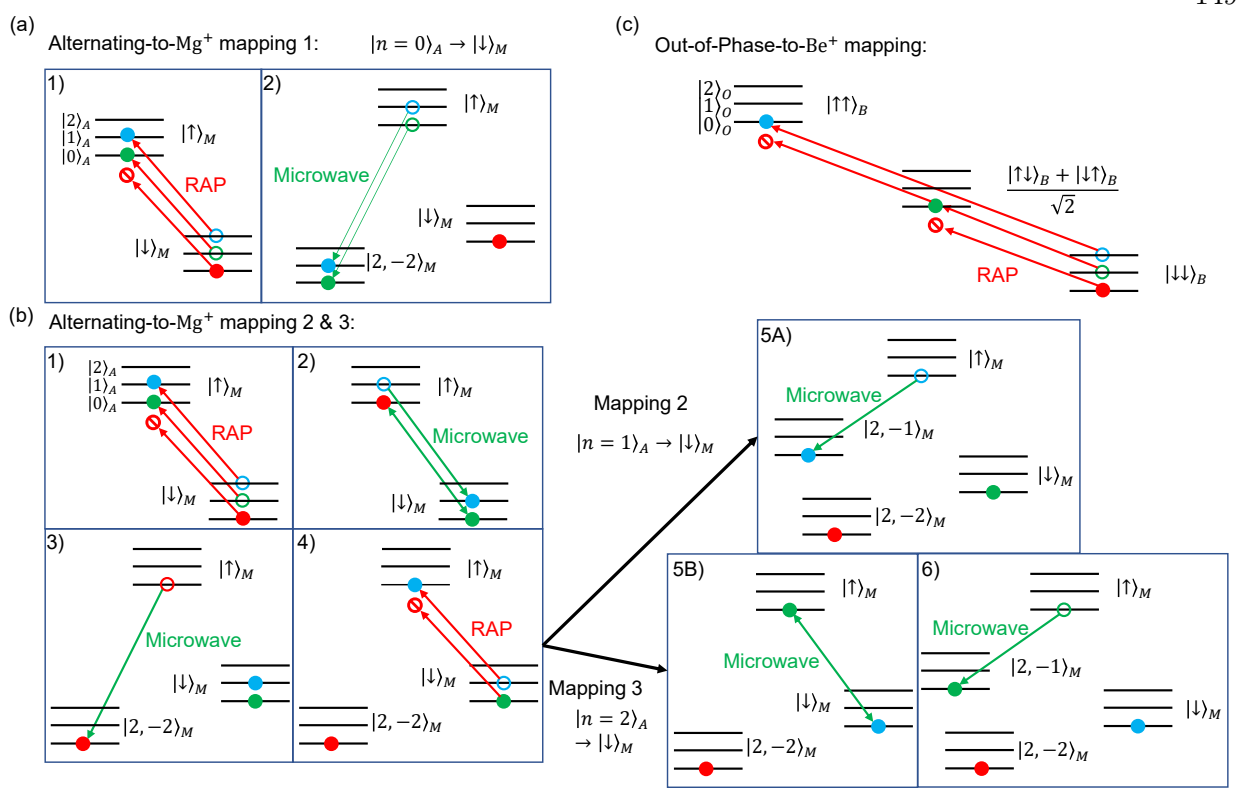


Figure 5.5: (a) shows the RAP pulse sequence for mapping $|0\rangle_A$ to $|\downarrow\rangle_M = |3,3\rangle_M$ (corresponding to a bright fluorescence result), called "mapping 1". The other two Fock states are transferred to individual Fock states with atomic state $|2,-2\rangle_M$, which is dark during fluorescence detection. (b) shows the RAP sequence used to separate the three ALT mode Fock states for the remaining cases where either $|1\rangle_A$ or $|2\rangle_A$ corresponds to $|\downarrow\rangle_M$: the remaining two are mapped to $|2,-2\rangle_M$ and $|2,-1\rangle_M$ which are both dark during fluorescence detection. These mappings are named "Mapping 2" and "Mapping 3" when $|1\rangle_A$ and $|2\rangle_A$ correspond to a bright fluorescence result, respectively. (c) shows the RAP pulse sequence for mapping $|0\rangle_A$, $|1\rangle_A$, and $|2\rangle_A$ to $|\uparrow\uparrow\rangle_B$, $\frac{1}{\sqrt{2}}(|\uparrow\downarrow\rangle_B + |\downarrow\uparrow\rangle_B)$, and $|\downarrow\downarrow\rangle_B$ respectively. Because the number of possible fluorescence results for the 2 $^9\mathrm{Be}^+$ matches the number of Fock states being probed, this sequence is much simpler.

the loss in contrast for Fig. 5.4(b)-(g) compared to the data shown in other parts of this chapter. By measuring the nine-state subspace, it was observed that often the ion motion would experience heating or the state would be prepared imperfectly in the first place, causing oscillations to appear over the duration of the experimental sequence in the subspaces with other total phonon numbers than intended, as shown in Appendix B.1.

5.5.3 Error Due to Repeated Swaps

In order to check the error caused by the swap operation itself, an experiment applying many swaps was compared to an experiment with delays in place of those swap operations. First, the operation frequency and swap time were calibrated. Then, the motion states were prepared as $|1\rangle_{\rm A}|0\rangle_{\rm O}$, and a varying number of swaps M, as shown in Fig. 5.6, was applied. Then, the phonon numbers of the nine joint motion states were determined as described in Sec. 5.5.2.1.

The populations P_{01} and P_{10} (second panel in Fig. 5.6(a)), corresponding to the probability of observing $|0\rangle_{\rm A}|1\rangle_{\rm O}$ and $|1\rangle_{\rm A}|0\rangle_{\rm O}$ respectively, exchanged with each swap, with slowly decreasing total population between the two. The lost population is seen to appear in the third panel down in Fig. 5.6(a), which are the states with total Fock number 2; this suggests that the population was primarily lost to heating. This is also seen in the data shown in Fig. 5.6(b), where instead of M swaps, a delay with equivalent duration was used in the sequence. In this case, no population was exchanged and only a slow population leakage from the initial state (red dots in the second panel) to primarily $|0\rangle_{\rm A}|0\rangle_{\rm O}$ (brown dots in the first panel) and $|2\rangle_{\rm A}|0\rangle_{\rm O}$ (blue dots in the third panel) is observed. The primary change was in the population of the ALT mode due to a much larger heating rate in that mode compared to the OOPH mode (heating rates are listed in Sec 3.6).

Comparing Fig. 5.6(a) and (b), it can be seen that the mode-coupling operation did not introduce a significant amount of population loss beyond what is expected from motion mode heating/diffusion. In order to quantify this, the fidelity of each data point to the initial density matrix, corresponding to the M=0 data in the first panel of Fig. 5.6(a) and (b), was extracted and shown in Fig. 5.6(c) and (d), respectively. The density matrix of each point is denoted as σ and the density matrix resulting from applying ideal swaps to the initial density matrix (M=0) for Fig. 5.6(a) is ρ (ρ is just the initial density matrix when analyzing the data of Fig. 5.6(b)). The density matrices σ and ρ are treated as a fully decohered mixture of nine joint number states (only diagonal terms are non-zero) and the fidelity is estimated with $F = (Tr\sqrt{\sqrt{\rho}\sigma\sqrt{\rho}})^2$.

The fidelities from the data in Fig. 5.6(a) (blue triangles) are fit to $F(M) = (1 - \epsilon)^M$ to extract

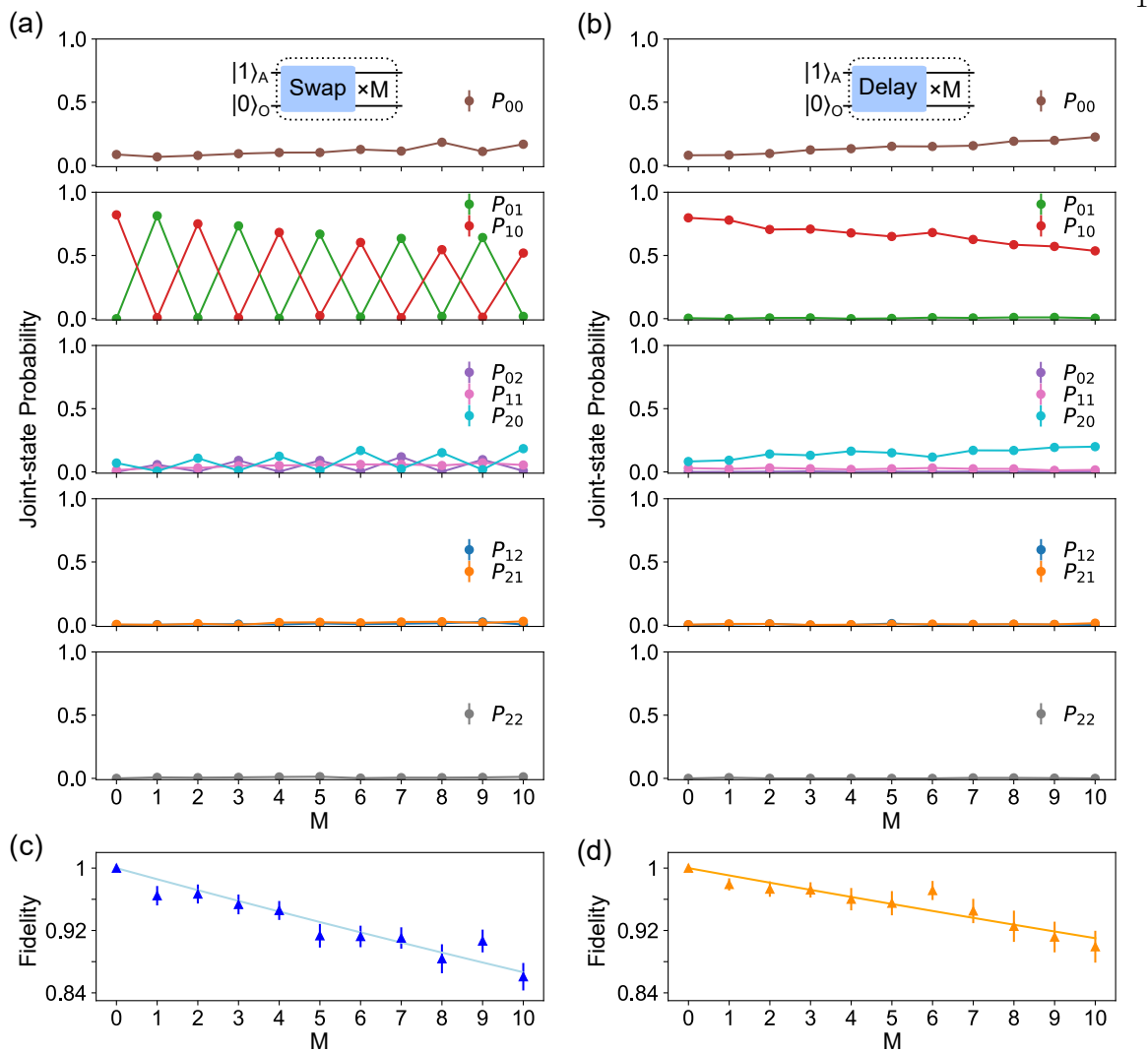


Figure 5.6: (a) shows data from the two modes prepared in $|1\rangle_{\rm A}|0\rangle_{\rm O}$, with M swap pulses applied and populations of the two-mode joint states determined. The second panel shows that the injected single phonon is swapped between the two modes. (b) shows data from a reference experiment where the coupling pulses are replaced with delays of equal duration to illustrate the effect of heating. Solid lines in (a) and (b) serve as guides to the eye. In (c), the fidelity of the density matrix (containing all nine joint states) after M swaps to a target density matrix is shown. The target density matrix is determined by ideal swaps applied to an initial density matrix (data at M=0 in (a)). The resulting fit gives an error per swap operation to be 1.4(1)%. To obtain the data shown in (d), the same analysis is performed for the reference experiment data (orange triangles) where the fidelity to the initial density matrix (data at M=0 in (b)) is shown and the error is found to be 0.9(1)%.

an error ϵ per swap operation of 1.4(1)%, while the analysis of the reference data (with delays instead of swaps, Fig. 5.6(b)) yielded an error per swap time of 0.9(1)%. Therefore, the error of the swap operation is dominated by heating, which can be suppressed by increasing the coupling strength to

reduce the swap time, or by lowering the heating rate, for example by operating in a similar trap at cryogenic temperatures.

5.6 Cooling Using Mode-Coupling

Here I begin by briefly returning to the motivation of using the mode-coupling operation to cool the OOPH mode through ²⁵Mg⁺. For the purposes of cooling with mode coupling, the terms "weakly-cooled modes" (WCM) and "strongly-cooled modes" (SCM) are introduced. In general, WCM may arise for a variety of reasons. For example, there could be low participation of a designated cooling ion due to mass differences in a mixed-species ion crystal, or mode symmetries as seen in our apparatus. WCM may also be caused by experimental constraints such as difficulty in implementing a particular beam angle, leading to little/no projection along a mode that is to be cooled. Using mode coupling to exchange the states of an SCM with a WCM, the WCM can be cooled indirectly through the SCM.

This may be done in two different ways. First, it can be done in an interleaved fashion, where the SCM can be sub-Doppler-cooled, then a full swap operation applied exchanging the state of the WCM with that of the SCM, and then applying sub-Doppler cooling again to the SCM. This can then be repeated as many times as necessary to reach the desired motional occupation on both the WCM and SCM, up to the competition between the cooling and heating rates. The second way is to do this simultaneously, with the mode-coupling operation on continuously while the SCM is cooled. Unfortunately, applying the mode coupling operation with coupling rate g (as defined in Eq. 5.8) causes the SCM and WCM to transform into two new dressed modes, with frequency splitting 2g. This poses a problem for cooling methods with very narrow frequency selectivity, such as Raman SBC, since a higher coupling rate is preferred for cooling the WCM quickly, but a higher coupling rate causes the splitting to increase, making frequency-selective cooling methods such as Raman SBC less efficient. Broadband cooling methods such as EIT cooling can overcome this issue, as

¹⁸It is possible to introduce a second frequency component to address both frequencies that appear as a result of the splitting, but this will decrease the total available laser power in each tone.

shown in Fig. 4.12.

Three different ion crystals are explored in this section, ${}^{9}\mathrm{Be^{+}}$, ${}^{9}\mathrm{Be^{+}}$, ${}^{9}\mathrm{Be^{+}}$, ${}^{25}\mathrm{Mg^{+}}$ and ${}^{9}\mathrm{Be^{+}}$. For the two-ion crystals, only the interleaved cooling method was attempted, while in ${}^{9}\mathrm{Be^{+}}$, ${}^{25}\mathrm{Mg^{+}}$, ${}^{9}\mathrm{Be^{+}}$ data resulting from both methods are shown.

5.6.1 Cooling WCMs in a Same-Species Crystal

For this demonstration, cooling beams with nominally axial projection (Be Raman 1 and 2 in Fig. 3.9) were used to cool the radial OOPH modes (as pictured in Fig. 5.7(a), purple arrows and text) of a ${}^{9}\text{Be}^{+}$ - ${}^{9}\text{Be}^{+}$ ion crystal. The axial, or **z**-OOPH mode at frequency $\omega_{zo} = 2\pi \times 6.304(1)$ MHz is an SCM, while the **x** and **y** (radial) OOPH modes xo and yo, with $\omega_{xo} = 2\pi \times 7.483(1)$ MHz and $\omega_{yo} = 2\pi \times 6.437(1)$ MHz, are WCMs, since the cooling radiation wavevector is orthogonal to the mode directions.

While a pair of Raman beams with axial projection only was used for the cooling demonstration, Be Raman 2 and 3 (Fig. 3.9) were also used to drive radial-mode Raman transitions. This was done in order to sideband-cool modes for calibrations; manipulate radial mode occupations; and characterize the thermal occupation of all radial OOPH modes directly. To calibrate the coupling between the zo and yo mode, all six normal modes were sideband-cooled close to their ground states. A microwave π pulse was then used to prepare $|\uparrow\rangle_{\rm B}$, and then approximately 1.4 phonons on average were injected into the yo mode by a pulse on $|\uparrow\rangle_{\rm B}|n\rangle \leftrightarrow |\downarrow\rangle_{\rm B}|n+1\rangle$ with Raman beams 2 and 3. Because two ions are involved in the interaction, driving a single sideband pulse does not yield the injection of a single phonon. A repump pulse was then used to reset the hyperfine states of the two ${}^{9}{\rm Be}^{+}$ ions to $|\downarrow\downarrow\rangle_{\rm B}$. Then (following a similar process as described in Sec. 5.4) a mode-coupling pulse was applied with varying frequency (yielding Fig. 5.7(b),(d)) or varying duration (Fig. 5.7(c), (d)). Finally, a motion-subtracting sideband pulse was driven and fluorescence detection was performed. The mode coupling pulse potential Φ used has nonzero $\partial^2\Phi/\partial x\partial z$ for coupling xo - zo and nonzero $\partial^2\Phi/\partial y\partial z$ for coupling yo - zo.

The average number of phonons in either mode can be approximated by the average number

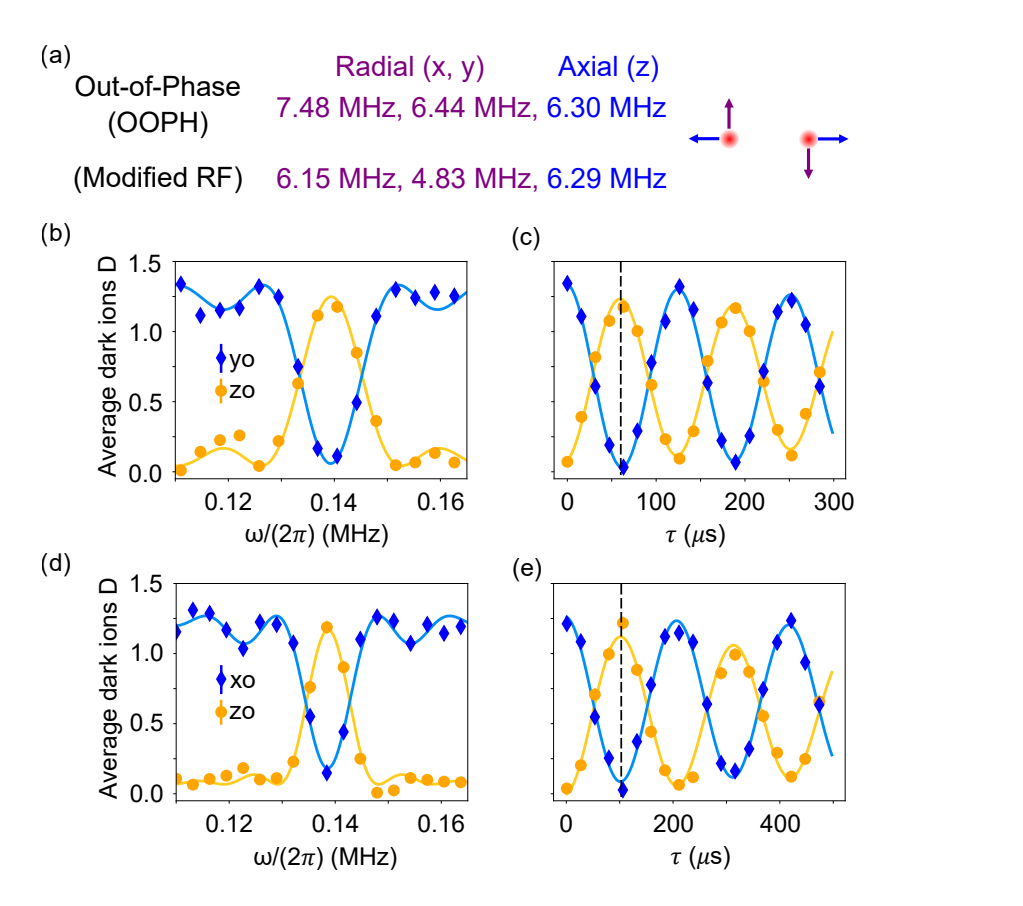


Figure 5.7: Axial to radial mode coupling characterization in a ${}^{9}\text{Be}^{+}$ - ${}^{9}\text{Be}^{+}$ ion crystal. (a) shows the mode participations of the OOPH modes in the three directions (zo, xo, and yo). The frequency, participation, and direction of the radial modes are indicated in purple, and the axial modes are indicated in blue. Two different wells were used, so the frequencies for both the initial confining well and the well with modified RF confinement are shown. Calibration data for the coupling between the zo and yo ((b) and (c)), and between zo and xo ((d) and (e)). Blue and orange points show the average number of dark ions (Eq. 5.38) after a mode coupling pulse and an RSB pulse on the xo (or yo) and zo modes respectively. A larger number of dark ions corresponds to a larger average phonon number before the RSB pulse. Solid lines are fits to an equation of the form Eq. 5.19 for the frequency scans (b) and (d) and a sinusoid with an exponential decay envelope for (c) and (e). Dashed vertical lines indicate the duration of single swap operations. Each data point is obtained from 300 experiments with a 68% confidence error bar, which is smaller than the plot symbols in some cases.

of dark ions D that is computed from the average fluorescence counts C as

$$D = 2\frac{C_2 - C}{C_2 - C_0},\tag{5.38}$$

where C_2 and C_0 are the average count rates for two or zero ions in the bright state, respectively.

It is shown in Sec. 5.4.1 that while two ions participate in the sideband pulse, the lineshape remains approximately of the same form as Eq. 5.19, so this was used to fit the frequency scans yielding the solid lines in Fig. 5.7(b),(d). An exponential sinusoid of the form Eq. 5.20 was used to fit the time scans, yielding the solid lines in Fig. 5.7(c),(e). The fits to the data for yo - zo mode coupling yield coupling frequency $\omega_{yo,zo} = 2\pi \times 0.139(1) \,\text{MHz} \approx \omega_{yo} - \omega_{zo}$ and a single swap duration of $\tau_{yo,zo} = 63(1)\mu\text{s}$.

The coupling between the zo and the xo mode was calibrated in a similar manner (Fig. 5.7(e) and (f)). However, coupling of two modes with a frequency difference above 1 MHz is strongly attenuated in our apparatus as discussed in Sec. 5.3. To obtain stronger coupling between these modes, their frequencies were brought closer together for the exchange by adiabatically ramping down the trap RF amplitude over 100 μ s before the coupling pulse and then ramping up again over 100 μ s after the coupling pulse. At the lower trap RF amplitude, the xo mode frequency became $2\pi \times 6.150(1)$ MHz and the zo frequency was slightly shifted to $2\pi \times 6.294(1)$ MHz, bringing the mode frequency difference $\omega_{xo} - \omega_{zo}$ into a range that could be driven on the control electrodes efficiently. The yo mode frequency was approximately $2\pi \times 4.83$ MHz. No appreciable motional excitation was observed from the ramping of the trap RF amplitude. From fits to data, the optimal values at this lower trap RF amplitude are $\omega_{xo,zo} = 2\pi \times 0.139(1)$ MHz for modulation frequency and $\tau_{xo,zo} = 106(1)$ μ s for swap duration. The parameters from the fits of the frequency and time data shown in Fig. 5.7 are summarized in Tabs. B.1 and B.2 respectively.

After initial Doppler cooling, the pulsed cooling scheme was implemented using N repetitions of the sequence shown in Fig. 5.8(a). The sequence began with a 270 μ s SBC pulse on the zo mode and the INPH axial and radial modes. To cool the xo mode, the trap RF amplitude was decreased, the (cold) zo and (hot) xo mode populations were swapped using the mode coupling operation, and the trap RF amplitude was then returned to the initial value. Then, another SBC pulse of 270 μ s was used to recool the zo mode, the zo and yo populations were swapped using another mode coupling pulse, then a final SBC pulse on the zo mode was performed. Each sequence had a total duration of ≈ 1.34 ms. After cooling, MAS and MSS pulses were used to determine the average

motional occupation \bar{n} in a given mode, assuming a thermal state of motion [68, 78]. The modes were determined sequentially in an interleaved fashion. Fig. 5.8(b) shows \bar{n} for all three modes versus the number of cooling cycles N (bottom axis) or total cooling duration (top axis).

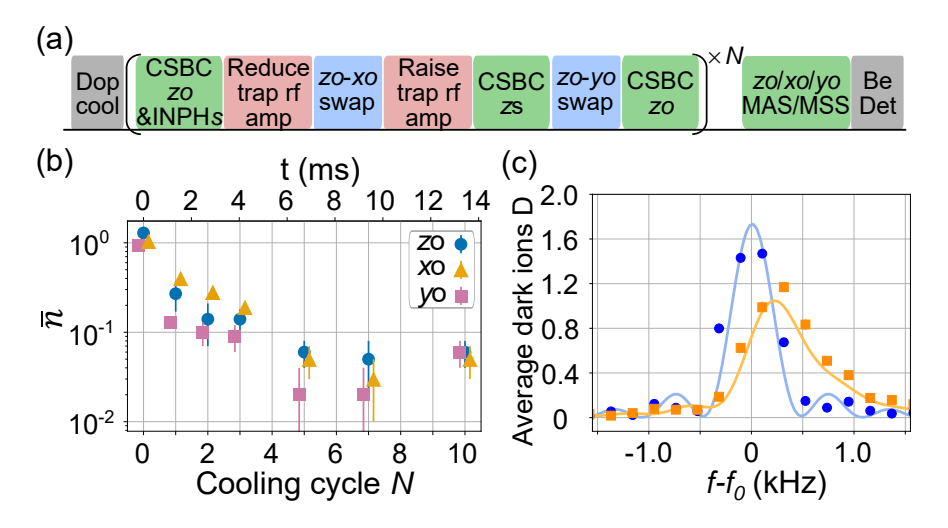


Figure 5.8: ${}^{9}\text{Be}^{+}$ cooling results. (a) Experimental sequence for ground-state cooling of the xo and yo modes via coupling to the zo mode. (b) Mean occupation \bar{n} of the three modes versus number of cooling cycles N (bottom) and cooling duration (top). Data points of xo and yo are laterally offset from nominal N values for legibility. (c) Sideband spectra of the zo mode with (blue) and without (orange) indirect ground-state cooling of the xo and yo modes. Lines are the fits to a theory model accounting for cross-Kerr coupling between modes (see main text for details). Each data point is obtained from 300 experiments with a 68% confidence error bar, which is smaller than the plot symbols for some points in (b) and (c).

The radial OOPH modes xo and yo are naturally coupled to the axial OOPH mode zo due to the nonlinearity of the Coulomb interaction, which can be expressed as a cross-Kerr coupling [27, 138]. The Hamiltonian can be written as

$$H_{K} = \hbar(\chi_{zo,xo}\hat{n}_{zo}\hat{n}_{xo} + \chi_{zo,yo}\hat{n}_{zo}\hat{n}_{yo}), \qquad (5.39)$$

where the $\{\hat{n}\}$ are number operators for the motional modes and the $\{\chi\}$ are the Kerr coupling strengths. The presence of non-zero motional population in either xo or yo causes frequency shifts on the zo mode, and vice versa. If the radial OOPH modes are in thermal states of motion, this coupling will cause dephasing of the zo mode, which impacts the fidelity of an entangling operation mediated

by the zo mode, or precision spectroscopy using the zo mode [1, 25, 28, 36, 94]. Using Eq. (16) in Ref. [138], the Kerr coupling rates in our experiments are calculated to be $\chi_{zo,xo} = 2\pi \times 75.86(5)$ Hz and $\chi_{zo,yo} = 2\pi \times 95.4(7)$ Hz.

This cross-Kerr dephasing effect was experimentally characterized by performing sideband spectroscopy on the zo mode. The two ${}^9\mathrm{Be^+}$ ions were prepared in $|\uparrow\uparrow\rangle_\mathrm{B}$ and the zo mode was cooled close to the ground state. Then a zo MSS π pulse of duration 1.8 ms on the "clock" transition $|\uparrow\rangle_\mathrm{B} \leftrightarrow |2,0\rangle_\mathrm{B}$ at reduced Rabi frequency was applied, followed by shelving and state-dependent fluorescence detection. The clock transition was chosen in this instance so that qubit dephasing does not contribute appreciably to the measured transition linewidth.

With the radial OOPH modes indirectly cooled to near their ground states, an approximately Fourier-limited resonance was observed when scanning the frequency of the sideband pulse, as seen in blue in Fig. 5.8(c). With only Doppler cooling of the radial OOPH modes (orange squares), the sideband resonance was shifted to higher frequencies by approximately 250 Hz, broadened, and reduced in contrast due to averaging of the cross-Kerr coupling over the thermal occupations of the radial OOPH modes. The data is fit to a model including the cross-Kerr couplings (described in more detail in Appendix D of Ref. [98]). This demonstration shows that the detrimental effect from cross-Kerr couplings can be suppressed without the need for extra laser beams or magnetic field gradients.

5.6.2 Cooling Ion Crystals with Different Charge-to-Mass Ratios

The approximate 9:25 mass ratio in a ${}^{9}\text{Be}^{+}$ - ${}^{25}\text{Mg}^{+}$ ion crystal leads to very unequal participations of the two species in all normal modes, as illustrated in Sec. 3.6. In the axial z-OOPH (zo) mode the ${}^{9}\text{Be}^{+}$ participation dominates, with $|\chi_{\text{Be},(\text{zo},\text{z})}| \approx 0.930$ and $|\chi_{\text{Mg},(\text{zo},\text{z})}| \approx 0.368$. The roles are reversed and more extreme in the radial \mathbf{x} and \mathbf{y} OOPH modes (xo and yo) with $|\chi_{\text{Be},(\text{xo}/\text{yo},\text{x}/\text{y})}| \approx 0.022$ and $|\chi_{\text{Mg},(\text{xo}/\text{yo},\text{x}/\text{y})}| \approx 0.999$; this large asymmetry means that the xo and

yo modes are WCMs if cooling is performed using ${}^{9}\mathrm{Be}^{+}.{}^{19}$

Indirect cooling of the xo mode ($\omega_{xo} = 2\pi \times 4.48(2)$ MHz) and yo mode ($\omega_{yo} = 2\pi \times 4.04(3)$ MHz) was performed by coupling each of these modes to the zo mode ($\omega_{zo} = 2\pi \times 4.722(1)$ MHz) with a potential with correct curvature according to Eqs. 5.11 and 5.8. The same potential as for the previous section (Sec. 5.6.1) is used, since the modes are along the same directions (but with different participations).

The couplings were also calibrated with a similar experimental sequence as in Sec. 5.4, illustrated in Fig. 5.9. The zo mode is prepared in $|1\rangle_{zo}$ and one ro mode in $|0\rangle_{ro}$, $ro \in \{xo, yo\}$. This is accomplished by iterating ${}^{9}\text{Be}^{+}$ SBC and a coupling pulse multiple times until both modes are close to the ground states, then injecting a phonon into zo. Next, a coupling pulse is applied with variable frequency ω , shown in Fig. 5.9(a) and (c), or variable duration τ with the coupling on resonance, plotted in Fig. 5.9(b) and (d). Since the ${}^{9}\text{Be}^{+}$ ion hardly participates in the ro modes, it is difficult to directly measure their occupations. Therefore, only the final state of zo is measured with an MSS π -pulse $|\downarrow\rangle_{\text{B}}|1\rangle_{zo} \rightarrow |\uparrow\rangle_{\text{B}}|0\rangle_{zo}$ followed by ${}^{9}\text{Be}^{+}$ fluorescence detection. The probability $P(|\uparrow\rangle_{\text{B}})$ of being in $|\uparrow\rangle_{\text{B}}$ is inferred from the fluorescence data, and this probability approximately equals the probability of finding the single phonon in the zo mode.

Data from a frequency scan of the yo-zo coupling is shown in Fig. 5.9(a) (blue circles). The fit (solid blue line) yields an exchange resonance frequency of $\omega_{yo,zo}=2\pi\times0.7116(1)$ MHz $\approx\omega_{zo}-\omega_{yo}$. Fig. 5.9(b) shows the yo-zo coupling dynamics when driven on resonance with an amplitude approximately twice as large as what was used in the frequency scan for faster indirect cooling. The resulting exchange dynamics are fit to a decaying sinusoid to yield the single swap time $\tau_{yo,zo}=49.5(5)~\mu$ s. The reduced contrast of ≈0.8 is limited by the initial occupation of the yo mode, which is predominantly caused by its high heating rate (which was determined independently). The corresponding data and fits for the xo-zo coupling are shown in Figs. 5.9(c) and (d). The fits yield $\omega_{zo,xo}=2\pi\times0.2485(1)$ MHz $\approx\omega_{zo}-\omega_{xo}$ and $\tau_{xo,zo}=47.6(9)~\mu$ s. The xo mode was cooled

 $^{^{19}}$ During this time, the Raman 3 25 Mg⁺ beam was unavailable for use, meaning that radial mode cooling could only be performed using 9 Be⁺.

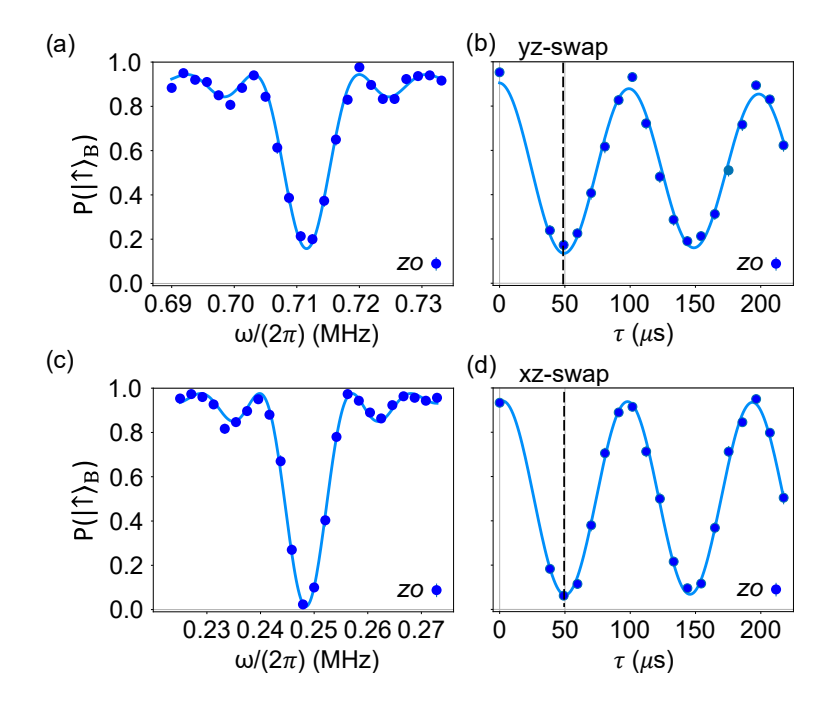


Figure 5.9: Mode coupling characterization in a ${}^{9}\text{Be}^{+}$ - ${}^{25}\text{Mg}^{+}$ ion crystal. Calibration results for the yo-zo (a),(b) and xo-zo (c),(d) coupling are shown. Vertical dashed lines denote the single-swap duration. All fits are from expressions (Eq. 5.19 and Eq. 5.20 as appropriate) fitted to the data. Each data point is obtained from 300 experiments with a 68% confidence error bar, which is smaller than the plot symbols for most points.

much closer to the ground state than the yo mode was in the previously described experiments. This results in the relatively higher of 0.88(4) for the data in Fig. 5.9(d) compared to Fig. 5.9(b).

After Doppler cooling, all three OOPH (and INPH) modes were cooled to near the ground state with repetitions of the sequence shown in parentheses in Fig. 5.10(a). A duration of 50 μ s was used for motion swap pulses, and each period of continuous sideband cooling (CSBC) of zo was performed on ${}^{9}\text{Be}^{+}$ for 75 μ s, followed by a 120 μ s CSBC pulse on the INPH axial mode to suppress the Debye-Waller effect from high occupation in this mode. The cooling sequence took 455 μ s and is repeated N times before determining the mode occupations.

The occupation \bar{n} of the xo and yo modes was determined by swapping the state to zo before performing sideband analysis with ${}^{9}\text{Be}^{+}$. Figure 5.10(b) shows the occupation \bar{n} of the three OOPH modes for different numbers of cooling cycles N (bottom axis) or cooling time (top axis). All three modes reach steady state for N > 10 cycles, with $\bar{n} = \{0.03(1), 0.23(2), 0.11(1)\}$ for the $\{xo, yo, zo\}$

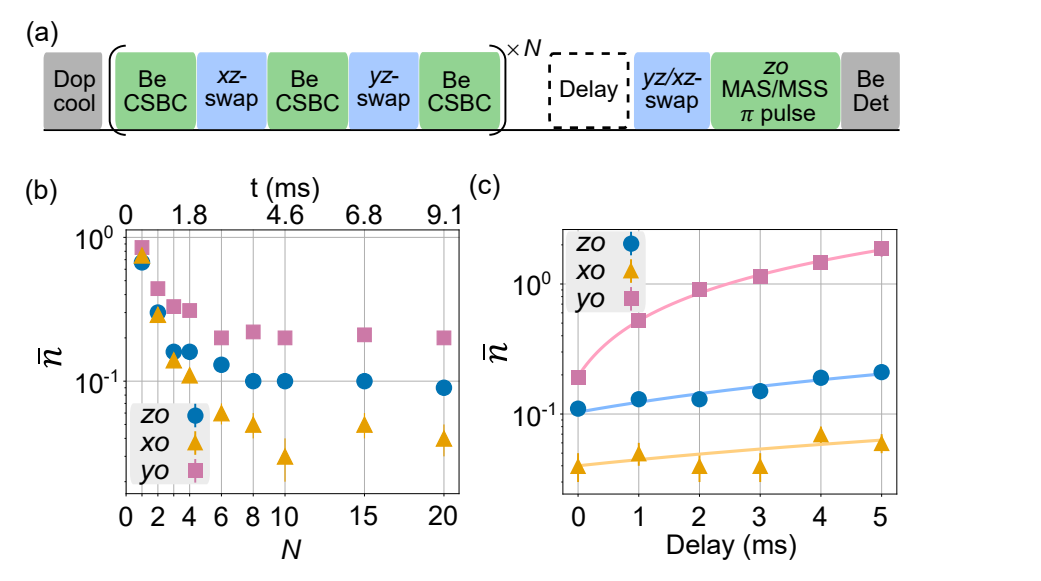


Figure 5.10: ${}^{9}\text{Be}^{+}\text{-}{}^{25}\text{Mg}^{+}$ cooling results. (a) Experimental sequence for cooling and heating measurements of all three OOPH modes. The xo and yo modes are indirectly cooled and measured by swapping their states to the zo mode. (b) Mean occupation number \bar{n} versus number of cooling cycles N (bottom) and cooling duration (top) for the three OOPH modes. (c) Occupations \bar{n} after 10 cooling cycles followed by a variable delay for the three out-of-phase modes. Solid lines are fits to a linear increase in average occupation over time, corresponding to constant heating rates. Each data point is obtained from 300 experiments with a 68% confidence error bar, which is smaller than the plot symbols for some points.

modes respectively at N=10. The mode heating rates were also characterized by cooling (N=10) and adding a variable delay time before sideband analysis. In Fig. 5.10(c), the \bar{n} of the three modes is shown as a function of the delay. The heating rates are the slopes of linear fits to \bar{n} versus delay time for each mode, shown as solid lines and yielding heating rates of $\{5(5), 330(30), 20(7)\}$ quanta per second for xo, yo, and zo respectively. The steady-state mode occupation was substantially higher for yo than xo and zo because of its much higher heating rate. The zo mode had a higher final \bar{n} than the indirectly cooled xo mode because the last cooling cycle swaps a thermal state of $\bar{n} \approx 0.2$ from the yo mode into the zo mode and the last SBC pulse was not long enough for zo to reach its steady state of $\bar{n} = 0.02(1)$. Increasing the duration of the last SBC pulse can reduce the final occupation of the zo mode at the expense of increasing the occupation of the other modes that will heat up during this pulse.

5.6.3 Modes with No Participation of the Coolant Ion

The participation of a specific ion in a normal mode can be exactly zero (for ideal confinements), for example due to symmetry. A crystal that has reflection symmetry around its center has axial modes that are either odd or even under reflection. If the crystal consists of an odd number N of ions, the center ion has zero participation for all (N-1)/2 normal modes that have even parity under reflection through the center of the crystal, and is ideally decoupled from these modes. Here, sympathetic cooling of all axial modes of a ${}^{9}\text{Be}^{+}$ - ${}^{25}\text{Mg}^{+}$ - ${}^{9}\text{Be}^{+}$ crystal with cooling light that only interacts with the middle ${}^{25}\text{Mg}^{+}$ ion is discussed.

The three axial modes are the in-phase (INPH), out-of-phase (OOPH) and alternating (ALT) modes, with respective frequencies $\{\omega_I, \omega_O, \omega_A\} = 2\pi \times \{1.501(1), 3.374(1), 3.655(1)\}$ MHz and eigenmode participations as shown in Fig. 3.20. The magnitudes of the $^{25}\text{Mg}^+$ ion participations for {INPH, OOPH, ALT} are $\approx \{0.83, 0, 0.56\}$ respectively, ideally vanishing for the OOPH mode. A potential with cubic variation in \mathbf{z} is used to couple the OOPH mode with the ALT mode, which has significant $^{25}\text{Mg}^+$ participation. The coupling is calibrated as in Sec. 5.4 to obtain the resonant frequency $\omega_{O,A} = 2\pi \times 0.2834(1)$ MHz $\approx \omega_A - \omega_O$.

Cooling of all axial modes to near their ground states using ²⁵Mg⁺ was accomplished by alternating CSBC and mode coupling swap pulses using the sequence shown in the upper row of Fig. 5.11(a), with the white box representing either the pulsed or continuous scheme, as detailed in the lower row.

$5.6.3.1 \qquad \text{Cooling 9Be}^{+}\text{-}{^{25}}\text{Mg}^{+}\text{-}^{9}\text{Be}^{+} \ \, \text{Using Mode Coupling and CSBC, Pulsed}$

In the pulsed cooling demonstration a 100 μ s swap pulse that exchanges the OOPH and ALT mode occupations was used. After Doppler cooling, a 300 μ s CSBC pulse on the second-order MSS of the INPH mode on 25 Mg⁺ was used to cool population in high number states, and was followed by first-order MSS pulses of 80 μ s and 150 μ s duration to perform CSBC of the INPH mode and ALT modes, respectively. These latter pulses were repeated eight times. A swap pulse then exchanged

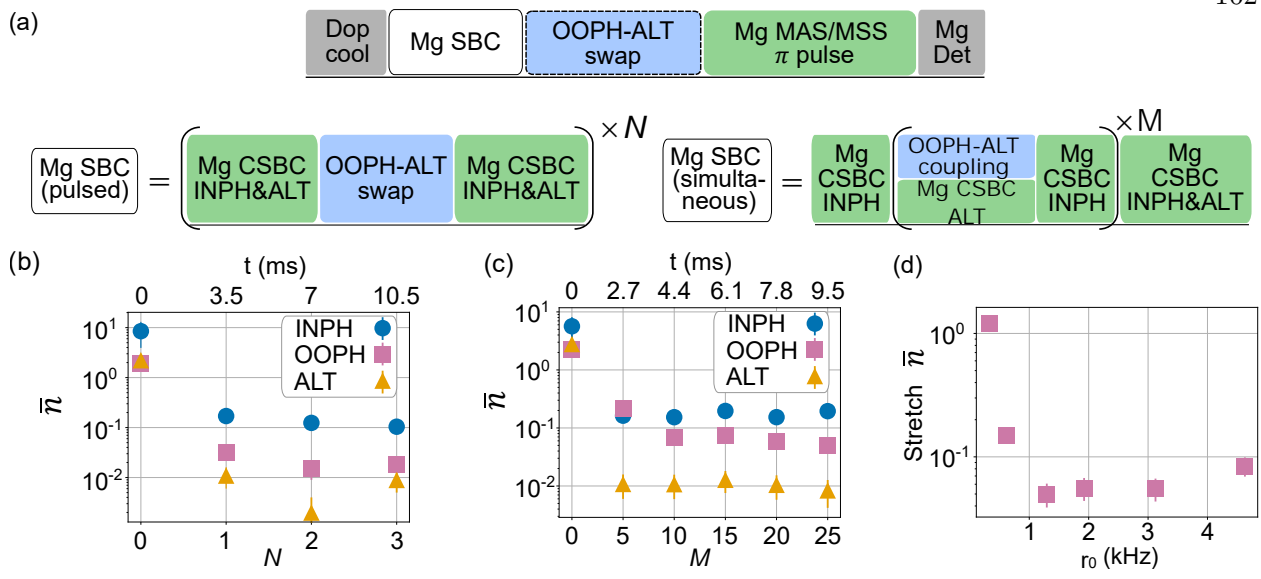


Figure 5.11: ${}^9\mathrm{Be}^{+}$ - ${}^2\mathrm{S}\mathrm{Mg}^{+}$ - ${}^9\mathrm{Be}^{+}$ indirect cooling results using mode coupling. (a) Experimental sequences for ground-state cooling the axial modes on ${}^{25}\mathrm{Mg}^{+}$. The OOPH mode is indirectly cooled to near its ground state using either the pulsed or simultaneous scheme and indirectly measured by swapping its state to the ALT mode. (b,c) Plots of mean occupation \bar{n} of the axial modes versus cooling cycle (bottom axis) and duration (top axis) when using (c) the pulsed scheme or (d) the simultaneous scheme with a coupling rate $\Omega_0 = 1.29\,\mathrm{kHz}$. (d) Mean occupation of the OOPH mode after M=25 pulsed cooling iterations versus coupling rate. Each data point is obtained from 300 experiments with a 68% confidence error bar, which is smaller than the plot symbols in some cases.

the occupations of the OOPH and ALT modes. The INPH and ALT modes were cooled by iterating $20~\mu s$ and $150~\mu s$ first order MSS SBC pulses on the two modes, respectively, eight times. Because $^{25}\text{Mg}^+$ ideally does not participate in the OOPH mode, photon recoil during cooling 20 of the INPH and ALT modes did not heat the OOPH mode significantly. This cooling sequence was repeated N times and sideband analysis was then performed to determine \bar{n} . The occupation of the OOPH mode was characterized by swapping its occupation to the ALT mode and then determining \bar{n} of the ALT mode.

The \bar{n} of all axial modes are shown in Fig. 5.11(b) as a function of the number of cooling cycles. All three modes were cooled close to their ground states, $\bar{n} = \{0.17(2), 0.03(1), 0.01(1)\}$ for {INPH, OOPH, ALT}, respectively, with just a single cooling cycle with a duration of about 3.5 ms. Slightly lower occupation can be achieved with more cycles, for example $\bar{n} = \{0.10(2), 0.018(6), 0.009(4)\}$

²⁰CSBC requires a repump step, which results in photon recoil.

with N=3. The \bar{n} of the OOPH mode was slightly higher than that of the ALT mode due to heating after the final swap and during the extra swap pulse needed for indirect characterization.

5.6.3.2 Cooling ${}^{9}\text{Be}^{+}$ - ${}^{25}\text{Mg}^{+}$ - ${}^{9}\text{Be}^{+}$ Using Mode Coupling and CSBC, Simultaneous

The OOPH and ALT modes can also be cooled by simultaneously applying CSBC on the ALT mode and driving the mode coupling operation to exchange mode occupations. Electric fields at the ²⁵Mg⁺ ion position from imperfections in generating the ideal cubic coupling potential can drive ²⁵Mg⁺ to oscillate at the parametric drive frequency, thus reducing the Rabi frequency of the cooling light. Similar to the technique used in Sec. 5.4.2, these extraneous electric fields were minimized by optimizing the sideband Rabi rate when the mode-coupling operation is on. The mode coupling operation was first detuned in order to prevent coupling, and the sideband Rabi rate as a function of coupling drive amplitude can be found; similar to trap RF micromotion sidebands, this dependence will follow a Bessel function. Then, the "twist term" described in Sec. 5.4.2 was used to adjust the coupling potential so that the dependence of sideband Rabi rate on mode coupling amplitude was as weak as possible. This is described in more detail in Appendix E of Ref. [98].

The cooling sequence is shown in right side of the lower row of Fig. 5.11(a), consisting of 40 μ s of CSBC on the first-order MSS of the INPH mode followed by 225 μ s of CSBC on the second-order MSS. The OOPH and ALT modes were then cooled simultaneously by driving the mode coupling operation and performing first-order CSBC of the ALT mode at the same time for 300 μ s, followed by 40 μ s of CSBC on the INPH mode. This latter sequence was repeated M times. Since the INPH mode occupation increases during the cooling of other modes due to anomalous heating and additional excitation from imperfect coupling pulses, final SBC pulses of 750 μ s total duration on the INPH and ALT modes were applied before analysis. For M=0, no SBC is implemented and the \bar{n} directly after Doppler cooling is shown.

Figure 5.11(c) shows the occupations \bar{n} versus M for the three axial modes when the ALT and OOPH modes were coupled at a rate of $\Omega_c = 2g_{O,A} = 1.29(2)$ kHz. Due to the pre-cooling of the INPH mode and the final cooling sequence for INPH and ALT modes, these modes reach

their steady state of $\bar{n}_I = 0.16(2)$ and $\bar{n}_A = 0.013(5)$ for all M > 0. The OOPH mode occupation decreases as M increases with $\bar{n}_O = 0.05(1)$ at M = 25. The final occupation of the OOPH mode is affected by the coupling rate. Fig. 5.11(d) shows \bar{n}_O at M = 25 as a function of Ω_c . Faster motional exchange reduces \bar{n}_O until imperfections in the parametric drive lead (even after minimization) to strong driven motion of $^{25}{\rm Mg}^+$ which reduces the MSS Rabi rate during SBC. The lowest OOPH mode \bar{n} is achieved for $\Omega_c \approx 1.29~{\rm kHz}$.

Both pulsed and simultaneous cooling using this mode-coupling operation are also shown with EIT instead of SBC in Fig. 4.12 in Chp. 4.

5.7 Repeated Non-Destructive (Projective) Readout of Ion Motion

While the lack of ²⁵Mg⁺ participation in the axial²¹ OOPH mode of ⁹Be⁺-²⁵Mg⁺-⁹Be⁺ causes complications for cooling, it can also be used as a powerful tool. Readout of ion motion has historically relied on the entanglement of the ion internal state with the motion, as discussed in Sec. 2.2.2.1, followed by detection of the internal state through fluorescence detection. This is a projective measurement that will collapse the motion state depending on the result of the internal state. However, fluorescence detection causes photon recoil if the internal state detected is the |Bright⟩ state. This means that the motion state entangled with the fluorescing internal state becomes corrupted by the detection itself, making mid-circuit readout difficult. Therefore, experiments with ion motion have always relied on either a single destructive measurement per shot (for example, at the end of the experiment sequence), or mid-circuit readout with post-selection on the non-fluorescing |Dark⟩ internal state readout result [16, 18, 32].

With the mode-coupling operation, this problem can be circumvented; in our case, the spinmotion entanglement can be performed with a mode having ²⁵Mg⁺ participation (ALT), and afterwards, the motion states of ALT and OOPH can be swapped. When ²⁵Mg⁺ is detected, it will ideally collapse the motion state that is now in the OOPH mode, and the photon recoil is only minimally coupled (ideally not coupled at all) to that mode. Thus, there is no additional

²¹In this section, only the axial modes are discussed so the direction of the mode is not specified.

alteration of the state beyond the projection performed by the spin state readout. We call this a "non-destructive measurement". In contrast to a "non-demolition measurement" it is emphasized that this measurement is projective. However, because it comes without photon recoil that further disturbs the state, it is non-destructive in comparison. This is the process described in Fig 5.12. It allows for multiple repeated projections, analogous to fluorescence detection for ion internal states. For a general sequence of repeated projective measurements, the leftmost part of the beige box in the quantum circuit can be replaced with any desired spin-motion entangling operation that allows to read out one bit of information about the motion through the internal state of the ion.

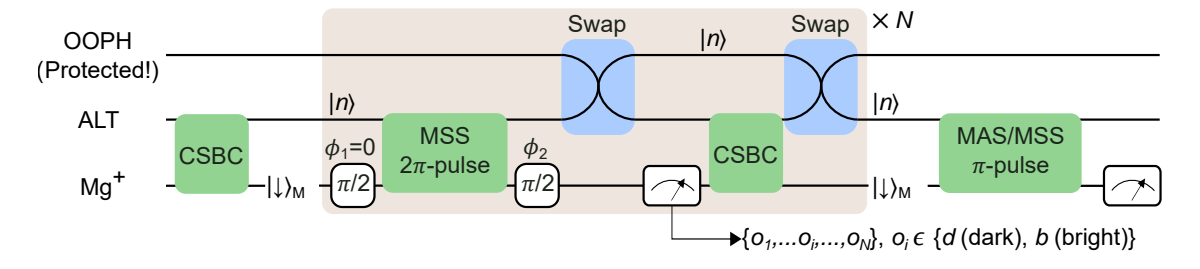


Figure 5.12: The quantum circuit above describes the procedure for performing repeated non-destructive (projective) measurements of ion motion by using the mode-coupling operation to access a mode that is protected from recoil during fluorescence detection. The modes in the crystal under consideration, ${}^9\mathrm{Be}^+-{}^{25}\mathrm{Mg}^+-{}^9\mathrm{Be}^+$, are OOPH (the protected mode) and ALT (the mode with participation of the detection ion, ${}^{25}\mathrm{Mg}^+$). In this sequence, the state is initialized by CSBC. Next, the motion information is transferred onto the internal state of ${}^{25}\mathrm{Mg}^+$ using a Cirac-Zoller type sequence that can be chosen to map the $|0\rangle$ and $|1\rangle$ Fock states to $|\mathrm{Bright}\rangle$ and $|\mathrm{Dark}\rangle$ respectively, or vice versa. Then, the motion state of interest is swapped into the protected mode before fluorescence detection (and then CSBC to reinitialize the motion states) is performed. The motion state of interest is then transferred back to the ALT mode for either another round of mid-circuit detection, or final sideband analysis that does not preserve the motion state.

Excitingly, this opens the door for mid-circuit readout of the ion motion, which is a necessity for bosonic error correction using trapped ions. In this case, the spin-motion entangling operation should correspond to the error syndrome used.

5.7.1 Experimental Sequence

To demonstrate this procedure, a proof-of-principle experiment distinguishing the $|0\rangle$ and $|1\rangle$ Fock states of motion repetitively using the sequence shown in Figure 5.12 was performed. These are motion states that could be prepared and characterized quite well, so they were suitable for this demonstration. The spin-motion entanglement required to extract motion information through fluorescence detection was a Cirac-Zoller (CZ) type interaction [1]. This relies on the fact that a (first-order) sideband 2π -pulse (with time $t = 2\pi/\Omega_{\rm eff}$, where $\Omega_{\rm eff} = \eta\Omega_0$ is the effective Rabi rate of the sideband as in Eq. 2.67) does not actually return the state to its original form, but rather flips the sign of the wavefunction. By using a motion-subtracting sideband (MSS) (and assuming that these are the only two motion Fock states present), if the motion was in the $|0\rangle$ Fock state, the wavefunction would be unaffected while if the motion was in the $|1\rangle$ Fock state, the wavefunction would change sign.

Since this phase is not observable without a reference state, a superposition state was created prior to the sideband pulse. At the beginning of the sequence, a superposition between the $^{25}\text{Mg}^+$ qubit states in the $^2\text{S}_{1/2}$ manifold was established using microwave operations: $\frac{1}{\sqrt{2}}(|2,0\rangle+|3,1\rangle)$. Then, the $|3,1\rangle$ state was transferred to $|2,2\rangle$ using a microwave π pulse, and an MSS 2π -pulse was applied between $^2\text{S}_{1/2}|2,2\rangle$ and $|3,3\rangle$ on the ALT mode. The $|2,2\rangle$ state was then returned to $|3,1\rangle$ with another π pulse, and the resulting superposition should be $\frac{1}{2}\left[(|2,0\rangle+|3,1\rangle)|0\rangle_{\text{A}}+(|2,0\rangle-|3,1\rangle)|1\rangle_{\text{A}}\right]$. A final microwave $\pi/2$ pulse was applied with a phase ϕ_2 such that $\phi_2=0$ gives the state $\frac{1}{\sqrt{2}}\left[|2,0\rangle|0\rangle_{\text{A}}-|3,1\rangle|1\rangle_{\text{A}}\right]$ and $\phi_2=\pi$ gives $\frac{1}{\sqrt{2}}\left[|3,1\rangle|0\rangle_{\text{A}}-|2,0\rangle|1\rangle_{\text{A}}\right]$. The $|2,0\rangle$ state is shelved to $|\text{Dark}\rangle$ while the $|3,1\rangle$ state was shelved to $|\text{Bright}\rangle$ prior to fluorescence detection. Therefore, depending on the phase of ϕ_2 used, each Fock state could be corresponded to a different fluorescence result.

Instead of being defined as 0 or π , this phase was determined empirically. The phase that yields $|0\rangle \to |\text{Dark}\rangle$ and $|1\rangle \to |\text{Bright}\rangle$ was labeled M1, while the inverse mapping was labeled M2. Depending on the desired mapping ($|0\rangle \to |\text{Bright}\rangle$ and $|1\rangle \to |\text{Dark}\rangle$ or vice-versa), the phase of the second $\pi/2$ pulse was scanned until the prepared state yielded the desired detection result, as shown in Fig. 5.13. This phase drifted on the timescale of tens of minutes, and therefore was important to calibrate before each set of experiment data.

It is important to note that using the CZ type interaction shown here only works if the motion

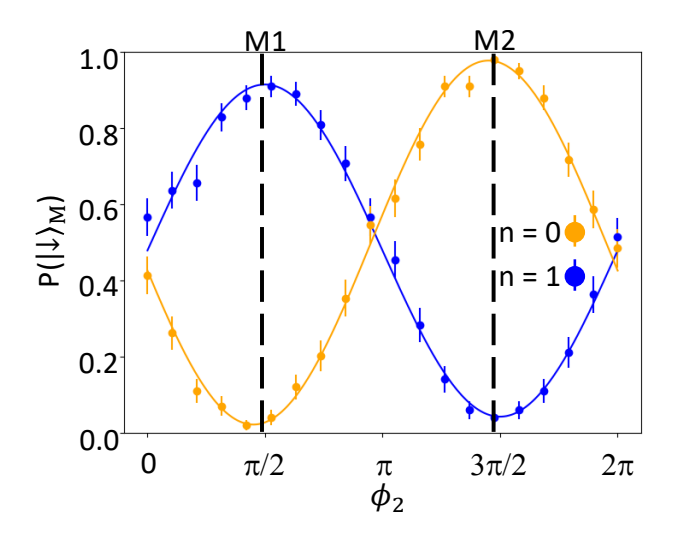


Figure 5.13: With the ALT mode prepared in $|0\rangle_A$ (orange) or $|1\rangle_A$ (blue), two sinusoidal curves are obtained via fluorescence detection of $^{25}\mathrm{Mg}^+$. These signals oscillate out of phase as a function of the phase ϕ_2 of the second $\pi/2$ pulse relative to the first $\pi/2$ pulse in the CZ sequence. The two vertical dashed lines indicate the phases for realizing mappings M1 and M2.

state is known to be in either $|0\rangle$ or $|1\rangle$. Any higher number Fock states will result in entanglement to the $^{25}\text{Mg}^+$ internal state according to the corresponding Rabi rate (Eq. 2.64), and the resulting projection will give an unexpected Fock state mixture. In theory, multiple Fock states can be distinguished in steps by performing the CZ type interaction with an n^{th} order sideband starting from the highest expected Fock state (which would not drive transitions for Fock states with Fock number less than n), then performing a projective measurement where only that Fock state is distinguished from all others, and then iterating with lower and lower sidebands until the readout sequence in Fig 5.12 is reached. For example, if $|0\rangle$, $|1\rangle$, and $|2\rangle$ are expected, the interaction can be first performed on the 2^{nd} -order motion-subtracting sideband. This will give no phase shift between the atomic state superpositions for $|0\rangle$, and $|1\rangle$, but will cause a phase shift if the motion state is in $|2\rangle$. Therefore, the motion state will be projected into $|2\rangle$ if the spin corresponding to the phase flip is projected, but $|0\rangle$ and $|1\rangle$ are not distinguished from each other. The operation can then be performed on the first sideband to distinguish $|0\rangle$ and $|1\rangle$ (if the readout does not correspond a Fock state of $|2\rangle$). It is important to perform this sequence beginning with the sideband corresponding to the highest Fock state probed in order to avoid any ambiguous projection results. Unfortunately,

this can be extremely time-consuming as higher-order sidebands can be very slow depending on the Lamb-Dicke parameter of the system.

In our apparatus, the above hypothetical sequence is difficult to perform, as our second-order ALT sideband was extremely slow at the parameters used for this experiment. The frequency drift of the transition relative to the linewidth (≈ 10 kHz FWHM) was such that it could not be properly driven ≤ 5 minutes after calibration. Thus, it was not realistic to use a second-order sideband as part of the motion detection sequence. Therefore, potential population in $|2\rangle_A$ at all was avoided by initializing the motion state with the CSBC sequence, which yielded a mixed state with 2% $|1\rangle_A$ and 98% $|0\rangle_A$.

After the CZ-type interaction entangled the spin and motion, the mode-coupling operation was used to perform a full swap of the motion from the ALT mode to the OOPH mode. Then, the internal state of 25 Mg⁺ was detected using standard fluorecence detection, and the two axial spectator modes, INPH and ALT, were re-cooled through 25 Mg⁺, in order to reduce Debye-Waller effects during state identification or the spin-motion entanglement sequence. If a motional mixture or superposition was prepared at the beginning of the sequence, the first detection projects the motion state of interest into $|0\rangle$ or $|1\rangle$. The swap operation was then performed again to complete the non-destructive motion detection sequence (highlighted in beige in Figure 5.12). This whole sequence was performed as many times as desired, and then a standard destructive sideband readout was performed to confirm the non-destructive measurement results (see Sec. 2.2.2.2, [68]).

5.7.2 Results

For this demonstration, up to three repeated mid-circuit detections were performed before the destructive analysis pulse.²² Fig. 5.14(a) and (b) show the mid-circuit readout (using the CZ-type interaction) results for mappings M1 and M2 respectively. When the repeated readout fluorescence

²²Recording of repeated results for projective measurements was performed in a binary manner, with up to 50 detection iterations attempted and the results recorded. The recording of repeated results as well as slow loss of the population after multiple swaps due to heating and other errors (see Fig. 5.6) were the primary limitations on the number of repeated detections that could be performed.

results disagreed, a decision could not be made on what Fock state to assign the result to. Disagreeing results can arise from mis-identification of the motion state during fluorescence detection or a true change of the Fock state during, in between, or as a result of the previous detection. For example, anomalous heating can cause $|0\rangle \rightarrow |1\rangle$ and $|1\rangle \rightarrow |2\rangle$, while an imperfect MSS 2π -pulse during the CZ sequence can cause $|1\rangle \rightarrow |0\rangle$. When two mid-circuit detections were made, the shots of the experiment that have disagreeing results must be discarded, as it was difficult to determine which of the two was more correct. When three mid-circuit detections were made, any shots with disagreeing results can be discarded (this is the result shown in Figure 5.14), or a "majority vote" approach can be taken (this was not done here but data for all combinations of detection results are available in Tab. B.5).

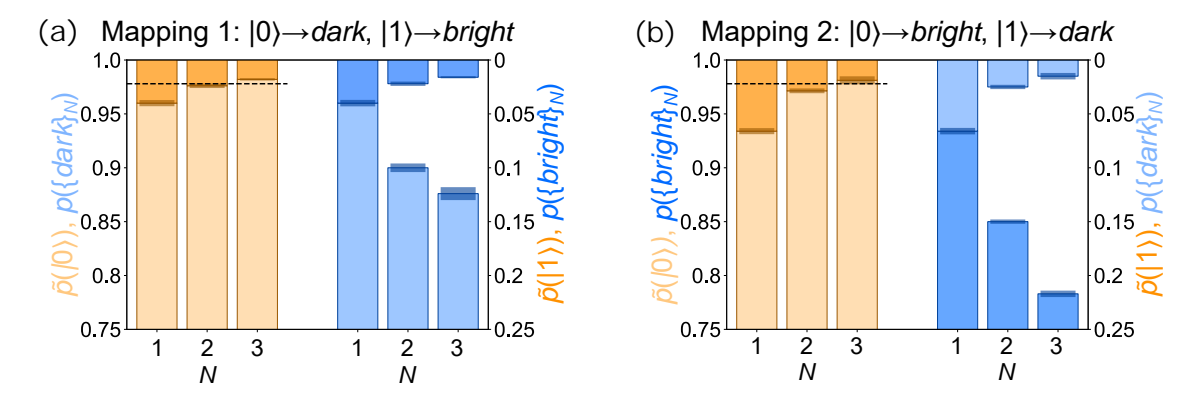


Figure 5.14: The repeated readout results distinguishing the $|0\rangle$ and $|1\rangle$ Fock states are shown. (a) shows mapping M1, where a dark fluorescence detection result ideally indicates $|0\rangle$ in the motion state of interest, while a bright detection indicates $|1\rangle$. (b) shows the inverse mapping M2. The bright blue bars are the fraction of N repeated readout results that are all bright fluorescence readouts, while the faded blue bars are the fraction of N repeated readout results that are all dark. These are normalized to bright orange and faded orange results indicating the Fock states corresponding to the mapping used. The error in each value is indicated by the shaded rectangle on the edge of each bar. The dotted black line is the expected ratio of $|0\rangle$ and $|1\rangle$ Fock states for a state prepared by SBC the ALT mode.

The bright and faded blue bars in Fig. 5.14 indicate the percentage of readout results that are all bright or dark respectively for N repetitions. It can be seen that there are detection results that disagree and therefore were discarded, leaving the gap between the bright and faded blue bars for N = 2, 3 detections. The detection results then can be normalized and interpreted as indicating that

the motion state was either $|0\rangle$ or $|1\rangle$ depending on the mapping used. This is shown as the orange data, and it can be seen that the ratio of data supporting Fock states $|0\rangle$ and $|1\rangle$ converges to the ratio expected after CSBC, indicated by the dashed black line.

After a sequence of N mid-circuit detections using the protected mode, the ion state was read out using motion-adding sidebands (MAS) and MSS, which exposed the motion state to photon recoil. The results from this non-motion preserving detection can be used to verify the mid-circuit readout results, as shown in Fig. 5.15. The data in Fig. 5.15 was first sorted by the number of repeated mid-circuit detection results (that all agree), and then by whether the detection results are bright or dark. Depending on the mapping, this should indicate either the $|0\rangle$ or $|1\rangle$ Fock state, and the MAS/MSS readout results are compared to the ideal MAS/MSS transition probabilities for the relevant Fock states (hatched bars).

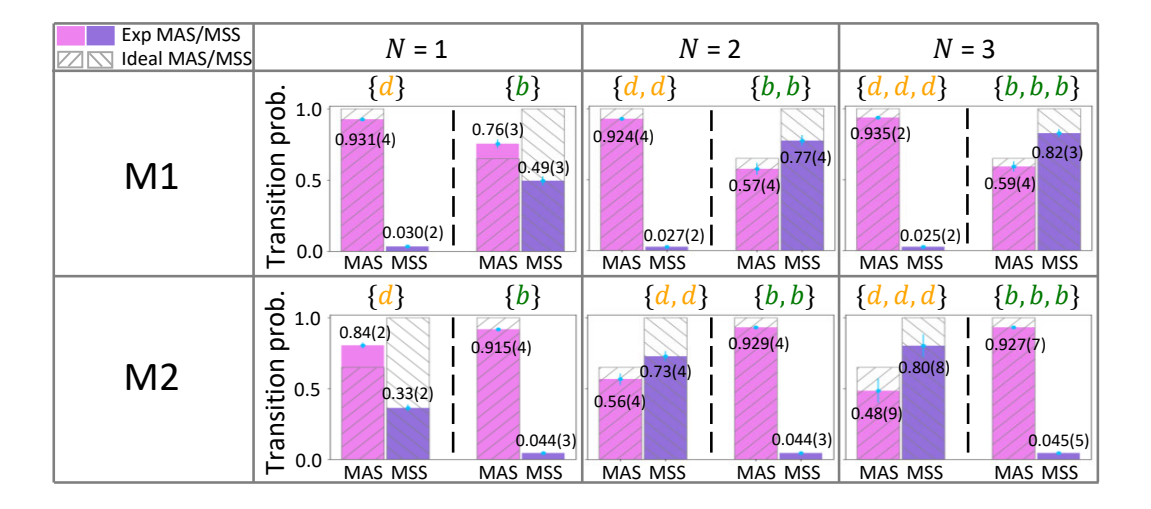


Figure 5.15: The MAS and MSS transition probability data are sorted by the results of repeated midcircuit measurements. A sequence of N repeated dark ("d" above) or bright ("b" above) fluorescence results indicate the motion state of interest is in $|0\rangle$ and $|1\rangle$ respectively if mapping M1 (upper data row) is used, with the inverse being true when mapping M2 (bottom row) is used. The MAS and MSS transition probabilities are shown in pink and purple respectively, with the hatched bars indicating the ideal MAS and MSS excitation results corresponding to the appropriate Fock state.

When the mid-circuit readout indicated that the motion state was $|0\rangle$ (dark for M1 and bright for M2), the experimental MAS and MSS results were quite close (within 9% and 5% respectively) to

the ideal result. However, the results corresponding to $|1\rangle$ were far from the ideal values. In fact, the data for the N=1 detection results for both mappings show the inverse probability — that driving a MAS is more likely to succeed than driving an MSS, which is the opposite of what is expected for a $|1\rangle$ Fock state. This is likely due to the lack of statistics for the $|1\rangle$ Fock state to be prepared initially; because the total number of shots of the experiment where $|1\rangle_{\rm O}$ was projected is much lower than that where $|0\rangle_{\rm O}$ was projected, mis-identifications of $|0\rangle$ as $|1\rangle$ from the mid-circuit detection contribute a relatively large number of experimental shots to the relevant statistics compared to the shots where $|1\rangle$ was correctly identified. Such mis-identifications should be reduced if multiple repetitions of the detection are performed, and it can be seen that the excitation probabilities do appear to approach the ideal values as the mid-circuit detection is repeated more times and disagreeing results are discarded (N=2,3 detection data in Fig. 5.15).

The data shown in Fig. 5.15 can also be analyzed by sideband thermometry (Sec. 2.2.2.2) to quantify how close the states determined to be $|0\rangle$ by the mid-circuit measurements are to the ground state. As seen in Fig. 5.16, the data obtained by post-selecting on mid-circuit measurements indicating the presence of the $|0\rangle$ state indeed appear to have the lowest average occupations (blue points). The data obtained using the mapping M2 (where $|0\rangle$ corresponds to the bright state) are in general higher than that obtained using M1 (where no fluorescence indicates $|0\rangle$), indicating that a small amount of recoil heating occurs despite the state being in the OOPH mode; this is discussed in Secs. 5.7.3 and 5.7.4. Even when no post-selection occurs, the average occupation obtained from the data from the repeated mid-circuit detection experiments (pink data points in Fig. 5.16) is lower than that when no swaps (or detection, cooling etc) occur at all (black data points). This is because during the experiment, the swap operations caused the state of interest to be stored in the OOPH mode for long periods of time, which has a much lower heating rate than ALT (where the state remains if no swaps are applied).

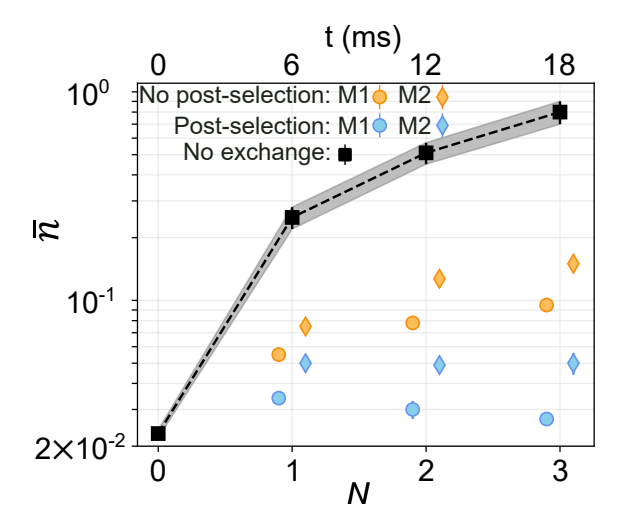


Figure 5.16: ALT mode mean occupation number (\bar{n}) post-selected on all N outcomes being $|0\rangle$ (blue symbols) is lower than corresponding \bar{n} with no post-selection (orange symbols). "No exchange" \bar{n} (black squares) are fluorescence detection results after applying a delay with the duration of N measurement blocks without swapping into the OOPH mode. Each data point with a 68% confidence error bar was obtained from 6,000 experiments except for M2 N=3, which was obtained from 2,000 experiments. Data points and bars are laterally offset from N values for legibility and error bars for some points are smaller than plot symbols.

5.7.3 Characterization of Heating from Measurement Sequence

A series of tests were performed to characterize the heating from each element (block or sequence of blocks) of the motional state measurement sequence in Fig. 5.12. All three axial modes were sideband cooled to near their ground states and the $^{25}\text{Mg}^+$ ion was prepared in $|\downarrow\rangle_M$. Then, modified measurement sequences were implemented with different combinations of CZ mapping, swap pulses, $^{25}\text{Mg}^+$ detection, and $^{25}\text{Mg}^+$ SBC of the INPH and ALT modes. Elements that were not applied were sometimes replaced with a delay of equal duration to account for anomalous heating. This was followed by either applying an ALT MAS or MSS π -pulse and performing sideband thermometry as described in Sec. 2.2.2.2, [68]. The results of these tests and detailed sequences (such as whether or not a delay was included) are shown in Tab. 5.1.

The mean occupation of the ALT mode immediately after SBC was determined to be $\bar{n}_{\rm SBC} = 0.023(1)$ as a reference value. In the "no swaps" test, the two swaps were replaced with two delays of equal duration, which yields $\bar{n} = 0.040(3)$, higher than $\bar{n}_{\rm SBC}$ by $\Delta \bar{n} = 0.017(3)$ due

to the heating of the ALT mode acting over the delay replacing the second swap. This test also approximately sets a lower bound for \bar{n} when at least one detection is performed and no outcome is used for post-selection. Next, a swap test where only two swap pulses were applied after SBC was performed. A change of \bar{n} by $\Delta \bar{n} = 0.021(4)$ from two swaps was observed. In the CZ heating test, a delay of equal duration as a CZ mapping sequence was inserted before swaps and further increased \bar{n} by $\Delta \bar{n} \approx 0.005$. To estimate the $\Delta \bar{n}$ due to heating of the OOPH mode during $^{25}{\rm Mg}^+$ detection and SBC of the other two modes, a delay equal to the duration of ²⁵Mg⁺ detection was applied followed by $^{25}{\rm Mg}^+~{\rm SBC}$ (between the two swap operations), yielding an increase of $\Delta\bar{n}=0.010(5).$ In the recoil heating test discussed in Sec. 5.7.4, fluorescence detection was applied between the swap operations to investigate the additional heating of the OOPH mode from recoil of photons scattered on $^{25}{\rm Mg}^+$. An estimated $\Delta \bar{n} \approx 0.012(5)$ was found to be added to \bar{n} from scattered photons alone. An ion typically scatters on the order of a few tens of photons during SBC while on the order of 10^3 photons are scattered during fluorescence detection in this apparatus. Assuming recoil heating is proportional to scattered photon number, scattering during SBC only causes a negligible gain in \bar{n} on the order of 10^{-4} . Lastly, a test (labelled as "No exchange" in Fig. 5.16) was implemented that replaces N=1,2,3 measurement blocks with an equal delay. This gives $\bar{n}=0.25(3),0.51(6),0.8(1),$ respectively, which are significantly higher than $\bar{n}_{\rm SBC}$, because the motional state resides longer in the ALT mode which has a higher heating rate, compared to N measurement blocks where the mode is swapped to the OOPH mode for substantial parts of the experiments, as discussed previously.

5.7.4 Effects of Recoil Heating

Even after ensuring that the ²⁵Mg⁺ is decoupled from the OOPH mode as described in Sec. 5.4.2, the amount of heating (or motion mode degradation in general) on the OOPH mode from ²⁵Mg⁺ detection light is non-negligible, as shown in tests described in Fig. 5.17. First, a state was prepared on the ALT mode, and then swapped into the OOPH mode. Next, ²⁵Mg⁺ fluorescence detection was applied followed by CSBC on the INPH and ALT modes. Finally, the OOPH mode was swapped back to the ALT mode and a sideband oscillation was observed (an MAS on the

ALT mode was applied for varying duration followed by fluorescence detection on $^{25}\mathrm{Mg}^+$). This sequence, shown in Fig. 5.17(b) was performed for three different initial states: $|0\rangle_{\mathrm{A}}|\downarrow\rangle_{\mathrm{M}}$ (results shown in Fig. 5.17(c)), $|1\rangle_{\mathrm{A}}|\downarrow\rangle_{\mathrm{M}}$ (Fig. 5.17(d)), and $\alpha|0\rangle_{\mathrm{A}}|\uparrow\rangle_{\mathrm{M}}+\beta|1\rangle_{\mathrm{A}}|\downarrow\rangle_{\mathrm{M}}$ where $|\alpha|^2\approx|\beta|^2\approx0.5$ (Fig. 5.17(e)). $|\downarrow\rangle_{\mathrm{M}}$ is the fluorescing state.

In Fig. 5.17(c) and Fig. 5.17(d), without (orange squares) and with (green triangles) scattering thousands of photons off the $^{25}\mathrm{Mg^+}$ ion, nearly identical MAS excitation traces were obtained, implying that the motional state is not perturbed substantially by the $^{25}\mathrm{Mg^+}$ ion recoil while stored in the OOPH mode. In Fig. 5.17(e), the blue dots are the MAS oscillation results averaged over all experimental trials while disregarding the detection outcome from $^{25}\mathrm{Mg^+}$ in the middle of the experiment, with a rapid decay of contrast due to the mixture of motional states that remained after detection. However, if the MAS results are sorted based on the mid-circuit detection outcomes, two traces are obtained depending on whether $|\uparrow\rangle_M$ or $|\downarrow\rangle_M$ was detected, projecting the motional state onto $|0\rangle_A$ (orange squares) and $|1\rangle_A$ (green triangles) respectively. The sorted trace for $|0\rangle_A$ ($|1\rangle_A$) is nearly identical to the trace in Fig. 5.17(c) (Fig. 5.17(d)) where $|0\rangle_A$ ($|1\rangle_A$) was directly prepared without a projection using $^{25}\mathrm{Mg^+}$ fluorescence detection. The decay of contrast in these oscillation curves was mainly caused by fluctuations in the Rabi frequency (Debye-Waller effect) due to substantial heating of the INPH mode.

Fig. 5.17(f) shows a circuit diagram to test whether motional coherence was preserved between $|0\rangle_{\rm A}$ and $|1\rangle_{\rm A}$ during $^{25}{\rm Mg}^+$ scattering. A carrier $\pi/2$ pulse driving $|\downarrow\rangle_M \leftrightarrow |\uparrow\rangle_M$ with a subsequent red-sideband (RSB) π pulse driving $|\downarrow\rangle_M |1\rangle_{\rm A} \leftrightarrow |\uparrow\rangle_M |0\rangle_{\rm A}$ prepared the ALT mode in a superposition state $1/\sqrt{2}(|0\rangle_{\rm A} + |1\rangle_{\rm A})$ and $^{25}{\rm Mg}^+$ in $|\downarrow\rangle_M$. After the recoil heating test sequence, another RSB π pulse and carrier $\pi/2$ pulse with varying phase ϕ relative to the first $\pi/2$ pulse close the motional Ramsey interferometer. (g) shows that the motional Ramsey fringes with (green triangles) or without (orange squares) $^{25}{\rm Mg}^+$ scattering have similar contrast which indicates the motional coherence was preserved despite fluorescence detection. The imperfect Ramsey contrast of both curves is likely caused by imperfect preparation, motional dephasing and readout errors.

In Fig. 5.17(h), the experimental sequence for varying detection periods is shown. This replaces

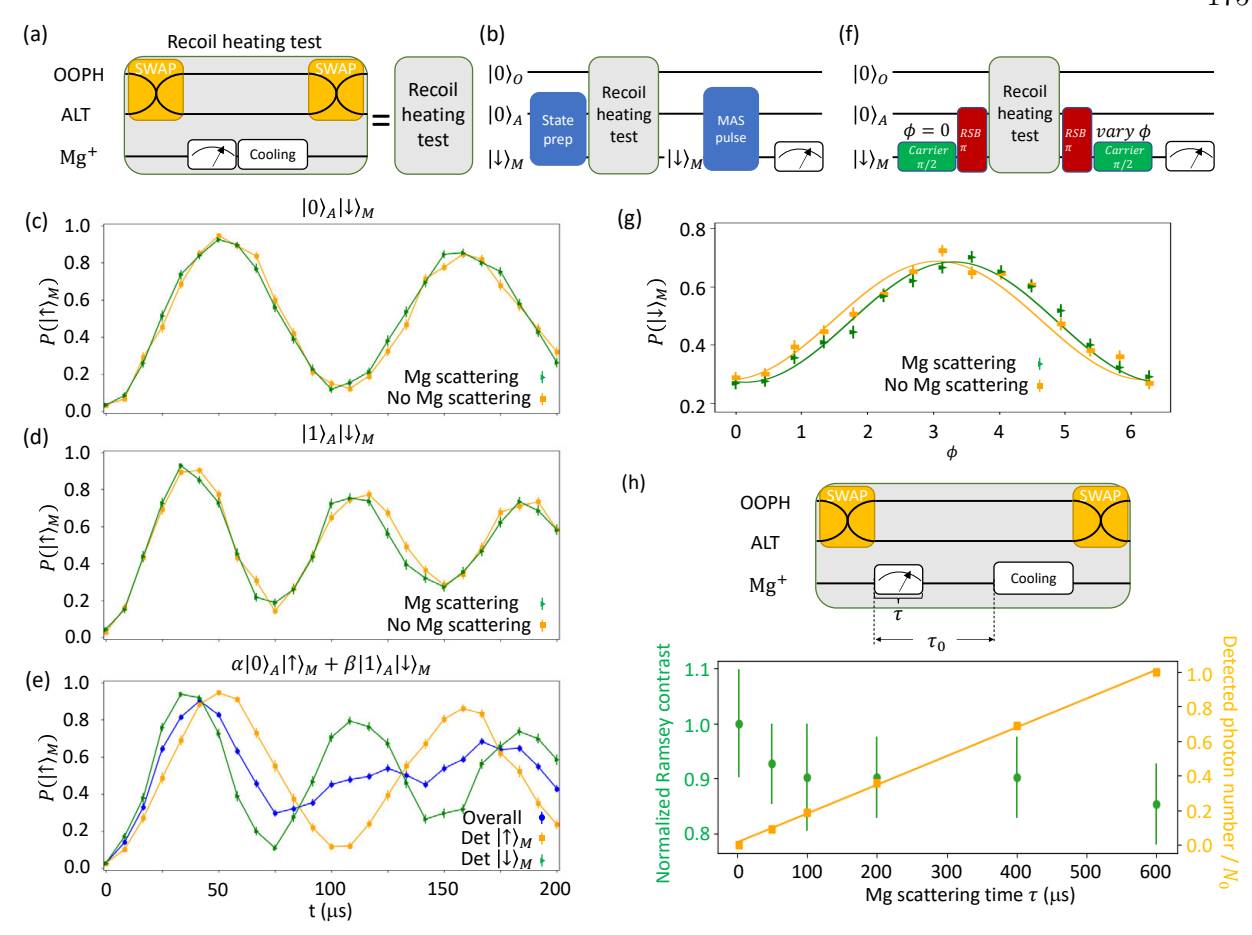


Figure 5.17: (a), Circuit diagram for ²⁵Mg⁺ recoil heating test. The test sequence consists of two swap pulses that exchange the states between the OOPH ("protected") and ALT mode, followed by ²⁵Mg⁺ detection, and a SBC sequence for the INPH mode. ²⁵Mg⁺ detection is replaced with a delay of the same duration for the "No Mg scattering" tests. (b), Circuit diagram for testing impact on an OOPH motion state after ²⁵Mg⁺ scattering. The ALT mode and ²⁵Mg⁺ ion internal state are prepared in $|0\rangle_{\rm A}|\downarrow\rangle_{M}$ (results shown in (c)), $|1\rangle_{\rm A}|\downarrow\rangle_{M}$ (results shown in (d)), and $\alpha|0\rangle_{\rm A}|\uparrow\rangle_{M}+\beta|1\rangle_{\rm A}|\downarrow\rangle_{M}$ where $|\alpha|^2 \approx |\beta|^2 \approx 0.5$ (shown in (e)), then the recoil test sequence with or without $^{25}\mathrm{Mg}^+$ scattering was applied, and finally an MAS pulse on the ALT mode was applied with a varying duration followed by ²⁵Mg⁺ fluorescence detection to obtain the oscillations in each data subfigure (c)-(e). (f), Circuit diagram for testing survival of motional coherence between $|0\rangle_A$ and $|1\rangle_A$ during $^{25}\mathrm{Mg}^+$ scattering using a Ramsey sequence; the results are shown in (g). (h). Upper panel shows the experimental sequence for varying detection periods that is used in place of the "recoil heating test" in (f). A fixed time $\tau_0 = 800 \,\mu s$ is set between the first swap and recooling of the INPH mode, and the $^{25} \mathrm{Mg}^+$ scattering time τ is increased. The detected photon number, normalized to $N_0 = 51.6$ is shown in orange squares, while the resulting normalized Ramsey contrast (normalized to 0.41, the Ramsey contrast with 0 μ s precession time) is shown in green squares.

the "recoil heating test" panel in Fig. 5.17(f). The time between the two swap operations is fixed

to $\tau_0 = 800 \,\mu\text{s}$. The detected photon number (orange squares, normalized to $N_0 = 51.6$) linearly increased over τ while the motional Ramsey contrast (green dots, normalized to the contrast of 0.41(4) for $\tau = 0 \,\mu\text{s}$) remained unchanged within the experimental uncertainty as more photons are scattered.

5.8 Extensions

As shown in Sec. 5.6, the mode-coupling operation already has clear applications in indirect cooling of motion modes, and it is used in our apparatus for cooling the axial OOPH mode of the ${}^{9}\text{Be}^{+}$ - ${}^{25}\text{Mg}^{+}$ - ${}^{9}\text{Be}^{+}$ ion crystal through ${}^{25}\text{Mg}^{+}$ as part of the standard ground-state cooling sequence.

The ability to perform projective mid-circuit measurements could lead to many other applications, such as its use in error correction using bosonic states [59, 60]. Ideally, an experiment similar to that performed with Fock states $|0\rangle$ and $|1\rangle$ as shown in Fig. 5.12 should be demonstrated with a true bosonic code state, showing stabilization of error correction subspaces through repeated measurement, rather than the Fock states demonstrated here.

Preparations to do so are already underway in the current apparatus. Most forms of experimental state analysis used require lasers or microwaves, and therefore the laser beams are being used to manipulate the motion states (rather than a field emitted by the electrodes, due to lack of PDQ synchronization with the ARTIQ crate). Displacement operations have been demonstrated using a set of beams with projection along the appropriate motion axis (similar to that used in Ref. [139]), enabling the Wigner state reconstruction of motion states [58]. Next, an appropriate method of spin-motion entanglement corresponding to the desired bosonic code state needs to be implemented, as well as a method to code this bosonic state onto the motion of the trapped ion.

5.9 Summary

Using a modulation of the trapping potential of suitable frequency and curvature, the coupling of various modes of a trapped ion crystal have been realized. The coupling is rapid on the scale of the motional coherence of the ions, and because it is an electronic coupling only, it does not require

laser-accessible transitions. This may be of particular interest in applications involving molecular ions, highly-charged ions, or ion species that do not have an easily accessible laser transition [28, 33]. A beamsplitter with a fidelity exceeding 97.9%²³ was demonstrated. This coupling was also used to cool modes that cannot be cooled well under given experimental conditions through modes that can be cooled well. Finally, the coupling operation enables the use of a protected mode to perform repeated mid-circuit read out of ion motion, which could have exciting implications for investigations using the ion motional modes, including uses in bosonic error correction.

 $^{^{23}}$ As previously stated, this is an 84% confidence lower bound of the average fidelity in the one-phonon subspace of the beamsplitter operation.

	CZ mapping	Swaps	Mg detection	Mg SBC	\bar{n}	$\Delta ar{n}$
SBC	No	No	No	No	0.023(1)	0
No-swaps test	Yes	Replaced with delay	Yes	Yes	0.040(3) $0.017(3)$	0.017(3)
Swap test	No	Yes	No	No	0.044(3) $0.021(4)$	0.021(4)
CZ heating test	Replaced with delay	Yes	No	No	0.049(4) $0.026(5)$	0.026(5)
Stretch heating test	Replaced with delay	Yes	Replaced with delay	Yes	0.059(4) $0.036(5)$	0.036(5)
Recoil heating test	Replaced with delay	Yes	Yes	Yes	0.071(5) 0.048(5)	0.048(5)
No exchange $(N=1)$ Replaced with delay Replaced with delay Replaced with delay Replaced with delay	0.25(3)	0.23(3)				
No exchange $(N=2)$ Replaced with delay Replaced with delay Replaced with delay Replaced with delay	0.51(6)	0.49(6)				
No exchange $(N=3)$ Replaced with delay Replaced with delay Replaced with delay Replaced with delay	0.8(1)	0.8(1)				

Table 5.1: A series of tests to determine the heating of different elements of the measurements, including CZ mapping, swaps, Mg detection, and Mg SBC. Each element is either applied ("Yes"), omitted ("No"), or "Replaced with delay" of the same duration as the element in these tests. The ALT mode \bar{n} of all tests and the relative increase compared to the state after sideband cooling $\Delta \bar{n} = \bar{n} - \bar{n}_{\rm SBC}$ are listed.

References

- [1] J. I. Cirac and P. Zoller, "Quantum computations with cold trapped ions", Phys. Rev. Lett. **74**, 4091 (1995) (Cited on pp. 1, 157, 166).
- [2] A. Sørensen and K. Mølmer, "Ion trap quantum computer with bichromatic light", Fortschritte der Physik: Progress of Phys. 48, 811 (2000) (Cited on pp. 1, 2, 123).
- [3] D. J. Wineland, M. Barrett, J. Britton, J. Chiaverini, B. DeMarco, W. M. Itano, B. Jelenkovic, C. Langer, D. Leibfried, V. Meyer, R. T., and T. Schätz, "Quantum information processing with trapped ions", Phil. Trans. R. Soc. Lond. A 361, 1349 (2003) (Cited on pp. 1, 30).
- [4] I. Buluta, S. Ashhab, and F. Nori, "Natural and artificial atoms for quantum computation", Rep. Prog. Phys. **74**, 104401 (2011) (Cited on pp. 1, 2, 75).
- [5] H. Häffner, C. Roos, and R. Blatt, "Quantum computing with trapped ions", Phys. Rep. 469, 155 (2008) (Cited on pp. 1, 2, 75).
- [6] C. Ospelkaus, U. Warring, Y. Colombe, K. R. Brown, J. M. Amini, D. Leibfried, and D. J. Wineland, "Microwave quantum logic gates for trapped ions", Nature 476, 181 (2011) (Cited on pp. 1, 20, 123).
- [7] J. T. Barreiro, M. Müller, P. Schindler, D. Nigg, T. Monz, M. Chwalla, M. Hennrich, C. F. Roos, P. Zoller, and R. Blatt, "An open-system quantum simulator with trapped ions", Nature 470, 486 (2011) (Cited on pp. 1, 2, 123).
- [8] R. Blatt and C. F. Roos, "Quantum simulations with trapped ions", Nature Phys. 8, 277 (2012) (Cited on pp. 1, 2, 123).
- [9] T. P. Harty, D. T. C. Allcock, C. J. Ballance, L. Guidoni, H. A. Janacek, N. M. Linke, D. N. Stacey, and D. M. Lucas, "High-fidelity preparation, gates, memory, and readout of a trapped-ion quantum bit", Phys. Rev. Lett. 113, 220501 (2014) (Cited on p. 1).
- [10] T. R. Tan, J. P. Gaebler, Y. Lin, Y. Wan, R. Bowler, D. Leibfried, and D. J. Wineland, "Multi-element logic gates for trapped-ion qubits", Nature **528**, 380 (2015) (Cited on p. 1).
- [11] T. P. Harty, M. A. Sepiol, D. T. C. Allcock, C. J. Ballance, J. E. Tarlton, and D. M. Lucas, "High-fidelity trapped-ion quantum logic using near-field microwaves", Phys. Rev. Lett. 117, 140501 (2016) (Cited on pp. 1, 20, 123).
- [12] J. P. Gaebler, T. R. Tan, Y. Lin, Y. Wan, R. Bowler, A. C. Keith, S. Glancy, K. Coakley, E. Knill, D. Leibfried, and D. J. Wineland, "High-fidelity universal gate set for ⁹Be⁺ ion qubits", Phys. Rev. Lett. **117**, 060505 (2016) (Cited on p. 1).
- [13] Y. Wan, D. Kienzler, S. D. Erickson, K. H. Mayer, T.-R. Tan, J. J. Wu, H. M. Vasconcelos, S. Glancy, E. Knill, D. J. Wineland, A. C. Wilson, and D. Leibfried, "Quantum gate teleportation between separated qubits in a trapped-ion processor", Science **364**, 875 (2019) (Cited on pp. 1, 2, 61, 64, 76, 124).

- [14] C. D. Bruzewicz, J. Chiaverini, R. McConnell, and J. M. Sage, "Trapped-ion quantum computing: progress and challenges", Appl. Phys. Rev. 6, 021314 (2019) (Cited on pp. 1, 2, 75).
- [15] M. A. Sepiol, A. C. Hughes, J. E. Tarlton, D. P. Nadlinger, T. G. Ballance, C. J. Ballance, T. P. Harty, A. M. Steane, J. F. Goodwin, and D. M. Lucas, "Probing qubit memory errors at the part-per-million level", Phys. Rev. Lett. 123, 110503 (2019) (Cited on p. 1).
- [16] C. Flühmann, T. L. Nguyen, M. Marinelli, V. Negnevitsky, K. Mehta, and J. P. Home, "Encoding a qubit in a trapped-ion mechanical oscillator", Nature 566, 513 (2019) (Cited on pp. 1, 3, 4, 123, 125, 164).
- [17] Y. Wan, R. Jördens, S. D. Erickson, J. J. Wu, R. Bowler, T. R. Tan, P.-Y. Hou, D. J. Wineland, A. C. Wilson, and D. Leibfried, "Ion transport and reordering in a 2d trap array", Advanced Quantum Technol. 3, 2000028 (2020) (Cited on pp. 1, 60, 61).
- [18] H. C. J. Gan, G. Maslennikov, K.-W. Tseng, C. Nguyen, and D. Matsukevich, "Hybrid quantum computing with conditional beam splitter gate in trapped ion system", Phys. Rev. Lett. 124, 170502 (2020) (Cited on pp. 1, 123–125, 164).
- [19] R. Srinivas, S. Burd, H. Knaack, R. Sutherland, A. Kwiatkowski, S. Glancy, E. Knill, D. Wineland, D. Leibfried, A. C. Wilson, et al., "High-fidelity laser-free universal control of trapped ion qubits", Nature 597, 209 (2021) (Cited on p. 1).
- [20] I. Pogorelov, T. Feldker, C. D. Marciniak, L. Postler, G. Jacob, O. Krieglsteiner, V. Podlesnic, M. Meth, V. Negnevitsky, M. Stadler, et al., "Compact ion-trap quantum computing demonstrator", PRX Quantum 2, 020343 (2021) (Cited on p. 1).
- [21] J. M. Pino, J. M. Dreiling, C. Figgatt, J. P. Gaebler, S. A. Moses, M. Allman, C. Baldwin, M. Foss-Feig, D. Hayes, K. Mayer, et al., "Demonstration of the trapped-ion quantum ccd computer architecture", Nature 592, 209 (2021) (Cited on p. 1).
- [22] S. A. Moses, C. H. Baldwin, M. S. Allman, R. Ancona, L. Ascarrunz, C. Barnes, J. Bartolotta, B. Bjork, P. Blanchard, M. Bohn, J. G. Bohnet, N. C. Brown, N. Q. Burdick, W. C. Burton, S. L. Campbell, J. P. Campora, C. Carron, J. Chambers, J. W. Chan, Y. H. Chen, A. Chernoguzov, E. Chertkov, J. Colina, J. P. Curtis, R. Daniel, M. DeCross, D. Deen, C. Delaney, J. M. Dreiling, C. T. Ertsgaard, J. Esposito, B. Estey, M. Fabrikant, C. Figgatt, C. Foltz, M. Foss-Feig, D. Francois, J. P. Gaebler, T. M. Gatterman, C. N. Gilbreth, J. Giles, E. Glynn, A. Hall, A. M. Hankin, A. Hansen, D. Hayes, B. Higashi, I. M. Hoffman, B. Horning, J. J. Hout, R. Jacobs, J. Johansen, L. Jones, J. Karcz, T. Klein, P. Lauria, P. Lee, D. Liefer, S. T. Lu, D. Lucchetti, C. Lytle, A. Malm, M. Matheny, B. Mathewson, K. Mayer, D. B. Miller, M. Mills, B. Neyenhuis, L. Nugent, S. Olson, J. Parks, G. N. Price, Z. Price, M. Pugh, A. Ransford, A. P. Reed, C. Roman, M. Rowe, C. Ryan-Anderson, S. Sanders, J. Sedlacek, P. Shevchuk, P. Siegfried, T. Skripka, B. Spaun, R. T. Sprenkle, R. P. Stutz, M. Swallows, R. I. Tobey, A. Tran, T. Tran, E. Vogt, C. Volin, J. Walker, A. M. Zolot, and J. M. Pino, "A race-track trapped-ion quantum processor", Phys. Rev. X 13, 041052 (2023) (Cited on p. 1).
- [23] D. M. Meekhof, C. Monroe, B. E. King, W. M. Itano, and D. J. Wineland, "Generation of nonclassical motional states of a trapped atom", Phys. Rev. Lett. 76, 1796 (1996) (Cited on pp. 1, 3, 25).
- [24] C. Monroe, D. M. Meekhof, B. E. King, and D. J. Wineland, "A "schrödinger cat" superposition state of an atom", Science **272**, 1131 (1996) (Cited on pp. 1, 3).

- [25] P. O. Schmidt, T. Rosenband, C. Langer, W. M. Itano, J. C. Bergquist, and D. J. Wineland, "Spectroscopy using quantum logic", Science 309, 749 (2005) (Cited on pp. 1, 2, 123, 157).
- [26] C. L. Degen, F. Reinhard, and P. Cappellaro, "Quantum sensing", Rev. Mod. Phys. 89, 035002 (2017) (Cited on pp. 1, 75).
- [27] C. Roos, T. Monz, K. Kim, M. Riebe, H. Häffner, D. James, and R. Blatt, "Nonlinear coupling of continuous variables at the single quantum level", Phys. Rev. A 77, 040302 (2008) (Cited on pp. 1, 156).
- [28] D. Leibfried, "Quantum state preparation and control of single molecular ions", New J. Phys. 14, 023029 (2012) (Cited on pp. 1, 123, 157, 177).
- [29] A. E. Nielsen, G. Sierra, and J. I. Cirac, "Local models of fractional quantum hall states in lattices and physical implementation", Nature Commun. 4, 2864 (2013) (Cited on pp. 1, 2, 123).
- [30] U. Warring, C. Ospelkaus, Y. Colombe, K. R. Brown, J. M. Amini, M. Carsjens, D. Leibfried, and D. J. Wineland, "Techniques for microwave near-field quantum control of trapped ions", Phys. Rev. A 87, 013437 (2013) (Cited on pp. 1, 20, 123).
- [31] K. Toyoda, R. Hiji, A. Noguchi, and S. Urabe, "Hong-ou-mandel interference of two phonons in trapped ions", Nature **527**, 74 (2015) (Cited on pp. 1, 147).
- [32] D. Kienzler, C. Flühmann, V. Negnevitsky, H.-Y. Lo, M. Marinelli, D. Nadlinger, and J. P. Home, "Observation of quantum interference between separated mechanical oscillator wave packets", Phys. Rev. Lett. 116, 140402 (2016) (Cited on pp. 1, 3, 125, 164).
- [33] F. Wolf, Y. Wan, J. C. Heip, F. Gebert, C. Shi, and P. O. Schmidt, "Non-destructive state detection for quantum logic spectroscopy of molecular ions", Nature 530, 457 (2016) (Cited on pp. 1, 2, 177).
- [34] K. C. McCormick, J. Keller, S. C. Burd, D. J. Wineland, A. C. Wilson, and D. Leibfried, "Quantum-enhanced sensing of a single-ion mechanical oscillator", Nature **572**, 86 (2019) (Cited on p. 1).
- [35] K. A. Gilmore, M. Affolter, R. J. Lewis-Swan, D. Barberena, E. Jordan, A. M. Rey, and J. J. Bollinger, "Quantum-enhanced sensing of displacements and electric fields with two-dimensional trapped-ion crystals", Science **373**, 673 (2021) (Cited on p. 1).
- [36] A. D. Ludlow, M. M. Boyd, J. Ye, E. Peik, and P. O. Schmidt, "Optical atomic clocks", Rev. Mod. Phys. 87, 637 (2015) (Cited on pp. 1, 2, 75, 157).
- [37] D. B. Hume and D. R. Leibrandt, "Probing beyond the laser coherence time in optical clock comparisons", Phys. Rev. A **93**, 032138 (2016) (Cited on p. 1).
- [38] C.-W. Chou, C. Kurz, D. B. Hume, P. N. Plessow, D. R. Leibrandt, and D. Leibfried, "Preparation and coherent manipulation of pure quantum states of a single molecular ion", Nature 545, 203 (2017) (Cited on pp. 1, 2, 123).
- [39] M. Delehaye and C. Lacroûte, "Single-ion, transportable optical atomic clocks", J. Mod. Opt. **65**, 622 (2018) (Cited on p. 1).
- [40] M. S. Safronova, D. Budker, D. DeMille, D. F. J. Kimball, A. Derevianko, and C. W. Clark, "Search for new physics with atoms and molecules", Rev. Mod. Phys. 90, 025008 (2018) (Cited on p. 1).

- [41] J. Keller, T. Burgermeister, D. Kalincev, A. Didier, A. P. Kulosa, T. Nordmann, J. Kiethe, and T. E. Mehlstäubler, "Controlling systematic frequency uncertainties at the 10⁻¹⁹ level in linear coulomb crystals", Phys. Rev. A **99**, 013405 (2019) (Cited on p. 1).
- [42] S. M. Brewer, J.-S. Chen, A. M. Hankin, E. R. Clements, C.-w. Chou, D. J. Wineland, D. B. Hume, and D. R. Leibrandt, "Al+ 27 quantum-logic clock with a systematic uncertainty below 10-18", Phys. Rev. Lett. **123**, 033201 (2019) (Cited on pp. 1, 2, 123).
- [43] P. Micke, T. Leopold, S. King, E. Benkler, L. Spieß, L. Schmoeger, M. Schwarz, J. Crespo López-Urrutia, and P. Schmidt, "Coherent laser spectroscopy of highly charged ions using quantum logic", Nature **578**, 60 (2020) (Cited on pp. 1, 2).
- [44] E. Burt, J. Prestage, R. Tjoelker, D. Enzer, D. Kuang, D. Murphy, D. Robison, J. Seubert, R. Wang, and T. Ely, "Demonstration of a trapped-ion atomic clock in space", Nature **595**, 43 (2021) (Cited on p. 1).
- [45] N.-H. Rehbehn, M. K. Rosner, H. Bekker, J. C. Berengut, P. O. Schmidt, S. A. King, P. Micke, M. F. Gu, R. Müller, A. Surzhykov, and J. R. C. López-Urrutia, "Sensitivity to new physics of isotope-shift studies using the coronal lines of highly charged calcium ions", Phys. Rev. A 103, L040801 (2021) (Cited on p. 1).
- [46] S. A. King, L. J. Spieß, P. Micke, A. Wilzewski, T. Leopold, E. Benkler, R. Lange, N. Huntemann, A. Surzhykov, V. A. Yerokhin, et al., "An optical atomic clock based on a highly charged ion", Nature 611, 43 (2022) (Cited on pp. 1, 2).
- [47] S. D. Erickson, J. J. Wu, P.-Y. Hou, D. C. Cole, S. Geller, A. Kwiatkowski, S. Glancy, E. Knill, D. H. Slichter, A. C. Wilson, and D. Leibfried, "High-fidelity indirect readout of trapped-ion hyperfine qubits", Phys. Rev. Lett. 128, 160503 (2022) (Cited on pp. 1, 2, 124).
- [48] E. Chertkov, J. Bohnet, D. Francois, J. Gaebler, D. Gresh, A. Hankin, K. Lee, D. Hayes, B. Neyenhuis, R. Stutz, et al., "Holographic dynamics simulations with a trapped-ion quantum computer", Nature Phys. 18, 1074 (2022) (Cited on p. 1).
- [49] S. Jain, T. Sägesser, P. Hrmo, C. Torkzaban, M. Stadler, R. Oswald, C. Axline, A. Bautista-Salvador, C. Ospelkaus, D. Kienzler, et al., "Penning micro-trap for quantum computing", Nature 627, 510 (2024) (Cited on p. 1).
- [50] D. J. Wineland, C. Monroe, W. M. Itano, D. Leibfried, B. E. King, and D. M. Meekhof, "Experimental issues in coherent quantum-state manipulation of trapped atomic ions", J. Res. Natl. Inst. Stand. Technol. 103, 259 (1998) (Cited on pp. 1, 2, 20, 27, 30, 75).
- [51] C. Langer, R. Ozeri, J. D. Jost, J. Chiaverini, B. DeMarco, A. Ben-Kish, R. B. Blakestad, J. Britton, D. B. Hume, W. M. Itano, D. Leibfried, R. Reichle, T. Rosenband, T. Schaetz, P. O. Schmidt, and D. J. Wineland, "Long-lived qubit memory using atomic ions", Phys. Rev. Lett. 95, 060502 (2005) (Cited on pp. 1, 3, 19, 77, 123).
- [52] P. K. Ghosh, Ion traps (Oxford University Press, 1995) (Cited on pp. 1, 5, 7, 9–11).
- [53] D. F. V. James, "Quantum dynamics of cold trapped ions with application to quantum computation", Appl. Phys. B **66**, 181 (1998) (Cited on pp. 1, 14–16).
- [54] A. Friedenauer, H. Schmitz, J. T. Glueckert, D. Porras, and T. Schätz, "Simulating a quantum magnet with trapped ions", Nature Phys. 4, 757 (2008) (Cited on pp. 2, 123).

- [55] M. D. Barrett, B. DeMarco, T. Schaetz, V. Meyer, D. Leibfried, J. Britton, J. Chiaverini, W. M. Itano, B. Jelenkovi ć, J. D. Jost, C. Langer, T. Rosenband, and D. J. Wineland, "Sympathetic cooling of ⁹Be⁺ and ²⁴Mg⁺ for quantum logic", Phys. Rev. A 68, 042302 (2003) (Cited on p. 2).
- [56] Y. Lin, J. P. Gaebler, T.-R. Tan, R. Bowler, J. D. Jost, D. Leibfried, and D. J. Wineland, "Sympathetic Electromagnetically-induced-transparency laser cooling of motional modes in an ion chain", Phys. Rev. Lett. **110**, 153002 (2013) (Cited on pp. 2, 3, 75, 76, 110).
- [57] G. Morigi and H. Walther, "Two-species coulomb chains for quantum information", The European Physical Journal D-Atomic, Molecular, Optical and Plasma Physics **13**, 261 (2001) (Cited on pp. 3, 143).
- [58] D. Leibfried, D. M. Meekhof, B. E. King, C. Monroe, W. M. Itano, and D. J. Wineland, "Experimental determination of the motional quantum state of a trapped atom", Phys. Rev. Lett. 77, 4281 (1996) (Cited on pp. 3, 176).
- [59] D. Gottesman, A. Kitaev, and J. Preskill, "Encoding a qubit in an oscillator", Phys. Rev. A 64, 012310 (2001) (Cited on pp. 4, 176).
- [60] M. H. Michael, M. Silveri, R. Brierley, V. V. Albert, J. Salmilehto, L. Jiang, and S. M. Girvin, "New class of quantum error-correcting codes for a bosonic mode", Phys. Rev. X 6, 031006 (2016) (Cited on pp. 4, 176).
- [61] B. de Neeve, T. L. Nguyen, T. Berhle, and J. P. Home, "Error correction of a logical grid state qubit by dissipative pumping", Nature Phys. 18, 296 (2022) (Cited on pp. 4, 123).
- [62] V. G. Matsos, C. H. Valahu, M. J. Millican, T. Navickas, X. C. Kolesnikow, M. J. Biercuk, and T. R. Tan, *Universal quantum gate set for gottesman-kitaev-preskill logical qubits*, 2024 (Cited on pp. 4, 123).
- [63] N. Ofek, A. Petrenko, R. Heeres, P. Reinhold, Z. Leghtas, B. Vlastakis, Y. Liu, L. Frunzio, S. M. Girvin, L. Jiang, et al., "Extending the lifetime of a quantum bit with error correction in superconducting circuits", Nature 536, 441 (2016) (Cited on p. 4).
- [64] A. Joshi, K. Noh, and Y. Y. Gao, "Quantum information processing with bosonic qubits in circuit qed", Quantum Sci. Technol. 6, 033001 (2021) (Cited on p. 4).
- [65] W. Cai, Y. Ma, W. Wang, C.-L. Zou, and L. Sun, "Bosonic quantum error correction codes in superconducting quantum circuits", Fundamental Res. 1, 50 (2021) (Cited on p. 4).
- [66] V. Sivak, A. Eickbusch, B. Royer, S. Singh, I. Tsioutsios, S. Ganjam, A. Miano, B. Brock, A. Ding, L. Frunzio, et al., "Real-time quantum error correction beyond break-even", Nature 616, 50 (2023) (Cited on p. 4).
- [67] W. Paul, "Electromagnetic traps for charged and neutral particles", Rev. Mod. Phys. 62, 531 (1990) (Cited on p. 5).
- [68] D. Leibfried, R. Blatt, C. Monroe, and D. Wineland, "Quantum dynamics of single trapped ions", Rev. Mod. Phys. 75, 281 (2003) (Cited on pp. 5, 9, 10, 13, 14, 20, 21, 25, 27, 30, 53, 71, 78, 79, 88, 90, 106, 108, 156, 168, 172).
- [69] F. Penning, "Die glimmentladung bei niedrigem druck zwischen koaxialen zylindern in einem axialen magnetfeld", Physica 3, 873 (1936) (Cited on p. 5).
- [70] L. S. Brown and G. Gabrielse, "Geonium theory: physics of a single electron or ion in a penning trap", Rev. Mod. Phys. **58**, 233 (1986) (Cited on pp. 5, 123).

- [71] S. Earnshaw, "On the nature of the molecular forces which regulate the constitution of the luminiferous ether", Trans. Cambridge Phil. Soc. 7, 97 (1848) (Cited on p. 5).
- [72] É. Mathieu, "Mémoire sur le mouvement vibratoire d'une membrane de forme elliptique.", fre, Journal de Mathématiques Pures et Appliquées 13, 137 (1868) (Cited on p. 7).
- [73] W. Paul, "Electromagnetic traps for charged and neutral particles", Nobel Lecture (1989) (Cited on p. 11).
- [74] R. J. Glauber, "Quantum theory of particle trapping by oscillating fields", in *Quantum measurements in optics* (Springer New York, NY, 1992) Chap. 1, pp. 3–14 (Cited on pp. 13, 21).
- [75] D. J. Berkeland, J. D. Miller, J. C. Bergquist, W. M. Itano, and D. J. Wineland, "Minimization of ion micromotion in a paul trap", J. Appl. Phys. 83, 5025 (1998) (Cited on pp. 14, 28, 96, 103).
- [76] D. Kiesenhofer, H. Hainzer, A. Zhdanov, P. C. Holz, M. Bock, T. Ollikainen, and C. F. Roos, "Controlling two-dimensional coulomb crystals of more than 100 ions in a monolithic radio-frequency trap", PRX Quantum 4, 020317 (2023) (Cited on p. 14).
- [77] D. J. Wineland and W. M. Itano, "Laser cooling of atoms", Phys. Rev. A 20, 1521 (1979) (Cited on p. 23).
- [78] Q. A. Turchette, D. Kielpinski, B. E. King, D. Leibfried, D. M. Meekhof, C. J. Myatt, M. A. Rowe, C. A. Sackett, C. S. Wood, W. M. Itano, C. Monroe, and D. J. Wineland, "Heating of trapped ions from the quantum ground state", Phys. Rev. A 61, 063418 (2000) (Cited on pp. 27, 156).
- [79] H. G. Dehmelt, "Monoion oscillator as potential ultimate laser frequency standard", IEEE Trans. Instrum. Meas. IM-31, 83 (1982) (Cited on p. 30).
- [80] D. J. Wineland, J. C. Bergquist, W. M. Itano, J. J. Bollinger, and C. H. Manney, "Atomic-ion coulomb clusters in an ion trap", Phys. Rev. Lett. **59**, 2935 (1987) (Cited on p. 30).
- [81] H. Nägerl, D. Leibfried, F. Schmidt-Kaler, J. Eschner, and R. Blatt, "Coherent excitation of normal modes in a string of ca+ ions", Opt. Express 3, 89 (1998) (Cited on p. 30).
- [82] B. E. King, C. S. Wood, C. J. Myatt, Q. A. Turchette, D. Leibfried, W. M. Itano, C. Monroe, and D. J. Wineland, "Cooling the collective motion of trapped ions to initialize a quantum register", Phys. Rev. Lett. 81, 1525 (1998) (Cited on p. 30).
- [83] D. J. Wineland, C. Monroe, W. M. Itano, B. E. King, D. Leibfried, D. M. Meekhof, C. Myatt, and C. Wood, "Experimental primer on the trapped ion quantum computer", Fortschr. Phys. 46, 363 (1998) (Cited on p. 30).
- [84] D. S. Bykov, L. Dania, F. Goschin, and T. E. Northup, A nanoparticle stored with an atomic ion in a linear paul trap, 2024 (Cited on p. 34).
- [85] A. C. Wilson, C. Ospelkaus, A. P. VanDevender, J. A. Mlynek, K. R. Brown, D. Leibfried, and D. J. Wineland, "A 750-mw, continuous-wave, solid-state laser source at 313 nm for cooling and manipulating trapped 9be+ ions", Appl. Phys. B 105, 741 (2011) (Cited on pp. 45, 189).
- [86] C. Monroe, D. M. Meekhof, B. E. King, S. R. Jefferts, W. M. Itano, D. J. Wineland, and P. Gould, "Resolved-sideband raman cooling of a bound atom to the 3d zero-point energy", Phys. Rev. Lett. 75, 4011 (1995) (Cited on p. 52).

- [87] Y. Colombe, D. Slichter, A. Wilson, D. Leibfried, and D. Wineland, "Single-mode optical fiber for high-power, low-loss uv transmission", Opt. Express 22, 10.1364/0E.22.019783 (2014) (Cited on p. 55).
- [88] D. R. Leibrandt and J. Heidecker, "An open source digital servo for atomic, molecular, and optical physics experiments", Rev. Sci. Instrum. 86, 123115 (2015) (Cited on pp. 56, 66, 198).
- [89] R. B. Blakestad, "Transport of trapped-ion qubits within a scalable quantum processor", PhD thesis (University of Colorado, Boulder, CO, 2010) (Cited on pp. 59–61, 63, 130, 132, 143).
- [90] R. B. Blakestad, C. Ospelkaus, A. P. VanDevender, J. M. Amini, J. Britton, D. Leibfried, and D. J. Wineland, "High-fidelity transport of trapped-ion qubits through an X-junction trap array", Phys. Rev. Lett. 102, 153002 (2009) (Cited on pp. 59, 60, 63, 132).
- [91] R. B. Blakestad, C. Ospelkaus, A. P. VanDevender, J. H. Wesenberg, M. J. Biercuk, D. Leibfried, and D. J. Wineland, "Near-ground-state transport of trapped-ion qubits through a multidimensional array", Phys. Rev. A 84, 032314 (2011) (Cited on pp. 59, 60, 63).
- [92] S. D. Erickson, "Mixed-species quantum logic with trapped ions for gate teleportation, metrology and high-fidelity indirect readout", PhD thesis (University of Colorado, Boulder, CO, 2021) (Cited on pp. 59, 64, 66).
- [93] R. Wehlitz, D. Luki ć, and J. B. Bluett, "Resonance parameters of autoionizing be $2pn\updownarrow$ states", Phys. Rev. A **68**, 052708 (2003) (Cited on p. 60).
- [94] D. Kienzler, Y. Wan, S. D. Erickson, J. J. Wu, A. C. Wilson, D. J. Wineland, and D. Leibfried, "Quantum logic spectroscopy with ions in thermal motion", Phys. Rev. X 10, 021012 (2020) (Cited on pp. 64, 123, 157).
- [95] R. Bowler, U. Warring, J. W. Britton, B. C. Sawyer, and J. Amini, "Arbitrary waveform generator for quantum information processing with trapped ions", Rev. Sci. Instrum. 84, 033108 (2013) (Cited on pp. 65, 110, 132).
- [96] T. R. Tan, "High-fidelity entangling gates with trapped-ions", PhD thesis (University of Colorado, Boulder, CO, 2016) (Cited on p. 66).
- [97] C. Flühmann, "Encoding a qubit in the motion of a trapped ion using superpositions of displaced squeezed states", PhD thesis (ETH Zurich, Zurich, 2019) (Cited on p. 67).
- [98] P.-Y. Hou, J. J. Wu, S. D. Erickson, G. Zarantonello, A. D. Brandt, D. C. Cole, A. C. Wilson, D. H. Slichter, and D. Leibfried, "Indirect cooling of weakly coupled trapped-ion mechanical oscillators", Phys. Rev. X 14, 021003 (2024) (Cited on pp. 71, 124, 157, 163).
- [99] F. Diedrich, J. C. Bergquist, W. M. Itano, and D. J. Wineland, "Laser cooling to the zero-point energy of motion", Phys. Rev. Lett. **62**, 403 (1989) (Cited on p. 75).
- [100] C. Monroe, D. M. Meekhof, B. E. King, S. R. Jefferts, W. M. Itano, D. J. Wineland, and P. Gould, "Resolved-sideband raman cooling of a bound atom to the 3d zero-point energy", Phys. Rev. Lett. 75, 4011 (1995) (Cited on p. 75).
- [101] J. Eschner, G. Morigi, F. Schmidt-Kaler, and R. Blatt, "Laser cooling of trapped ions", J. Opt. Soc. Am. B **20**, 1003 (2003) (Cited on p. 75).
- [102] J. I. Cirac, R. Blatt, A. S. Parkins, and P. Zoller, "Laser cooling of trapped ions with polarization gradients", Phys. Rev. A 48, 1434 (1993) (Cited on p. 75).
- [103] S. M. Yoo and J. Javanainen, "Polarization gradient cooling of a trapped ion", Phys. Rev. A 48, R30 (1993) (Cited on p. 75).

- [104] D. J. Wineland, J. Dalibard, and C. Cohen-Tannoudji, "Sisyphus cooling of a bound atom", J. Opt. Soc. Am. B 9, 32 (1992) (Cited on p. 75).
- [105] G. Birkl, J. A. Yeazell, R. Rückerl, and H. Walther, "Polarization gradient cooling of trapped ions", Europhysics Lett. **27**, 197 (1994) (Cited on p. 75).
- [106] S. Ejtemaee and P. C. Haljan, "3d sisyphus cooling of trapped ions", Phys. Rev. Lett. 119, 043001 (2017) (Cited on p. 75).
- [107] G. Morigi, J. Eschner, and C. H. Keitel, "Ground state laser cooling using electromagnetically induced transparency", Phys. Rev. Lett. 85, 4458 (2000) (Cited on pp. 75, 78, 79, 88, 90, 92).
- [108] G. Morigi, "Cooling atomic motion with quantum interference", Phys. Rev. A 67, 033402 (2003) (Cited on pp. 75, 78, 79, 88).
- [109] C. F. Roos, D. Leibfried, A. Mundt, F. Schmidt-Kaler, J. Eschner, and R. Blatt, "Experimental demonstration of ground state laser cooling with electromagnetically induced transparency", Phys. Rev. Lett. 85, 5547 (2000) (Cited on pp. 75, 76, 110).
- [110] R. Lechner, C. Maier, C. Hempel, P. Jurcevic, B. P. Lanyon, T. Monz, M. Brownnutt, R. Blatt, and C. F. Roos, "Electromagnetically-induced-transparency ground-state cooling of long ion strings", Phys. Rev. A 93, 053401 (2016) (Cited on pp. 75, 76, 110).
- [111] E. Jordan, K. A. Gilmore, A. Shankar, A. Safavi-Naini, J. G. Bohnet, M. J. Holland, and J. J. Bollinger, "Near ground-state cooling of two-dimensional trapped-ion crystals with more than 100 ions", Phys. Rev. Lett. **122**, 053603 (2019) (Cited on pp. 75, 76, 94, 110).
- [112] L. Feng, W. L. Tan, A. De, A. Menon, A. Chu, G. Pagano, and C. Monroe, "Efficient ground-state cooling of large trapped-ion chains with an electromagnetically-induced-transparency tripod scheme", Phys. Rev. Lett. **125**, 053001 (2020) (Cited on pp. 75, 77, 79, 91, 110).
- [113] M. Qiao, Y. Wang, Z. Cai, B. Du, P. Wang, C. Luan, W. Chen, H.-R. Noh, and K. Kim, "Double-electromagnetically-induced-transparency ground-state cooling of stationary twodimensional ion crystals", Phys. Rev. Lett. 126, 023604 (2021) (Cited on pp. 75, 77, 110).
- [114] J. Evers and C. H. Keitel, "Double-EIT ground-state laser cooling without blue-sideband heating", Europhysics Lett. **68**, 370 (2004) (Cited on pp. 77, 116, 117).
- [115] I. A. Semerikov, I. V. Zalivako, A. S. Borisenko, K. Y. Khabarova, and N. N. Kolachevsky, "Eit ground state cooling scheme of 171yb+ based on the 2s1/2→2p1/2 cooling transition", J. Russ. Laser Res. 39, 568 (2018) (Cited on p. 77).
- [116] C. Huang, C. Wang, H. Zhang, H. Hu, Z. Wang, Z. Mao, S. Li, P. Hou, Y. Wu, Z. Zhou, and L. Duan, "Electromagnetically induced transparency cooling of high-nuclear-spin ions", Phys. Rev. Lett. **133**, 113204 (2024) (Cited on p. 77).
- [117] W. W. Erickson, "Electromagnetically induced transperency", Bachelor's Thesis (Reed College, 2012) (Cited on pp. 80, 96).
- [118] J. Preskill, Lecture notes for quantum information, 2018 (Cited on p. 86).
- [119] H. J. Metcalf and P. Van der Straten, *Laser cooling and trapping* (Springer Science & Business Media, 1999) (Cited on p. 90).
- [120] J. R. Johansson, P. D. Nation, and F. Nori, "Qutip: an open-source python framework for the dynamics of open quantum systems", Comput. Phys. Commun. 183, 1760 (2012) (Cited on p. 95).

- [121] L. Deslauriers, S. Olmschenk, D. Stick, W. K. Hensinger, J. Sterk, and C. Monroe, "Scaling and suppression of anomalous heating in ion traps", Phys. Rev. Lett. **97**, 103007 (2006) (Cited on p. 97).
- [122] N. A. Nuñez Barreto, M. Drechsler, and C. T. Schmiegelow, "Three-laser coherent population trapping in a multi-Λ system: theory, experiment, and applications", Phys. Rev. A **106**, 053708 (2022) (Cited on p. **116**).
- [123] N. Scharnhorst, J. Cerrillo, J. Kramer, I. D. Leroux, J. B. Wübbena, A. Retzker, and P. O. Schmidt, "Experimental and theoretical investigation of a multimode cooling scheme using multiple electromagnetically-induced-transparency resonances", Phys. Rev. A 98, 023424 (2018) (Cited on p. 116).
- [124] Y. Lu, J.-Q. Zhang, J.-M. Cui, D.-Y. Cao, S. Zhang, Y.-F. Huang, C.-F. Li, and G.-C. Guo, "Dark-state cooling of a trapped ion using microwave coupling", Phys. Rev. A **92**, 023420 (2015) (Cited on p. 117).
- [125] J. Cerrillo, A. Retzker, and M. B. Plenio, "Fast and robust laser cooling of trapped systems", Phys. Rev. Lett. **104**, 043003 (2010) (Cited on p. 117).
- [126] J. D. Jost, J. P. Home, J. M. Amini, D. Hanneke, R. Ozeri, C. Langer, J. J. Bollinger, D. Leibfried, and D. J. Wineland, "Entangled mechanical oscillators", Nature 459, 683 (2009) (Cited on p. 123).
- [127] M. I. Fabrikant, P. Lauria, I. S. Madjarov, W. C. Burton, and R. T. Sutherland, *Cooling trapped ions with phonon rapid adiabatic passage*, 2024 (Cited on p. 123).
- [128] K. R. Brown, C. Ospelkaus, Y. Colombe, A. C. Wilson, D. Leibfried, and D. J. Wineland, "Coupled quantized mechanical oscillators", Nature **471**, 196 (2011) (Cited on p. 123).
- [129] D. J. Gorman, P. Schindler, S. Selvarajan, N. Daniilidis, and H. Häffner, "Two-mode coupling in a single-ion oscillator via parametric resonance", Phys. Rev. A 89, 062332 (2014) (Cited on p. 123).
- [130] A. C. Wilson, Y. Colombe, K. R. Brown, E. Knill, D. Leibfried, and D. J. Wineland, "Tunable spin–spin interactions and entanglement of ions in separate potential wells", Nature **512**, 57 (2014) (Cited on p. 123).
- [131] P.-Y. Hou, J. J. Wu, S. D. Erickson, D. C. Cole, G. Zarantonello, A. D. Brandt, A. C. Wilson, D. H. Slichter, and D. Leibfried, "Coherent coupling and non-destructive measurement of trapped-ion mechanical oscillators", Nat. Phys., https://doi.org/10.1038/s41567-024-02585-y (2024) (Cited on pp. 124, 147).
- [132] J. Metzner, C. Bruzewicz, I. Moore, A. Quinn, D. J. Wineland, J. Chiaverini, and D. T. C. Allcock, "Using 'protected' modes in trapped ions to enable mid-algorithm measurements for cvqc", in 52nd annual meeting of the aps division of atomic, molecular and optical physics (2021) (Cited on pp. 125, 134).
- [133] C. M. Caves, "Quantum-mechanical noise in an interferometer", Phys. Rev. D 23, 1693 (1981) (Cited on p. 130).
- [134] J. P. Home, D. Hanneke, J. D. Jost, D. Leibfried, and D. J. Wineland, "Normal modes of trapped ions in the presence of anharmonic trap potentials", New J. Phys. **13**, 073026 (2011) (Cited on p. 143).
- [135] L. Allen and J. Eberly, *Optical resonance and two-level atoms* (John Wiley and Sons, Inc., New York, 1975) (Cited on pp. 146, 148).

- [136] C. K. Hong, Z. Y. Ou, and L. Mandel, "Measurement of subpicosecond time intervals between two photons by interference", Phys. Rev. Lett. **59**, 2044 (1987) (Cited on p. 147).
- [137] S. Lloyd and S. L. Braunstein, "Quantum computation over continuous variables", Phys. Rev. Lett. 82, 1784 (1999) (Cited on p. 148).
- [138] X. R. Nie, C. F. Roos, and D. F. James, "Theory of cross phase modulation for the vibrational modes of trapped ions", Phys. Lett. A **373**, 422 (2009) (Cited on pp. 156, 157).
- [139] J. W. Britton, B. C. Sawyer, A. C. Keith, C.-C. J. Wang, J. K. Freericks, H. Uys, M. J. Biercuk, and J. J. Bollinger, "Engineered two-dimensional ising interactions in a trapped-ion quantum simulator with hundreds of spins", Nature 484, 489 (2012) (Cited on p. 176).
- [140] M. Kuznetsov, F. Hakimi, R. Sprague, and A. Mooradian, "High-power (>0.5-w cw) diode-pumped vertical-external-cavity surface-emitting semiconductor lasers with circular tem/sub 00/ beams", IEEE Photonics Technol. Lett. 9, 1063 (1997) (Cited on p. 189).
- [141] S. C. Burd, D. T. C. Allcock, T. Leinonen, J. P. Penttinen, D. H. Slichter, R. Srinivas, A. C. Wilson, R. Jördens, M. Guina, D. Leibfried, and D. J. Wineland, "Vecsel systems for the generation and manipulation of trapped magnesium ions", Optica 3, 1294 (2016) (Cited on p. 189).
- [142] M. Guina, A. Rantamäki, and A. Härkönen, "Optically pumped vecsels: review of technology and progress", J. Phys. D **50**, 383001 (2017) (Cited on p. 189).
- [143] S. C. Burd, J.-P. Penttinen, P.-Y. Hou, H. M. Knaack, S. Ranta, M. Mäki, E. Kantola, M. Guina, D. H. Slichter, D. Leibfried, and A. C. Wilson, "Vecsel systems for quantum information processing with trapped beryllium ions", J. Opt. Soc. Am. B 40, 773 (2023) (Cited on p. 189).
- [144] T. Hansch and B. Couillaud, "Laser frequency stabilization by polarization spectroscopy of a reflecting reference cavity", Opt. Commun. **35**, 441 (1980) (Cited on p. **201**).
- [145] R. Drever, J. L. Hall, F. V. Kowalski, J. Hough, G. M. Ford, A. J. Munley, and H. Ward, "Laser phase and frequency stabilization using an optical resonator", Appl. Phys. B 31, 97 (1983) (Cited on pp. 201, 202).
- [146] M. Aldous, J. Woods, A. Dragomir, R. Roy, and M. Himsworth, "Carrier frequency modulation of an acousto-optic modulator for laser stabilization", Opt. Express 25, 12830 (2017) (Cited on p. 202).
- [147] M. Eickhoff and J. Hall, "Optical frequency standard at 532 nm", IEEE Trans. Instrum. Meas. 44, 155 (1995) (Cited on pp. 202, 221, 230).

Appendix A

Hardware and Lab Tricks

Here are some additional details about lab hardware and optics layouts.

A.1 VECSELs

In 1G121, there are 4 VECSELs [140–143] currently in operation, outputting 1140 nm, (two at) 1120 nm, and 940 nm. The 1140 nm VECSEL was in operation before my arrival and operates extremely stably with little to no attention. The 940 nm VECSEL was built in a different lab and installed in 1G121; it operates similarly to the 1140 nm VECSEL. There also exists a 1252 nm VECSEL that was tested in 1G121 [143] but is not used because the current SFG [85] systems that use commercial 1050 nm and 1550 nm fiber lasers and amplifiers are fairly stable.

A.1.1 1120 nm VECSELs

The first 1120 nm VECSEL was built and was aligned to lase before my arrival. It is used for the $^{25}\text{Mg}^+$ $^2\text{S}_{1/2} \leftrightarrow ^2\text{P}_{1/2}$. However, it was found that water vapor absorption lines existed near 1120 nm (1118 nm and 1121 nm to be precise), which caused significant loss in the output power if the cavity is opened and no desiccant is used, or if the cavity is left alone for a period of time. The original design was intended to be fully sealed, however, significant air leaks were discovered near the front where the pump laser fiber passed into the VECSEL, as well as on the back where the Koolance brand quick-connect feedthroughs were used.

¹This VECSEL frequency is closer to 1121 nm but for convenience I use 1120 nm when describing it.

A new lid for the VECSEL was designed, which enabled the addition of a gas purge line to either flush or maintain a positive pressure of a dry gas in the laser cavity, as well as allowed a small desiccant cartridge containing a color-based humidity indicator to be inserted into a threaded hole in the lid. The humidity indicator covers the range 10%-30% and is usually blue; an air leak or loss of the purging gas causes the indicator to become fairly obviously pink. The purge line was initially used to flush dry argon through the cavity. However, it was later verified with J.-P. Penttinen at VEXLUM that although the defects on gain chips are a result of nitrogen-based impurities, dry nitrogen gas should have no detrimental effect on the gain chip after installation, and afterwards dry nitrogen recycled from the NIST cleanroom was used to flush the cavity. The flow rate used is similar to that used with the UV doublers: 0.2 SCFM.²

Likely due to the water vapor modifying the gain profile of at this wavelength, the 1121 nm VECSEL is extremely easy to unlock, for example by acoustic noise such as drawers opening and closing, ladders moving, and conversations near the VECSEL table. To mitigate this, it is boxed with a foam-board box padded with Pyrotek Soundlag acoustic insulating material (see Figs. A.33 and A.29). While this improved the stability of the VECSELs significantly, they are still somewhat sensitive to perturbations.

After the continuous failure of the 1120 nm MenloSystems OrangeOne lasers³ for the $^2S_{1/2}$ to $^2P_{3/2}$ transition in $^{25}Mg^+$, a second 1120 nm VECSEL was built using the same type of gain chip but outputting light at 1118 nm. This VECSEL had a slightly modified design with additional Viton o-rings between the VECSEL body and base intended to reduce vibrations, and a modified backplane to support CPC brand quick-connect fittings. These have a large gasket beneath a flange that offers a better seal than the Koolance brand quick-connect fittings in case a dry gas purge line is not used. In order to accommodate these new fittings, the inner wall of the VECSEL case was expanded, making it necessary to shift the outer screw holes for the lid slightly. Therefore, the lids

²Setting the flow rate higher than 0.2 SCFM is fine as long as it does not cause observable instability in the output power or frequency; this can also be done temporarily to dry the cavity more quickly. It can also be set lower in order to avoid instabilities caused by high flow rate.

³They would turn on for a period of ≈ 20 minutes to a few hours, outputting the correct power of approximately 1W, then give an error of PREAMP_FALSE_OFF and turn off.

of this design are not compatible with previous versions. The lid machined for this VECSEL can accommodate a purge line as well as the desiccant cartridge with humidity indicator. This VECSEL was also boxed with a Soundlag-padded foam box, but appears to be similarly sensitive to the $^2P_{1/2}$ 1120 nm VECSEL. During the construction of this VECSEL, a different curvature output coupler mirror than intended was used and a new etalon design that uses mostly metal parts as opposed to machined ceramic components was used, but these do not appear to significantly affect the performance of the VECSEL.

The temperatures of various elements of both VECSELs have to be adjusted periodically, often corresponding with large swings in outdoor temperature. For this reason, I believe that one modification that could be made to these VECSELs would be the addition of temperature stabilization of the VECSEL case in order to further isolate it from the environment.

A.1.2 VECSEL Lasing and Alignment Procedure

Here is my personal formula for getting the VECSEL to lase and aligning it afterwards. Some of these steps may seem overly cautious for VECSELs with wavelengths that differ from 1120 nm; most of my experience comes from those which are known to be temperamental.

- (1) First, the pump current should be turned as low as possible for the pump diode to lase, and an IR-capable imaging system (for example a Thorlabs CMOS detector) should be used to view the gain chip. At this point, all components (including the birefringent filter and etalon) can be installed if desired this is my personal preference. The output coupler mount should be in a fairly neutral position.
- (2) The pump output fiber's mount should be adjusted so that the pump spot is near the center of the gain chip. It should also be adjusted to focus on the gain chip by decreasing the spot size for this pump current as best as possible using the mount's forwards/back adjustment, but it should be fairly close by design; the pump spot should be viewed by the detector.
- (3) Now, the direction of the beam reflected from the output coupler can be verified with an

IR card (with the pump laser still at low current). Adjust the output coupler as necessary to overlap the return beam with the incident beam, and ensure that the beam is passing through all the optical components.

- (4) At this point, using the access holes in front, balldrivers or long Allen keys should be placed in the output coupler mount. Then, the VECSEL lid should be closed and a photodetector should be placed in front of it where the output beam is expected. A good option is the Thorlabs PDA50B2 as it has adjustable gain and a large detection area. Then, the current can slowly be turned up to where the VECSEL gain chip is expected to output the desired wavelength and lase, often around 10-13 A, although lasing has been observed at lower currents when the VECSEL is fully aligned. The photodetector may observe a signal from leakage pump light; in this case the detected signal will increase linearly with increasing current. When the signal increases or spikes as the current is increased, the VECSEL is lasing. It is also very likely that the VECSEL is not well aligned enough for lasing to occur at this stage. In this case, the pump current should be left where the VECSEL is expected to lase, for example 11 A or higher, and a careful raster scan of the output coupler mirror should be attempted (small vertical and horizontal tweaks in a grid pattern). Lasing may then be observed on an IR card or the photodetector. Once lasing occurs, the output coupler mount position should be carefully optimized.⁴
- (5) Once lasing is successful, an optical isolator should be installed at the output of the VECSEL and the output wavelength should be read into a wavemeter. The temperature of the etalon and birifringent filter should be adjusted in order to obtain the desired wavelength. If the wavelength cannot be reached by adjusting the temperature within a reasonable range alone (see wiki for reference temperatures of other VECSELs) the physical mounts of the etalon and birifringent filter may need to be adjusted, depending on how far away the wavelength

⁴If this step does not work at all, the birifringent filter and etalon can be removed and this process can be attempted again. However, it should be noted that both elements, once installed, will significantly affect the horizontal position of the beam, and therefore alignment will have to be carefully repeated afterwards.

- is. Then, the output coupler should be carefully adjusted in order to increase the output power while maintaining the correct wavelength (or close), but not too much effort should be put into this step, especially if the wavelength is known to be sensitive to water.
- (6) The VECSEL should be closed and sealed completely, with the exception of the holes accessing the output coupler. The cavity should be flushed with dry gas if this is desired; a few hours will be required for the cavity to equilibriate both in temperature and humidity. During this time, the temperatures of the etalon and birifringent filter as well as the output coupler should be adjusted to maintain approximately the correct wavelength and optimal power (without devoting too much effort to the latter). It should be observed that the total power increases over time with the introduction of dry gas if the VECSEL is known to be sensitive to humidity. The temperature of the gain chip can also be adjusted to optimize the power close to the end of this step.
- (7) After the VECSEL is assumed to be close to equilibrium in temperature and humidity, a final adjustment of all temperatures and the output coupler positioning should be attempted in order to maximize the output power. This step may have to be repeated periodically throughout the next few days to one month in order to fully stabilize the VECSEL.

A.1.3 Plumbing

The pump diode and gain chip of the VECSEL are both cooled by water. Prior to ~ 2019 , Koolance LIQ-702 coolant was used for the fluid. While this was recommended for use with Koolance fittings, small leaks in the Thermotek T255P chillers would result in a buildup of a white, soapy, crusty substance near the fittings, and this product had to be purchased very frequently from Koolance in order to replenish the coolant that leaked. I decided to switch over to a 10% isopropanol alcohol in de-ionized water solution as is used with the Coherent Verdi laser (which uses the same style of chiller) in order to have a cleaner and more readily available coolant that still had algaecidal properties. No issues have arisen as a result of this change.

Typically, there is a filter and flow switch (that acts as the interlock to the pump diode current) in the chiller line, in addition to the thermal reservoirs for the pump diode and gain chip. Koolance quick-connect fittings are used between these elements in order to isolate flow issues with minimal spilling. However, it has been found in two instances that the Koolance fitting itself is the cause of the flow blockage. In these cases, a gasket inside the fitting has failed, causing it to seal somehow. This can be verified visually as the center part of the female fitting will not retract normally.

A.2 Acousto-Optic Modulators

AOMs are used throughout 1G121 to control laser pulses in both frequency and time. The center frequencies of the AOMs vary from 80 MHz to 400 MHz and include those manufactured by Brimrose, IntraAction, Crystal Technologies, and Gooch & Housego. By using both the undiffracted and diffracted orders of the same beam, one beam can be split into two with different frequencies. By blocking the undiffracted beam and sending the diffracted beam through an iris or a fiber, an AOM can be used to switch a beam on and off. In order to bridge the large hyperfine splittings of ${}^{9}\text{Be}^{+}$ and ${}^{25}\text{Mg}^{+}$, AOMs are often used in a double-pass configuration, which is discussed in Sec. A.2.1. AOMs can even be used to spatially overlap beams, as discussed in Sec. A.2.2.

A.2.1 AOM Double-Pass Methods

AOMs can be used in a double-pass configuration in order to shift the frequency of the laser beam by twice the AOM center frequency. There are two ways to split the output light from the input light of a double-pass AOM: by polarization (Fig. A.1) or spatially (Fig. A.2). The total diffraction efficiency of double-pass AOM configurations can be quite high, as any intensity loss from a beam shape that is mismatched to the AOM ideally occurs only once on the forward pass.

Polarization-style AOM double-pass configurations rely on a quarter-wave plate and a beamsplitter. The light passes through the beamsplitter prior to reaching the AOM, therefore the input beam is horizontally polarized. The quarter-wave plate is placed in the beamline after the AOM so that the light passes through the waveplate on both the input and return passes. The light is

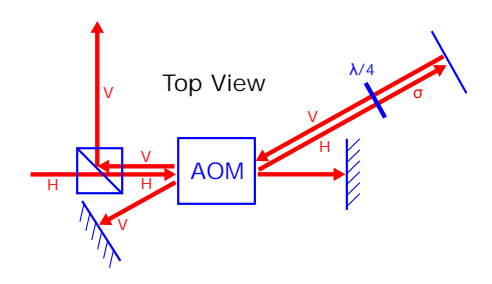


Figure A.1: The schematic for an AOM double-pass based on polarization is shown, as viewed from the top of the AOM. Optical elements are shown in blue while the laser is shown in red. All laser paths parallel to each other are offset for visibility and are in reality ideally physically overlapped. The polarization of each element is labeled with H for horizontal polarization, V for vertical polarization. A quarter-wave plate (labeled $\lambda/4$) is situated to rotate the horizontally polarized light to circular (labeled σ in this case for either σ^+ or σ^-) and then vertical on the return pass. The diffracted beam on the return pass should be overlapped with the incoming light and is reflected by the beamsplitter.

first rotated to be σ^{\pm} polarized on the forward pass and then vertically polarized on the return pass. When the vertically-polarized return light reaches the beamsplitter, it is diffracted towards the rest of the beamline. The polarization-style double-pass is only used in the ${}^{9}\text{Be}^{+}$ iodine locks. This is possibly because it is prone to stray light from reflections due to having many overlapped beams or slight changes to polarization due to transmission through/reflection by optics at an angle. Using a double-pass where the beams are spatially separated is less risky, especially for resonant beamlines when small amounts of light can cause detrimental changes to the ion state.

Another method of implementing an AOM in a double-pass configuration is to separate the input beam path spatially from the return beam path. Because the diffraction efficiency of AOMs are very sensitive in the horizontal direction, the input and return paths are separated in the vertical direction, as shown in Fig. A.2. Interestingly, I have found that most AOMs diffract better with a slight vertical angle, so this configuration naturally yields fairly optimal AOM performance for both the forward and return passes.⁵

Fig. A.2a) shows a configuration that can be used if the AOM has a large active area (such as an IntraAction brand AOM) and the collimated input beam does not need to be focused. While not strictly necessary, the lens after the AOM, with focal length f, helps to "correct" the path of

⁵Sometimes the *double-pass* (total) efficiency can be greater than 50%!

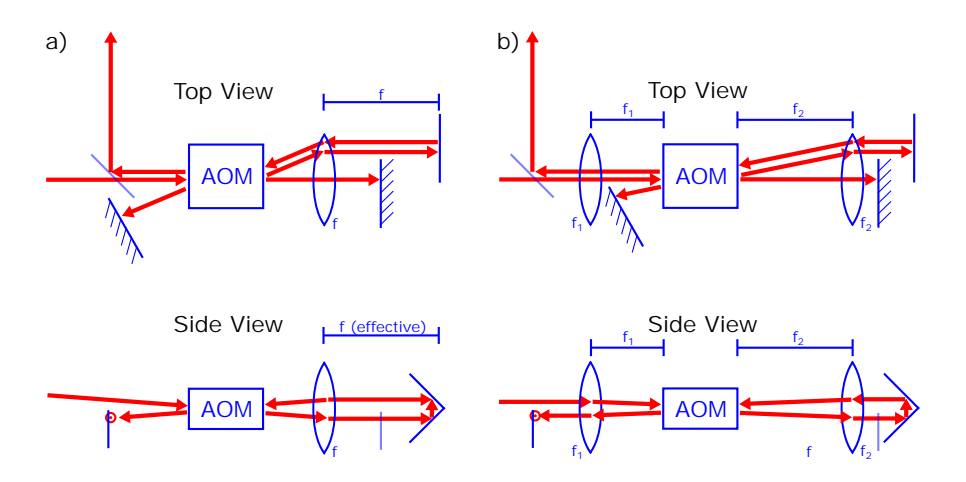


Figure A.2: Two schematics for an AOM double-pass based on vertical offset are shown, as viewed from the top and side of the AOM. Optical elements are shown in blue while the laser is shown in red. All laser paths parallel to each other are offset for visibility and are in reality ideally physically overlapped. All input beams are assumed to be collimated. a) shows a configuration that works for an AOM that has a large active area with one lens, while b) shows a configuration with two lenses, which is necessary for AOMs with small active areas.

the beam so that the retroreflecting mirror⁶ does not have to be placed at an angle. If the lens is placed as shown (with the undiffracted beam going through the lens center), it will have an increasing "corrective" effect as the beam is deflected at higher angles: the lens deflects the beam back proportional to how strongly it is diffracted by the AOM. This can be particularly helpful for beams that require a range of frequencies to be aligned to the trap (for example, the Raman beams for both ion species used should be aligned in order to drive both the qubit and cooling transition, which is about 200 MHz for ²⁵Mg⁺), because the diffraction angle typically varies with frequency, and the angle of the forwards and backwards pass will tend to cancel out as well. The bandwidth of aligned frequencies can likely be further increased by selecting the lens carefully. Geometrically, the return pass should be directly vertically offset from the forwards pass, and sometimes the UV beam is visible on the lens so that this alignment can be verified.⁷ The retroreflector must be placed so that the beam path length between the forward and return pass is approximately 2f, in order for

⁶This can be a prism-type retroreflector, two mirrors, or a set of mirrors performing the effective function of a retroreflector.

⁷My experience has been that if the forwards pass is optimized, aligning the return pass to the forwards pass in this manner will result in fairly good diffraction efficiency of the return pass without much effort, as long as the vertical angle is correct.

the output beam to be well-collimated.

If the AOM is a type that has a small active area (for example, Brimrose), there will be a lens placed in front of the AOM, illustrated in Fig. A.2b) with focal length f_1 , so that the focus is at the center of the AOM. There must then be a lens placed behind the AOM; in addition to correcting the angle of the beam as in the case with one lens, it helps to re-collimate the beam. This lens can have a different focal length f_2 than the first lens but should be placed at a distance f_2 away from the center of the AOM to ensure that the beam remains collimated.

For both configurations, the retroreflector should have many degrees of freedom to adjust the pointing of the return beam and ideally the lens between the AOM and retroreflector should also be adjustable to better collimate and deflect the beam.

A.2.2 Injecting Beams through an AOM

Many beamlines in 1G121 require the overlapping of many different frequencies of light, since the optic paths are set up to aim only one beam per species at the experimental zone from each direction as illustrated in Fig. 3.9. If two beams are of very different wavelengths, they can be combined using a dichroic mirror without losing much power. If they have orthogonal polarizations (horizontal and vertical or σ^+ and σ^-), a beamsplitter can be used. However, in many cases neither of these apply, and often a 50/50 (non-polarizing) beamsplitter is used, sacrificing half of the power of both beams. A fourth method that is implemented in this lab is taking advantage of AOMs that are used as switches ("switch AOMs") to add a second beam to an already existing beamline. As shown in Fig. A.3, the second beam can be injected through the AOM such that the beam is aligned to the same path as the diffracted path of the first beam. The second beam should ideally have a dedicated switch AOM situated before it is injected into this beam path.

This method is ideal if it is desired for two beams to share the same physical path but they do not need to be used at the same time. It allows both beams to be used at nearly full power with few drawbacks.⁸ If the two beams do need to be used simultaneously, this method will not work

⁸The main drawback is that either the edge of a circular mirror or a D-shaped mirror must be used to send the

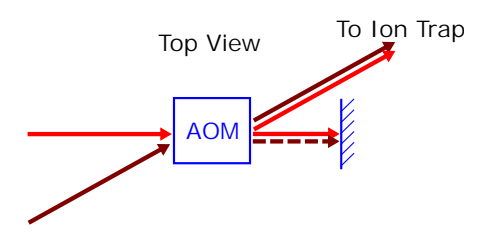


Figure A.3: Optical elements are shown in blue while the laser is shown in red. All laser paths parallel to each other are offset for visibility and are in reality ideally physically overlapped. The bright red arrow shows the original (first) beam path for which the illustrated AOM functions to switch the beam on and off. A second beam (illustrated in dark red) can be sent into this AOM at an angle that aligns with the diffracted order of the first beam. Ideally, the illustrated switch AOM is off when the second beam is on (and the second beam is controlled by a second switch AOM further upstream in the beamline); otherwise, some power is diffracted from the second beam, illustrated with the dashed arrow. If the first and second beams do not have to be on simultaneously, both beams can be used at full power with this configuration.

optimally because some power from the second beam will be diffracted by the switch AOM through which the beam is injected, (illustrated by the dotted arrow in Fig. A.3) but it will still do the trick.

A.3 Digital Servos

NIST digital servos (a. k. a. "Leibrandt boxes" [88]) are used widely in 1G121. They are used mainly to lock our eight UV doubling cavities and pulse-shape our six Raman beams (with PDQ inputs), as well as a few other places, for example stabilizing the magnetic field with a feedback loop on a sensor. Unfortunately, these digital servos were known to fail quite frequently when I first joined the group in 2018. Many digital servos had broken outputs or inputs. With some effort (as described below), the failure rate was reduced to about one digital servo per 6 months (or less) throughout the whole lab. It is worth noting that currently the motherboard Opal Kelly FPGA (XEM6010-LX150) is no longer being made, and an effort find a replacement servo is underway.

The most frequent failure mode of the NIST digital servos was the burning/melting/explosion of the op-amp AD8251 on either the input or output channels (nearest in the circuit to the SMA connector). This was suspected to be because the pre-amp (LTC6406) was not specified for the second beam into the switch AOM at a shallow angle (this angle is equal to the diffraction angle of the AOM), and

this may distort the beam shape if there is not enough space to situate the mirror further away from the AOM.

voltage rails it was soldered to. With the help of Dave Leibrandt, I found a drop-in replacement amplifier (LTC6405) which had negligible effect on the servo characteristics. After pre-emptively replacing all of these amplifiers on the digital servos that were not in use, as well as repairing the broken servos using the new component, I found the rate of this mode of failure to diminish significantly.

While debugging the above issue, there were a number of other potential failure modes. Loose internal SMA connections sometimes caused dropouts in the input/output signals. In one instance, the Opal Kelly itself was found to have failed – the FPGA chip became extremely hot and would not respond to programming. Also, while it is unknown whether this caused any significant issues, the ferrite bead "FB2" on the Opal Kelly should be removed to avoid a ground loop.

A.4 UV BBO Doublers

A.4.1 Ospelkaus-style UV Doubler Variations and Versions

Most of the UV doublers used in 1G121 have 10 mm BBO crystals. They are used to generate UV light at wavelengths of 313 nm, 285 nm, 280 nm, and 235 nm. The initial design used Lees mounts, which are no longer made, and were adapted to use Thorlabs POLARIS mounts shortly before my arrival in the group. Older versions used black-anodized components as well as a cover made of plastic.¹⁰ The new design is mostly metal, including the cover, and relies on sandblasted components where scatter is particularly worrisome, namely the crystal mount. There are also UV doubler variations for different piezo lengths, depending on whether responsivity or range is desired. However, the length of the piezo will change the required positioning of the relevant mount, so this must be determined before machining components to build such a doubler.

⁹During my whole time in the Ion Storage Group I have found only one such failure in 1G121, though Jose Valencia did show me a number of Opal Kellys with similar symptoms from the clocks experiments of the group.

¹⁰There is some belief that the plastic covers can either outgas or otherwise transfer some sort of debris onto the optics inside the doubler.

A.4.2 313 nm Doublers

Using the Ospelkaus-style doubler design (available on the wiki) I built two 626 nm-to-313 nm UV doublers for the ${}^{9}\text{Be}^{+}$ resonant wavelengths as my first project. The previous doublers were open to air and thus less stable. While the doublers themselves appear to be reasonably stable, in the future it is recommended to build on stiffer breadboards or directly on the optical table, since the 0.5"-thick aluminum breadboard that these were built on have clear flexing issues. When a support is placed on this breadboard, the vertical alignment of the UV beams would change when the laser barrier is put on top of that part of the table.

A.4.3 280nm Raman Doubler

I also built a new UV doubler for the Mg Raman system with a 20 mm long BBO crystal. This is the most powerful UV doubler outputting 280 nm light, with a 1.5 W 560 nm input beam, giving ≈ 500 mW output at maximum. Typically, it is run with about 200 mW output, and 1.3 W input. The increased length of the BBO crystal is intended to decrease the size of the beam at the input and output faces of the BBO crystal, making it less susceptible to burns. While burns are no longer observed on the crystal faces, it was found that the coating of the output coupling mirror often develops a bubble at the focus of the beam (on the timescale of roughly half a year) due to the high intensity, and this significantly decreases the doubling efficiency.

This UV doubler has significant thermal drifts and therefore it must be aligned while locked for optimum output power. Typically it needs to be adjusted briefly twice a day during normal operation to maintain enough power for Raman transitions. The old 10 mm BBO Raman doubler was used to replace the Mg PI UV doubler which was previously open-air and much less stable.

A.4.4 Oxygen Flow

Oxygen is flowed over the BBO crystal while the UV doublers are being pumped by visible light. This is intended to prevent damage to the crystal faces. Some of the tubing used to feed oxygen to the UV doublers in 1G121 was degraded and would turn to mush when rubbed between

the fingers. These were replaced with rigid plastic tubing which is then connected to flexible Tygon E-3603 tubing for the segment just before each UV doubler and internal to the UV doubler. Typically, the oxygen is only turned on when the UV doublers have input light going to them. While there have been a few days where the oxygen is not on by accident, these, as well as the overnight period without oxygen, do not appear to have detrimental effects on the UV doublers.

A.4.5 Hansch-Couillaud and Pound-Drever-Hall Locking

The UV doublers are locked using either Hansch-Couillaud [144] locks or PDH [145] locks. The theoretical basis for both these locking styles can be found in the references given. Briefly, Hansch-Couillaud locks rely on the comparison of different light polarizations, while PDH locks require a modulation of the laser light to provide a lock-in signal. The rest of this section describes how the lock is implemented in hardware in 1G121.

Hansch-Couillaud locks are implemented by taking the reflected light from the input coupler of the UV doubler and separating it by polarization to put on a differential photodetector (or two photodetectors whose signals are differenced electronically); the resulting difference signal is the lock signal. In 1G121, the light is set up to first pass through a half-wave plate and quarter-wave plate so that the intensity of each polarization can be tuned for optimal signal-to-noise ratio. Then the light is split using a Wollaston Prism (Thorlabs WP10-A) and the signal is sent to a NIST differential photodetector. When using this technique, a portion of the total reflected light may be used as a relock signal (if the detected light exceeds a certain intensity, relocking is attempted) or a pickoff may be placed in the UV output beam for relocking.

In order to generate the modulation on the light for PDH locking, EOMs (Qubig) are used in 1G121. The modulation frequencies vary from 20-50 MHz and are generated using Rigol multichannel function generators (such as the DG832). The reflected light from the input coupler of the UV doubler is sent to a photodetector with sufficient bandwidth (Thorlabs PDA10A2) and this signal is split using a bias tee (for example Minicircuits ZX86-12G-S+). The DC output of the bias tee functions as a monitor for the reflected power which can be used for relocking, while the RF

output is demodulated to generate the PDH lock signal using a mixer (for example Minicircuits ZMY-1+). The second output of the Rigol is used as a local oscillator in the demodulation; the phase of this signal relative to the EOM drive signal should be set to generate an appropriate PDH lock shape [145].

A.5 Iodine Locks

The resonant beams and ²⁵Mg⁺ PI beam frequencies are all locked to iodine spectrum lines with the visible light for each frequency.¹¹ Three different styles of iodine locks are used.

The first is Doppler-broadened iodine spectroscopy; this is used for the ²⁵Mg⁺ PI. The beam is split into two using a pickoff, and one beam is sent through the iodine cell while the second beam is used as a reference to remove common-mode noise. These two beams are then sent to a Nirvana 2007 Auto-Balanced Optical Receiver from Newport. This is simple and suitable for the PI because it does not have to be locked very precisely.

The other two iodine lock types are Doppler-free pump/probe spectroscopy configurations where two beams (one strong pump to saturate the transition and a weak probe to carry the resulting signal) are sent through an iodine gas cell in opposite directions. The probe beam is modulated with a low-frequency tone (a few MHz or less) to create sidebands [146], and this is demodulated with a second tone from the same source in order to create the iodine lock signal.

The configuration used for the ${}^9\mathrm{Be^+}$ ${}^2\mathrm{S}_{1/2} \leftrightarrow {}^2\mathrm{P}_{1/2}$ and ${}^2\mathrm{S}_{1/2} \leftrightarrow {}^2\mathrm{P}_{3/2}$ frequency locks use an FM modulation tone on the RF drive sent to an AOM in the pump beamline and the signal is demodulated using a SciTec 410 lock-in amplifier. The FM modulation is generated directly using the modulation option on an HP 8640B function generator from a separate modulation tone source.

On the other hand, the configuration used for the $^{25}\mathrm{Mg^{+}}$ $^{2}\mathrm{S}_{1/2} \leftrightarrow ^{2}\mathrm{P}_{1/2}$ and $^{2}\mathrm{S}_{1/2} \leftrightarrow ^{2}\mathrm{P}_{3/2}$ frequency locks rely on an EOM to provide a lock-in tone, as described in Ref. [147]. The source tone for the EOM and demodulation signals come from different channels of a Rigol DG832 function

 $^{^{11}\}mathrm{The}\ ^9\mathrm{Be}^+$ PI wavelength is locked to the wavemeter; nearly all other frequencies are monitored by the wavemeter for reference.

generator and are demodulated using a home-built lock-in setup based on a Minicircuits ZRPD-1+ phase detector.

A.6 Graphical Beam Overlay of Lab

The following section contains several photos of the lab beamlines with the various beam paths graphically overlaid on the photos, and some optical elements labeled. This aims to provide a guide to how each beam is aligned, but is not precise (for example the exact angles of the beams). Illustrated beams that are very close together and parallel can be taken to be physically overlapped. The colors of each beam are chosen for visibility and may change between photos for a single beam that passes through more than one image. The diffraction order through each AOM is intended to be true and are usually illustrated with a new arrow, except when the AOM is used in double-pass configuration.

The Figure (A.4) and Table (A.1) below can be used together to determine the approximate locations of the optics depicted in photos. The size and location of the covered area as shown by Fig. A.4 is approximate, as some photos have overlap. Areas that are not covered in Fig. A.4 are nominally empty or not being used as part of the main experiment.

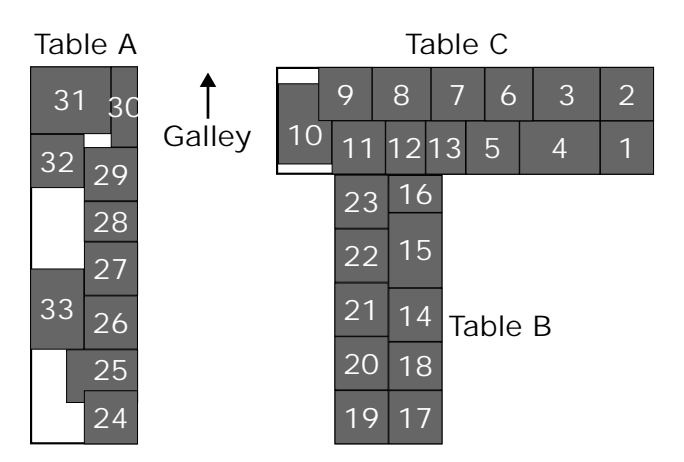


Figure A.4: The approximate locations of each photo number (correlating to Tab. A.1) is shown. The direction of the galley is given as a reference.

Table A	Figure	Table B	Figure	Table C	Figure
Location	rigare	Location	1 iguic	Location	riguic
24	A.29	14	A.19	1	A.5
25	A.30	15	A.20	2	A.6
26	A.31	16	A.21	3	A.7
28	A.32	17	A.22	4	A.8
29	A.33	18	A.23	5	A.9
30	A.34	19	A.24	6	A.10
31	A.35	20	A.25	7	A.11
32	A.36	21	A.26	8	A.12
33	A.37	22	A.27	9	A.13
		23	A.28	10	A.14
				11	A.15
				11	EIT cooling: A.16
				12	A.17
				13	A.18

Table A.1: The figure number of each beamline photo is correlated to the numbered location in Fig. A.4.

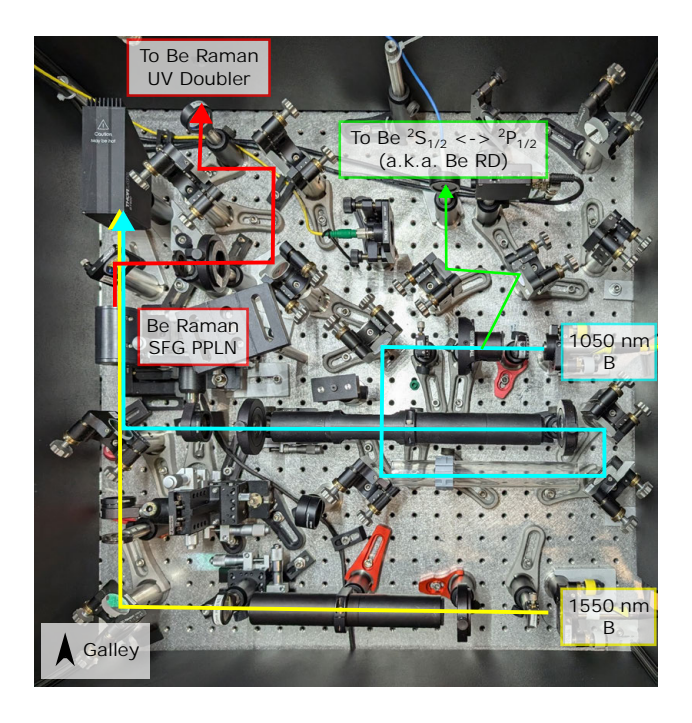


Figure A.5: Beamline overlaid on top of photo of ${}^9\mathrm{Be}^+$ Raman SFG setup. IR wavelengths 1550 nm (yellow arrow) and 1050 nm (blue arrow) are emitted from amplified fiber laser sources and physically overlapped in a PPLN crystal to generate 626 nm light (red arrow). Some light from the 1050 nm B is split off (green arrow) using an angled polarization element (for example a Glan-Laser or Glan-Taylor polarizer) and sent to the resonant SFG setup to be used for the ${}^9\mathrm{Be}^+$ ${}^2\mathrm{S}_{1/2} \leftrightarrow {}^2\mathrm{P}_{1/2}$ wavelength.

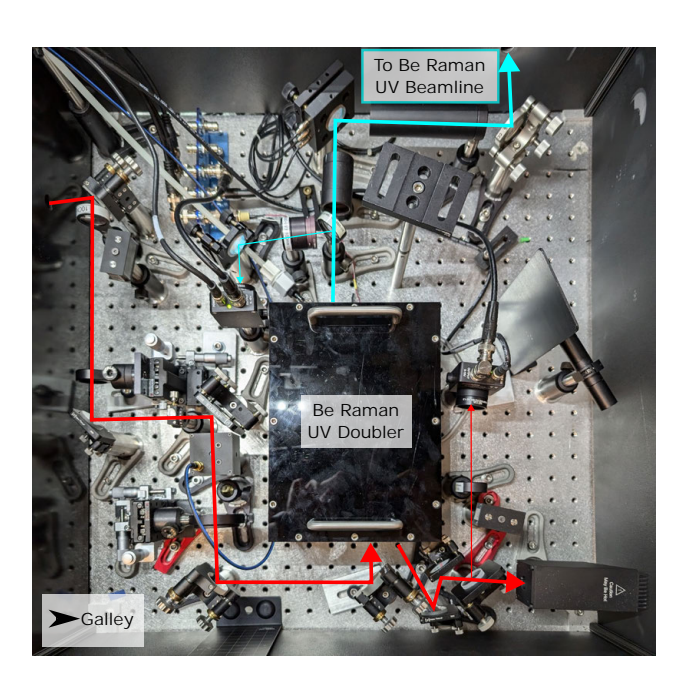


Figure A.6: Beamline overlaid on top of photo of area near $^9\mathrm{Be^+}$ Raman UV doubler. Light of 626 nm wavelength (red arrow) passes through an EOM (used for PDH locking, see Sec. A.4.5) before being converted to UV light (blue arrow) using a BBO crystal. A small portion of the UV light is sent to a photodetector for relocking the UV doubler.

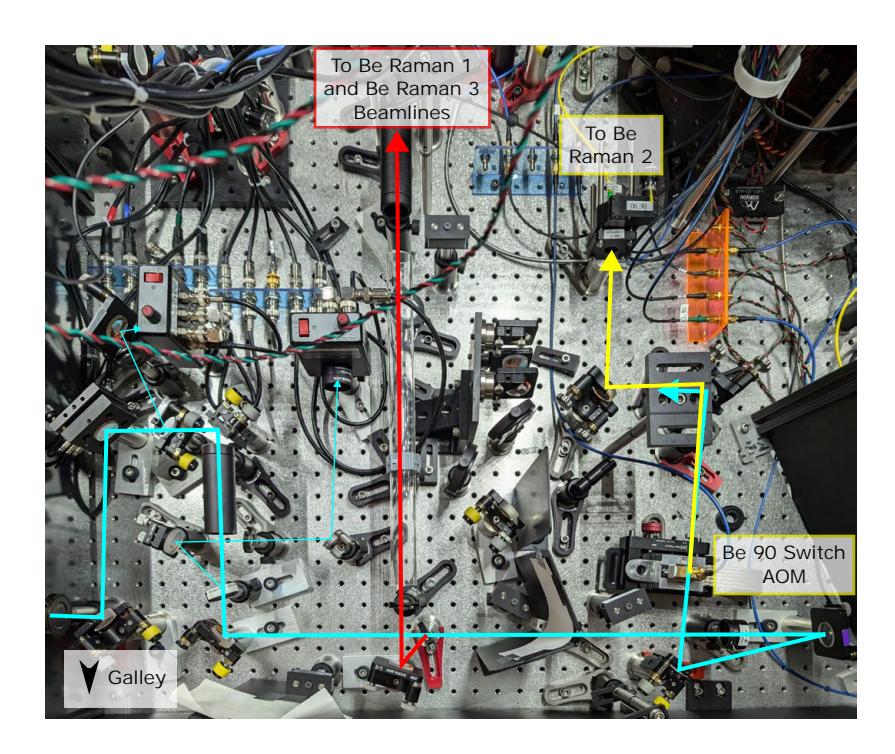


Figure A.7: Beamline overlaid on top of photo of area near Be Raman 2 AOM beamline. Pick-offs are used to send a small amount of light to two quadrant cell detectors; these are currently only used for reference but the signals can be used to feed back to mirror mounts with piezoelectric transducer knobs (one of which is shown to the middle left edge of the image; the other is in Fig. A.6). A beamsplitter is used to split more than half of the beam power to the Be Raman 1 and 3 beamlines (red arrow). The rest of the beam passes through the "Be 90 Switch" AOM, where the diffracted order passes into the Be Raman 2 fiber (yellow arrow).

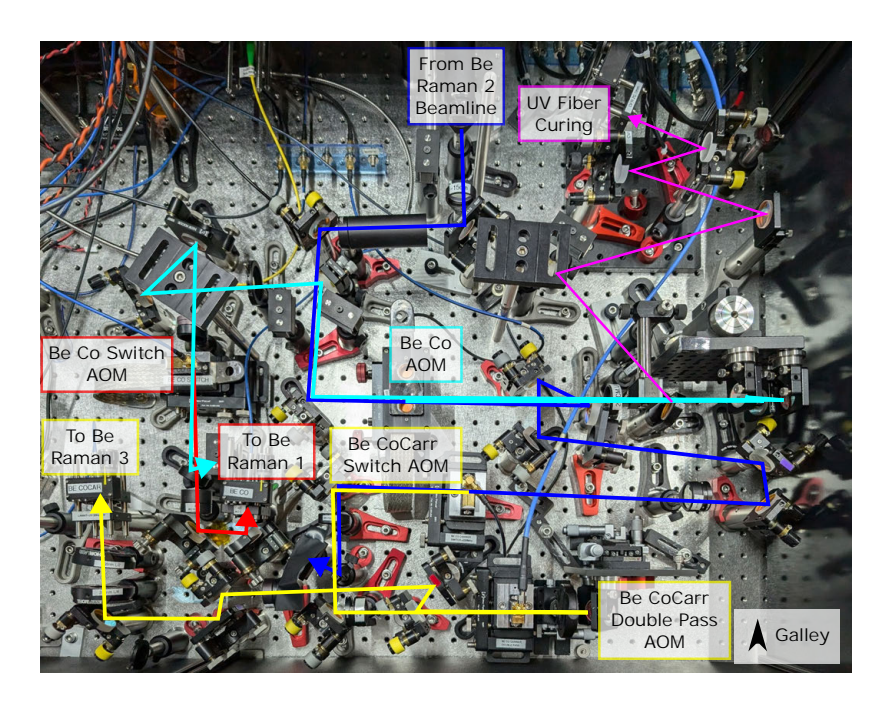


Figure A.8: Beamline overlaid on top of photo of area near Be Raman 1 and 3 AOM beamlines. The light from the ${}^9\mathrm{Be}^+$ Raman UV doubler (dark blue arrow) passes through the "Be Co" AOM. The undiffracted order is the source for the two-tone Raman 3 beamline after being diffracted through (yellow arrow) the "Be CoCarr Switch" AOM. both the totally undiffracted $(0,0)^{\mathrm{th}}$ order and doubly-diffracted $(-1,-1)^{\mathrm{th}}$ order of the "Be CoCarr Double Pass" AOM are aligned through the Be Raman 3 fiber with approximately equal intensity (this is very difficult to do). The double-pass diffracted order through the "Be Co" AOM (light blue arrow) passes through the "Be Co Switch" AOM; the diffracted order (red arrow) passes into the Be Raman 1 fiber. A flipper mirror can be used to reflect the diffracted order through the "Be Co" AOM towards the fiber-curing setup (upper right, magenta arrow) to perform UV fiber curing (see Sec. 3.2.9).

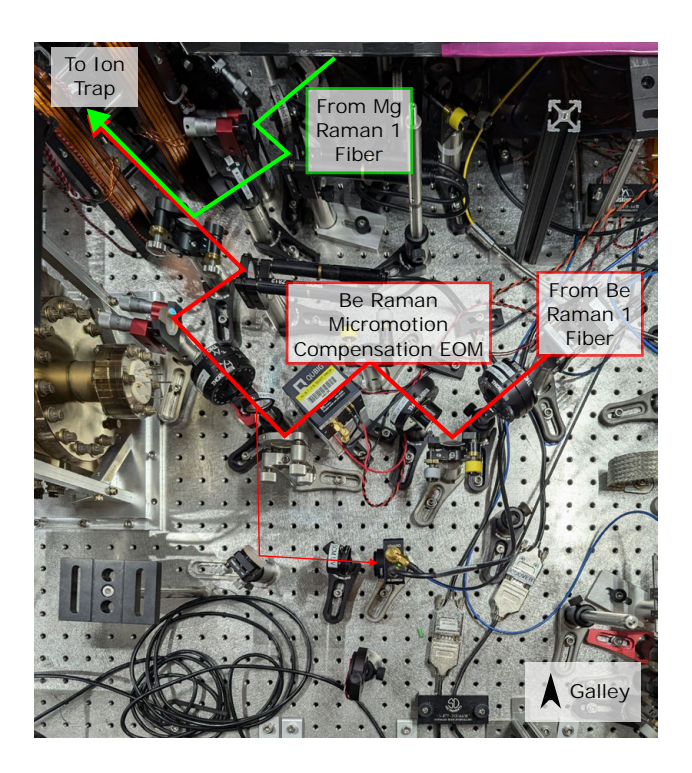


Figure A.9: Beamline overlaid on top of photo of area near Raman 1 input port for both ion species. The beam (red arrow) coming out of the Be Raman 1 fiber passes through the Be Raman Micromotion Compenesation EOM (Sec. 3.2.11) and passes through the dichroic into the ion trap. A small part of the power is picked off and sent to a linear photodetector; this is used for power stabilization (Sec. 3.2.10). The Mg Raman 1 beam comes from the upper part of this photo and is combined by the dichroic in front of the trap.

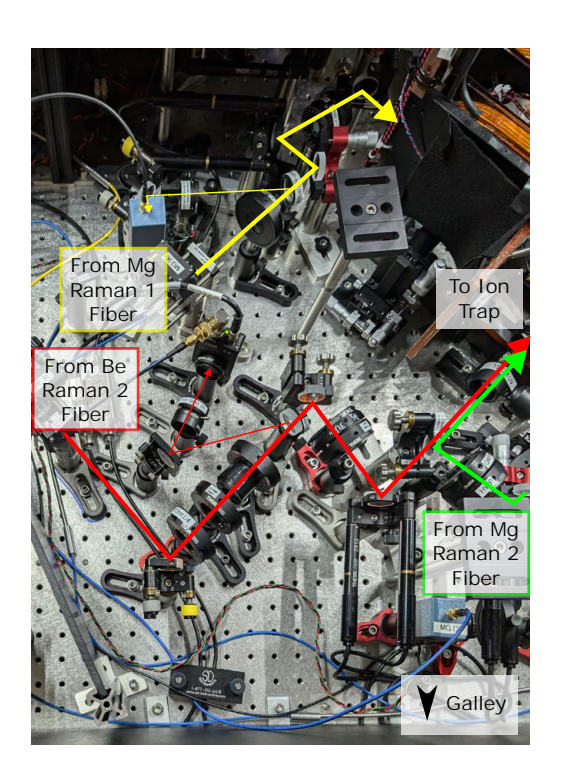


Figure A.10: Beamline overlaid on top of photo of area near Raman 2 input port for both ion species. The Mg Raman 1 beamline out of the fiber is also shown (yellow arrow), with a small amount being picked off for power stabilization (Sec. 3.2.10). The same occurs for the Be Raman 2 beam (red arrow) coming out of the fiber. The Mg Raman 2 beam (green arrow) is combined by a dichroic near the trap.

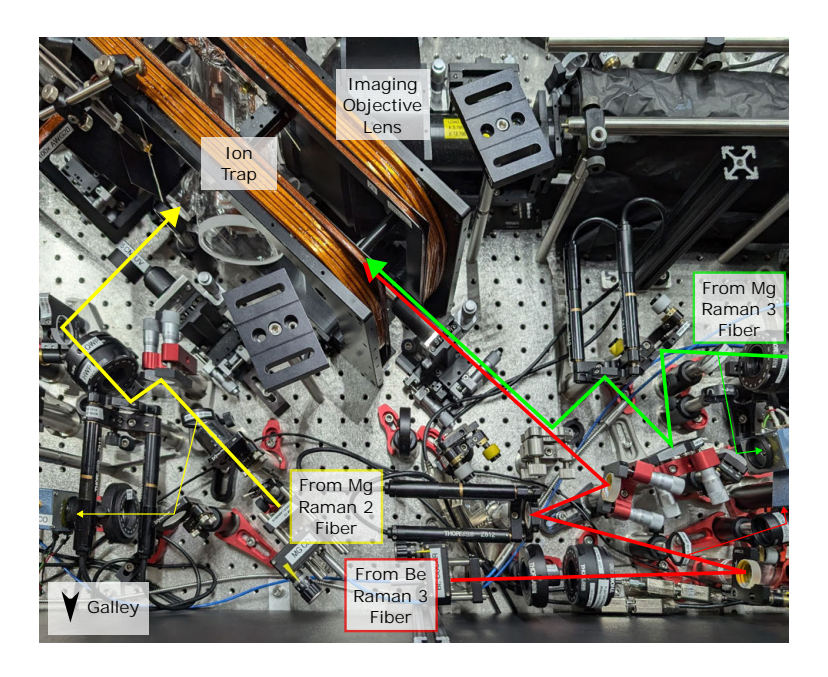


Figure A.11: Beamline overlaid on top of photo of area near Raman 3 input port for both ion species. The Mg Raman 2 beamline out of the fiber is also shown (yellow arrow), while the Be Raman 3 beam is shown in red and Mg Raman 3 in green. All three beams have a small amount of power picked off after coming out of the fiber for pulseshaping (Sec. 3.2.10). The Mg Raman 3 beam is combined with Be Raman 3 by a dichroic near the trap.

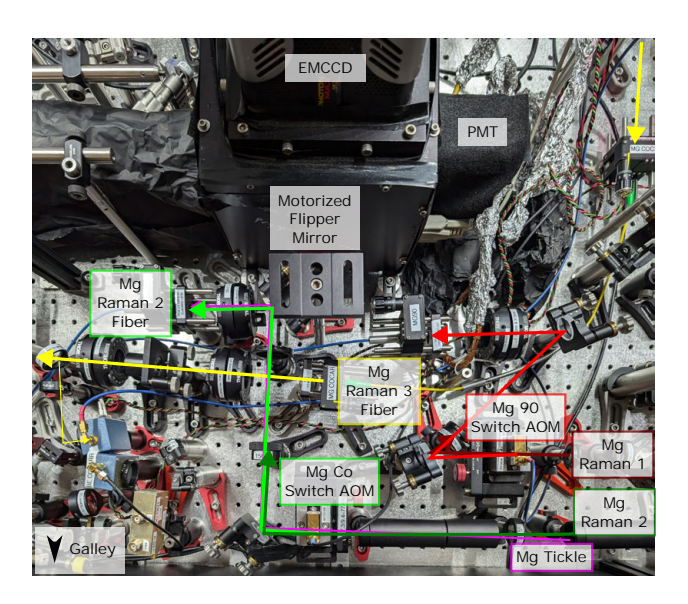


Figure A.12: Beamline overlaid on top of photo of area near ²⁵Mg⁺ Raman fiber inputs. Both the input and output ports of the Mg Raman 3 fiber (laser beam in yellow) can be seen. The Mg Raman 2 beam (dark green arrow) is diffracted by the "Mg Co Switch" AOM, and the diffracted order passes into the fiber. Also shown is the Mg Tickle beam (purple arrow) which is aligned to the fiber (Sec. A.2.2) and has full power when the "Mg Co Switch" AOM is off; this is used for a state-dependent force on the ion motion. The Mg Raman 1 beam (dark red arrow) similarly passes into the fiber when diffracted (bright red arrow) by the "Mg 90 Switch" AOM.

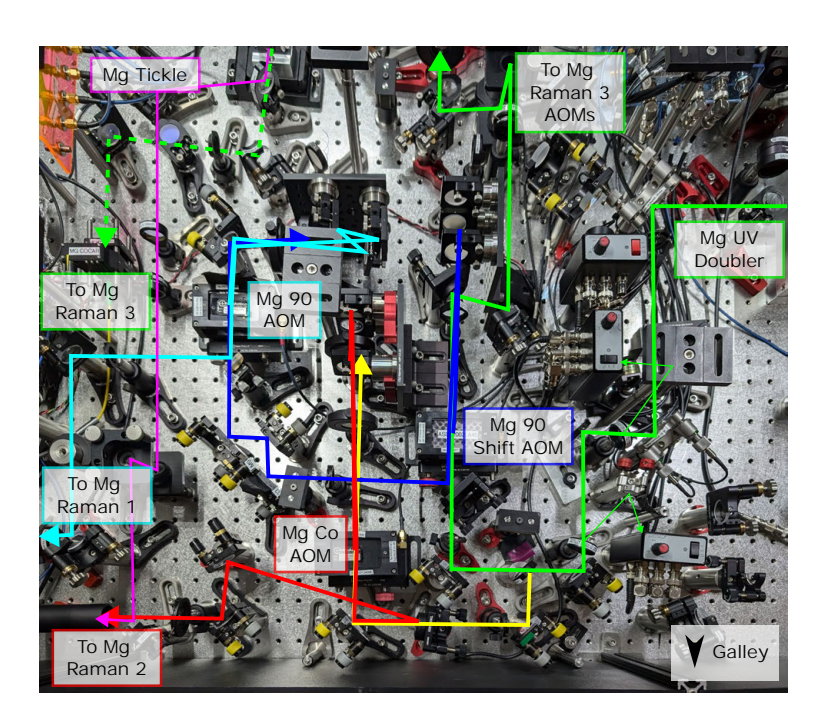


Figure A.13: Beamline overlaid on top of photo of area near ²⁵Mg⁺ Raman AOMs. The output of the ²⁵Mg⁺ UV doubler (green arrow, right side of photo) is monitored, but not currently actively servoed, by two quandrant detectors from small amounts of picked off light. The first two silver mirror mounts shown have PZT-drive knobs that can be used if an active servo is implemented. The undiffracted order of the "Mg 90 Shift" AOM passes to the Mg Raman 3 beamline, while the diffracted order (dark blue arrow) is sent to the "Mg 90" AOM where it is diffracted again (light blue arrow) and sent to the rest of the Mg Raman 1 beamline. A 50/50 beamsplitter splits a portion of the ²⁵Mg⁺ UV doubler output (yellow arrow) and this passes through the "Mg Co" AOM. The diffracted order (red) passes to the Mg Raman 2 beamline. The purple beam is an alternate configuration used for the experiment described in Sec. 5.8. It uses one of the frequencies normally used for Mg Raman 3; in order to use this beam to generate an axial spin-dependent force on the ion motion, it needs to be sent into the same port as the Mg Raman 2 beamline; it is injected using the "Mg Co Switch" AOM using the trick described in Sec. A.2.2. The dashed green arrow in the upper left is the normal Mg Raman 3 beam path for driving motion-insensitive qubit transitions on ²⁵Mg⁺; it cannot be used as the same time as the spin-dependent force.

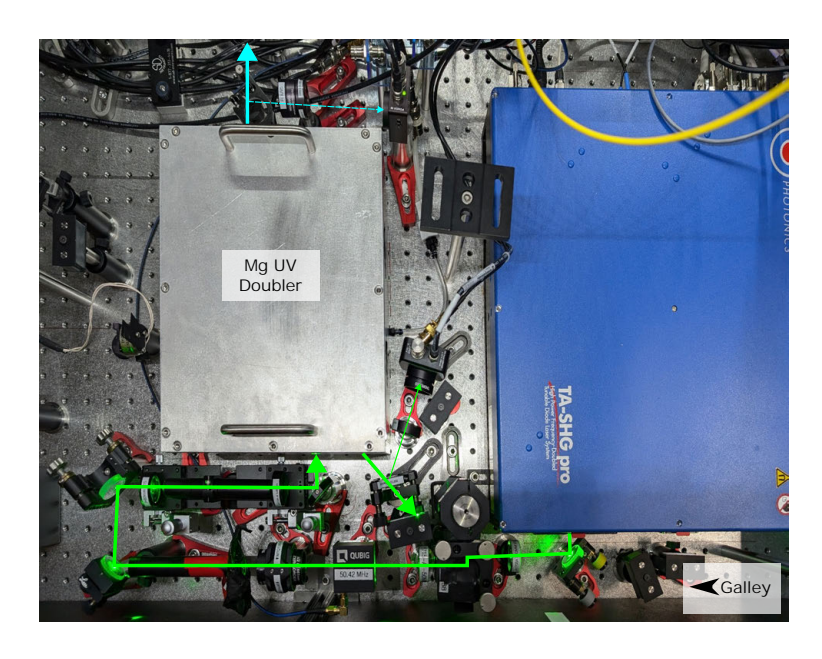


Figure A.14: Beamline photo overlay near Mg Raman UV doubler and Toptica TA-SHG pro. 560 nm light is emitted by the Toptica system (green arrow) and passes through an EOM (used for PDH locking, see Sec. A.4.5) before being converted to UV using a 20 mm long BBO crystal (blue arrow). The output can be optionally monitored for cavity alignment using the flipper mirror, illustrated by the blue dashed arrow.

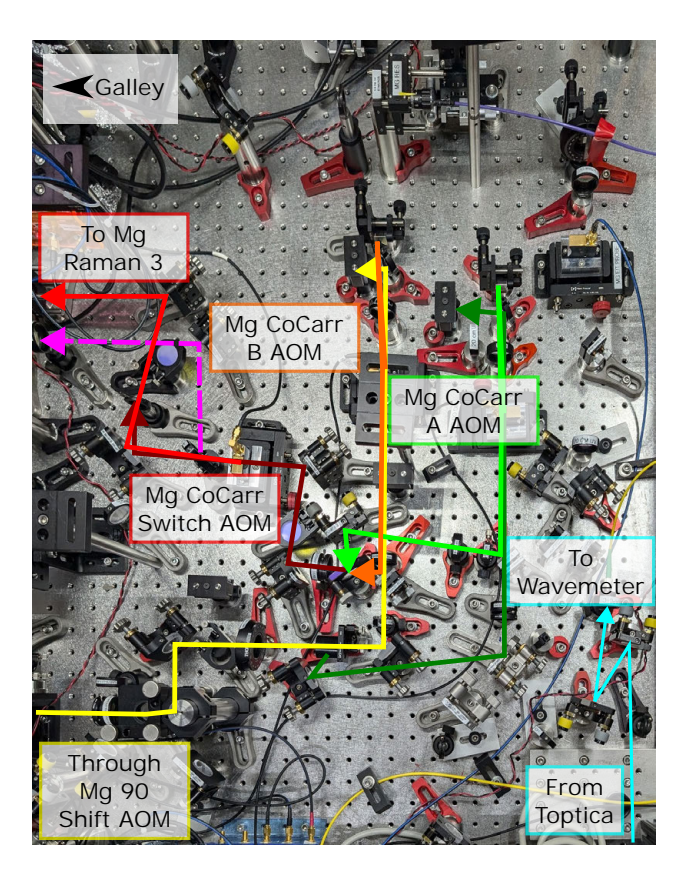


Figure A.15: Beamline photo overlay near Mg Raman 3 AOMs. The light passing through the "Mg 90 Shift" AOM (yellow arrow) is split using a polarization element (dark green arrow is the reflected light). Each of the transmitted and reflected light are modulated in double-pass configuration and combine at a 50/50 beamsplitter (light green and orange arrows). The overlapped light (dark red arrow) passes through one final AOM ("Mg CoCarr Switch") and the diffracted order passes into the Mg Raman 3 fiber. In order to use this configuration to create a state-dependent force on the ion motion, the path going through the "Mg CoCarr B" AOM can be blocked, and the diffracted light from the "Mg CoCarr A" path is injected into the Mg Raman 2 beamline using the flipper mirror (alternate path is illustrated by purple dashed arrow). The "Mg CoCarr Switch" is used as a switch for the state-dependent force beam, so the diffracted order through this AOM is the beam that is injected into the Mg Raman 2 beamline. A beam in the IR from the Toptica can be seen as well in the bottom left corner; this is sent to the wavemeter to monitor the frequency of the Mg Raman beam.

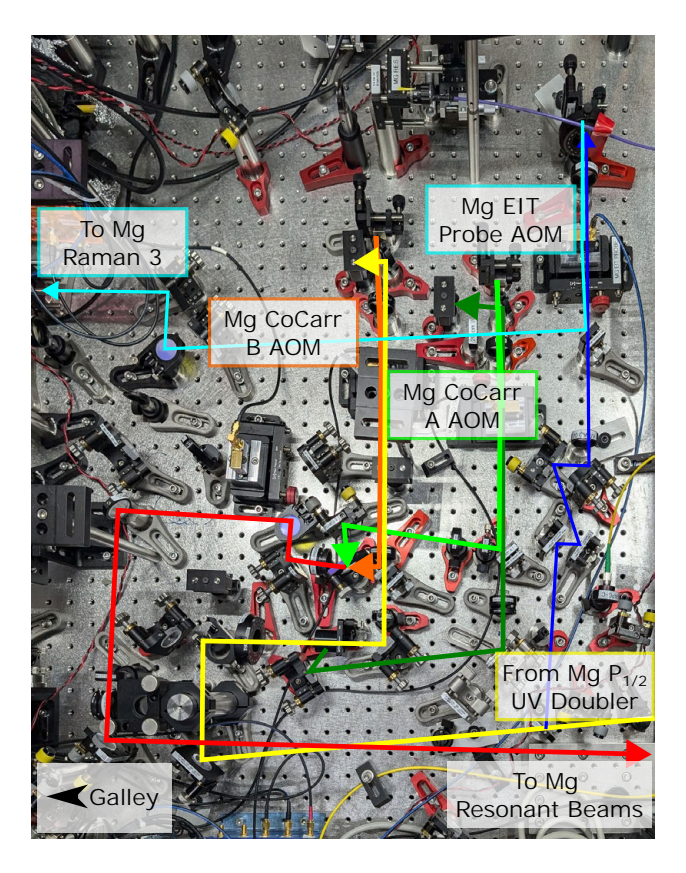


Figure A.16: Beamline photo overlay near Mg Raman 3 AOMs as used for EIT cooling. The light passes in from the 25 Mg⁺ 2 S_{1/2} \leftrightarrow 2 P_{1/2} beam (yellow arrow), and is injected into the 25 Mg⁺ Raman 3 AOMs ("Mg CoCarr A" and "Mg CoCarr B"). Similar to when it is used for two-tone qubit motion-insensitive qubit transitions, the doubly-diffracted orders through both are combined using a 50/50 beamsplitter and this light (red arrow) is rerouted to be injected into the 25 Mg⁺ resonant beamline. A small amount of the light coming into the system is picked off (dark blue arrow). This light is sent through a third 400 MHz center frequency AOM in double-pass configuration ("Mg EIT Probe") and the diffracted light is routed to the Mg Raman 3 fiber to become the π -polarized probe beam for EIT cooling. (In the current configuration, one of the mirror mounts for the laser-based spin-dependent force is blocking the probe beam to the Mg Raman 3 fiber.)

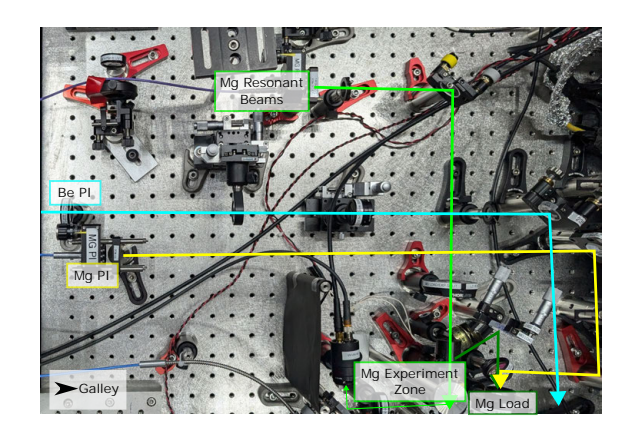


Figure A.17: Beamline photo overlay near $^{25}\mathrm{Mg^+}$ resonant and PI fiber outputs, showing $^9\mathrm{Be^+}$ PI (blue arrow, free space) as well. The $^{25}\mathrm{Mg^+}$ resonant beams all exit the same fiber (light green arrow) and are split using a polarization element. The light passing through the polarization element goes to the experiment zone $\mathcal S$ and a little is picked off to be monitored by a logarithmic photodetector (thin light green arrow). The reflected beam from the polarization element (dark green arrow) is combined with the $^{25}\mathrm{Mg^+}$ PI beam (yellow arrow) on a 50/50 beamsplitter and sent to the loading zone $\mathcal S$.

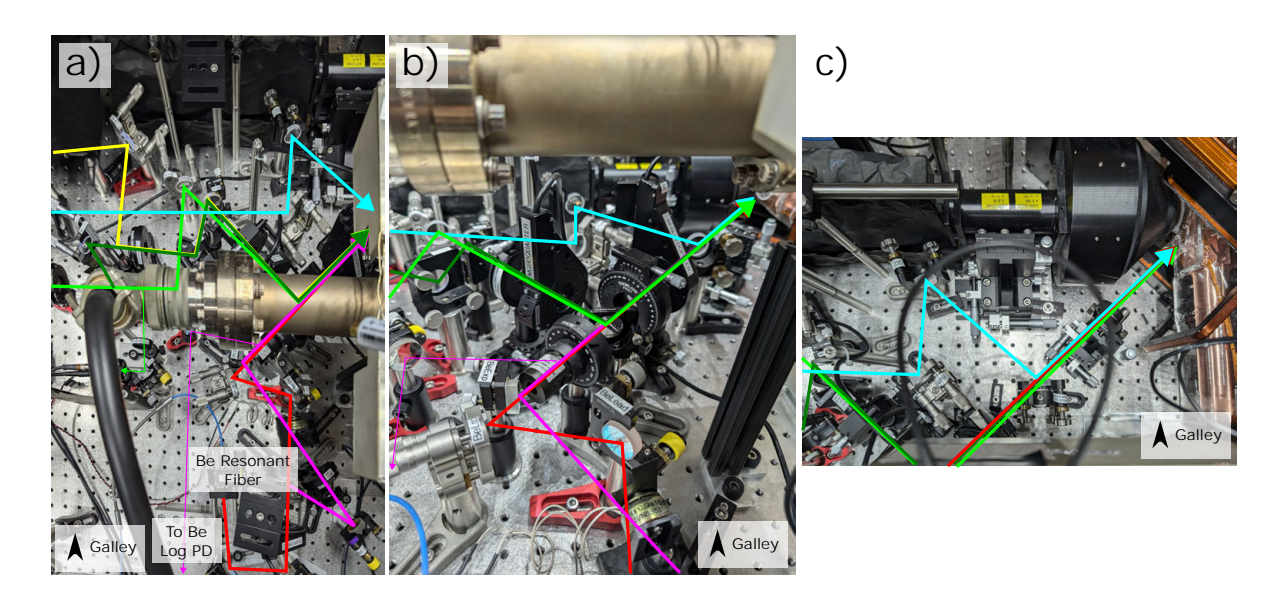


Figure A.18: Beamline photo overlay near ${}^9\mathrm{Be}^+$ resonant fiber output and input port to ion trap. a) shows the top-view photo, while b) shows the area blocked from above by the titanium sublimation pump. c) shows the input port to the ion trap; the area to the the upper-right of the view shown in a). All laser beam colors are consistent with each other in this figure. The splitting of the ${}^{25}\mathrm{Mg}^+$ loading zone beam (dark green arrow) from the experiment zone beam (bright green arrow) is shown, as well as the pick-off of the ${}^{25}\mathrm{Mg}^+$ experiment zone beam to the logarithmic photodetector (thin light green arrow). The two ${}^{25}\mathrm{Mg}^+$ resonant beams are reflected off a dichroic most easily seen near the center of b) 13 to combine with the ${}^{9}\mathrm{Be}^+$ resonant beams (red and magenta). In c), only one beam is shown to represent both ${}^{9}\mathrm{Be}^+$ beams. The ${}^{9}\mathrm{Be}^+$ PI beam is combined with all other beams with a dichroic right in front of the steering lens for the trap, most easily seen in b) and c). The beams aimed at the loading zone and experiment zone are separated by a few mm at the dichroic but are represented visually as overlapped in these images.

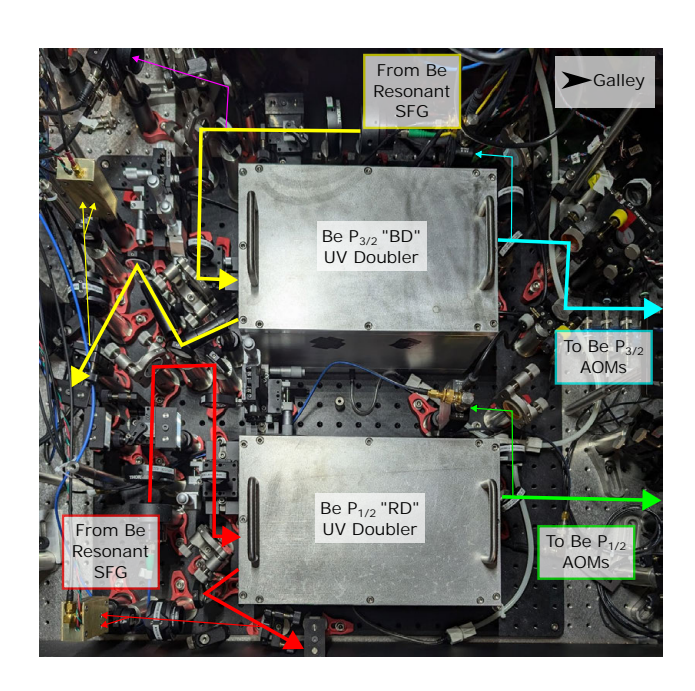


Figure A.19: Beamline photo overlay near ${}^9\mathrm{Be^+}$ resonant UV doublers. Light is output to each of the ${}^9\mathrm{Be^+}$ ${}^2\mathrm{S}_{1/2} \leftrightarrow {}^2\mathrm{P}_{3/2}$ (yellow arrow) and ${}^9\mathrm{Be^+}$ ${}^2\mathrm{S}_{1/2} \leftrightarrow {}^2\mathrm{P}_{1/2}$ (red arrow) UV doublers from the SFG setup. Both outputs (blue arrow, green arrow) have a small amount picked off to monitor; this signal is used to relock the doubler.

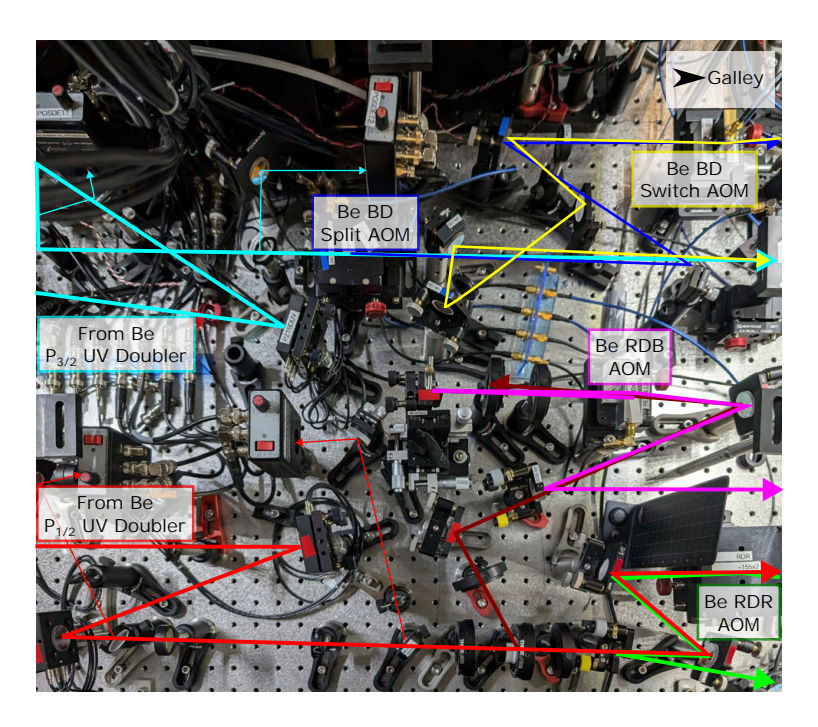


Figure A.20: Beamline photo overlay near ${}^9\mathrm{Be}^+$ resonant AOMs. After being output from the ${}^9\mathrm{Be}^+$ ${}^2\mathrm{S}_{1/2} \leftrightarrow {}^2\mathrm{P}_{3/2}$ UV doubler (light blue arrow), small parts of the beam are picked off (thin light blue arrows) to two quadrant cell photodetectors that have active feedback to two piezo-knob mirror mounts (the first is below the "Be BD Split" AOM in the photo, the second is the next mirror mount but is outside the photo). The beam is then diffracted by the "Be BD Split" AOM to the "Be BD Switch" AOM (dark blue arrow), where it diffracted in double-pass configuration to reach the Doppler-cooling or detection frequency. The ${}^9\mathrm{Be}^+$ ${}^2\mathrm{S}_{1/2} \leftrightarrow {}^2\mathrm{P}_{1/2}$ UV light (bright red arrow) similarly uses two quadrant cell detectors (thin bright red arrows) and feeds back to two piezo-knob mirror mounts (first two bounces of the bright red arrow). After, this light is split using a polarization element; the reflected beam (dark red arrow) passes through the "Be RDB" AOM in double-pass configuration, while the transmitted beam passes through the "Be RDR" AOM in double-pass configuration as well.

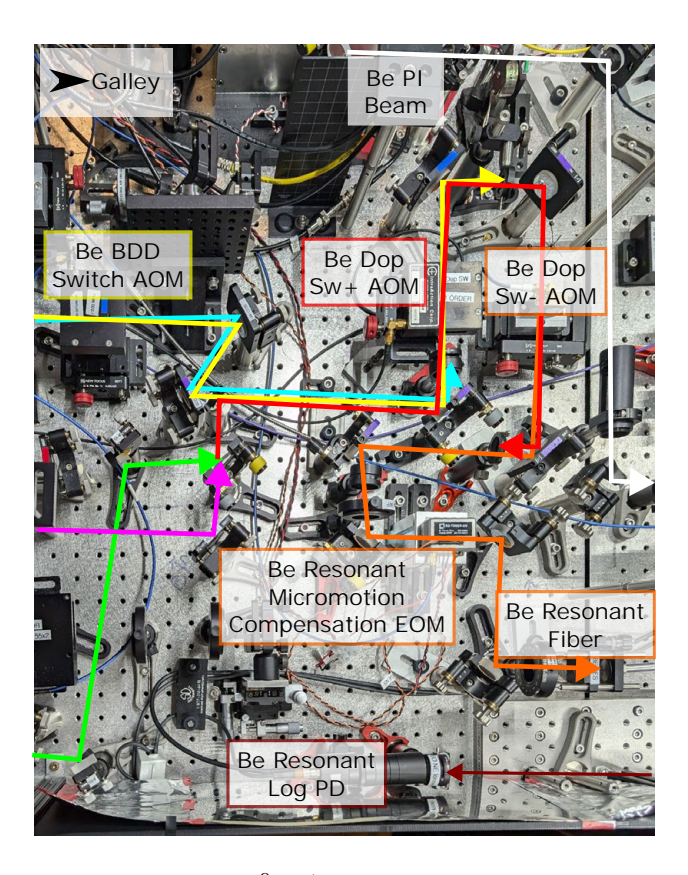


Figure A.21: Beamline photo overlay near ⁹Be⁺ resonant AOMs (second part). When the "Be BDD Switch" AOM is on, the detuned Doppler cooling ("BDD") beam (light blue arrow, path traveled by undiffracted order is shown) is diffracted to the same path as the yellow beam (which is the path traveled by the Doppler cooling/detection beam when the "Be BDD Switch" AOM is off); in other words the Doppler cooling/detection beam is combined with the detuned Doppler cooling beam using the AOM injection trick (Sec. A.2.2) through the "Be BDD Switch" AOM. This beam passes into the rest of the beamline when the "Be Dop Sw+" AOM is on (it follows the red arrow past this AOM). The ${}^9\mathrm{Be}^+$ ${}^2\mathrm{S}_{1/2}|1,1\rangle$ (green arrow) and ${}^2\mathrm{S}_{1/2}|2,1\rangle$ (magenta arrow) repumpers are combined using a 50/50 beamsplitter into the red arrow. This passes into the rest of the beamline at maximum power when the "Be Dop Sw+" AOM is off but the "Be Dop Sw-" AOM is on. In other words, the beams from the ${}^{9}\text{Be}^{+2}\text{S}_{1/2}\leftrightarrow {}^{2}\text{P}_{3/2}$ beamline (upper part) are combined with the beams from the ${}^9\mathrm{Be^{+2}S_{1/2}} \leftrightarrow {}^2\mathrm{P}_{1/2}$ beamline (lower part) through the "Be Dop Sw+" AOM using the AOM injection trick, while the "Be Dop Sw-" AOM functions to switch all ${}^9\mathrm{Be}^+$ resonant beams on and off. The diffracted order from the "Be Dop Sw-" AOM (orange arrow) passes through the ⁹Be⁺ resonant micromotion compensation EOM before passing into the ⁹Be⁺ resonant fiber. Also shown are the picked off light from the output of the fiber that travels to the experiment zone (dark red beam near bottom) and ⁹Be⁺ PI beam (white arrow, upper right).

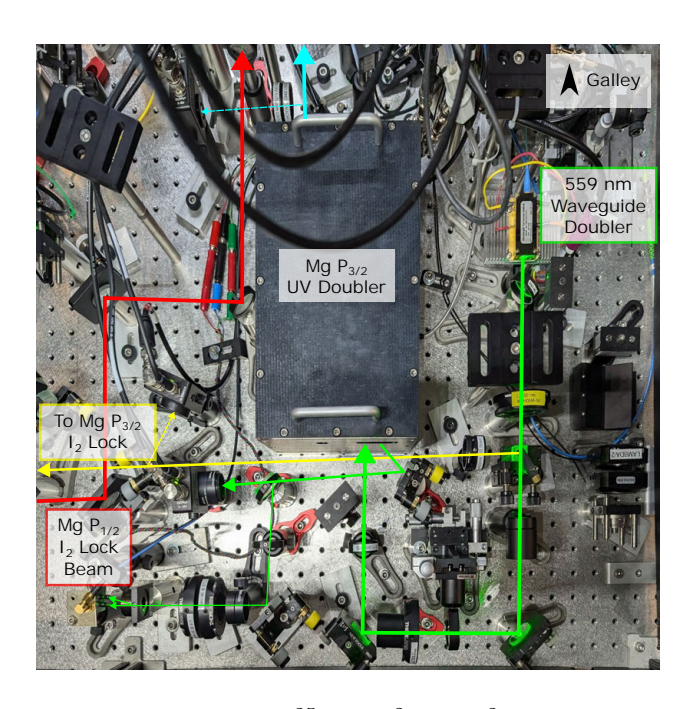


Figure A.22: Beamline photo overlay near $^{25}\mathrm{Mg^{+}}$ $^{2}\mathrm{S}_{1/2} \leftrightarrow ^{2}\mathrm{P}_{3/2}$ UV doubler. The light emitted by a NTT PPLN waveguide doubler (green arrow) is used to pump the $^{25}\mathrm{Mg^{+}}$ $^{2}\mathrm{S}_{1/2} \leftrightarrow ^{2}\mathrm{P}_{3/2}$ UV doubler. The reflected light is used to relock the UV cavity, and a small amount of light is picked off to use for a Hansch-Couillard lock (Sec. A.4.5). Some of the emitted light from the NTT waveguide doubler is reflected by a polarizing beam-splitter cube for the iodine lock (yellow arrow), and some of the iodine lock light is also picked off to be monitored. At the output of the UV doubler, there is a flipper mirror that can be used to deflect the output beam onto a photodetector for cavity alignment (blue dashed arrow). Also shown is the beam path of the iodine lock for the $^{2}\mathrm{S}_{1/2} \leftrightarrow ^{2}\mathrm{P}_{1/2}$ wavelength (red arrow).

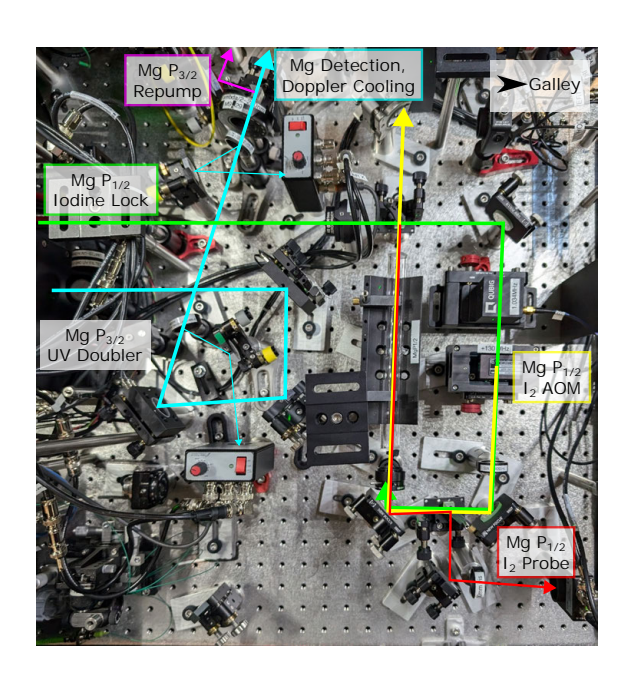


Figure A.23: Beamline photo overlay near $^{25}\mathrm{Mg}^+$ $^2\mathrm{S}_{1/2}\leftrightarrow^2\mathrm{P}_{1/2}$ iodine lock and output of $^{25}\mathrm{Mg}^+$ $^2\mathrm{S}_{1/2}\leftrightarrow^2\mathrm{P}_{3/2}$ UV doubler. The output of the UV doubler (blue arrow) is picked off and sent to two quadrant cell detectors; this signal is used for reference but the two large, square shaped mounts have piezo-knobs that can be used for active feedback. After some light is reflected by a polarizing beamsplitter (magenta beam) for the repump beam for $^{25}\mathrm{Mg}^+$ $^2\mathrm{S}_{1/2}|2,2\rangle$, the rest of the beam is used for (near and far-detuned) Doppler cooling and detection of $^{25}\mathrm{Mg}^+$. The image also shows the iodine lock for the $^{25}\mathrm{Mg}^+$ $^2\mathrm{S}_{1/2}\leftrightarrow^2\mathrm{P}_{1/2}$ wavelength (green arrow). Most of the light passes through a polarizing beam splitter and as described in Ref. [147], passes through an EOM is used for the modulation tone, and is diffracted by an AOM. This is the pump light that passes through the iodine cell (yellow arrow). Some light is reflected by the polarizing beamsplitter in the iodine lock (red arrow); this is the weaker probe beam. After passing through the iodine cell in the opposite direction from but overlapped with the pump beam, the light is reflected onto a photodetector. The intensity of the probe beam contains a signal due to absorption of the iodine molecules of the modulated probe beam.

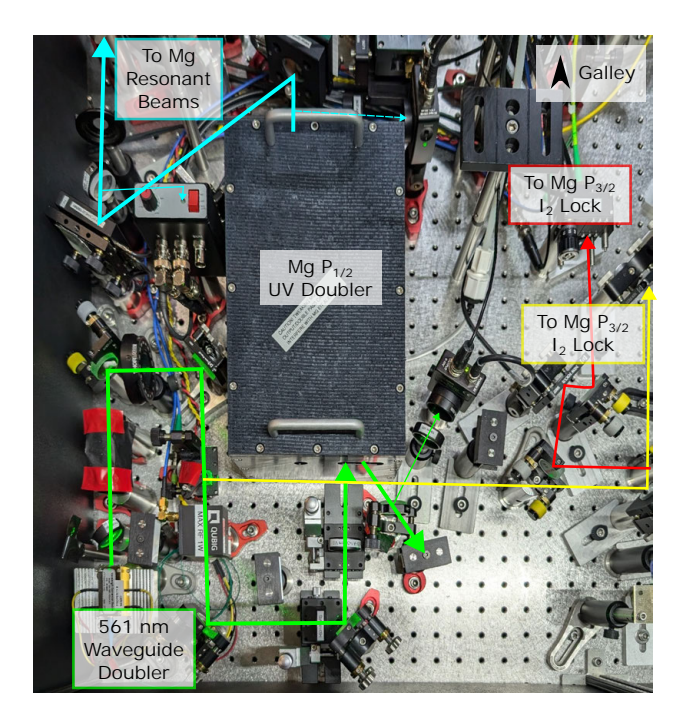


Figure A.24: Beamline photo overlay near $^{25}\mathrm{Mg}^+$ $^2\mathrm{S}_{1/2}\leftrightarrow^2\mathrm{P}_{1/2}$ UV doubler. The light emitted by a NTT PPLN waveguide doubler (green arrow) is used to pump the $^{25}\mathrm{Mg}^+$ $^2\mathrm{S}_{1/2}\leftrightarrow^2\mathrm{P}_{1/2}$ UV doubler, passing through an EOM for PDH locking. The light reflected from the cavity input mirror is sent through a bias tee; the RF component is used for the cavity lock and the DC part of the signal is used to relock the cavity. Part of the output of the UV doubler output (blue arrow) is picked off and monitored by a quadrant-cell detector (a second one is located in the region above this photo). This is currently only used to monitor the light but can be used for active feedback on the piezo-knob mounts (the two large mirror mounts immediately after the cavity output). A flipper mirror can be used to reflect the UV output onto a photodetector for cavity alignment (dashed blue arrow). The output of the NTT PPLN doubler is reflected by a polarizing beamsplitter (yellow arrow) for the $^{25}\mathrm{Mg}^+$ $^2\mathrm{S}_{1/2}\leftrightarrow^2\mathrm{P}_{1/2}$ iodine lock. Also shown is the light for the $^{25}\mathrm{Mg}^+$ $^2\mathrm{S}_{1/2}\leftrightarrow^2\mathrm{P}_{3/2}$ iodine lock (red arrow) that is coupled into a fiber to the iodine lock setup.

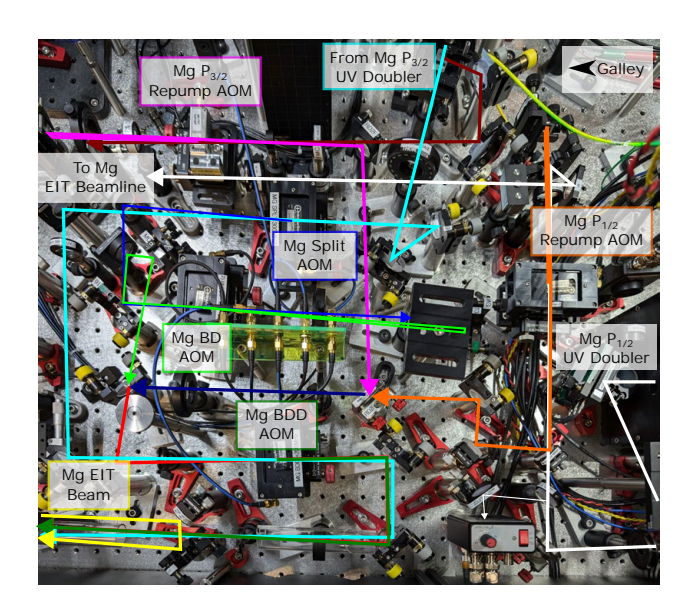


Figure A.25: Beamline photo overlay near $^{25}\mathrm{Mg}^+$ resonant AOMs. Some of the light emitted from the $^{25}\mathrm{Mg}^+$ $^2\mathrm{S}_{1/2}\leftrightarrow^2\mathrm{P}_{3/2}$ UV doubler (light blue arrow) is split off as the repump for $^2\mathrm{S}_{1/2}|2,2\rangle$ (dark red arrow), which is diffracted in double-pass configuration by the "Mg $^2\mathrm{P}_{3/2}$ Repump" AOM. This is combined with the light from the $^{25}\mathrm{Mg}^+$ $^2\mathrm{S}_{1/2}\leftrightarrow^2\mathrm{P}_{1/2}$ UV doubler (white arrow) after it is doubly-diffracted by the "Mg $^2\mathrm{P}_{1/2}$ Repump" AOM (orange arrow) on a 50/50 beamsplitter into the navy arrow. The (near/final) Doppler cooling and detection light is diffracted from the far detuned cooling light by the "Mg Split" AOM (dark blue arrow); this AOM is always on. The Doppler cooling/detection light is doubly diffracted by the "Mg BD" AOM (light green arrow) where it is combined with both repumpers by a 50/50 beamsplitter as the red arrow. Finally, the far detuned repump light is diffracted to travel the same path as these other resonant beams with the "Mg BDD AOM"; these are combined using the AOM injection trick (Sec. A.2.2). The $^{25}\mathrm{Mg}^+$ EIT cooling beams are also shown; the white arrow showing the undiffracted light from the "Mg $^2\mathrm{P}_{1/2}$ Repump" AOM is sent to the Mg EIT beamline; the yellow arrow near the bottom right is the return beam with the EIT cooling pump and repump beams overlapped; these are injected using the AOM injection trick with the "Mg Resonant Switch" AOM (not shown).

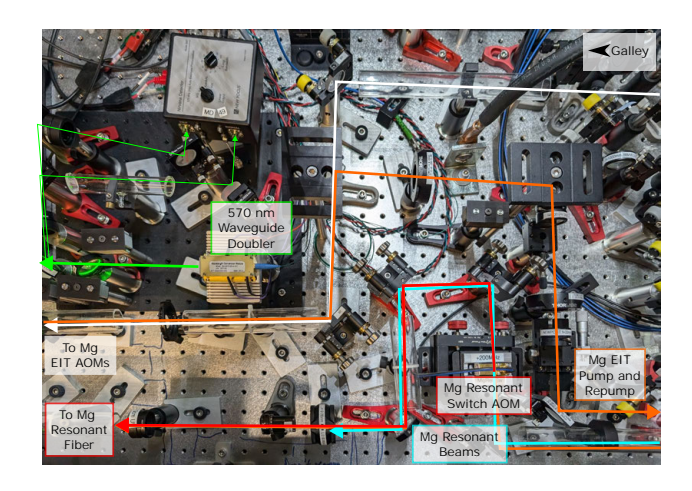


Figure A.26: Beamline photo overlay near $^{25}\text{Mg}^+$ PI iodine lock, showing the "Mg Resonant Switch" AOM and some of the $^{25}\text{Mg}^+$ EIT cooling beamline. The overlapped $^{25}\text{Mg}^+$ resonant beams (blue arrow, includes Doppler cooling, detection, and repump frequencies) is diffracted to pass into the $^{25}\text{Mg}^+$ resonant fiber by the "Mg Resonant Switch AOM". The $^{25}\text{Mg}^+$ EIT light from the $^{25}\text{Mg}^+$ $^2\text{S}_{1/2} \leftrightarrow ^2\text{P}_{1/2}$ UV doubler (white arrow) passes at a different height than the diffracted then overlapped $^{25}\text{Mg}^+$ EIT pump and repump beams (orange arrow), which are injected into the resonant fiber using the AOM injection trick (Sec. A.2.2) using the "Mg Resonant Switch AOM". Also shown is the $^{25}\text{Mg}^+$ PI waveguide doubler outputting 570 nm light (green arrow) which is picked off with a window to use for iodine locking. This iodine lock is coarse and does not use pump/probe spectroscopy but rather a single pass through the iodine cell (lower thin green arrow). The signal from the beam that passes through the iodine cell is compared to a reference beam (upper thin green arrow) using a balanced photodetector.

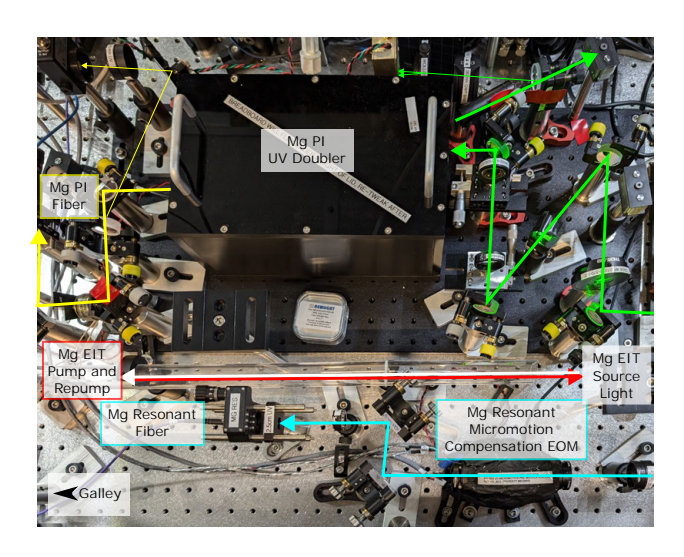


Figure A.27: Beamline photo overlay near $^{25}\mathrm{Mg^+}$ PI UV doubler and the $^{25}\mathrm{Mg^+}$ resonant fiber input. The $^{25}\mathrm{Mg^+}$ resonant light passes through a micromotion compensation EOM (encased in foil to keep the temperature stable) before passing into the fiber. The $^{25}\mathrm{Mg^+}$ EIT cooling beams are also shown; the source light from the $^{25}\mathrm{Mg^+}$ $^2\mathrm{S}_{1/2} \leftrightarrow ^2\mathrm{P}_{1/2}$ UV doubler (white arrow) travels to the left, and some of the light at the frequencies for $^{25}\mathrm{Mg^+}$ EIT cooling pump and repump beams return (red arrow) at a different height. The $^{25}\mathrm{Mg^+}$ PI light at 570 nm (green arrow) from the NTT waveguide doubler is used to pump the $^{25}\mathrm{Mg^+}$ PI UV doubler. The light reflected from the doubler cavity input mirror is used for a Hansch-Couillaud style lock (Sec. A.4.5). The output of the UV doubler (yellow arrow) is monitored using a small amount of picked off light (thin yellow arrow) for relocking the cavity; the rest of the light passes into a UV fiber (slightly out of photo frame to the left).

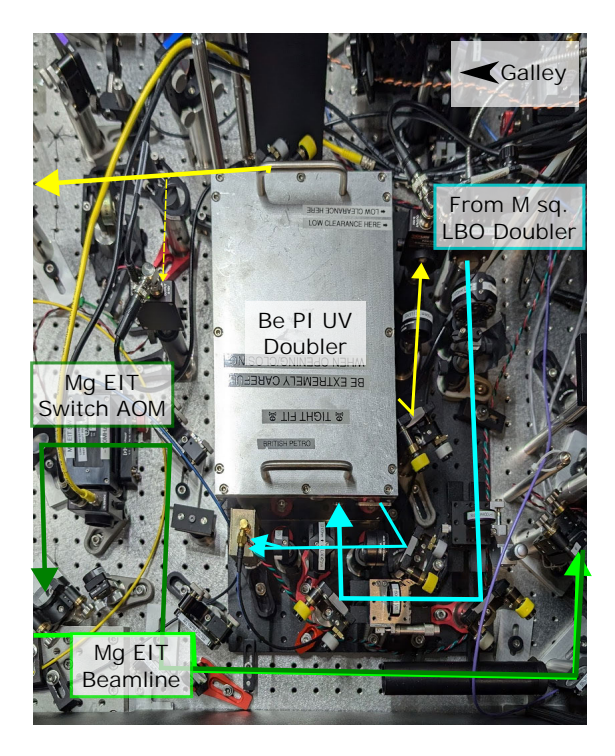


Figure A.28: Beamline photo overlay near ${}^{9}\text{Be}^{+}$ PI UV doubler, also showing part of the ${}^{25}\text{Mg}^{+}$ EIT beamline. The light is sent from the M Squared LBO doubler through a fiber to this table (blue arrow) and the reflected light from the input coupler of the ${}^{9}\text{Be}^{+}$ PI UV doubler is used for Hansch-Couillaud locking (Sec. A.4.5). The relock signal is the reflected UV light from one of the BBO crystal faces that exits a hole on the side of the UV doubler (yellow arrow near middle). The UV output beam (upper yellow arrow) can also be monitored directly (dashed yellow arrow). The lower part of the photo shows the ${}^{25}\text{Mg}^{+}$ EIT beamline. The beam passes to the left (dark green arrow) and then back towards the right (light green arrow) through vertically offset paths; the beam going to the AOMs shown in Fig. A.16 passes through the "Mg EIT Switch" AOM first (diffracted order not shown, but this is the order that passes to the rest of the EIT beamline).



Figure A.29: Beamline photo overlay near $^{25}\mathrm{Mg}^+$ $^2\mathrm{S}_{1/2}\leftrightarrow^2\mathrm{P}_{3/2}$ VECSEL. The output light (red arrow) passes through an optical isolator (large, silver) and is sent to the waveguide doubler through a fiber in the IR. A small amount of this light is picked off to use as an interlock signal (green arrow) so that this beam will be shuttered in front of the fiber if the power exceeds a certain threshold, in order to protect the waveguide doubler. A small amount of the light from this signal is picked off (yellow arrow) and sent to the wavemeter to monitor the frequency of this VECSEL. Because this VECSEL is sensitive to acoustics, temperature, and humidity, this whole area is encased in a padded foam box that can be seen at the edges of the photo.

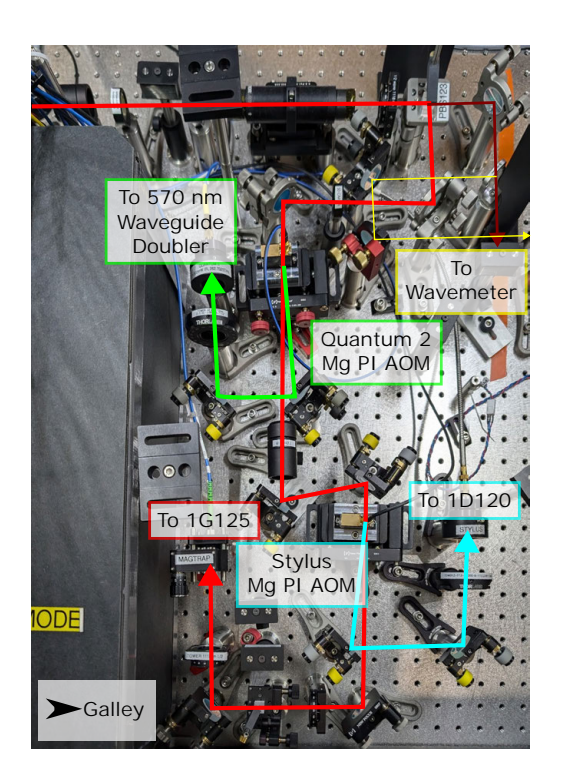


Figure A.30: Beamline photo overlay near ²⁵Mg⁺ PI light distribution optics. The light (red arrow) emitted from the ²⁵Mg⁺ PI VECSEL (upper left, slightly out of frame) passes through an optical isolator and is mainly reflected by a polarizing beamsplitter. This light is the same frequency as that needed for the (high magnetic field) "Magtrap" experiment, and the undiffracted order passes into a fiber going to 1G125. The first AOM ("Quantum 2 Mg PI") diffracts light into a fiber that sends light to the 570 nm NTT waveguide doubler elsewhere in this lab. The second AOM ("Stylus Mg PI") diffracts light in the other frequency direction for the (0.9 mT magnetic field) "Stylus" experiment in 1D120. All experiments receive light simultaneously and the frequency of the light is locked in this lab (see Fig. A.26). A small amount of light is transmitted through the polarizing beamsplitter near the beginning of the beam path and is picked off to be sent to the wavemeter.

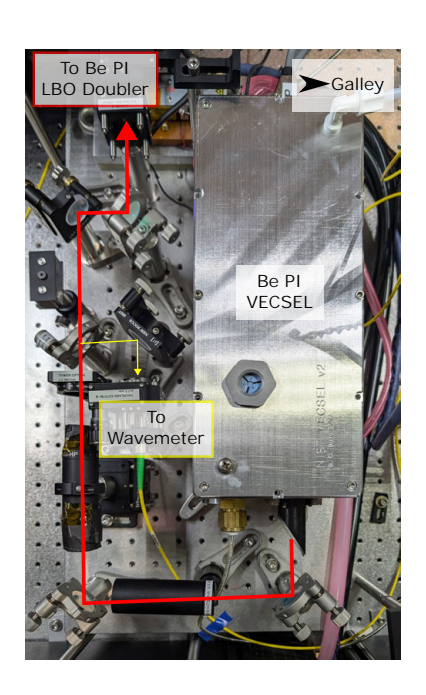


Figure A.31: Beamline photo overlay near ${}^9\mathrm{Be^+}$ PI VECSEL. The light (red arrow) emitted from the ${}^9\mathrm{Be^+}$ PI VECSEL passes through an optical isolator and passes into a fiber to pump an LBO doubler. A small amount of light is also picked off to monitor the frequency of this VECSEL using the wavemeter. The frequency of this VECSEL is locked using the wavemeter.

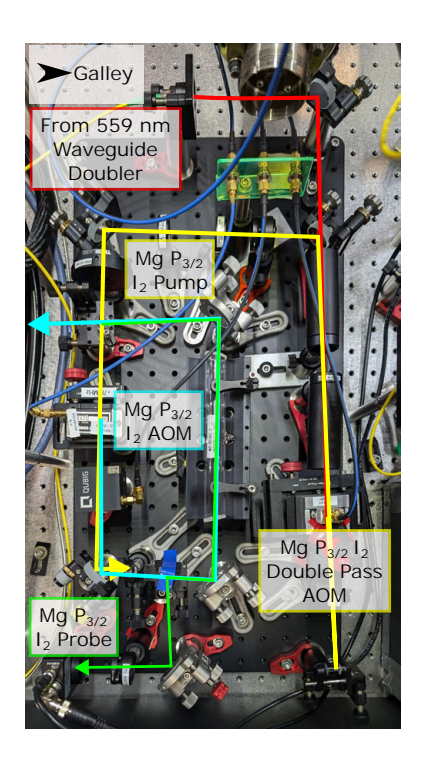


Figure A.32: Beamline photo overlay near $^{25}\mathrm{Mg}^+$ $^2\mathrm{S}_{1/2}\leftrightarrow^2\mathrm{P}_{3/2}$ iodine lock. Similar to the $^{25}\mathrm{Mg}^+$ $^2\mathrm{S}_{1/2}\leftrightarrow^2\mathrm{P}_{3/2}$ iodine lock, this is a pump-probe spectroscopy type setup using the EOM for modulation as described in Ref. [147]. The fiber output from the NTT waveguide doubler at 559 nm (red arrow) is first sent through the "Mg $^2\mathrm{P}_{3/2}$ I₂ Double Pass" AOM (used in double-pass configuration, yellow beam output) to offset the frequency so that it is close to a group of iodine molecule fringes. Most of the light passes through a polarizing beamsplitter is diffracted by an AOM (blue arrow); this is the pump light that passes through the iodine cell. Some light is reflected by the polarizing beamsplitter in the iodine lock (green arrow); this is the weaker probe beam. After passing through the iodine cell in the opposite direction from but overlapped with the pump beam, the light is reflected onto a photodetector. The intensity of the probe beam contains a signal due to absorption of the iodine molecules of the modulated probe beam.

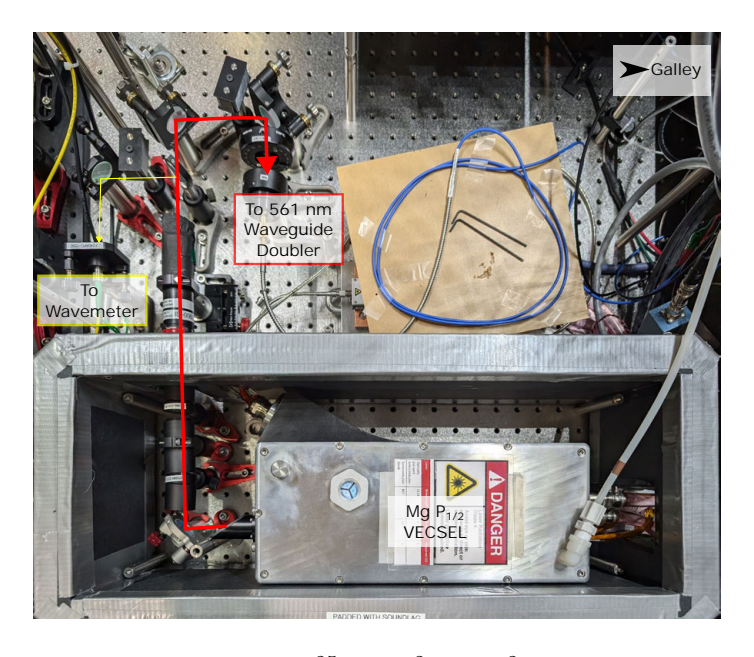


Figure A.33: Beamline photo overlay near $^{25}\mathrm{Mg}^+$ $^2\mathrm{S}_{1/2}\leftrightarrow^2\mathrm{P}_{1/2}$ VECSEL. The output light (red arrow) passes through an optical isolator and is sent to the waveguide doubler through a fiber in the IR. A small amount of the light from this beam is picked off (yellow arrow) and sent to the wavemeter to monitor the frequency of this VECSEL. Because this VECSEL is sensitive to acoustics, temperature, and humidity, the VECSEL can be seen to be encased in a foam-padded box.

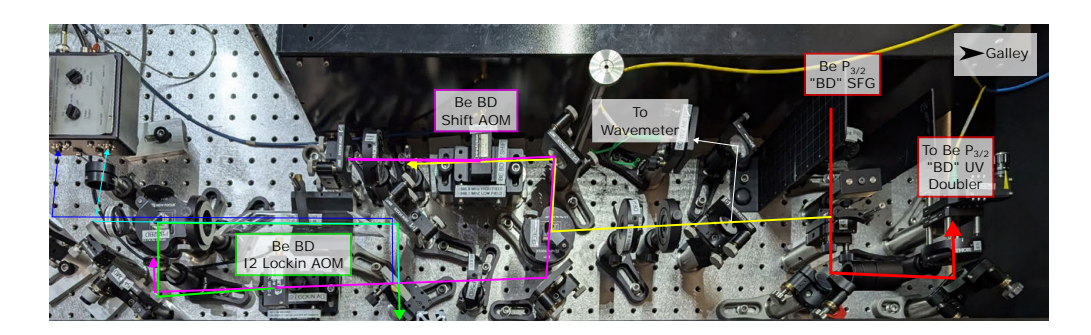


Figure A.34: Beamline photo overlay near ${}^9\mathrm{Be^+}$ ${}^2\mathrm{S}_{1/2} \leftrightarrow {}^2\mathrm{P}_{3/2}$ ("BD") iodine lock. The beam from the SFG setup is mainly sent to a fiber to the ${}^9\mathrm{Be^+}$ ${}^2\mathrm{S}_{1/2} \leftrightarrow {}^2\mathrm{P}_{3/2}$ ("BD") UV doubler, but some is reflected by a polarizing beamsplitter to be used for the iodine lock (yellow arrow). A small portion of this light is picked off (white arrow) to be monitored using the wavemeter. The light for the iodine lock is first shifted in frequency (magenta arrow) by the "Be BD Shift" AOM, used in double-pass configuration. A thick piece of glass is used to generate a double reflection, one for a probe beam (light blue arrow) that is overlapped with the pump beam, and another that is a reference beam (dark blue arrow). This style of iodine lock relies on a modulation on the RF signal driving the "Be BD I2 Lockin" AOM. The diffracted beam (green arrow) passes through the iodine cell and is overlapped with the probe beam.

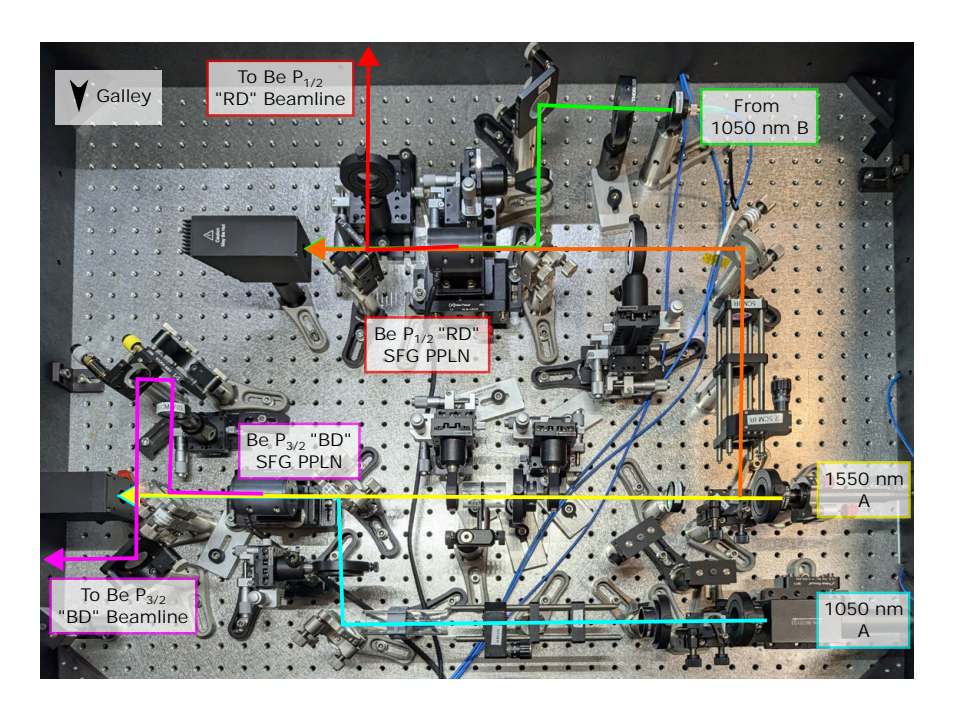


Figure A.35: Beamline photo overlay for ${}^9\mathrm{Be}^+$ resonant SFG setups (for both ${}^9\mathrm{Be}^+$ ${}^2\mathrm{S}_{1/2}\leftrightarrow{}^2\mathrm{P}_{1/2}$ and ${}^9\mathrm{Be}^+$ ${}^2\mathrm{S}_{1/2}\leftrightarrow{}^2\mathrm{P}_{3/2}$). IR wavelengths 1550 nm (yellow arrow) and 1050 nm (blue arrow) are emitted from amplified fiber laser sources and physically overlapped in a PPLN crystal to generate 626 nm light (magenta arrow) for the ${}^9\mathrm{Be}^+$ ${}^2\mathrm{S}_{1/2}\leftrightarrow{}^2\mathrm{P}_{3/2}$ ("BD") beamline. Some light from the 1550 nm A is split off (orange arrow) using a polarizing beamsplitter element and sent to the resonant SFG setup to be used for the ${}^9\mathrm{Be}^+$ ${}^2\mathrm{S}_{1/2}\leftrightarrow{}^2\mathrm{P}_{1/2}$ wavelength; this is overlapped with fibered light from 1050 nm B to generate 626 nm light (red arrow) for the ${}^9\mathrm{Be}^+$ ${}^2\mathrm{S}_{1/2}\leftrightarrow{}^2\mathrm{P}_{1/2}$ ("RD") beamline.

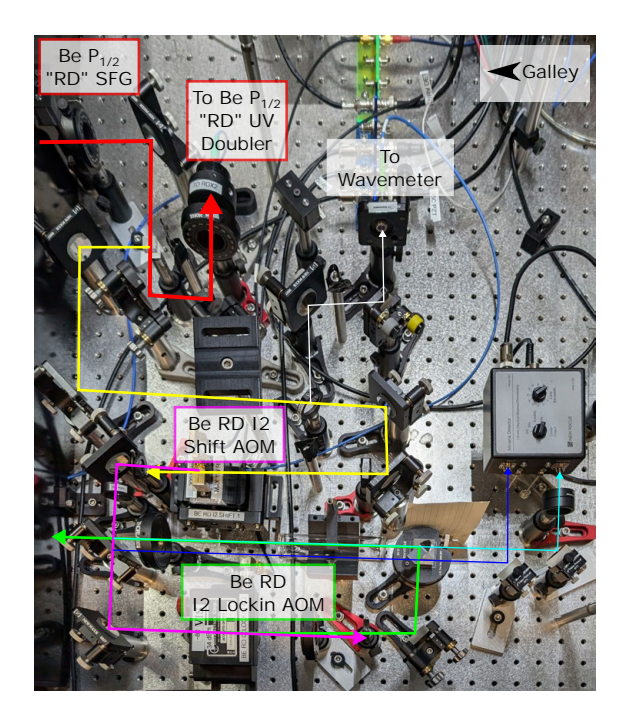


Figure A.36: Beamline photo overlay near ${}^9\mathrm{Be}^+$ ${}^2\mathrm{S}_{1/2} \leftrightarrow {}^2\mathrm{P}_{1/2}$ ("RD") iodine lock. The beam from the SFG setup is mainly sent to a fiber to the ${}^9\mathrm{Be}^+$ ${}^2\mathrm{S}_{1/2} \leftrightarrow {}^2\mathrm{P}_{1/2}$ ("RD") UV doubler, but some is reflected by a polarizing beamsplitter to be used for the iodine lock (yellow arrow). A small portion of this light is picked off (white arrow) to be monitored using the wavemeter. The light for the iodine lock is first shifted in frequency (magenta arrow) by the "Be RD I2 Shift" AOM. A thick piece of glass is used to generate a double reflection, one for a probe beam (light blue arrow) that is overlapped with the pump beam, and another that is a reference beam (dark blue arrow). This style of iodine lock relies on a modulation on the RF signal driving the "Be RD I2 Lockin" AOM. The diffracted beam (green arrow) passes through the iodine cell and is overlapped with the probe beam.

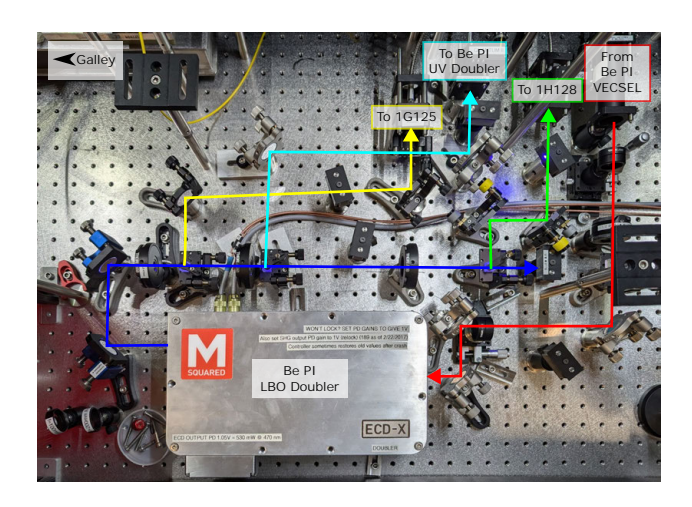


Figure A.37: Beamline photo overlay near ${}^9\mathrm{Be}^+$ PI LBO doubler and light distribution system. The light from the ${}^9\mathrm{Be}^+$ PI VECSEL (red arrow) pumps the M Squared LBO doubler which outputs 570 nm light (dark blue arrow). Depending on the polarization of this light (which can be controlled by a series of waveplates) the light is sent to the "Triangle Trap" experiment in 1G125 (yellow arrow) the ${}^9\mathrm{Be}^+$ PI UV doubler in this lab (light blue arrow) or the Penning trap experiment in 1H128 (green arrow). Unfortunately, the output of the LBO doubler is such that there is not sufficient power to distribute to all experiments simultaneously. Moreover, the ionization frequency required for the Penning trap is significantly different from that required for the other two experiments, so the VECSEL etalon temperature is changed by $\approx 4^\circ\mathrm{C}$ to change between the two frequencies.

Appendix B

Mode Coupling Extended Data

B.1 Mode Coupling Joint Population Measurements

The following are figures showing joint population measurement results for mode coupling in the nine-state subspace $\{|0\rangle_{\rm O}, |1\rangle_{\rm O}, |2\rangle_{\rm O}\} \otimes \{|0\rangle_{\rm A}, |1\rangle_{\rm A}, |2\rangle_{\rm A}\}$ using the six-state fluorescence result space $\{|\uparrow\rangle_{\rm Mg}, |\downarrow\rangle_{\rm Mg}\} \otimes \{|\uparrow\uparrow\rangle_{\rm Be}, |\uparrow\downarrow\rangle_{\rm Be}, |\downarrow\downarrow\rangle_{\rm Be}\}$ for the ${}^9{\rm Be}^+$ - ${}^2{\rm SMg}^+$ - ${}^9{\rm Be}^+$ crystal. As mentioned in the maintext, three iterations of the experiment are performed where each of the ALT mode Fock states are mapped to $|\uparrow\rangle_{\rm Mg}$, while RAP is used to map $|0\rangle_{\rm O} \to |\downarrow\downarrow\rangle_{\rm Be}$ and $|1\rangle_{\rm O} \to |\uparrow\downarrow\rangle_{\rm Be}/|\downarrow\uparrow\rangle_{\rm Be}$.

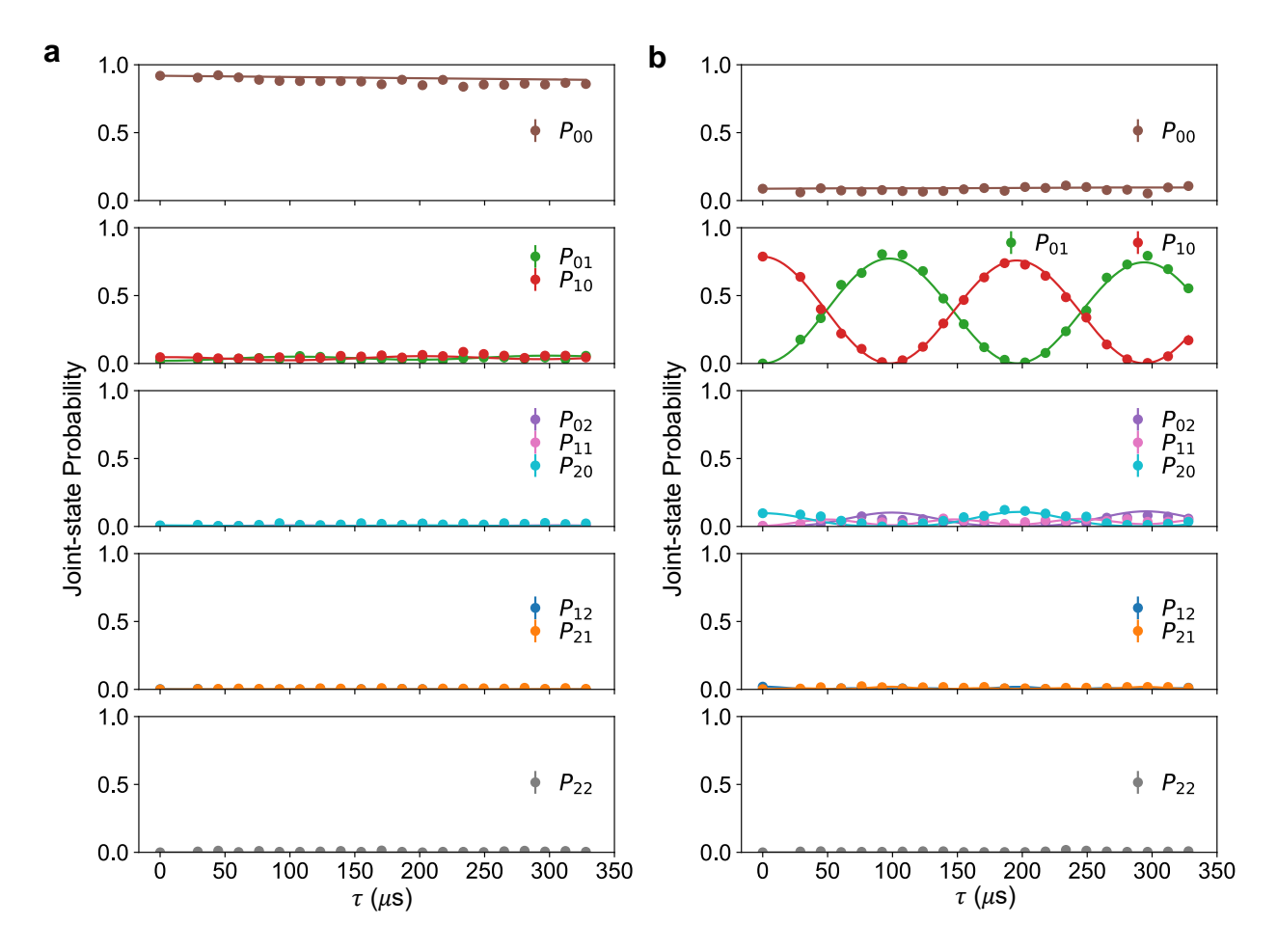


Figure B.1: The two normal modes are prepared in (a) $|0\rangle_A |0\rangle_O$ or (b) $|1\rangle_A |0\rangle_O$. The plots show population in the nine joint number states (where $P_{a,b}$ denotes a phonons in ALT and b phonons in OOPH) of the ALT mode and the OOPH mode as a function of coupling time τ in five separate panels with (from top to bottom) 0 to 4 total quanta of motion in the two modes. Imperfect state preparation and measurement cause the population of the target initial state to deviate from one at $\tau=0$ while the other state populations may start with a non-zero value.

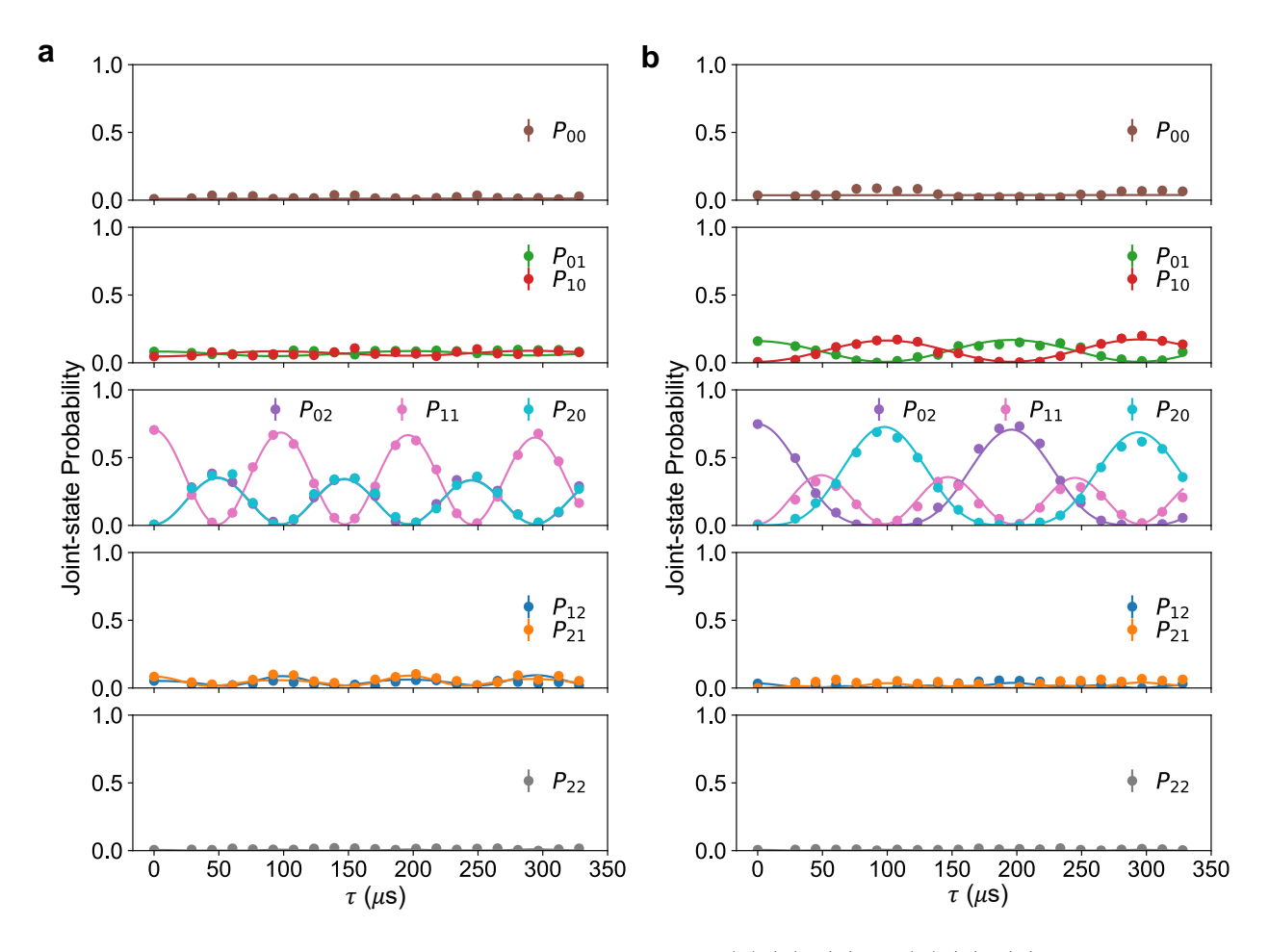


Figure B.2: The ALT and OOPH modes are prepared in (a) $|1\rangle_{\rm A} |1\rangle_{\rm O}$, (b) $|0\rangle_{\rm A} |2\rangle_{\rm O}$. The coupling time is scanned and the resulting observed population for 0 to 4 total quanta (panels top to bottom) are shown.

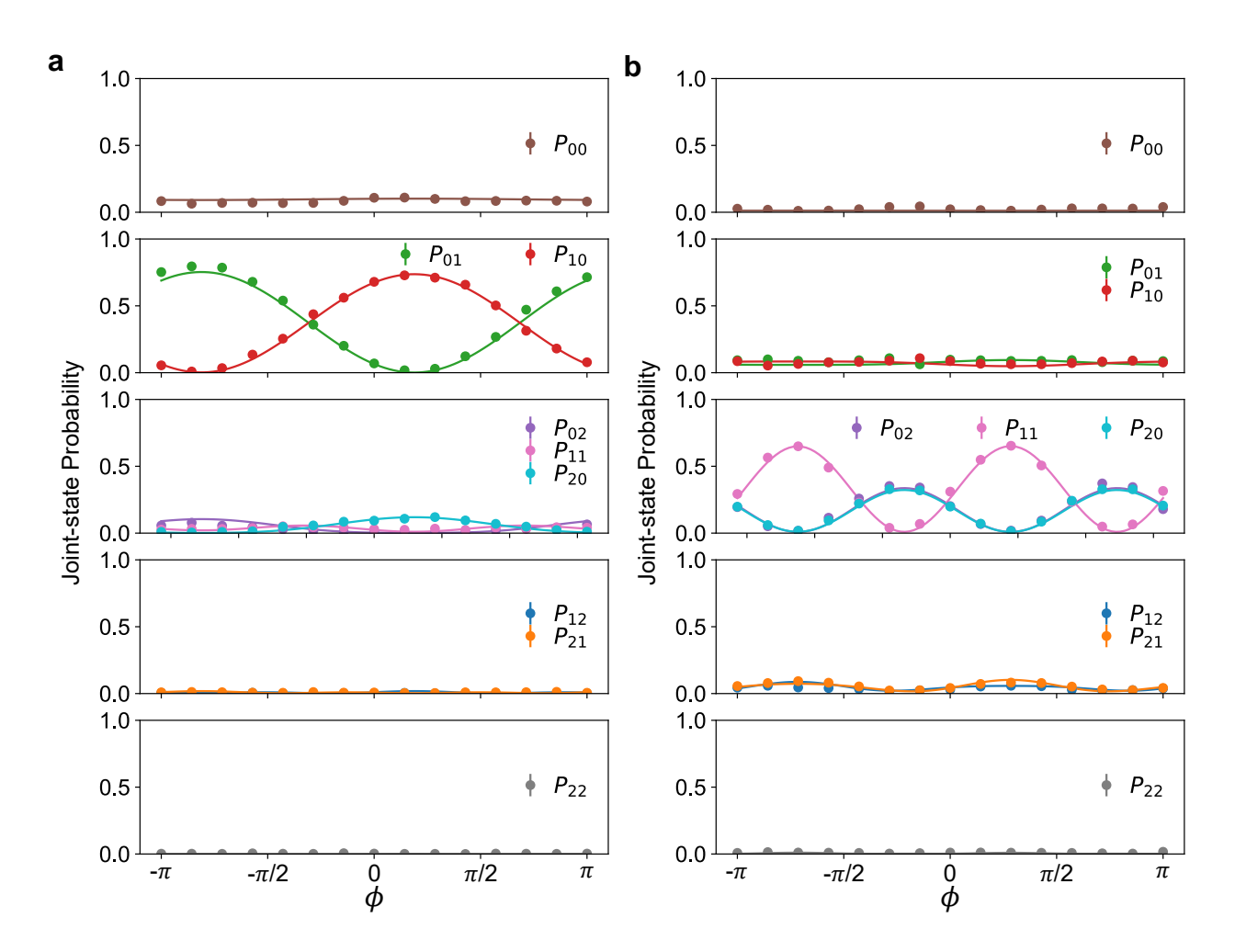


Figure B.3: Phonon interference with the initial states (a) $|1\rangle_{\rm A} |0\rangle_{\rm O}$ and (b) $|1\rangle_{\rm A} |1\rangle_{\rm O}$ is shown.

B.2 Cooling Using Mode Coupling Two-Ion Fit Data

Here, the fit results from the indirect cooling using mode coupling of the two ion crystals ${}^{9}\text{Be}^{+}$ - ${}^{9}\text{Be}^{+}$ and ${}^{9}\text{Be}^{+}$ - ${}^{25}\text{Mg}^{+}$ are summarized.

Crystal	Coupled	Measured	A	$\Omega/(2\pi)$	$T (\mu s)$	$\omega_0/2\pi$	P_0
Ciystai	modes	mode	Α	(kHz)	μ (μ s)	(MHz)	10
$^9\mathrm{Be}^+$ - $^9\mathrm{Be}^+$	zo-yo	zo	1.2(1)	7(2)	67(5)	0.1394(3)	0.07(3)
⁹ Be ⁺ - ⁹ Be ⁺	zo-yo	yo	-1.29(7)	8(1)	65(3)	0.1393(2)	1.36(2)
$^9\mathrm{Be}^+$ - $^9\mathrm{Be}^+$	zo-xo	zo	1.1(2)	4(1)	96(5)	0.1386(1)	0.21(1)
$^{9}{ m Be}^{+}$ - $^{9}{ m Be}^{+}$	zo-xo	xo	-1.1(1)	3.6(6)	84(3)	0.1386(2)	1.34(2)
$^{9}{\rm Be}^{+}$ - $^{25}{\rm Mg}^{+}$	zo-yo	zo	-0.79(3)	5.2(4)	101(3)	0.7116(1)	0.944(7)
$^{9}{\rm Be}^{+}$ - $^{25}{\rm Mg}^{+}$	zo - xo	zo	-0.97(2)	5.4(3)	98(2)	0.2485(1)	0.976(5)

Table B.1: Fit parameters from frequency-scan data for coupling operations used for indirect cooling of ${}^{9}\text{Be}^{+}$ - ${}^{9}\text{Be}^{+}$ and ${}^{9}\text{Be}^{+}$ - ${}^{25}\text{Mg}^{+}$, where xo, yo, and zo denote x-OOPH, y-OOPH, and z-OOPH respectively. The results shown in Fig. 5.7 (b) and (d) (${}^{9}\text{Be}^{+}$ - ${}^{9}\text{Be}^{+}$) and Fig. 5.9 (a) and (c) (${}^{9}\text{Be}^{+}$ - ${}^{25}\text{Mg}^{+}$) are fitted to Eq. 5.19. The fitted values and uncertainties for all parameters are listed.

Crystal	Coupled modes	Measured mode	A	$\Omega_c/(2\pi)$ (kHz)	$\phi_c \text{ (rad)}$	$\tau_c \; (\mathrm{ms})$	y_0
⁹ Be ⁺ - ⁹ Be ⁺	zo-yo	zo	1.20(6)	7.84(6)	-1.38(6)	1.5(8)	0.67(1)
⁹ Be ⁺ - ⁹ Be ⁺	zo - yo	yo	1.34(4)	7.91(4)	1.66(4)	2.6(1.6)	0.69(1)
${}^{9}{\rm Be^{+}}$ - ${}^{9}{\rm Be^{+}}$	zo - xo	zo	1.12(8)	4.70(5)	-1.42(8)	1.3(5)	0.68(1)
$^9\mathrm{Be^+}$ - $^9\mathrm{Be^+}$	zo-xo	xo	1.10(6)	4.77(6)	1.64(6)	3.7(3.0)	0.78(1)
$^{9}{\rm Be^{+}}$ - $^{25}{\rm Mg^{+}}$	zo - yo	zo	0.78(6)	10.1(1)	1.58(1)	1.4(1.1)	0.514(9)
$^{9}{\rm Be}^{+}$ - $^{25}{\rm Mg}^{+}$	zo - xo	zo	0.88(4)	10.5(1)	1.42(6)	16(83)	0.502(6)

Table B.2: Fit parameters from time-scan data for coupling operations used for indirect cooling of ${}^{9}\text{Be}^{+}$ - ${}^{9}\text{Be}^{+}$ and ${}^{9}\text{Be}^{+}$ - ${}^{25}\text{Mg}^{+}$, where xo, yo, and zo denote x-OOPH, y-OOPH, and z-OOPH respectively. The results shown in Fig. 5.7 (c) and (e) (${}^{9}\text{Be}^{+}$ - ${}^{9}\text{Be}^{+}$) and Fig. 5.9 (b) and (d) (${}^{9}\text{Be}^{+}$ - ${}^{25}\text{Mg}^{+}$) are fitted to Eq. 5.20. The values of Ω_c for the ${}^{9}\text{Be}^{+}$ - ${}^{25}\text{Mg}^{+}$ ion crystal are larger than those (labeled Ω) in Table II because stronger coupling drives are used.

B.3 Mode Coupling Repeated Measurement Results

Exp.		M1 (N=1))		M2 (N=1))
$\{o_1\}$	$\{d\}$	$\{b\}$	Overall	$\{d\}$	$\{b\}$	Overall
MAS	0.931(4)	0.76(3)	0.924(3)	0.84(2)	0.915(4)	0.910(4)
MSS	0.030(2)	0.49(3)	0.048(3)	0.33(2)	0.044(3)	0.064(3)
Prob.	0.960(3)	0.040(3)	1	0.066(3)	0.934(3)	1

Table B.3: Sideband transition probabilities conditioned on different motional state measurement outcomes for N=1. The table shows the probability of a spin flip after a MAS or MSS π pulse, conditioned on outcome $\{o_1\}=\{d\}$ and $\{b\}$ for mapping M1 and M2 and the probability of outcomes d (dark) and b (bright). The overall sideband spin-flip probabilities with no conditioning on measurement outcomes are also shown.

Exp.			$\mathrm{M1} \ (N=2)$					M2 (N=2)		
$\{o_1,o_2\}$	$\{d,d\}$	$\{d,b\}$	$\{d,b\}$ $\{b,d\}$ $\{b,b\}$ Overall $\{d,d\}$ $\{d,b\}$ $\{b,d\}$ $\{b,d\}$ Overall	$\{b,b\}$	Overall	$\{d,d\}$	$\{d,b\}$	$\{b,d\}$	$\{b,b\}$	Overall
MAS	MAS 0.924(4)	0.78(2)	$ \begin{array}{c ccccccccccccccccccccccccccccccccccc$	0.57(4)	0.908(4)	0.56(4)	0.91(2)	0.73(2)	0.929(4)	0.903(4)
$\overline{\mathrm{MSS}}$	0.027(2)	0.46(3)	46(3) 0.08(2) 0.77(4) 0.066(3) 0.73(4) 0.05(1) 0.53(2) 0.044(3) 0.102(4)	0.77(4)	0.066(3)	0.73(4)	0.05(1)	0.53(2)	0.044(3)	0.102(4)
Prob.	Prob. $0.900(4)$	0.049(3)	049(3) $0.029(2)$ $0.022(2)$	0.022(2)	1	0.025(2)	0.025(2) $0.042(3)$ $0.083(4)$ $0.850(5)$	0.083(4)	0.850(5)	1

Table B.4: Sideband transition probabilities conditioned on different motional state measurement outcomes for N = 2. Similar to table B.3, listing results for all combinations of two measurement outcomes.

		M1 (7	$\mathrm{M1}\ (N\!=\!3)$				
MAS $0.935(2)$ $0.74(2)$ $0.89(2)$ $0.64(3)$ $0.93(2)$ $0.60(8)$ MSS $0.025(2)$ $0.51(2)$ $0.13(2)$ $0.78(2)$ $0.03(1)$ $0.78(7)$ Prob. $0.876(6)$ $0.036(2)$ $0.020(1)$ $0.024(1)$ $0.021(1)$ $0.0028(5)$ Exp. $A.A.A.A.A.A.A.A.A.A.A.A.A.A.A.A.A.A.A.$	$\{d, b, d\}$ $\{d, b, b\}$ $\{b, d\}$	$,d\} \qquad \{b,d,b\}$	$\{b,b,d\}$	$\{b,b,b\}$	$\{ {\rm Majority}\ d \}$	$\{ {\rm Majority}\ b \}$	Overall
MSS $0.025(2)$ $0.51(2)$ $0.13(2)$ $0.78(2)$ $0.03(1)$ $0.78(7)$ Prob. $0.876(6)$ $0.036(2)$ $0.020(1)$ $0.024(1)$ $0.021(1)$ $0.0028(5)$ Exp. A	0.64(3)		0.75(6)	0.59(4)	0.926(2)	0.63(2)	0.912(3)
Prob. $0.876(6)$ $0.036(2)$ $0.020(1)$ $0.024(1)$ $0.021(1)$ $0.0028(5)$ Exp. A	0.78(2)		0.22(6)	0.82(3)	0.047(2)	0.74(2)	0.08(2)
	0.020(1) 0.024(1) 0.02	(1) 0.0028(5)	0.0046(6)	0.016(1)	0.952(1)	0.048(1)	1
		M2 (1	V = 3				
0.48(9) 1.0 0.8(1) 0.92(3) 0.66(5) 0.80(8) 0.07(7) 0.4(2) 0.03(2) 0.76(5)	$\{d, b, d\}$ $\{d, b, b\}$ $\{b, d\}$		$\{b, d, b\}$ $\{b, b, d\}$		$\{b,b,b\}$ {Majority $d\}$ {Majority $b\}$ Overall	${\rm \{Majority\ }b\}$	Overall
0.80(8) 0.07(7) 0.4(2) 0.03(2) 0.76(5)	0.92(3)		0.72(4)	0.927(7)	0.64(4)	0.908(7)	0.891(7)
	0.03(2)		0.46(4)	0.045(5)	0.68(4)	0.077(6)	0.118(7)
Prob. $0.015(3) 0.004(1) 0.006(2) 0.034(4) 0.043(5) 0.042(5)$	0.006(2) 0.034(4) 0.04;		0.075(6)	0.783(9)	0.067(4)	0.933(4)	1

Table B.5: Sideband transition probabilities conditioned on different motional state measurement outcomes for N=3. Similar to the previous two tables. In addition, majority d or b is conditioned on at least two out of three outcomes being d or b.